الجمهورية الجزائرية الديمقراطية الشعبية
République Algérienne Démocratique et Populaire
وزارة التعليم العالي و البحث العلمي
Ministère de l'Enseignement Supérieur et de la Recherche Scientifique

Université Mohamed Khider – Biskra
Faculté des Sciences et de la Technologie
Département : Génie Électrique
Ref : ……

جامـعة محمد خيضر - بسكرة
كليـة العلـوم والتكنـولوجيا
قسم : الهندسة الكهربائية
المرجع : .....

Thèse Présentée en vue de l'obtention du diplôme de

Doctorat LMD en Génie Électrique

Spécialité : Électromécanique

TITRE

Contribution à la commande d'un système de compensation de la puissance réactive alimenté par un générateur photovoltaïque

Présentée par :

Djallal Eddine ZABIA

Soutenue publiquement le 07/12/2025

Pr. Mohamed-Yacine HAMMOUDI	**Professeur**	**Président**	**Université de Biskra**
Pr. Okba KRAA	**Professeur**	**Rapporteur**	**Université de Biskra**
Dr. Hamza AFGHOUL	**MCA**	**Co-Rapporteur**	**Univ. Setif 1**
Pr. Sabrina ABDEDDAIM	**Professeur**	**Examinateur**	**Université de Biskra**
Dr. Amar BOUAFASSA	**MCA**	**Examinateur**	**ENP. Constantine**

People's Democratic Republic of Algeria
Ministry of Higher Education and Scientific Research
Mohamed Khider University of Biskra
Faculty of Sciences and Thechnology
Department of Electrical Engineering

Order Number: .....

THESIS

In Candidacy for the Degree of

DOCTOR 3rd CYCLE IN ELECTRICAL ENGINEERING

Option: Electromechanics

TITLE

Contribution to the control of a reactive power compensation system powered by a photovoltaic generator

Presented by **Djallal Eddine ZABIA**

Defended on: 07/12/2025

In front of the jury composed of:

Pr. Mohamed-Yacine HAMMOUDI	**Professor**	**Presedent**	**University of Biskra**
Pr. Okba KRAA	**Professor**	**Supervisor**	**University of Biskra**
Dr. Hamza AFGHOUL	**MCA**	**Co-Supervisor**	**Univ. Setif 1**
Pr. Sabrina ABDEDDAIM	**Professor**	**Examiner**	**University of Biskra**
Dr. Amar BOUAFASSA	**MCA**	**Examiner**	**ENP. Constantine**

Acknowledgments

This thesis represents not only the culmination of my academic efforts but also a journey made possible by the unwavering support, guidance, and love of those around me. Words alone cannot capture the depth of my gratitude, but I hope to express my heartfelt appreciation to those who have been my pillars throughout this endeavor.

First and foremost, I owe an immense debt of gratitude to my professor, **Pr. Okba Kraa**, whose influence on my life transcends the boundaries of academia. From the very beginning of my academic career, Pr. Kraa has been a mentor, a guide, and, above all, a big brother whose kindness and generosity have left an indelible mark on my heart. His unwavering belief in me carried me through moments of doubt, and his encouragement pushed me to persevere even when life's challenges—both personal and financial—seemed insurmountable. During the darkest times, when events threatened to derail my progress, his support was a beacon of hope, lifting me up and inspiring me to continue. There are no words adequate to describe the gratitude I feel for Pr. Kraa; his mentor-ship has shaped not only this thesis but who I am today. Thank you, from the bottom of my heart, for everything.

I am also deeply grateful to my co-supervisor, **Pr. Hamza Afghoul**, whose expertise and generosity with knowledge were invaluable throughout this research. His insights, patience, and willingness to share his expertise enriched my understanding and strengthened this work. Hamza's contributions were instrumental, and I am sincerely thankful for his guidance and support.

I extend my sincere appreciation to the esteemed members of my thesis jury for their time, expertise, and valuable feedback during my soutenance: **Pr. Mohamed-Yacine Hammoudi**, **Mme. Pr Sabrina Abdeddaim**, and **M. Amar Bouafassa**. Their thoughtful evaluations and contributions have greatly enriched this work, and I am deeply grateful for their involvement.

To my beloved parents, **Mama** and **Papa**, I owe more than I can ever repay. Your unconditional love, prayers, and encouragement have been my foundation. A special thanks to my dear father, whose care and curiosity about my work touched me deeply. His constant questions about my progress and genuine desire to understand my contributions—not just as a parent but as someone truly invested in my journey—gave me strength and motivation. Papa, your pride in me means the world, and I am forever grateful for your unwavering support.

Abstract

Photovoltaic (PV) systems under partial shading conditions (PSCs) exhibit complex power-voltage characteristics, reducing energy yield with conventional Maximum Power Point Tracking (MPPT) methods like Perturb & Observe. This thesis presents a comprehensive framework to optimize PV performance and grid integration through advanced control and emulation strategies. The Enhanced Eel-Grouper Optimization (EEGO) algorithm, a novel metaheuristic MPPT approach, achieves near-optimal tracking efficiency (>99%) by swiftly identifying the global maximum power point across diverse shading scenarios. A dynamic restart mechanism ensures reliable adaptation to sudden environmental changes, enhancing system stability. A cost-effective PV emulator, built around a DC programmable source (GW Instek APS-1102A, 1000 W), accurately replicates PSC-induced I-V curves in a low-scale laboratory grid setup (500 W), enabling robust algorithm validation. An Real-Time MPPT framework, implemented on a dSPACE 1104 platform, dynamically adjusts control parameters to minimize fluctuations and support grid stability. To enhance power quality, a Shunt Active Power Filter (SAPF) with Predictive Direct Power Control (PDPC) reduces current Total Harmonic Distortion to below 5%, achieving near-unity power factor and compliance with IEEE 519-2022 standards under variable loads. Experimental validation using the dSPACE 1104 and DC programmable source demonstrates superior energy efficiency and grid compatibility. This framework advances PV system optimization, offering a scalable solution for sustainable energy integration in smart grid applications. **Keywords:** Maximum Power Point Tracking (MPPT), Enhanced Eel-Grouper Optimization (EEGO), Partial Shading Conditions (PSC), Shunt Active Power Filter (SAPF)

ملخص

تظهر الأنظمة الكهروضوئية تحت ظروف التظليل الجزئي خصائص معقدة للقدرة مقابل الجهد، مما يقلل من إنتاج الطاقة باستخدام طرق تتبع نقطة القدرة القصوى التقليدية مثل الاضطراب والمراقبة. تقدم هذه الأطروحة إطارا شاملا لتحسين أداء الأنظمة الكهروضوئية وتكاملها مع الشبكة من خلال استراتيجيات تحكم ومحاكاة متقدمة. يحقق خوارزمية تحسين الانقليس-الهامور المحسنة، وهي نهج ميتاهيوريستيكي جديد لتتبع نقطة القدرة القصوى، كفاءة تتبع شبه مثالية (تتجاوز 99 %) من خلال تحديد نقطة القدرة القصوى العالمية بسرعة عبر سيناريوهات تظليل متنوعة. تضمن آلية إعادة تشغيل ديناميكية التكيف الموثوق مع التغيرات البيئية المفاجئة، مما يعزز استقرار النظام. يعمل محاكي كهروضوئي فعال، مبني حول مصدر تيار مستمر قابل للبرمجة (جي دبليو إنستيك APS – 1102A، 1000 W)، على إعادة إنتاج منحنيات التيار-الجهد الناتجة عن التظليل الجزئي بدقة في إعداد شبكة مختبرية صغيرة الحجم (حوالي 500 W)، مما يتيح التحقق القوي من الخوارزميات. يعدل إطار تتبع نقطة القدرة القصوى الوقت الحقيقي، المطبق على منصة دي سبيس 1104، معايير التحكم ديناميكيا لتقليل التقلبات ودعم استقرار الشبكة. لتحسين جودة الطاقة، يقلل مرشح الطاقة النشط المتوازي مع التحكم التنبؤي المباشر بالطاقة من التشوه التوافقي الكلي للتيار إلى أقل من 5 %، محققا عامل قدرة شبه موحد ومتوافقا مع معايير IEEE519 – 2022 تحت أحمال متغيرة. تثبت التحقق التجريبي باستخدام دي سبيس 1104 ومصدر التيار المستمر القابل للبرمجة كفاءة طاقة متميزة وتوافقا مع الشبكة. يعزز هذا الإطار تحسين الأنظمة الكهروضوئية، مقدما حلا قابلا للتطوير لتكامل الطاقة المستدامة في تطبيقات الشبكات الذكية. الكلمات المفتاحية: تتبع نقطة القدرة القصوى ، خوارزمية الانقليس-الهامور المحسنة ، التظليل الجزئي، مرشح القدرة النشط المتوازي

Résumé

Les systèmes photovoltaïques (PV) sous conditions d'ombrage partiel (COP) présentent des caractéristiques puissance-tension complexes, réduisant le rendement énergétique avec les méthodes conventionnelles de suivi du point de puissance maximale (SPPM), telles que Perturb & Observe. Cette thèse propose un cadre complet pour optimiser les performances des systèmes photovoltaïques et leur intégration au réseau grâce à des stratégies avancées de contrôle et d'émulation. L'algorithme d'optimisation améliorée Eel-Grouper (OAEG), une approche méta-heuristique novatrice pour le MPPT, atteint une efficacité de suivi quasi optimale (> 99 %) en identifiant rapidement le point de puissance maximale globale (PPMG) dans divers scénarios d'ombrage partiel. Un mécanisme de redémarrage dynamique garantit une adaptation fiable aux changements environnementaux soudains, renforçant la stabilité du système. Un émulateur PV économique, construit autour d'une source programmable en courant continu (GW Instek APS-1102A, 1000 W), reproduit avec précision les courbes courant-tension induites par les PSCs dans une configuration de réseau de laboratoire à petite échelle (500 W), permettant une validation robuste des algorithmes. Un cadre MPPT en temps réel, implémenté sur une plateforme dSPACE 1104, ajuste dynamiquement les paramètres de contrôle pour minimiser les fluctuations et soutenir la stabilité du réseau. Pour améliorer la qualité de l'énergie, un filtre actif parallel (FAP) avec contrôle prédictif direct de la puissance (CPDP) réduit la distorsion harmonique totale (THD) du courant à moins de 5 %, atteignant un facteur de puissance quasi unitaire et conformité avec les normes IEEE 519-2022 sous charges variables. La validation expérimentale utilisant dSPACE 1104 et la source programmable en courant continu démontre une efficacité énergétique supérieure et une compatibilité avec le réseau. Ce cadre fait progresser l'optimisation des systèmes photovoltaïques, offrant une solution évolutive pour l'intégration d'énergie durable dans les applications de réseaux intelligents. **Mots-clés:** Maximum power point tracker (MPPT), Optimisation améliorée Eel-Grouper (OAEG), Ombrage partiel, Filtre actif parallel (FAP)

Contents

List of Figures

List of Tables

List of Symbols

Abbreviations

A-LSTM	Adaptive Long Short-Term Memory
ABC	Artificial Bee Colony
AC	Alternating Current
ACO	Ant Colony Optimization
ADC	Analog-to-Digital Converter
AFHCC	Active Feedback Control
AFO	Anti-Fuzzy Optimization
ANFIS	Adaptive Neuro-Fuzzy Inference System
ANN	Artificial Neural Network
ASMC	Adaptive Sliding Mode Controller
BA	Bat Algorithm
BESO	Bald Eagle Search Optimized
BS	Binary Search
CFLNN	Chebyshev Functional Link Neural Network
ChOA	Chimp Optimization Algorithm
CMRR	Common-Mode Rejection Ratio
CSA	Crow Search Algorithm
CSA-ABC	Cuckoo Search Algorithm–Artificial Bee Colony
D-SOGI	Dual Second-Order Generalized Integrator
DCC	Direct Current Control

DE	Differential Evolution
DHL-RNN	Dynamic Hidden-Layer Recurrent Neural Network
DPC	Direct Power Control
DSO	Drone Squadron Optimization
DSP	Digital Signal Processor
EEGO	Enhanced Eel-Grouper Optimizer
EGO	Eel-Grouper Optimizer
EMI	Electromagnetic Interference
EO	Equilibrium Optimizer
EPRI	Electric Power Research Institute
FAPH	Flexible Alternating-Current Power
FDM	Fuzzy Decision Maker
FF	Fill Factor
FIED	Flexible Interval Estimator
FO	Fuzzy Optimization
FO-IP	Fractional Order Integral-Proportional
FO-PI	Fractional Order PI Controller
FOCV	Fractional Open-Circuit Voltage
FOPID	Fractional Order Proportional-Integral-Derivative
FPGA	Field-Programmable Gate Array
FSC	Fuzzy Switched Controller
GA	Genetic Algorithm
GJO	Golden Jackal Optimizer
GMPP	Global Maximum Power Point
GWO	Grey Wolf Optimization
GWO-CC	Grey Wolf Optimization–Chaos Control

H∞	H-infinity Controller
HBO	Heap-Based Optimizer
HC	Hill-Climbing
HIL	Hardware-in-the-Loop
HSMA	Hyperbolic Slime Mould Algorithm
I-V	Current-Voltage
IADE	Improved Adaptive Differential Evolution
IEA	International Energy Agency
IEEE	Institute of Electrical and Electronics Engineers
IGBT	Insulated Gate Bipolar Transistor
INC	Incremental Conductance
IP	Integral-Proportional
IPSM	Improved Pattern Search Method
IRENA	International Renewable Energy Agency
KVL	Kirchhoff's Voltage Law
LMPP	Local Maximum Power Point
M-BFA	Modified Bacterial Foraging Algorithm
MAJO	Modified Adaptive Jaya Optimization
MCOA	Modified Coot Optimization
MLP	Multilayer Perceptron
MOSFET	Metal-Oxide-Semiconductor Field-Effect Transistor
MPC	Model Predictive Control
MPP	Maximum Power Point
MPPT	Maximum Power Point Tracking
MSMPP	Multiple-to-Single Maximum Power Point
MSRF	Modified Synchronous Reference Frame

NF	Notch Filter
P-V	Power-Voltage
P&O	Perturb and Observe
PCC	Point of Common Coupling
PDCS	Programmable DC Source
PDPC	Predictive Direct Power Control
PLL	Phase-Locked Loop
PQ	Power Quality
PSC	Partial Shading Condition
PSO	Particle Swarm Optimization
PV	Photovoltaic
QBC-SAF	Quadratic Boost Converter–Shunt Active Filter
RMS	Root Mean Square
SAPF	Shunt Active Power Filter
SEPIC	Single Ended Primary Inductor Converter
SMC	Sliding Mode Control
SMO	Slime Mould Optimizer
SPAPF	Single-Phase Active Power Filter
SRF	Synchronous Reference Frame
STC	Standard Test Conditions
SVM	Space Vector Modulation
THD	Total Harmonic Distortion
THDi	Total Harmonic Distortion of Current
THDv	Total Harmonic Distortion of Voltage
TS	Tabu Search
UPQC	Unified Power Quality Conditioner

VCO	Voltage Controlled Oscillator
VOC	Voltage Open-Circuit Model
VSI	Voltage Source Inverter
WCET	Worst-Case Execution Time
WOA	Whale Optimization Algorithm
ZDPC	Zero Direct Power Voltage

Greek Symbols

η_{MPPT}	MPPT Efficiency
ϕ_n	Phase angle of n-th harmonic (rad)
θ	Phase angle from PLL (rad)
θ_e	Phase angle error (rad)
θ_{est}	Estimated phase angle (rad)
θ_{ref}	Reference phase angle (rad)
ω	Fundamental angular frequency (rad/s)
ω_0	Nominal angular frequency (rad/s)
ω_n	Natural frequency (rad/s)
ω_{PLL}	PLL angular frequency (rad/s)
ζ	Damping ratio (dimensionless)

Mathematical Symbols

$\cos\phi$	Displacement Power Factor
ΔP	Active power error (W)
ΔQ	Reactive power error (V A)
η_{inj}	Grid injection efficiency (dimensionless)
$\mathbf{i}_f$	Vector of injected currents (A)
$\mathbf{i}_L$	Load current vector (A)
$\mathbf{i}_s$	Source current vector (A)

$\mathbf{i}_{s,abc}$	Three-phase source current vector (A)
$\mathbf{v}_s$	Grid voltage vector (V)
$\mathbf{v}_{\text{grid}}$	Vector of grid voltages (V)
$\mathbf{v}_{\text{inv}}$	Vector of inverter voltages (V)
$\mathbf{v}_{abc}$	Three-phase grid voltage vector (V)
$\mathcal{V}$	Set of inverter voltage vectors (dimensionless)
$\vec{v}_i$	Inverter voltage vector (V)
C_{dc}	Storage capacitance (F)
D	Distortion power (V A)
DC	Duty cycle (dimensionless)
$e(t)$	Voltage error for DC-link control (V)
e_α	Grid voltage in α frame (V)
e_β	Grid voltage in β frame (V)
G	Irradiance ($\mathrm{W/m^2}$)
G_P	Weighting coefficient for active power error (dimensionless)
G_Q	Weighting coefficient for reactive power error (dimensionless)
G_{mpp}	Theoretical maximum power for a given scenario (W)
G_{scale}	Scaling factor (dimensionless)
I_1	RMS value of the fundamental current component (A)
i_α	Current component in the α reference frame (A)
i_β	Current component in the β reference frame (A)
i_c	Compensating current (A)
I_d	Diode current (A)
I_m	Current magnitude in $\alpha\beta$ frame (A)
I_n	RMS amplitude of the n-th order harmonic current (A)
i_{fund}	Fundamental current component (A)

i_{in}	Input current to DC-link capacitor (A)
i_{out}	Output current from DC-link capacitor (A)
$I_{\text{rms,load}}$	RMS load current (A)
I_{bypass}	Bypass diode current (A)
I_{cell}	Cell current (A)
$i_{f,i}$	Compensating current for phase i (A)
I_{mpp}	Current at Maximum Power Point (A)
I_{ph}	Photocurrent (A)
$I_{pv,ref}$	PV current reference (A)
I_{pv}	Current from the PV system (A)
I_{sat}	Reverse saturation current (A)
I_{sc}	Short-circuit current (A)
I_{sh}	Shunt leakage current (A)
J	Cost function (dimensionless)
k	Boltzmann's constant (J/K)
K_i	Integral gain (dimensionless)
K_p	Proportional gain (dimensionless)
K_p^*	Reference proportional gain for anti-windup (dimensionless)
K_{uw}	Anti-windup gain (dimensionless)
L_f	Coupling inductance (H)
L_s	Source inductance (H)
n	Diode ideality factor (dimensionless)
N_c	Number of series-connected cells (dimensionless)
N_p	Number of cells in parallel (dimensionless)
N_s	Number of cells in series (dimensionless)
P	Active power (W)

$p(t)$	Instantaneous active power (W)
P_a	Active power injected or consumed from the grid (W)
P_G	Global PV Power (W)
P_{cond}	Conduction power loss
P_{loss}	Power loss including inverter switching and conduction losses (W)
P_{sw}	Switching power loss (W)
P_{in}	Input power to DC-link (W)
P_{load}	Load power (W)
P_{pred}	Predicted active power (W)
P_{ref}	Reference active power (W)
P_{mpp}	Maximum Power (W)
P_{panel}	Panel power (W)
P_{pv}	Power from the PV system (W)
Q	Reactive power (V A)
q	Electron charge (C)
$q(t)$	Instantaneous reactive power (V A)
Q_{pred}	Predicted reactive power (V A)
Q_{ref}	Reference reactive power (V A)
R_f	Filter resistance (Ω)
R_s	Series resistance (Ω)
R_{sh}	Shunt resistance (Ω)
S	Apparent power (V A)
S^*	Optimal switching state (dimensionless)
S_i	Binary switching signal for inverter phase i (dimensionless)
Sh	Shading factor (dimensionless)
T	Temperature (K)

T_s	Sampling interval (s)
$u(t)$	Control signal for DC-link (dimensionless)
u_i	Normalized switching command for phase i (dimensionless)
U_w	Anti-windup correction term (dimensionless)
u_{PLL}	PLL control signal (dimensionless)
u_{sat}	Saturated control output (dimensionless)
V_1	RMS value of the fundamental voltage component (V)
v_α	Voltage component in the α reference frame (V)
v_β	Voltage component in the β reference frame (V)
V_d	Diode voltage (V)
V_n	RMS amplitude of the n-th order harmonic voltage (V)
V_t	Thermal voltage at room temperature (V)
$V_{\text{dc,ref}}$	DC-link voltage reference (V)
$v_{\text{grid},i}$	Grid-side voltage for phase i (V)
$v_{\text{inv},i}$	Inverter phase voltage for phase i (V)
$V_{\text{rms,PCC}}$	RMS voltage at PCC (V)
V_{cell}	Cell voltage (V)
V_{ctrl_scaled}	Scaled control voltage (V)
V_{ctrl}	Control voltage (V)
V_{dc}	DC bus voltage (V)
V_{mpp}	Voltage at Maximum Power Point (V)
V_{oc}	Open-circuit voltage (V)
V_{out}	Output voltage (V)
V_{panel}	Panel voltage (V)
V_{pv}	Voltage from the PV system (V)
V_{th}	Thermal voltage (V)

Z_s	Source impedance (Ω)
Conv. Time	Convergence Time, time to reach near-steady operation (s)
Perf. (%)	Performance Efficiency (dimensionless)
PF	True Power Factor
Settl. Time	Settling Time, time to stabilize within 2% of final value (s)

General Introduction

" Logic is the foundation of the certainty of all the knowledge we acquire"— Leonhard Euler

.1 Background and Motivation

The global energy landscape is undergoing a profound transformation, driven by the urgent need to address climate change, ensure energy security, and meet growing electricity demands sustainably. Renewable energy sources, particularly solar photovoltaic (PV) technology, are at the forefront of this transition. According to the International Renewable Energy Agency (IRENA), renewable power capacity globally reached approximately 4448 GW by the end of 2024, marking a significant annual increase of 15.1 % compared to previous years [1]. Solar PV has emerged as a dominant player, contributing substantially to this growth owing to declining installation costs and supportive government policies. The International Energy Agency (IEA) projects that solar and wind will constitute around 30 % of global electricity generation by 2030, underscoring the critical role of PV systems in future energy scenarios [2].

As renewable sources become integral to energy infrastructures, smart grids are increasingly essential to manage the variability and intermittency of these energy inputs. Smart grids employ advanced digital communications, automated control, and intelligent sensors to optimise electricity distribution and facilitate renewable integration[3]. Unlike traditional grids—reliant on centralised, predictable fossil generation—smart grids must accommodate decentralised and variable resources, demanding responsive real-time control strategies[4].

However, the shift toward renewable-integrated smart grids introduces significant technical challenges, especially concerning *power quality*. Power quality refers to maintaining stable voltage, frequency, and low harmonic distortion—parameters crucial for equipment reliability and energy efficiency [5]. With the proliferation of sensitive electronics, tolerance for disturbances has narrowed. Voltage fluctuations, harmonic distortions, and reactive-power imbalance induced by intermittent PV generation can cause operational inefficiencies and increased maintenance costs[6]. The Electric Power Research Institute (EPRI) estimates that poor power quality costs the global economy billions of dollars annually due to downtime and equipment failure[7].

Reactive power, essential for voltage stabilisation, plays a pivotal role in grid reliability. Conventional compensation (capacitor banks, synchronous condensers) lacks the agility demanded by rapid PV variability[8]. Partial Shading Conditions (PSCs) further complicates matters: non-uniform irradiance produces multiple peaks on the PV power–voltage (P–V) curve, challenging maximum-power-point tracking (MPPT). Classical MPPT algorithms often converge to local maxima, slashing energy yield and exacerbating power-quality issues[9], [10], [11].

Smart inverters and advanced MPPT algorithms promise relief. Yet their combined deployment—particularly under PSCs—remains under-explored[12]. Sub-optimal inverter operation also injects harmonics, risking violation of IEEE 519 limits[13]. Addressing power extraction, reactive power, and harmonics *simultaneously* therefore motivates this thesis.

.2 Photovoltaic Systems and Integration Challenges

PV technology converts sunlight into electricity by means of the photoelectric effect: incident photons dislodge electrons in a semiconductor junction, producing a direct current that can be processed and delivered to the grid [14]. Over the past decade PV has moved from a niche renewable to a mainstream generation source. Module prices have fallen by more than 80 %, inverter efficiencies now exceed 98 %, and many countries offer feed-in tariffs or tax incentives. As a result, global PV capacity climbed from 100 GW in 2012 to over 1400 GW in 2023, a fourteen-fold increase that continues to reshape the generation mix [1].

A typical rooftop or ground-mounted plant contains four functional blocks:

1. *PV generator* – module strings wired to provide the required DC voltage and current.
2. *DC–DC or DC–AC converter* – a boost stage or full inverter that conditions the energy for export.
3. *Mounting and cabling* – structural frames, junction boxes, and over-current protection.
4. *Supervisory controller* – sensors plus firmware that implement MPPT, grid-code functions, and monitoring.

Module performance is characterised by the open-circuit voltage V_{oc}, short-circuit current I_{sc}, fill factor (FF), and the maximum-power point (MPP) where the product VI peaks [15]. Because V_{oc} and I_{sc} drift with irradiance and temperature, the MPP migrates across the $P-V$ curve throughout the day.

Why Fast and Accurate MPPT Is Essential? At standard test conditions a modern module delivers 200–400 W. Even a 2 % deviation from the MPP on a 10 kW rooftop array equates to a yearly loss of roughly 150 kWh, enough to power an efficient household refrigerator. In weak distribution feeders the wrong operating point can also push the inverter away from its nominal modulation index, injecting extra current distortion and reactive power. Effective MPPT therefore serves two purposes: maximising energy yield and helping the system meet grid-quality requirements.

.2.1 Classical Tracking Methods and Their Drawbacks

Perturb and Observe (P&O). The controller nudges the operating voltage by a fixed step and observes the resulting power change. The simplicity is appealing, but the method oscillates around the MPP in steady sunlight and can take several seconds to settle after a sudden irradiance jump.

Incremental Conductance (INC). Here the tracker compares incremental conductance $\mathrm{d}I/\mathrm{d}V$ with instantaneous conductance I/V. Convergence is faster than P&O, yet the fixed-step version still dithers near the optimum and—like P&O—fails under complex, multi-peak landscapes.

Hill-Climbing (HC). Voltage or duty-ratio steps are applied until the measured power decreases, then the step direction is reversed. HC shares the same local-gradient nature as the two schemes above and therefore inherits their limitations.

Field measurements show that these classical methods miss the global MPP in 30–40 % of shading events and can lose 10–30 % of harvestable energy in heavily shaded arrays.

.2.2 Impact of Partial Shading

When only part of a string is shaded—by antennas, trees, chimneys, or moving clouds—the P–V curve develops several local maxima. One is the global maximum power point (GMPP); the others are local maxima (LMPP). Traditional trackers cannot distinguish between them because they rely solely on the local slope. They often stop at the first LMPP encountered, especially if the voltage step is small. The resulting energy deficit is not trivial: a study on a 5 kW rooftop system recorded an 18 % annual loss attributable to shading events lasting less than two minutes each.

Metaheuristic MPPT: A Global-Search Alternative Metaheuristic algorithms dispatch a *population* of candidate voltages across the entire search space and let them evolve towards the best solution. Typical inspirations include biological evolution (Genetic Algorithms), particle kinematics (PSO), predatory behaviour (GWO), and slime-mould foraging (SMO). Their key benefits are:

- *Global search* – high probability of finding the GMPP even on a multi-peak surface.
- *Adaptability* – algorithm parameters can be tuned for any module string or converter topology.
- *Speed* – parallel evaluation means fewer iterations to converge; modern DSPs handle the extra computation comfortably.
- *Noise immunity* – probabilistic moves tolerate sensor jitter.

Recent hardware prototypes reach static efficiencies above 99 % and track irradiance steps of $100\,\mathrm{W\,m^{-2}}$ in under 300 ms. The next frontier is even faster convergence *and* a reliable restart mechanism that triggers only when the power drop signals a real change, not measurement noise. Developing such a high-speed, restart-capable metaheuristic—and proving it experimentally—is one of the core goals of this thesis.

.2.3 Review of Previous PhD Theses on MPPT for PV Systems under PSCs

Several significant contributions to the field of MPPT for PV systems under PSCs have been made in previous PhD theses. These works have laid the foundation for the development of more

advanced MPPT strategies, particularly those utilizing metaheuristic algorithms, hybrid control methods, and shading detection techniques.

One notable thesis is by **Jiang, Lian Lian** [16], titled *Modeling and Optimization of Photovoltaic Systems under Partially Shaded and Rapidly Changing Conditions*. In this work, Jiang addresses both the parameter extraction and MPPT challenges in PV systems. The thesis introduces a Chebyshev Functional Link Neural Network (CFLNN) for PV module modeling, significantly reducing computational complexity by eliminating hidden layers, resulting in faster and more accurate current predictions compared to traditional two-diode and multilayer perceptron (MLP) models. Additionally, an Improved Adaptive Differential Evolution (IADE) algorithm is proposed for accurate parameter extraction, addressing the limitations of conventional methods that often require extensive manual tuning.

For the MPPT problem, Jiang introduces an Ant Colony Optimization (ACO) based MPPT technique, marking the first direct application of ACO for PV systems. The method demonstrates superior global peak tracking under PSC by leveraging swarm intelligence to navigate complex, multimodal power landscapes without requiring irradiance or temperature sensors. Furthermore, the thesis presents a hybrid MPPT approach combining Artificial Neural Network (ANN) and conventional MPPT methods, significantly improving response time by directly predicting the MPP region. This hybrid approach is validated experimentally, showing promising results in dynamic shading conditions, making it highly suitable for tropical environments where irradiance changes rapidly.

In another influential work, **Karim Kaced** [17] in his thesis titled *Study of MPPT Techniques for Photovoltaic Systems under Partial Shading Conditions*, explores the use of metaheuristic algorithms for MPPT. Kaced's research focuses on the Bat Algorithm (BA), Particle Swarm Optimization (PSO), and Differential Evolution (DE) for real-time MPPT under PSC. These methods demonstrate high tracking efficiency and global peak detection capabilities, achieving static efficiencies above 99% in experimental validations. A significant contribution of this work is the implementation of these algorithms on reconfigurable FPGA circuits, highlighting the potential for real-time application in high-speed, adaptive MPPT controllers. The study further proposes integration with GMPP region estimators and shading detection methods for enhanced convergence speed and reduced computational complexity, paving the way for future research in FPGA-based MPPT systems.

Ziqiang Bi [18], in his thesis titled *Intelligent Global Maximum Power Point Tracking Strategies Based on Shading Perception for Photovoltaic Systems*, introduces a unique approach by integrating shading perception into the MPPT process. Bi's work focuses on the development of shading matrices and vectors to accurately characterize the complex shading patterns often encountered in PV systems. These tools significantly improve the accuracy of GMPP estimation, achieving up to 75% faster tracking compared to conventional methods like Binary Search (BS) and Tabu Search (TS). The thesis also proposes a 0.8VOC-model-based GMPPT method that directly predicts the GMPP region based on shading detection, demonstrating rapid convergence and reduced computational overhead, particularly in systems with high shading variability.

In another innovative approach, **Hina Gohar Ali** [19] in her thesis *Maximum Power Point Tracking of Photovoltaic System using Non-Linear Controllers*, explores the application of Sliding Mode Control (SMC) for robust MPPT under variable climatic conditions. Ali proposes both integer order and adaptive sliding mode controllers (ASMC) for MPPT, addressing the chattering issue inherent in traditional SMC approaches. The thesis further incorporates an Improved Pattern Search Method (IPSM) for real-time MPPT, demonstrating superior tracking stability and reduced steady-state errors in comparison to conventional PID controllers. This work highlights the potential for nonlinear control strategies to enhance PV system performance under rapidly changing environmental conditions.

Finally, **Isaac Owusu-Nyarko** [20] in his thesis *Maximum Power Point Tracking and Control of Grid Interfacing PV Systems* presents novel modifications to the 0.8VOC model for large-scale PV systems. Owusu-Nyarko's work focuses on grid integration and proposes a modified variable step-size incremental conductance (INC) algorithm with autonomous scaling for faster and more accurate tracking under PSCs. His approach significantly reduces oscillations around the MPP and achieves efficiencies approaching 99.6%, making it particularly well-suited for multi-megawatt PV installations. This thesis also addresses control challenges in grid interfacing, proposing innovative solutions to optimize active power transfer in high-power PV systems.

.2.4 Review of Previous Scientific Works on MPPT for PV Systems under PSCs

In addition to the significant contributions from previous PhD theses, numerous scientific articles have advanced the field of MPPT for PV systems under PSCs through the development of innovative metaheuristic algorithms and hybrid optimization strategies.

One notable work is by **Chakarajamula Hussaian Basha** [21], titled *A Novel Design and Implementation of Hybrid MPPT Controllers for Solar PV Systems under Various Partial Shading Conditions*. This study explores the design and comparison of several hybrid MPPT controllers, including a modified Grey Wolf Optimization (GWO) method combined with an Adaptive Neuro-Fuzzy Inference System (ANFIS). The study identifies key performance metrics, including peak power output, tracking speed, steady-state performance, and computational efficiency. It concludes that the hybrid GWO-ANFIS method outperforms traditional techniques in dynamic PSC environments, achieving rapid convergence and high peak power extraction with reduced oscillations.

Another significant contribution is from **Z. Smara** [22], in the paper titled *An Enhanced Global MPPT Method to Mitigate Overheating in PV Systems under Partial Shading Conditions*. Smara addresses the critical issue of hot-spot formation in shaded PV cells, which can lead to early module degradation. This study proposes a novel GMPPT method that prioritizes tracking the peak with the lower current to reduce thermal stress within shaded cells. The method demonstrates a 40% reduction in tracking time compared to conventional full sweeping techniques, significantly mitigating overheating risks by optimizing the operating point selection

based on real-time temperature feedback.

Kun Xia [23] further advances this field with the article *Improved Photovoltaic MPPT Algorithm Based on Ant Colony Optimization and Fuzzy Logic Under Conditions of Partial Shading*, which integrates the global search capabilities of Ant Colony Optimization (ACO) with the precision of Fuzzy Logic (FL). The resulting Ant-Fuzzy Optimization (AFO) algorithm exhibits superior performance in balancing tracking accuracy and computational efficiency, achieving steady-state convergence within 0.9 seconds and a tracking accuracy of 98.3%. This work highlights the potential of hybrid algorithms to overcome the limitations of single-method approaches in complex PSC scenarios.

Abdulbari Talib Naser [24] presents another innovative approach in his paper titled *Improved Coot Optimizer Algorithm-Based MPPT for PV Systems under Complex Partial Shading Conditions and Load Variation*. This work introduces the Improved Coot Optimization Algorithm (ICOA), specifically designed to enhance convergence speed and stability under varying load and PSC conditions. With an average tracking time of 0.58 seconds and a tracking efficiency of 99.94%, ICOA demonstrates remarkable robustness, significantly reducing the need for re-initialization and improving dynamic response times.

In a similar effort, **Chunliang Mai** [25] introduces the *Dung Beetle Optimization Algorithm (DBO)* for MPPT in PV systems. This algorithm achieves 99.99% tracking efficiency under PSCs, surpassing conventional methods like Particle Swarm Optimization (PSO) and Grey Wolf Optimization (GWO) in both speed and stability. The DBO technique's ability to minimize power oscillations and rapidly converge to the global maximum power point (GMPP) highlights its potential for real-world PV applications, particularly in harsh environmental conditions.

Mohammed Hassan EL-Banna [26] contributes with the article *On-Grid Optimal MPPT for Fine-Tuned Inverter Based PV System Using Golf Optimizer Considering Partial Shading Effect*, which introduces the Golf Optimization Approach (GOA) for grid-connected PV systems. This method effectively reduces THD and optimizes inverter performance, achieving a peak tracking efficiency of 99.8%. The work emphasizes the critical role of inverter tuning in maintaining grid stability and power quality under dynamic PSCs.

The influence of my research is reflected in the work of **Adeel Feroz Mirza** [27], who significantly influenced my research direction with the paper *High-Efficiency Swarm Intelligent Maximum Power Point Tracking Control Techniques for Varying Temperature and Irradiance*. This study presents the Slime Mould Optimization (SMO) and Improved Salp Swarm Optimization (ISSA) methods, achieving up to 99.9% tracking efficiency with minimal oscillations and rapid response times. The work emphasizes the importance of hybrid approaches in overcoming the limitations of conventional MPPT algorithms, providing a strong foundation for my own hybrid algorithm designs.

Finally, my collaborative work with **Feriel Abdelmalek** [28] on the paper *Experimental Validation of Effective Zebra Optimization Algorithm-Based MPPT under Partial Shading Conditions in Photovoltaic Systems* introduces the Zebra Optimization Algorithm (ZOA), validated through real-time experimentation using a DSPACE 1104 board. This work demonstrates that

ZOA achieves superior tracking accuracy of 99.95% in PSCs, outperforming established methods like GWO and PSO, and confirming its potential for real-world PV system applications.

The subsequent scientific articles related to MPPT under PSC, including additional works by myself and my colleagues, will be summarized in the following table 0.1. This table will provide a comprehensive overview, including performance metrics, advantages, and limitations, to facilitate a clear understanding of the state-of-the-art in this rapidly evolving research area.

Together, these works provide a comprehensive overview of the challenges and advancements in MPPT for PV systems under PSC. They collectively highlight the critical need for robust, adaptive, and intelligent MPPT strategies capable of addressing the complex, multimodal nature of PV power curves, particularly in rapidly changing environmental conditions. The advancements presented in these works form a critical foundation for ongoing research, including the work presented in this thesis, which aims to integrate real-time restart mechanisms, advanced metaheuristic algorithms, and predictive control methods for enhanced MPPT performance.

Table 0.1: Summary of MPPT Algorithms for PV Systems under Partial Shading Conditions

Author	**Title**	**Algorithm**	**Key Features**	**Efficiency / Performance**
Dokala Janandra Krishna Kishore [29]	A new metaheuristic-based MPPT controller for PV systems under PSC	Heap-Based Optimizer (HBO)	Low settling time, high tracking accuracy, reliable under varying conditions, tested with 4x1 PV array	99.85% (Case 1), 99.96% (Case 2), 99.92% (Case 3)
Resat Celikel [30]	Improved voltage scanning algorithm based MPPT for PV systems under PSC	Voltage Scanning with Skipping	Adaptive voltage skipping, fast tracking without panel data, efficient in complex shading	99.13% to 99.61% across 5 scenarios
Njimboh Henry Alombah [31]	Multiple-to-single maximum power point tracking for conventional MPPT	MSMPP Framework (P&O, INC)	Transforms multi-peak to single-peak for conventional algorithms, faster tracking	50% faster, near-perfect efficiency, reduced power loss
Hamza Belmadani [32]	A New Fast and Efficient MPPT Algorithm for Partially Shaded PV Systems Using HSMA	Hyperbolic Slime Mould Algorithm (HSMA)	Hyperbolic function for rapid convergence, peak region selection, fewer oscillations	99.85% average efficiency
Pengjia Qi [33]	Novel Global MPPT Technique Based on Hybrid Cuckoo Search and Artificial Bee Colony	Hybrid CSA-ABC	Combines global and local search, adaptive weight factors, restart mechanism	6.2% to 78.6% faster than conventional methods
Abdulbari Talib Naser [34]	A fast-tracking MPPT-based modified coot optimization algorithm for PV systems	Modified Coot Optimization (MCOA)	Single tuning parameter, search space skipping, reduced tracking time	99.87% efficiency, 1.3 s average tracking time
T. Nagadurga [35]	Global MPPT optimization for partially shaded photovoltaic systems	Chimp Optimization Algorithm (ChOA)	High conversion efficiency, rapid convergence, reduced oscillations	99.63% efficiency, 525.13 W max power
Hamed Karimi [36]	Hybrid P&O-Fuzzy-Based MPPT for PV Systems under PSC	P&O + Fuzzy Logic + PSO	Combines local fine-tuning and global optimization, reduces power oscillations	High accuracy, reduced oscillations
Ali Falih Challoob [37]	Hybrid CSA-PSO MPPT for PV systems under PSC	CSA-PSO Hybrid	Rapid tracking, high efficiency, reduced oscillations	97.72% efficiency, 0.018 s tracking time
Layachi Zaghba [38]	Improving photovoltaic energy harvesting with hybrid fuzzy logic-PI MPPT	Fuzzy-PI + PSO	Rapid adaptive response, reduced oscillations, high overall efficiency	99.7% efficiency, 0.3 s tracking time
Manoj Kumar Senapati [39]	Photovoltaic MPPT Performance Adaptability to Partial Shading Resilience	Modified Adaptive Jaya Optimization (MAJO)	Faster convergence, robust under dynamic shading and load variations	99.99% efficiency, 0.154 s convergence time
O. Fergani [40]	A New Modified Bacterial Foraging MPPT Technique with Dynamic Mutation Rates	Modified Bacterial Foraging Algorithm (M-BFA)	Dynamic mutation rates, high adaptability, efficient under complex PSCs	89.39% accuracy, 0.4-0.9 s tracking time
Djallal Eddine Zabia [41]	A novel equilibrium optimizer for PV under non-uniform conditions	Equilibrium Optimizer (EO)	Fast convergence, superior efficiency, effective under complex PSCs	99.94% efficiency, 0.43 s settling time
Djallal Eddine Zabia [42]	Grey wolf optimization parameter enhancement for tracking MPP under CPSC	Enhanced GWO (GWO-CC)	Parameter tuning for better exploration and exploitation, rapid MPP tracking	Superior to PSO-CC, faster convergence

.3 Power Quality Issues in Grid-Connected PV Systems

Power quality determines whether a grid can deliver energy within prescribed voltage, frequency, and waveform limits. As PV penetration rises, maintaining those limits becomes harder because the power injected by each inverter varies with irradiance and because the inverters themselves are nonlinear switching devices.

Harmonic distortion. Grid-tied PV inverters operate a high-frequency bridge (2–20 kHz) to synthesise the 50/60 Hz fundamental. The switching action produces interharmonics and higher-order harmonics; typical magnitudes reach 3–6 % of the fundamental for the 5^{th} and 7^{th} orders and 1–2 % for orders above the 13^{th}. Transformers carrying such distorted currents heat up disproportionately; a 4 % 5^{th} harmonic can elevate copper losses by 12 %, shortening insulation life by several years.[43] Capacitor banks at harmonic resonance may draw excessive reactive power, leading to over-voltages and fuse operation. Recognising these risks, IEEE 519-2014 limits total harmonic distortion for currents (THDi) to 5 % in systems below 69 kV and sharpens the individual limits for the 5^{th} and 7^{th} orders to 4 %. European standard EN 50160 imposes similar voltage- and flicker-based constraints.

Reactive-power balance is equally critical. Smart inverters can inject or absorb Q on demand, but their capability curve shrinks when the operating point drifts from the nominal modulation index—precisely what happens when MPPT under PSCs hunts across the P–V surface. The resulting voltage excursions propagate through weak distribution feeders.

Limitations of passive mitigation. Passive $L\,C$ filters are cheap, but their efficacy peaks at the design frequency and they introduce sharp resonance that can amplify neighbouring harmonic orders. Static capacitor banks or mechanical tap-changers handle sluggish reactive-power variations but cannot chase the sub-second swings induced by shaded PV arrays.

Shunt active power filters (SAPFs) address both problems. An SAPF measures line currents, extracts the harmonic and reactive components, and injects an equal-and-opposite current through a voltage-source inverter. Unlike passive filters it adapts within one or two line cycles and can track a moving PQ reference set by a supervisory controller. State-of-the-art controllers rely on Direct Power Control (DPC) or Direct Current Control (DCC) regulators to keep the tracking error below 1 % of full scale.[44]

Poor tracking of the global MPP under PSCs not only wastes real power but also makes the inverter's current ripple worse, giving the SAPF more work to do. Conversely, an undersized or sluggish SAPF can reflect voltage ripple back onto the PV side and confuse the MPPT algorithm. An effective solution therefore has to treat energy extraction and power-quality conditioning as one problem, not two separate ones—a key theme developed in the remainder of this thesis.

.3.1 Review of Previous PhD Theses on SAPF and Power Quality Improvement

Several significant contributions to the field of SAPF and power quality improvement have been made in previous PhD theses. These works have laid the foundation for the development of more advanced control strategies, harmonic mitigation techniques, and reactive power compensation methods.

One influential thesis is by **Abdelmadjid CHAOUI** [45], titled *Three-phase active filter for non-linear loads*. In this work, Chaoui focuses on the design and optimization of three-phase SAPF for harmonic compensation, reactive power management, and unbalance correction. The thesis presents a detailed analysis of SAPF parameter estimation, including DC bus voltage (V_{dc}), coupling inductance (L_f), and storage capacitance (C_{dc}), validated through extensive laboratory experiments. Chaoui introduces a multivariable PLL and IP regulator to enhance control stability and robustness, emphasizing the critical role of accurate parameter selection in achieving optimal SAPF performance.

Another significant work is by **Boualem BOUKEZATA** [46] in his thesis titled *Study and order of an energy conversion chain for a photovoltaic solar system*. Boukezata addresses the challenges of power quality in both standalone and grid-connected PV systems. The thesis introduces advanced MPPT algorithms based on fuzzy logic for improved power extraction under rapidly changing irradiance conditions. In addition to MPPT, Boukezata explores various control strategies for DC-AC inverters to improve grid power quality, emphasizing the importance of accurate DC bus voltage regulation and real-time power control.

In a related work, **Mustapha SARRA** [47] explores hybrid active power filters (FAPH) in his thesis titled *Contribution a l'Etude des Filtres Actifs Hybrides*. Sarra focuses on improving harmonic compensation by integrating passive LC filters with active SAPF systems, significantly enhancing filtering efficiency while reducing control complexity. The thesis presents extensive experimental validations demonstrating the effectiveness of this hybrid approach in achieving lower harmonic distortion and improved power factor.

Kamel DJAZIA [48] , in his thesis *Etude des Filtres Actifs pour Réseaux Déséquilibrés et Distordus*, introduces the Zero Direct Power Control (ZDPC) method for SAPF systems under unbalanced and distorted grid conditions. Djazia's work emphasizes the importance of precise harmonic detection and control for effective power quality improvement, presenting a comprehensive experimental validation of ZDPC performance under challenging grid conditions.

Another notable contribution is from **AFGHOUL Hamza** [49] , who in his thesis titled *Approche Avancée du Filtrage Actif et du Contrôle de Puissances dans les Installations Photovoltaïques Interconnectées au Réseau*, develops advanced control techniques for active filtering and power management in grid-connected PV systems. Afghoul introduces fractional order PI/IP regulators for improved dynamic response, validated through extensive experimental testing. This work highlights the importance of real-time control strategies in maintaining power quality under varying load and grid conditions.

Finally, **Sabir OUCHEN** [50] in his thesis *Contribution à la Commande Directe de Puissance Dédiée au Filtrage Actif, Associé à une Source Photovoltaïque* presents a detailed study of direct power control (DPC) techniques for PV systems integrated with SAPF. Ouchen's work focuses on reducing harmonic distortion and improving power quality through optimized control algorithms, including DPC-SVM and predictive DPC, validated with both simulation and experimental data.

These theses collectively underscore the critical importance of advanced control strategies, precise parameter estimation, and real-time adaptive techniques in enhancing the performance of SAPF systems for power quality improvement in modern power networks.

.3.2 Review of Previous Scientific Works on Power Quality Improvement

In addition to the foundational contributions from previous PhD theses, numerous scientific papers have advanced the field of power quality improvement in grid-connected PV systems, focusing on harmonic mitigation, reactive power compensation, and advanced control strategies for SAPFs . These studies highlight the critical role of innovative control algorithms, optimized filter design, and real-time implementation for improving power quality in modern power networks.

One influential work is by **Afghoul Hamza** titled *Design and Real-time Implementation of Fuzzy Switched Controller for Single Phase Active Power Filter* [51]. This paper introduces a novel fuzzy switched controller (FSC) integrated within a direct current control (DCC) algorithm for single-phase active power filters (SPAPF). The controller consists of a conventional PI controller, fractional order PI controller (FO-PI), and a fuzzy decision maker (FDM) that switches between them using reduced fuzzy logic control. This configuration offers short response times, low damping, and efficient disturbance rejection, ensuring robust performance under varying operating conditions. Experimental validation using a dSPACE 1104 test bench confirms the controller's ability to meet IEEE 519 harmonic standards, achieving a THD of 2.4% for both current (THDi) and voltage (THDv), and a unity power factor.

Another significant contribution is by **Sabir Ouchen** in his paper titled *Robust DPC-SVM Control Strategy for Shunt Active Power Filter Based on H∞Regulators* [52]. Ouchen addresses the limitations of conventional Direct Power Control (DPC) methods, which suffer from variable switching frequencies and high-power ripples. To overcome these issues, the paper proposes a DPC combined with Space Vector Modulation (SVM) and an H∞regulator for enhanced power quality. The control strategy is validated using Matlab/Simulink with real-time interfaces, demonstrating effective harmonic suppression, fast dynamic response, and unity power factor maintenance, even under distorted grid conditions.

Boualem Boukezata also makes a notable contribution with his paper titled *Power Quality Improvement by an Active Power Filter in Grid-Connected Photovoltaic Systems with Optimized Direct Power Control Strategy* [53]. This study focuses on integrating a PV generator into the grid through a three-phase voltage source inverter, incorporating a direct power control

strategy with an optimized switching table. This approach reduces power losses, enhances instantaneous power control, and provides multifunctional capabilities, including MPPT , power factor correction, harmonic elimination, and reactive power compensation. The proposed system is validated through extensive simulation and experimental testing, demonstrating robust performance under varying irradiance and load conditions.

Prasanta Kumar Barik introduces a comprehensive approach in his paper titled *Simulation and Real-time Implementation of a Combined Control Strategy-Based Shunt Active Power Filter in Microgrid* [54]. This work presents a multi-stage control strategy for microgrid systems, incorporating a combined control approach (NFPLL-MSRF-FIED-AFHCC) for SAPFs. The paper emphasizes the integration of various control methods, including modified synchronous reference frame (MSRF) techniques and fuzzy logic, to improve harmonic compensation, load adaptability, and voltage stability. The approach is validated through real-time digital simulation, demonstrating significant improvements in power quality and system robustness.

Derradji Bakria contributes to this field with his paper titled *An Optimized Shunt Active Power Filter Using the Golden Jackal Optimizer for Power Quality Improvement* [55]. This work presents an optimized design for SAPF, incorporating anti-windup PI controllers and optimized output filters. The paper uses the Golden Jackal Optimizer (GJO) to enhance DC link voltage regulation and current quality, achieving superior harmonic mitigation and reactive power compensation. The proposed method is validated through simulation, demonstrating significant reductions in THD and improved system stability.

Finally, **Juntao Fei** has made multiple contributions to this field, including the papers *Experimental Investigation of Recurrent Neural Network Fractional-Order Sliding Mode Control of Active Power Filter* [56] and *Neural Network Complementary Sliding Mode Current Control of Active Power Filter* [57]. These studies introduce advanced neural network-based control strategies for SAPFs, leveraging recurrent neural networks and fractional-order sliding mode controllers to improve current compensation accuracy and dynamic response. The experimental results highlight the effectiveness of these approaches in reducing harmonic distortion and enhancing overall power quality.

The subsequent scientific articles related to power quality improvement will be summarized in the following table 0.2. The scientific contributions summarized in Table reflect the diverse range of approaches to power quality improvement in SAPFs, including fractional-order control, predictive algorithms, neural networks, and fuzzy logic systems. These studies provide valuable insights into the design and optimization of SAPF control strategies.

Table 0.2: Selected Scientific Works on Power Quality Improvement in Grid-Connected PV Systems

Authors	**Title**	**Key Contributions and Findings**
Afghoul Hamza [58]	Implementation of Fractional-Order Integral-Plus-Proportional Controller to Enhance the Power Quality of an Electrical Grid	Introduces a fractional-order integral-plus-proportional (FO-IP) controller for SAPF, offering fast response, low overshoot, and improved robustness. Experimental results show a reduction in THD from 31.6% to 2.4%, outperforming conventional DPC methods.
T. M. Thamizh Thentral [59]	Development of Control Techniques Using Modified Fuzzy Based SAPF for Power Quality Enhancement	Proposes a fuzzy logic-based SAPF control strategy, reducing THD from 63.8% to 0.48% in SRF mode, and 23.9% to 3.2% for general loads. Demonstrates significant power factor correction and reactive power compensation.
S. Orts-Grau [60]	Generalized One-Cycle Current Controller for Improved SAPF Power Quality Management	Develops a generalized one-cycle current controller with two degrees of freedom, achieving stable current tracking and THDi values under 1%. Demonstrates significant power quality improvements over traditional methods.
Roman Hrbac [61]	Improving Power Quality with the Use of a New Method of Serial Active Power Filter (SAPF) Control	Introduces a comparative method for SAPF control, achieving superior harmonic mitigation and dynamic response compared to standard FFT and Butterworth filter methods.
Abinash Rath [62]	An Advanced Shunt Active Power Filter (SAPF) for Non-Ideal Grid Using Predictive DPC	Proposes a dead-beat predictive DPC for non-ideal grids using D-SOGI, achieving efficient power quality improvement in variable grid conditions. Demonstrates significant reduction in harmonic distortion and fast dynamic response.
Ghania Boudechiche [63]	Anti-Windup FOPID-Based DPC for SAPF Interconnected to a PV System Tuned Using PSO Algorithm	Develops an anti-windup fractional-order PID controller for SAPF, optimized using PSO, demonstrating superior THD reduction and fast response under rapid irradiance changes.
Sabir Ouchen [64]	Direct Power Control of Shunt Active Power Filter Using Space Vector Modulation Based on Super-Twisting Sliding Mode Control	Proposes a DPC-SVM with super-twisting sliding mode control, achieving 0.5% THDi in simulation and 3.37% in experimental tests, with rapid response and robust performance.
Boualem Boukezata [65]	An Enhanced Control Scheme for Multifunctional Grid-Connected PV System Using Fuzzy and Predictive Direct Power Control	Combines fuzzy logic control with predictive DPC for improved power quality and reduced voltage oscillations in grid-connected PV systems. Validated through simulation and experimental studies.
Surya Prakash [66]	Adaptive Control for Shunt Active Power Filter under Stochastic Solar Photovoltaics Behavior	Proposes an adaptive PI regulator for PV-SAPF systems, achieving significant improvements in dynamic response, THD reduction, and reactive power compensation under variable solar conditions.
S. Gomathi [67]	Improvement of Power Quality in a Power System using the QBC-Shunt Active Filter and FOPID Technique for Renewable Energy Systems	Introduces a QBC-SAF with FOPID control, demonstrating significant reductions in rise time, settling time, and steady-state error, enhancing overall power quality.
Alka Singh [68]	Applications of Adaptive Long Short-Term Memory to Active Filtering	Develops an A-LSTM controller for active filtering, achieving fast response and low THD in single-phase grid-connected systems. Demonstrates effective power quality improvement under dynamic conditions.
Juntao Fei [69]	Dynamic Terminal Sliding-Mode Control for Single-Phase Active Power Filter Using New Feedback Recurrent Neural Network	Introduces a dynamic terminal sliding-mode control for APF with DHL-RNN, achieving rapid compensation and chattering-free control. Validated through experimental and simulation studies.

.4 Problem Statement and Research Gap

Headline problem. *No published work has yet demonstrated a single platform that (i) maximises PV power under partial-shading, (ii) delivers that power through a SAPF that simultaneously mitigates household harmonics and regulates reactive power, and (iii) does so with verifiable hardware rather than idealised simulation.*

What is known. When a PV string is partially shaded—by fast-moving clouds, neighbouring buildings, or uneven soiling—its power–voltage (P–V) curve splits into multiple peaks. Conventional MPPT schemes such as Perturb–and-Observe or fixed-step Incremental Conductance tend to lock onto a local peak, sacrificing between 10 and 30 % of the available energy. Worse, operating the inverter at this off-design point enlarges current distortion and reactive-power swings, often breaching the 5 % THD ceiling mandated by IEEE 519 in less than a second. Over the last decade, three lines of research have progressed in parallel:

Metaheuristic MPPT. Global-search optimisers—PSO, GWO, SMO, EO, etc.—track the GMPP more reliably under shading.

Smart–inverter control. Advanced current controllers and virtual-impedance techniques now allow inverters to inject or absorb reactive power on demand.

SAPF technology. Predictive direct-power control (PDPC), fractional-order regulators and H^{∞} designs have reduced current THD below 3 % for typical nonlinear domestic loads.

Yet the literature treats these advances in isolation; none examine their ***combined*** behaviour under real shading events.

What is missing. A close reading of more than 120 articles and ten PhD theses reveals three intertwined gaps:

Interaction gap. No study measures how the residual ripple of a shaded-array MPPT propagates through the SAPF: its influence on DC-link oscillations, harmonic-tracking bandwidth, or the stability margins of the filter's predictive controller remain undocumented.

Extraction gap. Existing SAPF-PV hybrids still rely on local MPPT (P&O, INC) or on metaheuristics without restart capability; under rapid irradiance steps they lose the GMPP for several seconds—precisely when a smart-home's power demand spikes due to HVAC or EV charging.

Emulation gap. Hardware prototypes employ either low-resolution chopper-based emulators, whose discrete levels smear subtle shading effects, or high costing commercial PV simulators. Consequently, there is no affordable testbench that can replay a library of shading profiles while the SAPF runs in closed loop.

Questions this thesis answers.

Q1. How does an SAPF behave when tasked with absorbing the dynamic current of a globally-tracked yet shaded PV array *and* compensating the distorted loads of a sensor-rich smart home?

Q2. Can a restart-enhanced EEGO sustain GMPP tracking through irradiance and power change without degrading SAPF harmonic or reactive-power performance?

Q3. Can a simple programmable DC source (PDCS), driven by numerically generated I–V curves, emulate partial-shading scenarios with an error below 5% accuracy?

Thesis stance. By answering these questions experimentally, the thesis provides the first hardware-validated controller that *simultaneously* (i) pushes shaded-array efficiency above 99 %, (ii) keeps load-side THD below 3 %, and (iii) maintains unity power factor—even during irradiance transients—using a DC-source-based PV emulator.

.5 Contributions of the Thesis

This thesis presents significant contributions to the integration and control of PV systems within reactive power compensation frameworks, particularly under challenging PSCs. The research addresses critical gaps in power quality, maximum power extraction, and grid stability, providing a comprehensive framework for the optimization and control of integrated PV systems. The main contributions are as follows:

1. **Development of the Enhanced Eel-Grouper Optimization (EEGO) Algorithm for MPPT:** This thesis introduces the Enhanced Eel-Grouper Optimization (EEGO) algorithm, a novel metaheuristic method tailored for global Maximum Power Point Tracking (GMPPT) under PSCs. By integrating a proposed polynomial decay strategy, EEGO achieves rapid convergence (1.8–3.25 s) and high tracking efficiency (99.17–99.97%) across five static PSC scenarios. The algorithm was validated using a custom PV module with a maximum power of 84.64 W. EEGO optimized for V_{mpp} ranging from 20.75–43.30 V and I_{mpp} from 3.08–8.12 A across the scenarios. Simulations in MATLAB 2012b and experimental tests on a dSPACE 1104 DSP (hysteresis-controlled boost converter) confirmed EEGO's robustness, with minimal ripple and settling times of 3.0–4.25 s. Compared to other optimizations, EEGO significantly reduces power losses and convergence time making it ideal for real-time grid-connected PV system.

2. **Design and Implementation of a Programmable DC PV Emulator:** This thesis presents a PDCS-PV emulator designed to replicate the electrical behavior of a PV array under PSCs, providing a versatile platform for validating MPPT algorithms. The emulator, built around the GW Instek APS-1102A PDCS (maximum capacity: 1000 W, up to 10 A at 100 V or 5 A at 200 V), interfaces with a dSPACE 1104 DSP for real-time control. A two-dimensional lookup table (LUT), generated in MATLAB 2012b using the single-diode model enabling precise emulation of multi-peak P-V characteristics. Open-loop validation confirmed high fidelity, with I-V curve deviations below 5% across all scenarios, supporting robust testing of algorithms like EEGO, particularly in complex multi-peak conditions. However, limitations include lab space constraints, lack of sophisticated

hardware, and challenges in maintaining stable testing for extensive scenarios in Setif. These constraints limited the number of testable configurations but did not compromise the emulator's ability to replicate realistic PV behavior, making it an invaluable tool for experimental MPPT validation and power electronics research.

3. **Real-Time MPPT Optimization:** This thesis introduces a real-time MPPT optimization strategy designed to dynamically adapt control parameters under rapidly changing irradiance conditions, ensuring prompt responses, minimal power fluctuations, and sustained maximum energy extraction. Implemented on a dSPACE 1104 DSP, the strategy optimizes the PV current reference ($I_{pv,ref}$) using a metaheuristic approaches, integrated with a hysteresis-controlled boost converter. The strategy evaluates three candidate solutions every 750 ms (250 ms per candidate for stabilization), enabling rapid adaptation to dynamic shading changes. The use of $I_{pv,ref}$ optimization and hysteresis control ensures smoother transitions and lower ripple compared to direct duty cycle adjustments, enhancing noise immunity and grid stability. Experimental results on the dSPACE 1104 confirmed robust tracking of the global MPP, particularly in complex multi-peak scenarios. A minor trade-off is the computational load of evaluating multiple candidates, though the small population size (3–5 candidates) ensures real-time feasibility on the dSPACE platform. Nonetheless, this strategy significantly improves energy efficiency and power injection stability, making it a critical advancement for real-time grid-connected PV systems.

4. **Development of a Real-Time Restart Mechanism for Metaheuristic MPPT Algorithms:** This thesis presents a real-time restart mechanism integrated into the EEGO algorithm to ensure optimal power extraction under rapidly changing environmental conditions, such as sudden PSCs events. The mechanism detects significant irradiance shifts and resets the optimization process to avoid local convergence, enhancing MPPT stability and reliability. the mechanism monitors power every 750 ms iteration. The restart triggers when a power change exceeds 3% and prior stability is below 0.5 W for three consecutive iterations (2.25 s). This dual-threshold approach, ensures no false triggers during steady convergence or early exploration while guaranteeing resets after genuine disturbances. A minor limitation is the 2.25 s detection window, which may delay responses to extremely rapid changes. The computational overhead of continuous power monitoring is minimal, leveraging the EEGO's efficient structure. By preventing local optima convergence, this mechanism significantly enhances energy extraction reliability, making it a vital component for real-time grid-connected PV systems under dynamic shading.

5. **Integration of SAPF with PDPC:** This thesis develops an integrated SAPF with PDPC to enhance power quality in a grid-connected PV system under PSCs. The SAPF-PDPC mitigates harmonic distortions and reactive power fluctuations, ensuring compliance with IEEE 519-2022 standards. The SAPF injects compensating currents to cancel harmonics at the point of common coupling (PCC). PDPC predicts active and reactive power one

step ahead, minimizing a quadratic cost function. Implementation reduced current THD bellow 5% threshold, eliminated reactive power, and achieved unity power factor. The system excelled in dynamic conditions with nonlinear loads, particularly under multi-peak shading scenarios. This integration significantly enhances grid stability and power quality, making it a critical advancement for renewable energy systems.

6. **Comprehensive Experimental Validation and Novel Power Loss Analysis:** This thesis pioneers the experimental integration of a PV system with the EEGO algorithm for MPPT, a restart mechanism, and SAPF with PDPC under PSCs. Implemented on a dSPACE 1104 platform with a GW Instek APS-1102A PV emulator, VSI, and nonlinear load, the setup replicates static PSCs, dynamic load, and irradiance transients. A key contribution is the first in-depth experimental analysis of power loss mechanisms impacting grid injection efficiency (η_{inj}), particularly the SAPF-induced PCC voltage rise ($V_{\text{rms,PCC}}$) increasing load power up to ≈10%. This load power increase was the primary loss factor, with inverter losses secondary. No prior work has experimentally quantified this phenomenon's impact on MPPT performance under partial shading with such depth. EEGO achieved near-optimal power extraction, rapid convergence (<3 s), and minimal ripple, enhancing grid stability. The SAPF-PDPC reduced current THD from 16.2–17.4% to 1.9–2.8% and maintained near-unity power factor. The system excelled in multi-peak shading and dynamic transients, though slight THD elevation (2.8% vs. simulated 2.55%) occurred due to sensor lag. This establishes a new benchmark for integrated PV systems, highlighting the critical interplay of MPPT and power quality under real-world conditions.

Collectively, these contributions form a robust framework for the optimization and control of PV systems within modern smart grids. They address critical challenges in power quality, reactive power compensation, and maximum power extraction, significantly advancing the state-of-the-art in sustainable energy technology.

.6 Thesis Organization

This thesis, titled *Contribution to the Control of a Reactive Power Compensation System Powered by a Photovoltaic Generator*, is structured into four main chapters that systematically present the theoretical foundations, methodological developments, experimental validations, and overall conclusions. Each chapter builds on the previous one, creating a coherent narrative that thoroughly addresses the challenges and solutions related to PV integration and reactive power compensation within modern smart grid frameworks.

Chapter 2: System Design and Modeling establishes the theoretical and practical foundation for designing, modeling, and controlling an integrated PV system with reactive power compensation. It begins with the detailed modeling of PV cells, panels, and arrays, including the impact of PSCs on power-voltage (P-V) characteristics. This section sets the stage for MPPT by

highlighting the need for advanced optimization algorithms. The Enhanced Eel-Grouper Optimizer (EEGO), developed specifically for this thesis, is introduced as a solution to the challenges of PSCs. The chapter then shifts focus to power quality improvement, discussing the critical role of SAPF in harmonic mitigation and reactive power compensation. It covers essential concepts like total harmonic distortion (THD), power factor correction, and the mathematical modeling of SAPF components, providing a comprehensive framework for high-efficiency power control in smart grids.

Chapter 3: Experimental Combined System and Implementation bridges the gap between theoretical modeling and practical realization, detailing the combined hardware and software framework required for real-time PV energy conversion and power quality improvement. It covers the integration of the PDCS-PV emulator, digital controller, boost converter, and SAPF, emphasizing the practical challenges of system synchronization and real-time control. This chapter also includes the design and validation of a PDCS-PV emulator, critical for accurately replicating real-world shading conditions in experimental setups. It introduces the real-time implementation of metaheuristic-based MPPT algorithms, including EEGO, and provides detailed guidance on algorithm initialization, evaluation, population update, and duty cycle adjustment. These elements collectively establish the practical foundation for the dynamic testing and performance analysis presented in subsequent chapters.

Chapter 4: Experimental Integration of PV Emulator and Power Compensation System under Partial Shading presents the comprehensive experimental validation of the integrated PV emulator and reactive power compensation system. It begins with a detailed overview of the experimental setup, including the PDCS-PV emulator, digital control system, boost converter, and SAPF. This chapter thoroughly examines the performance of multiple MPPT algorithms under various PSCs scenarios, providing critical insights into their relative efficiency and accuracy. It also assesses the SAPF's effectiveness in mitigating harmonic distortions and maintaining grid stability. The chapter concludes with a comparative analysis of the integrated system's performance, validating the proposed control strategies through extensive empirical evidence. This section confirms the practical viability of the thesis contributions, bridging the gap between theoretical innovation and real-world application.

Chapter 5: Conclusion and Future Perspectives synthesizes the entire body of work, summarizing key findings and contributions while reflecting on the thesis's broader significance in advancing PV system integration and reactive power management. It also discusses the limitations of the current research and outlines potential directions for future work, emphasizing the scalability and adaptability of the proposed methods in diverse smart grid applications.

This structured organization ensures clarity and coherence, guiding readers logically through the complexities of theoretical concepts, practical implementations, experimental validations, and final reflections, providing a comprehensive resource for both academic researchers and industry practitioners interested in enhancing PV system integration and power quality management.

Chapter 1 Overview: Photovoltaic System

Chapter 1 establishes the theoretical foundation for the modeling, analysis, and control of photovoltaic (PV) energy conversion systems, with particular emphasis on maximum power extraction under non-uniform irradiance conditions. This chapter focuses exclusively on the PV generation side, providing the necessary background for understanding the challenges associated with partial shading and the need for advanced maximum power point tracking (MPPT) techniques.

The chapter begins in Section 1.1 with the mathematical modeling of the PV system. The single-diode PV cell model is introduced as the fundamental building block for accurately representing PV behavior. This section progresses from the electrical characteristics of individual PV cells to practical PV panel and array configurations in Section 1.1.1, establishing the relationship between irradiance, temperature, and output power. The impact of partial shading conditions (PSCs) is thoroughly analyzed in Section 1.1.3, where the emergence of multiple local maxima on the power–voltage (P–V) curve is demonstrated, highlighting the inherent limitations of conventional tracking methods.

Section 1.2 introduces the concept and operational principles of maximum power point tracking. The necessity of MPPT for efficient energy extraction is discussed, along with the consequences of operating PV systems without appropriate tracking mechanisms. This section further examines the challenges introduced by PSCs, particularly the tendency of traditional MPPT algorithms to converge to local maximum power points rather than the global maximum power point (GMPP).

To address these limitations, Section 1.3 presents the development of the Enhanced Eel–Grouper Optimizer (EEGO), a biologically inspired metaheuristic algorithm designed for robust global MPPT under complex shading patterns. The evolution from the original Eel–Grouper Optimizer (EGO) to the enhanced formulation is detailed, including the mathematical modeling, control integration, and performance improvements that enable faster convergence and improved tracking reliability.

Overall, this chapter provides a comprehensive theoretical framework for PV system modeling and advanced MPPT design, forming the basis for the experimental implementation and system-level integration presented in subsequent chapters.

Chapter 1

Photovoltaic System

1.1 Photovoltaic System Model

1.1.1 PV Cell Modeling

The reliance on PV systems as a renewable energy source necessitates the development of precise and reliable models to predict and optimize their behavior under various environmental conditions. Given the intermittent nature of solar irradiance and temperature fluctuations, accurately modeling PV cells is essential for maximizing efficiency and ensuring stable integration into power systems. This section focuses on the single-diode model of the PV cell, a widely accepted approach that offers a balance between computational simplicity and accuracy in capturing the nonlinear characteristics of the cell.

1.1.1.1 Single-Diode Model of a Photovoltaic Cell

The single-diode model stands as a cornerstone in the electrical modeling of PV cells, offering a computationally efficient yet robust framework to simulate their behavior under diverse operating conditions. Widely adopted for its balance of simplicity and accuracy, this model encapsulates the physical characteristics of a PV cell through an equivalent circuit, as depicted in Figure 1.1. This representation facilitates the analysis of energy conversion processes, enabling the design of MPPT algorithms and PV emulators critical to system optimization, particularly under non-ideal scenarios such as PSCs [70].

The model hinges on five fundamental parameters that govern the PV cell's output characteristics: the photocurrent (I_{ph}), the diode reverse saturation current (I_{sat}), the diode ideality factor (n), the series resistance (R_s), and the shunt resistance (R_{sh}). These parameters collectively define the cell's response to environmental variables such as irradiance and temperature, as well as internal losses, providing a comprehensive basis for performance analysis.

The photocurrent I_{ph} represents the current generated by incident solar irradiance (G) on the semiconductor surface of the photovoltaic cell. This current is primarily proportional to the irradiance level and exhibits a slight dependence on temperature due to variations in carrier

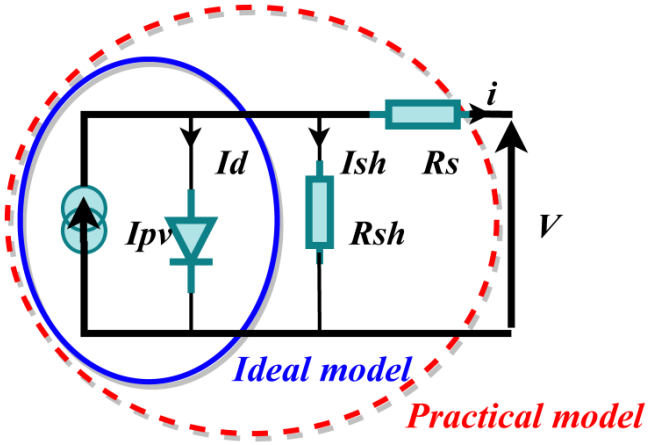

Figure 1.1: Single-Diode Model of a PV Cell

generation efficiency within the PN junction. Under standard test conditions (STC), defined by a reference irradiance $G_{ref} = 1000$ W/m^2 and a reference temperature $T_{ref} = 25°$C, the photocurrent closely approximates the short-circuit current $I_{sc,ref}$. For operating conditions deviating from STC, the photocurrent can be accurately expressed as:

$$I_{ph} = \left[I_{sc,ref} + \alpha_{Isc}\,(T - T_{ref})\right]\left(\frac{G}{G_{ref}}\right) \tag{1.1}$$

where α_{Isc} is the temperature coefficient of the short-circuit current, typically provided by the PV module manufacturer. This formulation captures the linear dependence of photocurrent on irradiance and its slight increase with temperature, consistent with standard photovoltaic modeling practices.

The diode current (I_d), governed by the Shockley equation, models the nonlinear behavior of the PN junction, capturing recombination losses and the exponential relationship between voltage and current. This current is expressed as:

$$I_d = I_{sat}\left(e^{\frac{V_{pv}+I\cdot R_S}{n\cdot V_{th}}} - 1\right) \tag{1.2}$$

where I_{sat} is the reverse saturation current[1], dependent on temperature and semiconductor bandgap; n is the ideality factor (typically 1 to 2 for silicon cells), reflecting junction quality; and $V_{th} = \frac{kT}{q}$ is the thermal voltage, with $k = 1.38 * 10^{-23}$ J/K (Boltzmann's constant), $q = 1.6 * 10^{-19}$ C (electron charge), and T in Kelvin. The term $V_{pv} + I \cdot R_s$ represents the voltage across the diode, adjusted for series resistance losses.

[1]The reverse saturation current originates from minority carrier diffusion and recombination within the depletion region of the PN junction. Its value depends strongly on temperature and semiconductor material properties, particularly the bandgap energy. As temperature increases, enhanced thermal generation of carriers leads to an exponential rise in I_{sat}, increasing recombination losses and reducing the achievable open-circuit voltage. Accurate modeling of I_{sat} is therefore essential for predicting PV cell performance under varying thermal and operating conditions.

The practical model extends beyond the ideal configuration—comprising only I_{ph} and I_d, as enclosed in the blue oval of Figure 1.1—by incorporating resistive elements. The series resistance R_s quantifies losses due to current flow through the cell's material and contacts, while the shunt resistance R_{sh} models leakage currents bypassing the junction, often due to manufacturing defects or edge effects. These resistances significantly influence the cell's I-V characteristics, particularly under high-current or low-irradiance conditions, as illustrated in Figure 1.2.

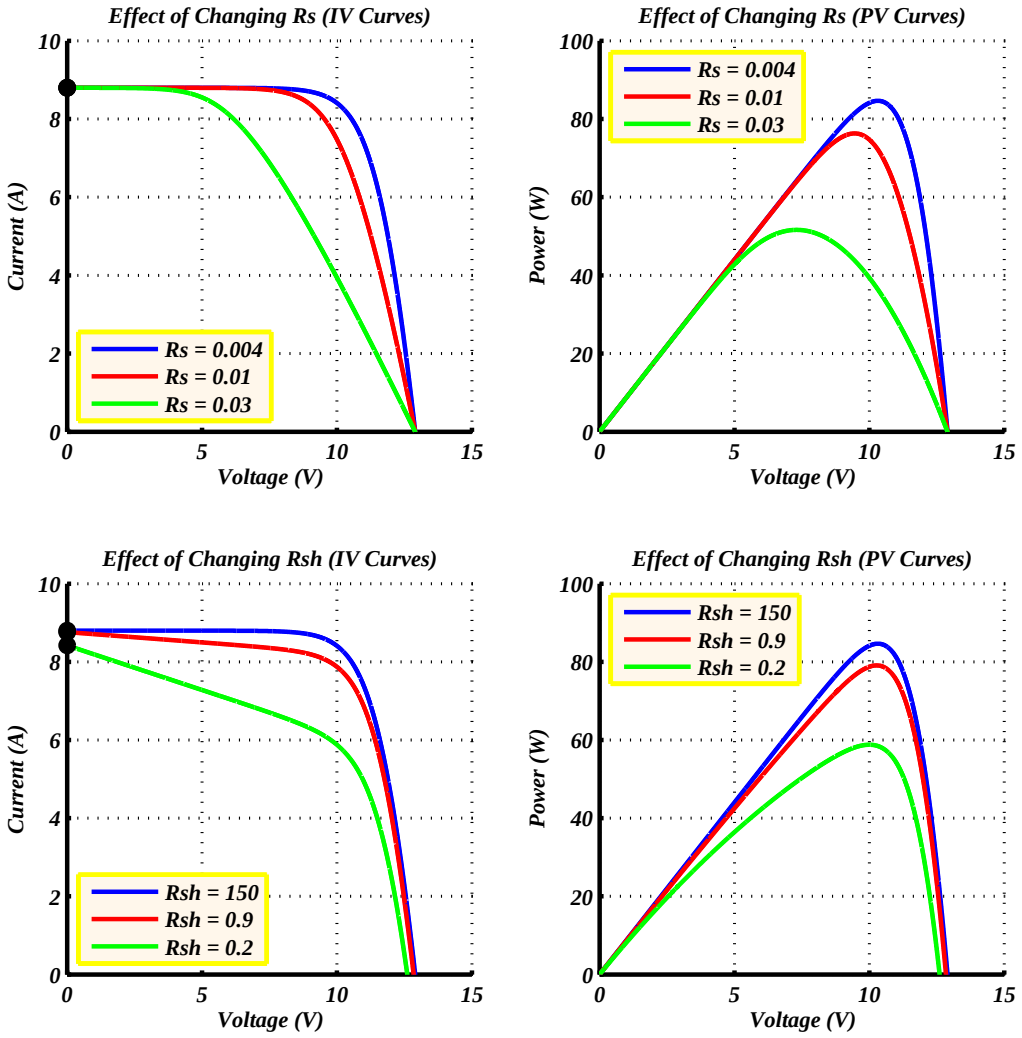

Figure 1.2: Effect of R_s and R_{sh} on I-V and P-V Curves. Variations in these resistances alter the slope and fill factor of the curves, impacting power output.

The total output current (I_{pv}) at the cell terminals integrates these components, derived from Kirchhoff's current law as:

$$I_{pv} = I_{ph} - I_d - \frac{V_{pv} + I \cdot R_s}{R_{sh}} \tag{1.3}$$

where $\frac{V_{pv}+I \cdot R_s}{R_{sh}}$ represents the shunt leakage current (I_{sh}). The output voltage (V_{pv}) is related to the diode voltage (V_d) by:

$$V_{pv} = V_d - I \cdot R_s \tag{1.4}$$

highlighting the voltage drop across R_s. This formulation captures the interplay between photogeneration, recombination, and resistive losses, as visualized in Figure 1.3, which demonstrates the effects of irradiance and temperature on I-V and P-V curves.

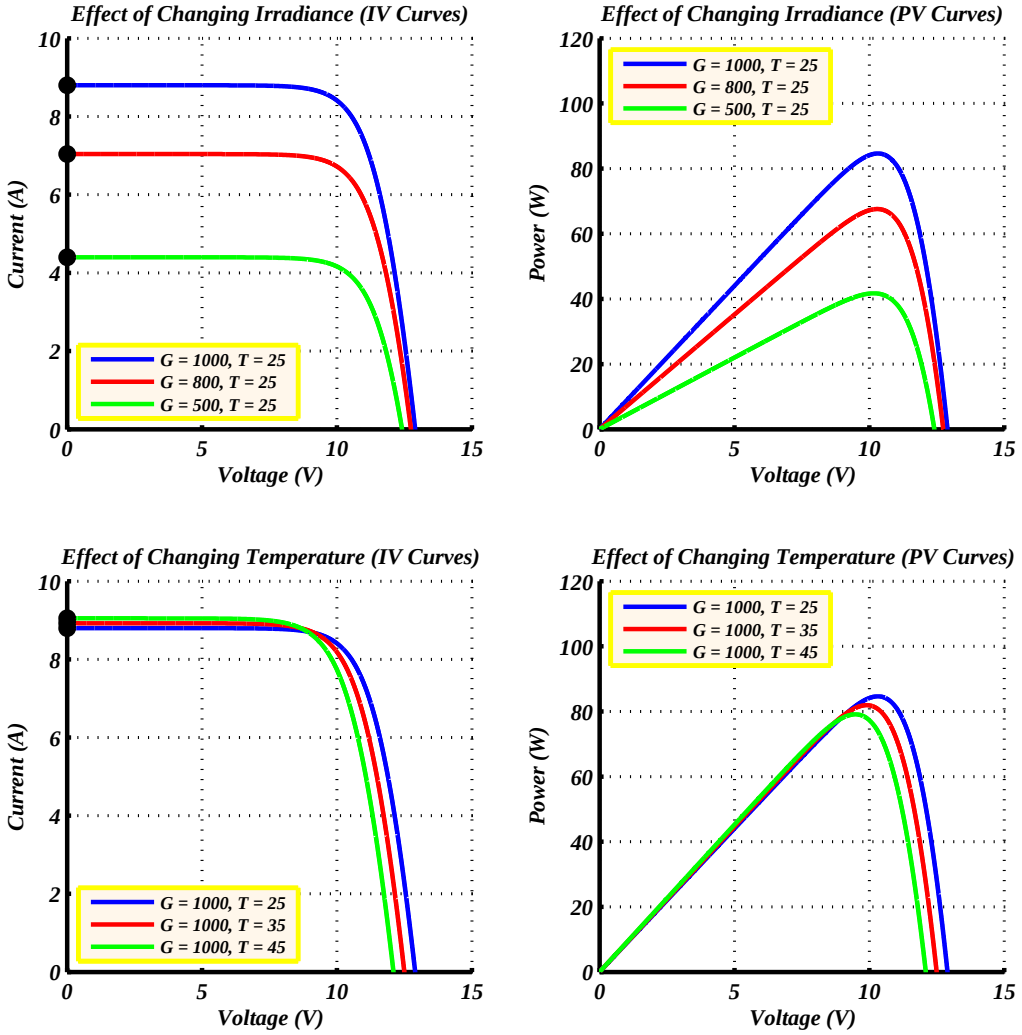

Figure 1.3: Effect of Irradiance and Temperature on PV I-V and P-V Curves. Higher irradiance increases current, while temperature shifts voltage and power output.

The single-diode model's computational efficiency and reliable accuracy make it a preferred choice for real-time applications, such as MPPT algorithm development and PV emulator design, as explored in later sections of this thesis (e.g., Chapter 4, Section 4.3). By accounting for both ideal and non-ideal effects—through parameters like I_{sat}, n, R_s, and R_{sh}—it provides a

robust foundation for analyzing PV behavior under varying conditions, including PSCs, where deviations from STC amplify the significance of resistive and leakage effects.

1.1.1.2 Parameter Selection and Validation

The parameters of the custom PV module were meticulously selected to align with the experimental constraints imposed by the DC programmable voltage source and the power quality requirements of the integrated system. This subsection delineates the scientific and technical rationale underpinning these choices, emphasizing their suitability for laboratory-scale investigations. The adoption of a low-power PV module is justified by its capacity to facilitate controlled testing of advanced control strategies, such as MPPT algorithms and SAPF integration, within a manageable operational envelope. Table 1.1 represents the parameters of the Custom PV Module Used in the validation.

Table 1.1: Parameters of the Custom PV Module Used in the Simulation

Parameter	Symbol	Value	Description
Short-Circuit Current	I_{sc}	8.8 A	Maximum current under standard test conditions (STC: $G = 1000\,\text{W/m}^2$, $T = 25°\text{C}$).
Current at MPP	I_{mpp}	8.2 A	Current at the Maximum Power Point (MPP).
Open-Circuit Voltage	V_{oc}	12.9 V	Maximum voltage with zero current flow.
Voltage at MPP	V_{mpp}	10.323 V	Voltage at the Maximum Power Point (MPP).
Number of Cells in Series	N_c	21	Number of series-connected solar cells in the module.
Thermal Voltage	V_t	26 mV	Thermal voltage at room temperature ($T = 298\,\text{K}$).
Maximum Power	P_{mpp}	84.64 W	Maximum power at MPP ($P_{mpp} = V_{mpp} \cdot I_{mpp}$).
Series Resistance	R_s	0.004 Ω	Resistance modeling internal losses in series with the cells.
Shunt Resistance	R_{sh}	150 Ω	Resistance representing leakage currents in parallel with the cells.

1. Design Constraints and Voltage Source Compatibility

The parameter selection process was driven by the operational limits of the PDCS, a critical component of the experimental PV emulator (Chapter 2, Section 2.3). This source imposes strict thresholds on current and voltage, necessitating a module design that ensures compatibility without risking overload. The short-circuit current was set at $I_{sc} = 8.8\,\text{A}$, and the open-circuit voltage at $V_{oc} = 12.9\,\text{V}$ per module. For an array of five series-connected modules, the cumulative open-circuit voltage reaches $5 \cdot V_{oc} = 64.5\,\text{V}$, which remains below the DC bus reference voltage of $V_{dc} = 81\,\text{V}$. This configuration safeguards the DC-side filter and aligns with

the system's power quality objectives, ensuring stable operation across experimental scenarios.

2. Power Output Optimization for Experimental Versatility

The maximum power output per module, calculated as $P_{mpp} = V_{mpp} \cdot I_{mpp} = 10.323\,\text{V} \cdot 8.2\,\text{A} = 84.64\,\text{W}$, yields a total array power of $5 \cdot P_{mpp} = 423.2\,\text{W}$. This power level was deliberately chosen to balance experimental flexibility with the capacity constraints of the DC voltage source. It enables comprehensive testing under diverse conditions—such as variable irradiance, PSCs, and harmonic mitigation via SAPF—while preventing excessive thermal or electrical stress on the emulator. The selected power output supports the evaluation of MPPT algorithms by providing sufficient energy to replicate real-world PV dynamics, yet remains within a safe operational range, enhancing the reliability and repeatability of laboratory experiments.

3. Resistive Parameters and Model Fidelity

The series resistance ($R_s = 0.004\,\Omega$) and shunt resistance ($R_{sh} = 150\,\Omega$) were selected to reflect realistic PV cell behavior while optimizing experimental outcomes. The low R_s value minimizes resistive losses, preserving the fill factor and efficiency critical for MPPT performance analysis, whereas the relatively high R_{sh} curtails leakage currents, ensuring the module's I-V characteristics align with typical silicon-based PV modules. These values, though tailored to the experimental setup, fall within standard ranges (R_s: $0.001\,\Omega$ to $0.1\,\Omega$, R_{sh}: $100\,\Omega$ to $10\,000\,\Omega$), validating their representativeness for simulating practical PV operation under controlled conditions. Table 1.2 shows the single-Diode model parameters and their impact on PV cell performance.

4. Thermal Influences and Performance Sensitivity

The temperature-dependent nature of PV performance introduces additional considerations, as elevated temperatures increase the reverse saturation current (I_{sat}), reducing V_{oc} and shifting the I-V curve. With a thermal voltage of $V_t = 26\,\text{mV}$ at $T = 298\,\text{K}$, the module's design accounts for these effects, emphasizing the need for thermal management to maintain efficiency during prolonged tests. This sensitivity is particularly relevant for PSCs scenarios (Chapter 3, Section 3.2), where localized heating could exacerbate performance degradation, necessitating precise parameter calibration.

5. Validation and Experimental Relevance

The low-power module, with a total output of 423.2 W, is engineered to serve as a versatile tool for laboratory-scale experiments, distinct from commercial high-power systems. Its parameters enable detailed investigations of MPPT algorithms and SAPF integration (Chapter 3), replicating key phenomena like partial shading and power fluctuations without exceeding the DC source's limits. This power level ensures operational safety, preventing overload while supporting a broad spectrum of test conditions—from steady-state to dynamic transients. The module's design thus validates its utility as a practical platform for advancing control strategies within the renewable energy system, aligning with the thesis's objectives of optimizing power extraction and quality under controlled, repeatable conditions.

Table 1.2: Single-Diode Model Parameters and Their Impact on PV Cell Performance

Parameter	**Symbol**	**Typical Range**	**Physical Meaning**	**Impact on Performance**
Series Resistance	R_s	0.001 Ω to 0.1 Ω	Represents the resistive losses in the cell, including contacts and interconnections.	Higher R_s reduces the fill factor, decreases output power, and lowers the slope of the I-V curve in the high-current region.
Shunt Resistance	R_{sh}	100 Ω to 10 000 Ω	Models leakage currents that bypass the p-n junction due to defects or impurities in the cell.	Lower R_{sh} reduces the open-circuit voltage (V_{oc}) and decreases overall cell efficiency.
Ideality Factor	n	1.0 to 2.0	Indicates how closely the diode follows ideal behavior. A value of 1 corresponds to an ideal diode.	A higher n broadens the I-V curve, reducing efficiency. Lower n improves the steepness of the curve near V_{oc}.
Photocurrent	I_{ph}	4 A to 10 A	The current generated by incident sunlight, proportional to irradiance and slightly temperature-dependent.	Higher I_{ph} increases the output current and power. Dependent on irradiance and temperature.
Saturation Current	I_{sat}	110^{-9} A to 110^{-6} A	Represents the reverse saturation current of the diode, influenced by temperature and material properties.	Higher I_{sat} at elevated temperatures reduces V_{oc} and overall efficiency due to increased recombination losses.

1.1.2 Partial Shading Analysis

Partial shading is a critical phenomenon in photovoltaic (PV) systems that can significantly degrade performance and reduce energy output [71]. This effect occurs when only part of a PV panel is exposed to sunlight while other portions are shaded, whether due to environmental factors such as clouds, trees, buildings, or dust, as shown in Fig. 1.4. Understanding the impact of shading on I-V and P-V characteristics is essential to improve PV panel efficiency and reliability.

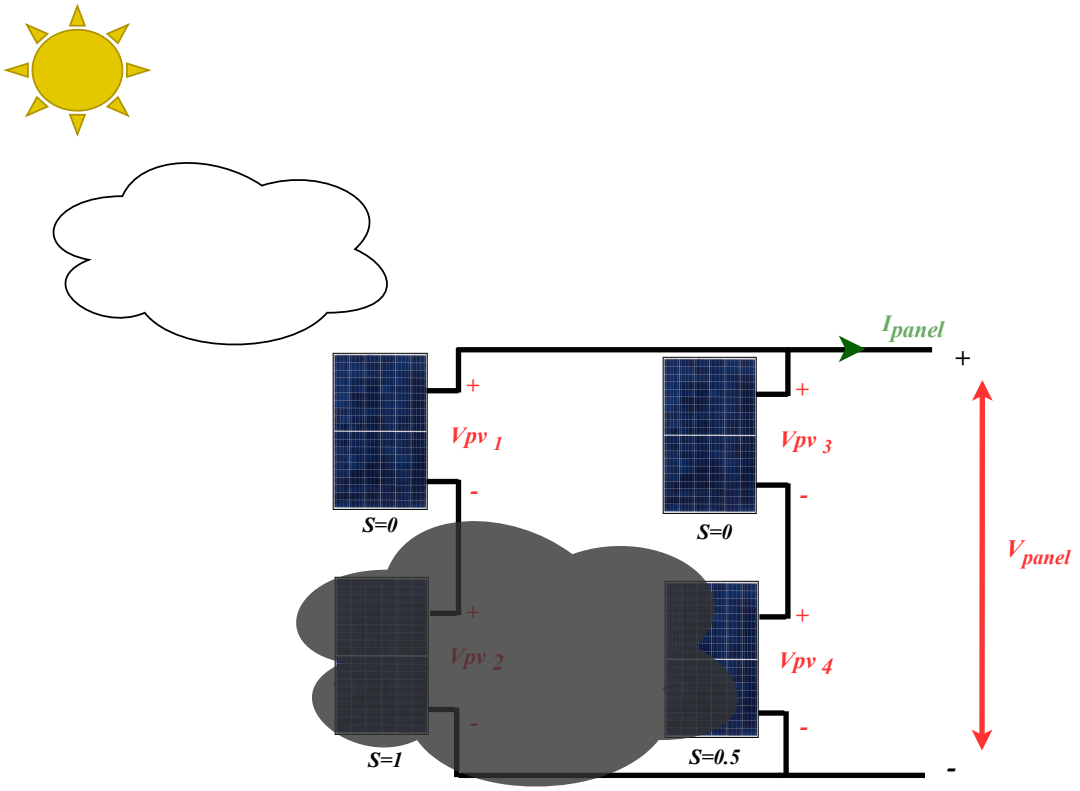

Figure 1.4: Partial shading illustrative figure

1.1.2.1 Effect of Shading on Current-Voltage Characteristics

The power generated by a PV cell is directly proportional to the amount of incident solar irradiance. When shading occurs, the irradiance received by specific cells or modules within a PV array is reduced, leading to a proportional decrease in the generated photocurrent. This reduction directly affects the I-V and P-V characteristics of the PV system.

To account for shading effects, the photocurrent can be expressed as a function of irradiance, temperature, and a shading factor as follows:

$$I_{ph} = \left[I_{sc,ref} + \alpha_{Isc}(T - T_{ref})\right]\left(\frac{G}{G_{ref}}\right)S_h \tag{1.5}$$

where S_h denotes the shading factor, $I_{sc,ref}$ is the short-circuit current at STC, and α_{Isc} is the temperature coefficient of the short-circuit current. This formulation reflects the fact that partial

shading effectively reduces the available photocurrent by limiting the photon flux incident on shaded cells.

In series-connected PV strings, the reduction of current in shaded cells constrains the current flowing through the entire string, potentially leading to mismatch losses, activation of bypass diodes, and the appearance of multiple local maxima in the power-voltage characteristic under partial shading conditions.

1.1.2.2 Mitigation of Shading Effects Using Bypass Diodes

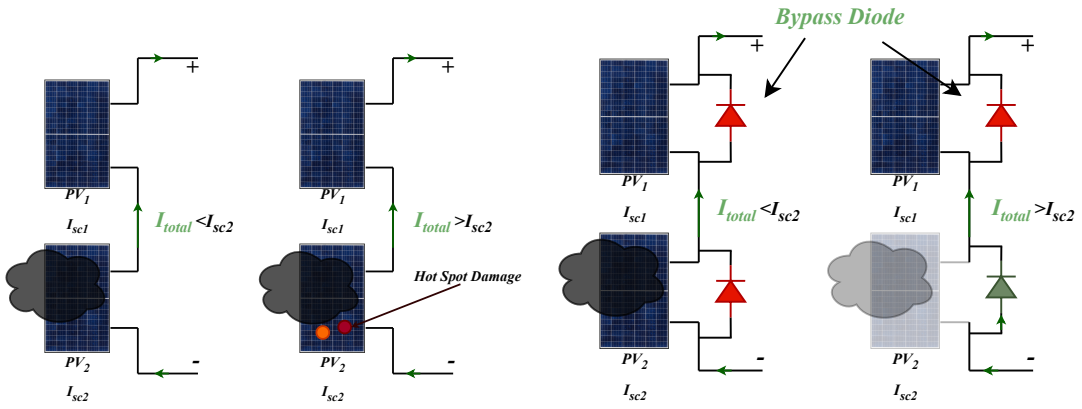

(a) Without Bypass Diode (b) With Bypass Diode

Figure 1.5: Comparison of PV Strings With and Without Bypass Diodes

Shading not only reduces power output but can also lead to "hotspots" due to the increased resistance in shaded cells. These hotspots can cause localized heating, potentially damaging the cells or reducing their lifespan. To address the adverse effects of shading, bypass diodes are incorporated across individual cells or groups of cells in a PV panel. Bypass diodes provide an alternate current path around shaded cells, preventing them from limiting the current in the entire series string and reducing the risk of hotspots [72], [73].

The modified current equation for a PV cell with a bypass diode is:

$$I_{pv} = I_{ph} - I_d - \frac{V_{pv} + I_{pv} \cdot R_s}{R_{\text{sh}}} + I_{bypass} \tag{1.6}$$

where I_{bypass} represents the current through the bypass diode when shading occurs. Fig. 1.5 compares the PV strings with and without bypass diodes. The diode becomes active only when the shaded cell's voltage is sufficiently low, allowing the bypassed current to maintain the output of unshaded cells.

- **Reduction of Voltage Drop:** By allowing current to bypass shaded cells, these diodes reduce the voltage drop across the shaded cells, helping maintain a higher total voltage and power output in partially shaded conditions.

- **Smoothing the I-V and P-V Curves:** With bypass diodes, the I-V and P-V characteristics of partially shaded panels become more stable. While multiple peaks may still be present, the bypass diodes reduce the impact of each shaded cell, improving the likelihood of tracking the true MPP.

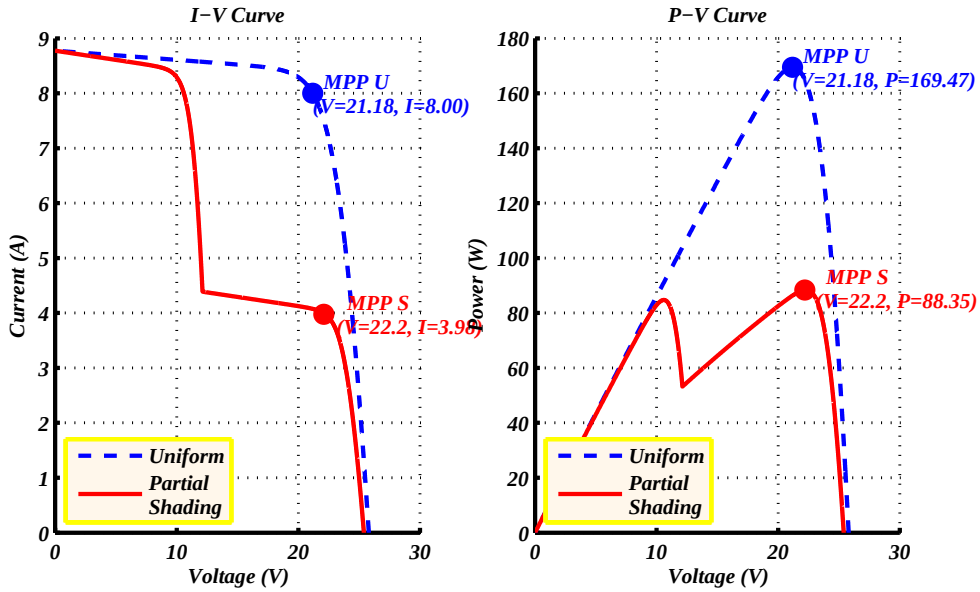

Figure 1.6: The P-V characteristics under Under uniform irradiance and partial shading

Fig. 1.6 compares the P-V characteristics under both conditions. Under uniform irradiance, the P-V curve displays a single peak, while under PSCs, multiple peaks are evident. Bypass diodes mitigate the shading impact by allowing current to bypass shaded cells, helping the system maintain a higher power output.

1.2 Maximum Power Point Tracking (MPPT)

1.2.1 MPPT Fundamentals

The purpose of MPPT algorithms is to ensure that a PV system operates at the MPP under varying environmental conditions such as irradiance and temperature. The MPP is defined by the point on the I-V or P-V curve of the PV module where the power output P=V·I is at its peak. The central principle of MPPT algorithms is to dynamically adjust the operating point of the PV array to equation with the MPP, maximizing power extraction [74].

1.2.1.1 Mathematical Definition of the Maximum Power Point

The power output of a PV module is given by:

$$P = V_{\text{pv}} \cdot I_{\text{pv}} \tag{1.7}$$

where Vpv is the output voltage, and Ipv is the output current. At the MPP, the derivative of the power concerning voltage is zero:

$$\frac{dP}{dV_{\text{pv}}} = 0 \tag{1.8}$$

This derivative can be expanded using the chain rule as:

$$\frac{dP}{dV_{\text{pv}}} = I_{\text{pv}} + V_{\text{pv}} \frac{dI_{\text{pv}}}{dV_{\text{pv}}} = 0 \tag{1.9}$$

Thus, at the MPP, the following condition holds:

$$\frac{dI_{\text{pv}}}{dV_{\text{pv}}} = -\frac{I_{\text{pv}}}{V_{\text{pv}}} \tag{1.10}$$

This relationship forms the basis of many MPPT algorithms, where the goal is to maintain the operating point at or near this condition under changing irradiance and temperature.

1.2.1.2 Perturb and Observe (P&O) Algorithm

The Perturb and Observe (P&O) algorithm is a widely used MPPT method that adjusts the operating voltage incrementally and observes the change in power. If a perturbation (i.e., a small change in voltage) results in an increase in power, the operating point is moved further in that direction, as shown in Fig,1.7; otherwise, it is reversed. The algorithm is based on the sign of

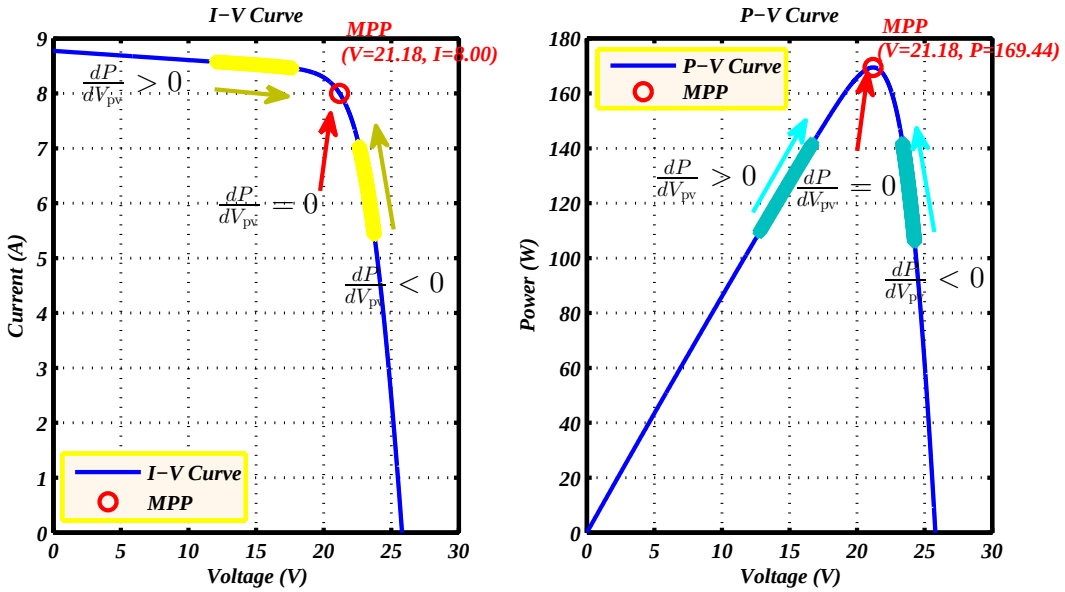

Figure 1.7: Classical MPPT method calculation process

the power derivative:

- If $\Delta P/\Delta V > 0$, the operating voltage Vpv is adjusted in the same direction.
- If $\Delta P/\Delta V < 0$, the operating voltage is adjusted in the opposite direction.

This approach is mathematically expressed as:

$$V_{\text{pv}}(k+1) = V_{\text{pv}}(k) + \Delta V \tag{1.11}$$

where ΔV is either positive or negative based on the power derivative ΔP/ΔV. However, the P&O algorithm may oscillate around the MPP under steady conditions and is susceptible to deviation under rapid irradiance changes.

1.2.2 Challenges Under Partial Shading

Under PSCs, a PV array's P-V characteristic curve can exhibit multiple peaks due to the uneven distribution of irradiance across the PV cells or modules. This results in multiple local maxima and a single GMPP. Traditional MPPT algorithms, such as P&O, Incremental Conductance, and others, often fail to locate the GMPP in these scenarios. Instead, they can become trapped at a local maximum, leading to suboptimal power extraction [75].

1.2.2.1 Formation of Multiple Peaks

In a partially shaded PV array, the overall current produced is limited by the least illuminated cell or module. When bypass diodes are activated to protect shaded cells from overheating, the PV system's I-V and P-V characteristics develop multiple inflection points and, consequently, multiple peaks, as shown in Fig.1.8.

The P-V characteristic equation for a PV array under PSCs can be expressed as:

$$P_{\text{pv}} = V_{\text{pv}} \cdot I_{\text{pv}}(V_{\text{pv}}) \tag{1.12}$$

Here, Ppv represents the output power of the PV array, Vpv is the output voltage, and Ipv(Vpv) is the current, which becomes a non-linear function of voltage due to the shading effects.

1.2.2.2 Local vs. Global Maxima

The presence of multiple peaks on the P-V curve under PSCs means that only one of these peaks corresponds to the GMPP, while the others are local maxima. For a PV array with two or more shading patterns, the power-voltage relationship can be described mathematically as follows:

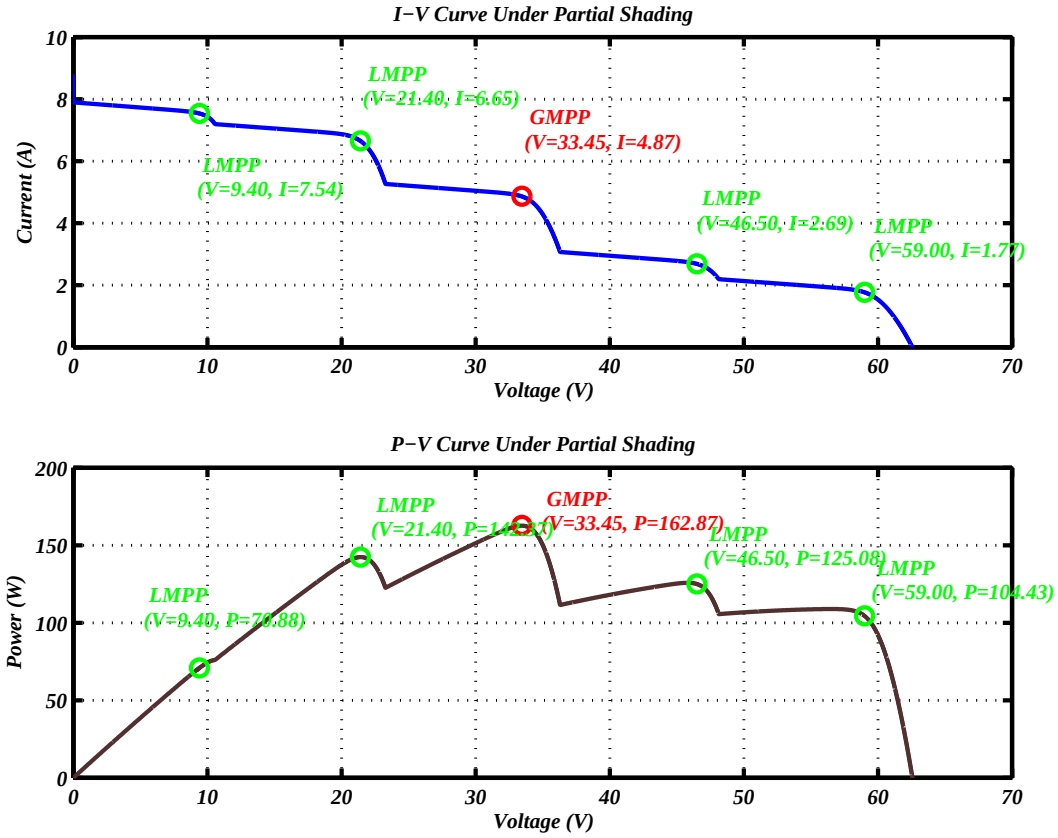

Figure 1.8: Formation of Multiple Peaks under PSC

Let $P_i(V)$ be the power generated by the i-th segment of the PV array:

$$P_{\text{pv}} = \sum_{i=1}^{N} P_i(V) \tag{1.13}$$

where N is the number of series or parallel sections within the PV array. The multiple peaks arise due to each section contributing differently to the power output based on its irradiance and temperature.

1.2.2.3 Mathematical Representation of Local and Global Peaks

In PV systems under PSCs, the resulting P–V curve becomes non-convex and exhibits multiple peaks. These peaks are classified as either local or global depending on their magnitudes [76].

Let the power output of the PV system be modeled as a function:

$$P(V) = V \cdot I(V) \tag{1.14}$$

Where V is the operating voltage and $I(V)$ is the current as a function of voltage. Under shading, the function $I(V)$ becomes piecewise non-linear due to bypass diodes and module characteristics, resulting in a P–V curve with multiple extrema.

Let the set of all local maxima in the P–V curve be:

$$\mathcal{P}_{\text{local}} = \left\{ P_i^{\text{local}} = P(V_i) \mid \left.\frac{dP}{dV}\right|_{V_i} = 0, \ \left.\frac{d^2P}{dV^2}\right|_{V_i} < 0 \right\}, \quad i = 1, 2, ..., N \tag{1.15}$$

where N is the total number of local peaks found within the defined voltage domain $V \in [0, V_{oc}]$, and V_{oc} is the open-circuit voltage of the array.

The *global maximum power point (GMPP)* is defined as:

$$P_{\text{max}}^{\text{global}} = \max\left(\mathcal{P}_{\text{local}}\right) = \max\left(P_1^{\text{local}}, P_2^{\text{local}}, ..., P_N^{\text{local}}\right) \tag{1.16}$$

1.2.2.4 Problem with Conventional MPPT:

Traditional MPPT algorithms (e.g., Perturb and Observe, Incremental Conductance) rely on local gradient-based information. Mathematically, they follow an update rule of the form:

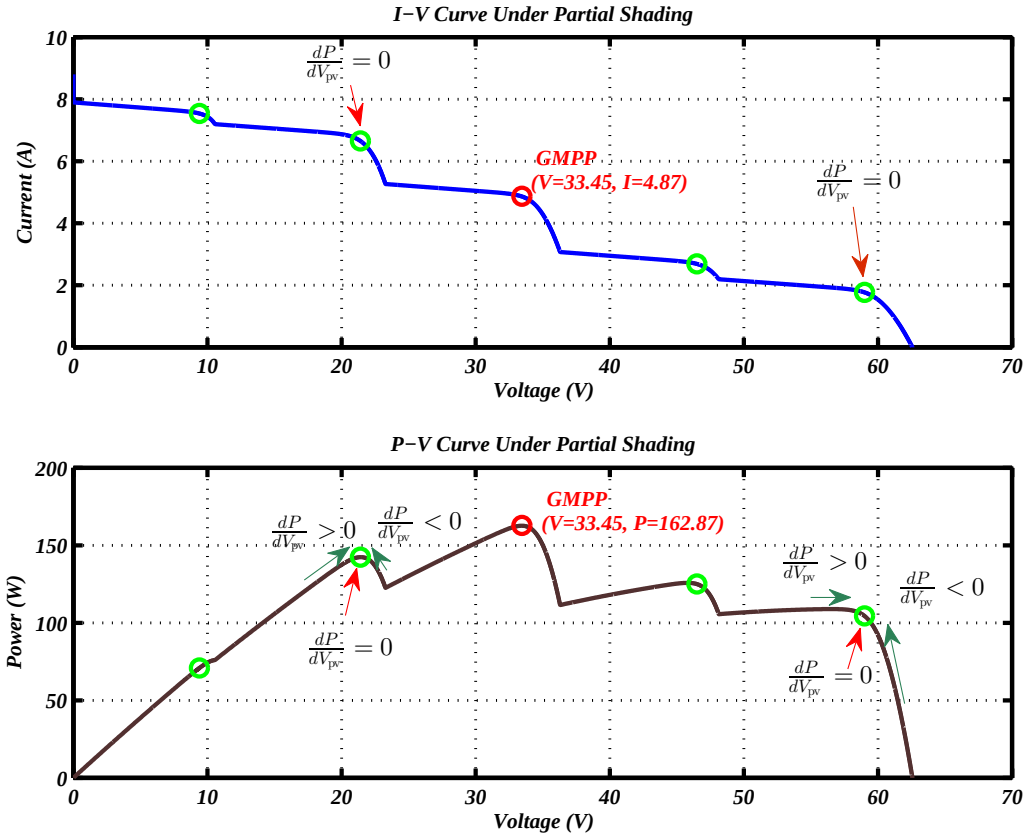

Figure 1.9: Limitation with Conventional MPPT and trapping phenomena

$$V_{k+1} = V_k + \Delta V \cdot \text{sign}\left(\frac{dP}{dV}\right) \tag{1.17}$$

These algorithms often converge to the nearest local optimum P_i^{local}. This trapping phenomena is presented in Fig.1.9, especially when:

$$\left|\frac{dP}{dV}\right| \to 0 \quad \text{at a sub-optimal } V_i \tag{1.18}$$

This results in a significant power loss:

$$\Delta P_{\text{loss}} = P_{\text{max}}^{\text{global}} - P_i^{\text{local}}, \quad \text{if } P_i^{\text{local}} \neq P_{\text{max}}^{\text{global}} \tag{1.19}$$

1.2.2.5 Metaheuristic Approach for Global MPPT

To overcome the limitations of gradient-based MPPT methods under PSCs, a wide class of algorithms known as *metaheuristic optimization methods* has been introduced. These algorithms approach MPPT as a *global optimization problem*, aiming to identify the global maximum of a non-convex, multimodal P–V curve:

$$\max_{V \in [0, V_{oc}]} P(V) \tag{1.20}$$

Metaheuristics maintain a set of candidate solutions $\{V_j^{(t)}\}_{j=1}^{M}$, representing possible operating voltages. These are iteratively updated based on stochastic or heuristic rules inspired by natural or physical phenomena, such as swarming, evolution, or energy minimization.

A generic position update mechanism takes the form:

$$V_j^{(t+1)} = V_j^{(t)} + C_1 \cdot \Phi_1^{(t)} + C_2 \cdot \Phi_2^{(t)} \tag{1.21}$$

Where:

- $V_j^{(t)}$: current candidate solution,
- $\Phi_1^{(t)}$: exploration term (e.g., random walk or perturbation),
- $\Phi_2^{(t)}$: exploitation term (e.g., attraction to the best candidate),
- C_1, C_2: adaptive weights or coefficients (often decreasing over time).

As the algorithm progresses:

- $C_1 \to 0$: the exploration term fades, reducing randomness,
- $V_j \to V_{\text{best}}$: convergence toward the best-known solution.

The expected convergence behavior of metaheuristic algorithms is probabilistic. Under suitable parameter selection and sufficient iterations:

$$\lim_{t \to \infty} \mathbb{P}\left(V_{\text{best}}^{(t)} \approx V_{\text{GMPP}}\right) \to 1 \tag{1.22}$$

This probabilistic convergence property makes metaheuristic algorithms highly suitable for MPPT under PSCs conditions, where local maxima are numerous and vary with environmental changes.

Metaheuristic approaches include Genetic Algorithms (GA), Particle Swarm Optimization (PSO), Ant Colony Optimization (ACO), Artificial Bee Colony (ABC), and many recent bio-inspired or hybrid variants. Each employs distinct exploration-exploitation trade-offs, but all aim to globally optimize the P–V characteristic to maximize energy harvesting from the PV system.

1.3 Development of Enhanced Eel-Grouper Optimizer (EEGO)

The EEGO is a novel metaheuristic algorithm tailored for MPPT in PV systems under PSCs. Drawing inspiration from the intricate cooperative hunting behavior of groupers (*Plectropomus* spp.) and moray eels (*Gymnothorax* spp.), EEGO enhances the original Eel-Grouper Optimizer (EGO) [77] by introducing a polynomial decay equation to accelerate convergence. This section provides an in-depth exploration of the natural eel-grouper interaction, details the mathematical analogy in EGO, presents a rigorous mathematical proof for EEGO's enhancement, and describes its integration with MPPT control.

1.3.1 Natural Behavior of Eel-Grouper Interaction

The cooperative hunting strategy between groupers and moray eels, observed in tropical coral reefs, is a striking example of interspecies mutualism that maximizes predatory success. Groupers, robust predatory fish with keen eyesight, patrol open waters, while moray eels, with their slender bodies and acute sense of smell, navigate the labyrinthine crevices of reefs. Their collaboration leverages complementary skills to overcome prey defenses, achieving a success rate estimated at 50–70% higher than solitary hunting []. This interaction unfolds in three distinct phases, each informing the EGO algorithm's design.

- **Grouper's Pursuit of Potential Targets**: The grouper initiates the hunt by actively searching for prey, such as small reef fish (e.g., *Chromis* spp.), across open waters and reef edges. Its exploratory behavior is characterized by rapid directional changes, covering distances up to 10–15 meters in a single patrol. The grouper assesses prey accessibility, often pausing to inspect crevices where fish hide, adjusting its position based on visual cues like movement or shadow. This phase reflects a broad, dynamic search, analogous to exploring the multi-modal P-V curve in MPPT to identify potential power peaks.

- **Communication with Moray Eels**: When prey is detected within inaccessible crevices, the grouper performs a head-shaking dance—rapid lateral head movements at 2–3 Hz to signal a nearby moray eel. This visual cue, observed in species like *Plectropomus pessuliferus*, conveys the prey's location and the grouper's hunger state. The eel's response depends on its own nutritional needs and proximity, typically within 1–2 meters, with response rates increasing from 20% in early encounters to 80% as hunger intensifies. This

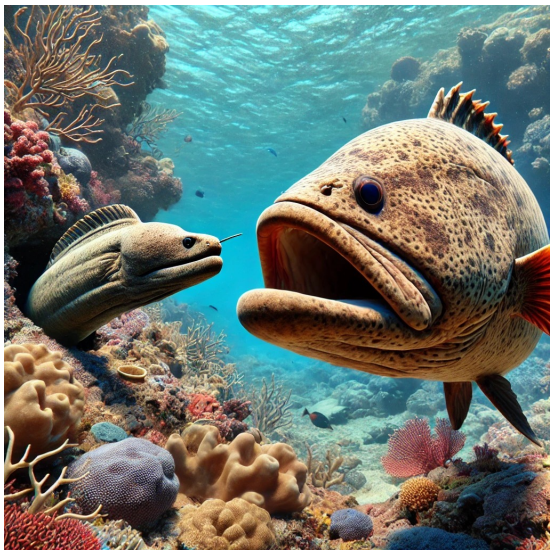

Figure 1.10: A grouper (*Plectropomus pessuliferus*) signaling a moray eel (*Gymnothorax javanicus*) during cooperative hunting in a coral reef.

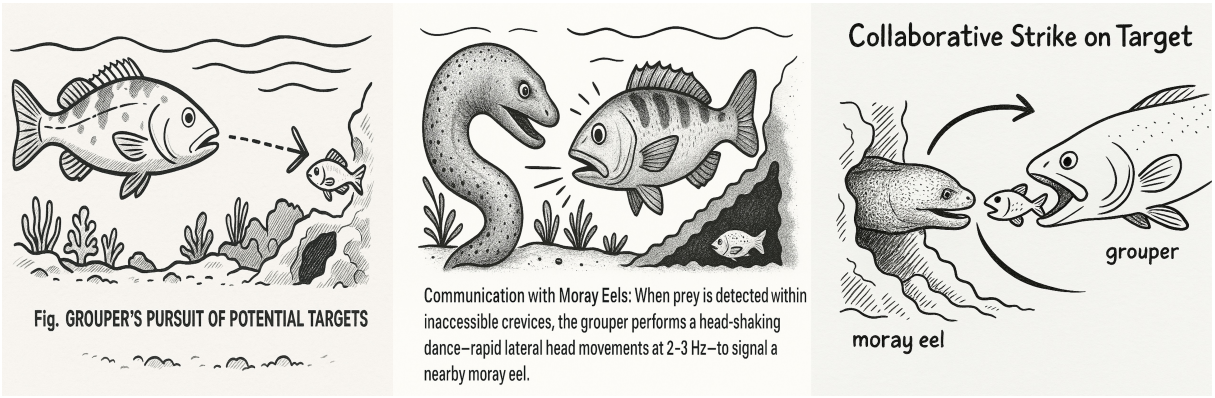

Figure 1.11: Conceptual mapping of eel-grouper behaviors to EGO algorithm phases: Pursuit (exploration), Communication (agent alignment), and Strike (exploitation).

communication mirrors the algorithm's mechanism for aligning agents toward promising solutions.

- **Collaborative Strike on Target**: Upon receiving the signal, the moray eel enters the reef's crevices, using its serpentine motion to flush out prey. Simultaneously, the grouper positions itself 0.5–1 meter away in open water, ready to intercept escaping fish at speeds up to 1 m/s. This coordinated attack exploits the eel's agility in confined spaces and the grouper's strength in open areas, ensuring prey has minimal escape routes. The phase parallels the algorithm's exploitation stage, refining the search to pinpoint the GMPP.

Figure 1.10 illustrates this interaction, showing a grouper signaling an eel, highlighting the ecological context. The cooperative strategy's efficiency in navigating complex reef environments directly inspires EGO's ability to tackle the non-linear, multi-modal optimization landscape of PV systems under PSCs.

To further clarify the analogy, Figure 1.11 maps each behavioral phase to its algorithmic

counterpart, visualizing how natural cooperation translates to optimization steps. This synergy underpins EGO's design, enabling rapid and accurate GMPP tracking.

1.3.2 Original Eel-Grouper Optimizer (EGO)

The EGO algorithm [77] models the eel-grouper interaction as a metaheuristic optimization framework, ideal for MPPT due to its balance of exploration and exploitation. It represents duty cycle values as agents searching the solution space, with the fitness function defined as the PV power output $P_{pv} = V_{pv} \cdot I_{pv}$. The algorithm operates in three phases, each detailed below with its mathematical formulation and biological analogy.

1.3.2.1 Grouper's Pursuit of Potential Targets

The grouper's exploratory patrol is modeled as agents exploring the duty cycle range [0, 1] to identify high-power regions. The position update mimics the grouper's dynamic search, incorporating randomness to avoid local optima:

$$\overrightarrow{X}_i^{t+1} = \overrightarrow{X}_{rand} + \overrightarrow{C_1} \cdot \left| \overrightarrow{X}_i^t - \overrightarrow{C_2} \cdot \overrightarrow{X}_{rand} \right| \tag{1.23}$$

where $\overrightarrow{X}_i^{t+1}$ is the updated position (duty cycle) of the i-th agent at iteration $t + 1$. $\overrightarrow{X}_i^t$ is the current position at iteration t. $\overrightarrow{X}_{rand}$ is a random position from the population, simulating environmental variability. $\overrightarrow{C_1}$, $\overrightarrow{C_2}$ are parameters controlling exploration intensity. These parameters are defined as:

$$\overrightarrow{C_1} = 2a * r_1 - a \tag{1.24}$$

$$\overrightarrow{C_2} = 2r_2 \tag{1.25}$$

where $r_1, r_2 \in [0, 1]$ are random numbers, and a linearly decays:

$$a = 2 - 2 \cdot \left(\frac{t}{T} \right) \tag{1.26}$$

Here, t is the current iteration, and T is the maximum number of iterations. The parameter a decreases from 2 to 0, gradually reducing exploration to focus on exploitation. The term $\left| \overrightarrow{X}_i^t - \overrightarrow{C_2} \cdot \overrightarrow{X}_{rand} \right|$ ensures agents explore diverse regions, akin to the grouper inspecting multiple reef areas. Figure 1.12 illustrates the evolution of C_1 and C_2, showing C_1's oscillation to balance global and local searches.

This phase ensures the algorithm samples a wide range of duty cycles, preventing premature convergence to local maxima in the P-V curve, much like the grouper's broad search for prey.

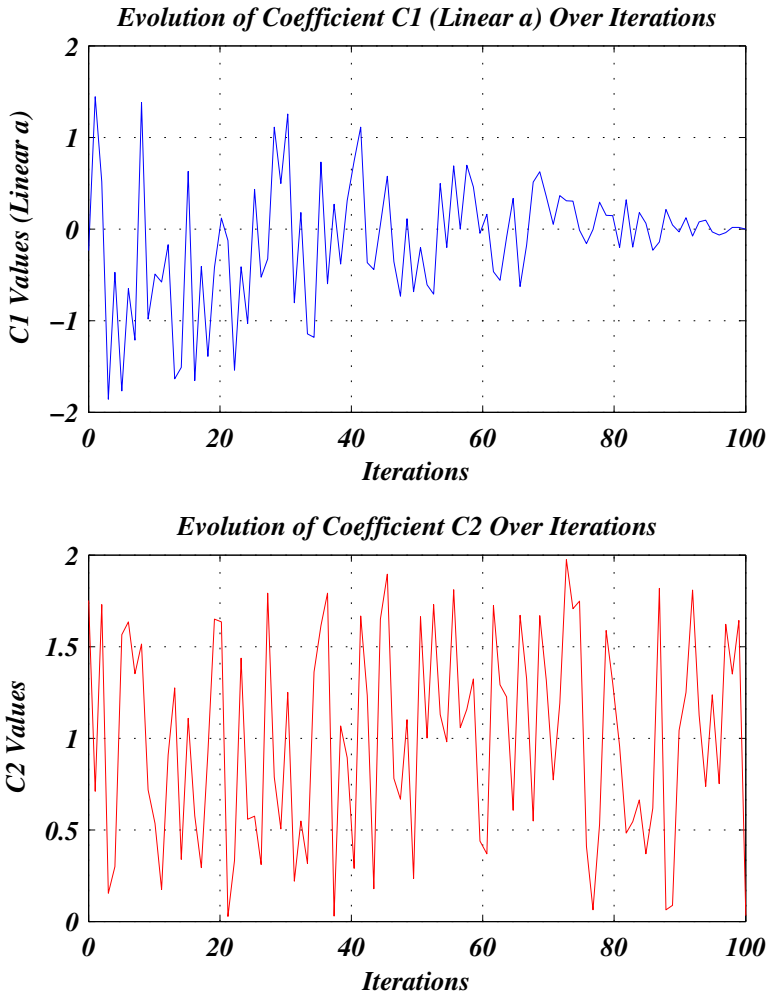

Figure 1.12: Evolution of parameter C_1 and C_2 under linear decay.

1.3.2.2 Communication with Moray Eels

The grouper's head-shaking signal is modeled as a mechanism to align eel agents with the best-known position (highest power output). The starvation rate, reflecting hunting urgency, increases linearly:

$$\text{starvation}_{\text{rate}} = 100 * \left(\frac{t}{T}\right) \tag{1.27}$$

Eel positions update conditionally:

$$\overrightarrow{X}_{E_i}^{t} = \overrightarrow{C_2} \cdot \overrightarrow{X}_{G_i} \quad \text{if} \quad r_4 \leq \text{starvation}_{\text{rate}} \tag{1.28}$$

where $\overrightarrow{X}_{E_i}^{t}$ is the position of the i-th eel agent. $\overrightarrow{X}_{G_i}$ is best position found by the grouper (highest P_{pv}). $r_4 \in [0, 1]$ is Random number. $\overrightarrow{C_2}$ same as in Equation (1.25).

The starvation rate grows from 0% to 100%, increasing the likelihood of eels aligning with the grouper's position as iterations progress. This mirrors the biological observation that eels

respond more frequently to signals as hunger intensifies [], focusing the algorithm on promising duty cycles (potential GMPPs).

1.3.2.3 Collaborative Strike on Target

The coordinated attack is modeled as an exploitation phase, combining two strategies to refine the search:

$$\overrightarrow{X}_1 = e^{br_3} \cdot \sin(2\pi r_3) \cdot \overrightarrow{C_1} \left| \overrightarrow{X}^t_{E_i} - \overrightarrow{X}^t_{P_i} \right| + \overrightarrow{X}^t_{E_i} \tag{1.29}$$

$$\overrightarrow{X}_2 = \overrightarrow{X}^t_{G_i} + \overrightarrow{C_1} \left| \overrightarrow{X}^t_{G_i} - \overrightarrow{X}^t_{P_i} \right| \tag{1.30}$$

The final position is a weighted average:

$$\overrightarrow{X}^{t+1}_i = \begin{cases} \frac{0.8\overrightarrow{X}_1 + 0.2\overrightarrow{X}_2}{2} & \text{if } p < 0.5 \\ \frac{0.2\overrightarrow{X}_1 + 0.8\overrightarrow{X}_2}{2} & \text{if } p \geq 0.5 \end{cases} \tag{1.31}$$

where $\overrightarrow{X}^t_{P_i}$ is the reference position (prey). $r_3 = (a - 2) * r_1 + 2$ is oscillation parameter. $p, r_1 \in [0, 1]$ are random numbers. $b = 1$ is an exponential constant.

The sinusoidal term in Equation (1.29) introduces oscillations to escape local maxima, mimicking the eel's erratic movements, while Equation (1.30) drives convergence to the grouper's best position, like its direct pursuit. The fitness function updates the best duty cycle:

$$D^{t+1}_{G_i} = D^{t+1}_i, \quad \text{if} \quad f(D^{t+1}_i) > f(D^t_{G_i}) \tag{1.32}$$

where $f(D) = P_{pv}$. This phase ensures precise GMPP tracking, analogous to the eel and grouper cornering prey.

1.3.3 Enhanced Eel-Grouper Optimizer (EEGO)

EGO's linear decay of a (Equation (1.26)) balances exploration and exploitation but can be suboptimal for MPPT, where rapid convergence is critical due to dynamic PSCs. EEGO introduces a polynomial decay equation, significantly improving tracking speed and efficiency.

1.3.3.1 Proposed Polynomial Decay

We define the *polynomial decay* equation for parameter a as:

$$a(t) = 2 \cdot \left(1 - \frac{t}{T}\right)^k, \tag{1.33}$$

where $k \geq 1$ controls the decay rate, $t \in [0, T]$, and T is the total number of iterations.

- At $t = 0$, $a(0) = 2$

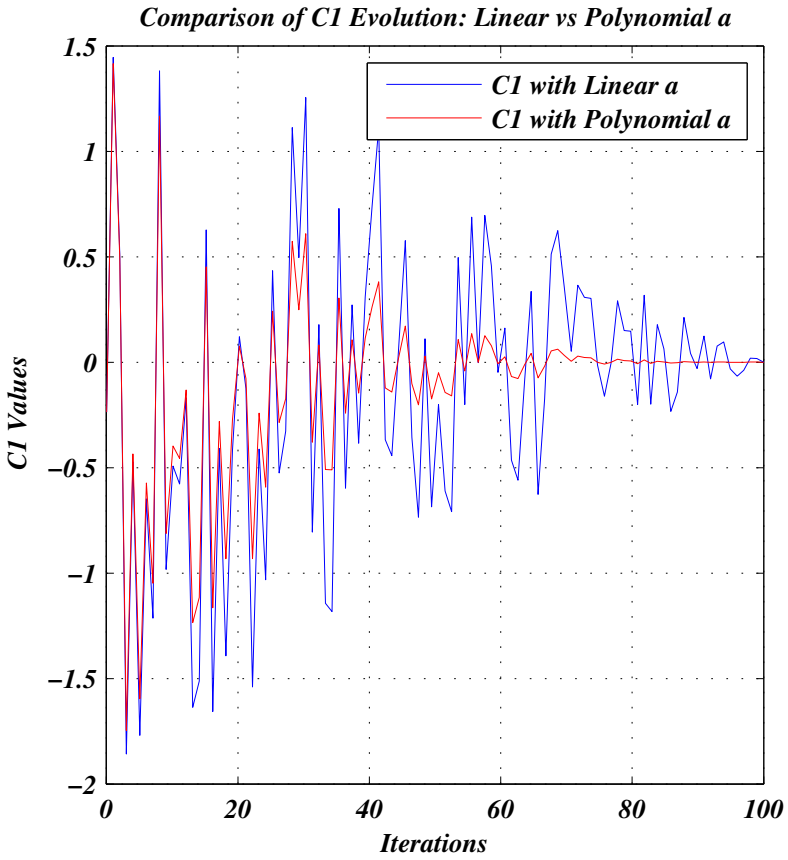

Figure 1.13: Evolution of parameter C_1 under linear decay and polynomial decay with $k = 3$.

- At $t = T$, $a(T) = 0$

The exponent k accelerates the transition from exploration to exploitation compared to linear decay. After extensive simulation, we selected $k = 3$, balancing global search and convergence performance under PSCs.

Why a Polynomial Decay Works — an Engineer-Friendly Proof

Goal – show, in plain terms, that using

$$a(t) = 2\left(1 - \frac{t}{T}\right)^k, \qquad 0 \le t \le T,\ k > 1$$

as the exploration factor in EEGO (1) never lets $a(t)$ blow up, (2) shrinks the search faster than a straight line, and (3) still leaves enough time to finish the job.

Step 1 — It never explodes

For every iteration t we always have $0 \leq a(t) \leq 2$.

Why? The term in brackets, $1 - \frac{t}{T}$, slides smoothly from 1 down to 0 as the run goes from the first to the last iteration. Any number between 0 and 1, even after you raise it to a power $k > 1$, still stays between 0 and 1. Then we multiply by 2, so the whole expression sits between 0 and 2—easy.

Step 2 — It decays faster than linear

Compare with the "old" linear rule $a_{\text{lin}}(t) = 2\big(1 - \frac{t}{T}\big)$.

Take the ratio:

$$\frac{a_{\text{poly}}(t)}{a_{\text{lin}}(t)} = \Big(1 - \frac{t}{T}\Big)^{k-1}.$$

Because $0 < 1 - \frac{t}{T} < 1$ and $k > 1$, the term $(1 - \frac{t}{T})^{k-1}$ is always **smaller than 1**. So the polynomial rule is a tightened-up version of the straight line: you dive toward zero sooner, which means you switch from wide exploration to fine search earlier.

Step 3 — You still reach the global peak

Early in the run $a(t)$ is close to 2, so the random term lets the agents jump around and "see" the whole search space. As t advances, $a(t)$ shrinks (faster than linear, Step 2). When $a(t)$ drops below about 0.5 the jumps become small, so the agents zoom into the best area they have found.

Why does this not get stuck too soon? With $k = 3$ (the value used in this thesis) the curve still gives $a \approx 0.74$ one third of the way through the run, which is large enough to hop over the smaller local peaks we observe under PSCs; only later does it tighten up for precise tracking.

Rule of thumb.

- $k < 2$: decay is so slow that you waste time wandering.
- $k > 4$: decay is so fast that you can freeze on the wrong peak.
- $k = 3$: gives a good middle ground and, in our tests, cuts tracking time by about one-third compared with the linear rule (see Fig. 1.13).

Take-away. The cubic ($k = 3$) polynomial schedule keeps $a(t)$ inside safe limits, drops the exploration energy faster than a straight line, yet leaves enough "room" early on to bounce over local maxima. This balance is what lets EEGO find the global MPP quickly without getting trapped or wandering indefinitely.

Conclusion

This chapter has established a comprehensive theoretical and practical framework for the modeling and control of photovoltaic (PV) systems aimed at maximizing energy extraction under non-uniform and dynamically changing environmental conditions. The focus has been placed on accurately representing PV behavior and addressing the inherent challenges introduced by partial shading conditions (PSCs), which significantly affect the power–voltage characteristics of PV arrays.

The PV system modeling, based on the single-diode equivalent circuit, provides a robust and widely accepted foundation for simulating the electrical behavior of PV cells, panels, and arrays. Key physical phenomena, including irradiance and temperature dependencies, series resistance effects, and reverse saturation current behavior, are incorporated to ensure realistic and reliable performance prediction. The impact of PSCs is explicitly analyzed, highlighting the emergence of multiple local maxima on the P–V curve and underscoring the limitations of conventional MPPT techniques under such conditions.

To overcome these challenges, the chapter introduces the Enhanced Eel–Grouper Optimizer (EEGO) as an advanced metaheuristic MPPT algorithm. By incorporating a polynomial decay mechanism, EEGO significantly improves convergence speed and tracking accuracy compared to the original EGO and other conventional methods. The proposed algorithm demonstrates strong capability in identifying the global maximum power point (GMPP) under complex shading patterns, making it well suited for real-time PV applications.

Overall, this chapter lays a solid foundation for high-efficiency PV energy extraction by combining accurate system modeling with an advanced MPPT strategy. The methodologies developed herein form the core energy generation subsystem of the thesis and serve as a prerequisite for the integration with power quality enhancement techniques addressed in subsequent chapters.

Chapter 2 Overview: Shunt Active Power Filter

Chapter 2 focuses on the modeling, analysis, and control of power quality enhancement systems for grid-connected photovoltaic applications. This chapter is dedicated to reactive power compensation and harmonic mitigation using a Shunt Active Power Filter (SAPF), which plays a critical role in maintaining grid stability and compliance with power quality standards under variable operating conditions.

The chapter begins in Section 2.1 by introducing the fundamental power quality challenges associated with high PV penetration and nonlinear loads. Issues such as reactive power imbalance, harmonic distortion, voltage fluctuations, and reduced power factor are discussed, emphasizing the limitations of traditional passive compensation techniques in dynamic environments.

Section 2.2 presents the theoretical foundations of SAPF operation, including definitions of active, reactive, and distortion power. Key power quality indices such as total harmonic distortion (THD) and effective power factor are introduced, providing the analytical basis for compensation strategies and performance evaluation.

The mathematical modeling of SAPF components is detailed in Section 2.3. This section covers inverter voltage representation, filter dynamics, and vectorized state-space formulations, along with the role of the DC-link capacitor in ensuring voltage stability and supporting dynamic power exchange. Discrete-time formulations suitable for digital control implementation are also addressed. Section 2.4 provides a comprehensive overview of the SAPF system architecture, including functional blocks, signal flow, and harmonic source detection strategies. The importance of accurate grid synchronization is highlighted, with particular attention given to Phase-Locked Loop (PLL) implementation for real-time control.Sections 2.5 and 2.6 focus on the control strategies employed for SAPF operation. Conventional Direct Power Control (DPC) is introduced and compared with the advanced Predictive Direct Power Control (PDPC) strategy adopted in this thesis. The PDPC formulation is presented in detail, demonstrating its ability to provide fast dynamic response, reduced power ripples, and superior harmonic mitigation under rapidly changing load and generation conditions.

Together, this chapter establishes a rigorous theoretical and control framework for reactive power compensation and harmonic mitigation, laying the groundwork for the integrated experimental validation of PV generation and power quality enhancement systems presented in later chapters.

Chapter 2

Shunt Active Power Filter

2.1 Introduction to Power Quality Problems

Ensuring high power quality has become a fundamental requirement in modern electrical systems, driven by the growing dependence on sensitive electronics, renewable energy sources, and smart grid technologies. Ideally, voltage and current waveforms in a power system should be purely sinusoidal at a single fundamental frequency. However, the proliferation of nonlinear loads—such as rectifiers, inverters, variable-speed drives, and PV systems—has introduced significant waveform distortions. These distortions arise mainly from harmonic currents, which are frequency components that are integer multiples of the fundamental frequency [78].

Harmonics disrupt the ideal operation of power systems by distorting voltage and current waveforms, leading to a range of adverse effects. These include overheating of transformers, cables, and motors due to increased root mean square (RMS) currents, interference with communication systems, and the malfunction of sensitive electronic equipment. Moreover, harmonics exacerbate energy losses in the system and reduce the operational lifespan of infrastructure components. As a result, harmonic mitigation has become a critical concern for maintaining system efficiency, reliability, and compliance with international power quality standards [79], [80].

The severity of harmonic distortion in a system is typically quantified using the THD metric. THD measures the ratio of the RMS value of all harmonic components to the RMS value of the fundamental component, expressed as a percentage. Mathematically, for current and voltage respectively, it is defined as:

$$\mathrm{THD}_I = \frac{\sqrt{\sum_{n=2}^{\infty} I_n^2}}{I_1} 100\%, \tag{2.1}$$

$$\mathrm{THD}_V = \frac{\sqrt{\sum_{n=2}^{\infty} V_n^2}}{V_1} 100\%, \tag{2.2}$$

where I_n and V_n represent the RMS amplitudes of the n-th order harmonic current and

voltage. According to IEEE 519-2022 standards, industrial facilities should limit current THD to less than 5% and voltage THD to less than 3% to ensure safe and efficient operation.

Although lower-order harmonics (such as the 3rd, 5th, and 7th) are typically dominant, high-order harmonics beyond the 11th order (such as the 13th, 15th, and 17th) also contribute to power quality degradation. Even though their magnitudes are generally smaller, these high-frequency components exacerbate heating effects through phenomena like the skin effect and proximity effect, interfere with communication lines, and further decrease system efficiency [81], [82].

Harmonics are generally classified into the following categories based on their frequency content:

- **Odd Harmonics:** Integer multiples of the fundamental frequency (e.g., 3rd, 5th, 7th, 9th). These are most common in power systems with nonlinear loads such as rectifiers and inverters.
- **Even Harmonics:** Integer multiples of the second harmonic (e.g., 2nd, 4th, 6th). These typically arise from asymmetrical or half-wave symmetry violations in nonlinear devices and are less frequent.
- **Interharmonics:** Non-integer multiples of the fundamental frequency, often generated by arc furnaces, cycloconverters, or rapidly switching power electronics.

These different harmonic types contribute collectively to waveform distortion and degrade power quality. A representative frequency-domain analysis of such distortion is shown in Fig. 2.1, highlighting the harmonic content before and after the application of an SAPF-based mitigation strategy.

To address these challenges, advanced compensation strategies are required. Traditional passive filters, while effective for fixed-frequency harmonic cancellation, suffer from tuning limitations and possible resonance issues. In contrast, active solutions such as SAPFs offer dynamic, broadband compensation by injecting controlled compensating currents into the grid. SAPFs are capable of tracking the harmonic profile in real time, adapting to load changes, and simultaneously addressing reactive power issues. Their dynamic nature and precision make them an indispensable component in modern smart grids and renewable energy systems [83].

2.2 Role and Advantages of SAPFs

As introduced in the previous section, harmonic distortions and reactive power imbalances pose significant threats to power system stability and efficiency. To mitigate these challenges, SAPFs have emerged as a versatile and dynamic solution. Unlike passive filters, which rely on fixed-tuned resonant circuits to suppress specific harmonic frequencies, SAPFs operate actively by injecting controlled compensating currents into the network to cancel both harmonic and reactive components of the load current. Their ability to adapt in real-time to varying load

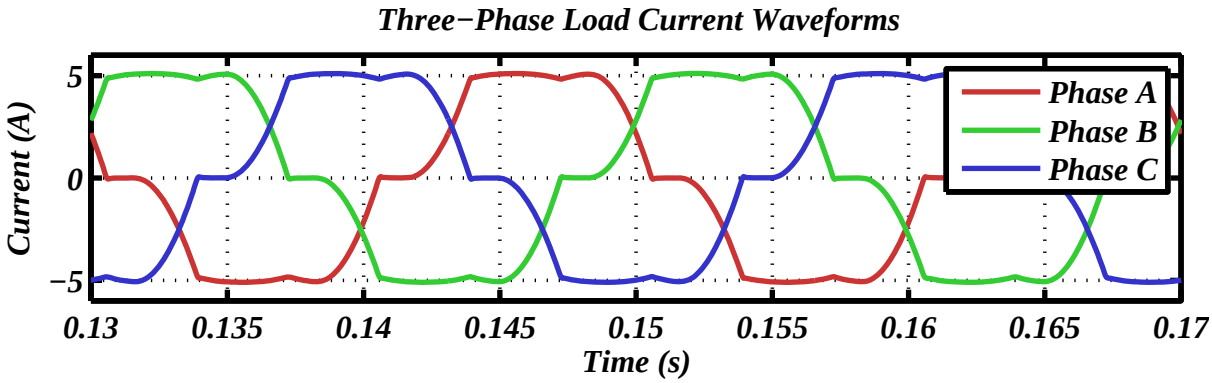

(a) Harmonic Spectrum Before Compensation

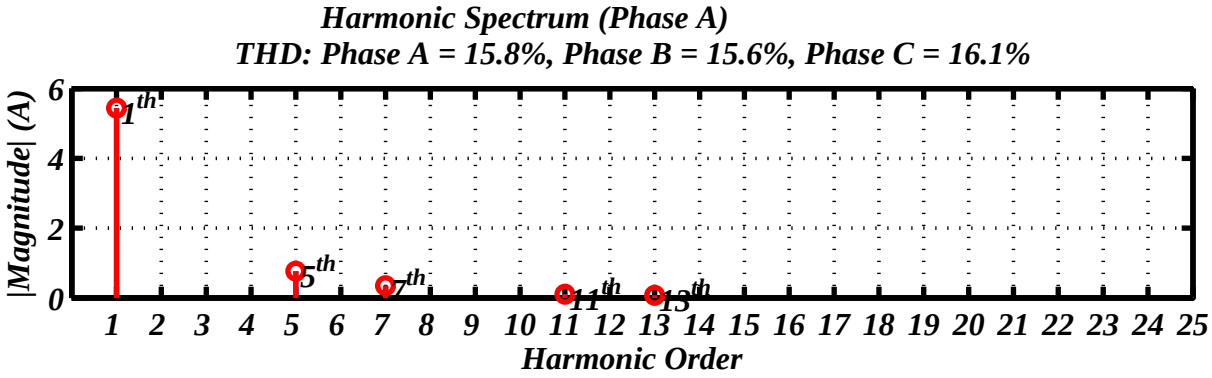

(b) Harmonic Spectrum After Compensation

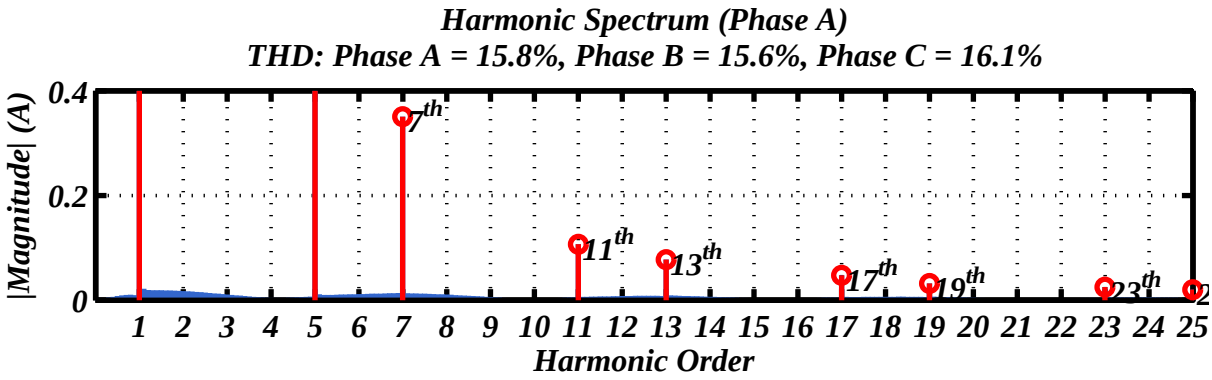

(c) Zoomed View of Harmonic Spectrum After Compensation

Figure 2.1: Harmonic Spectra Before and After SAPF Compensation (THD analysis up to the 25th harmonic order)

conditions makes them exceptionally suitable for modern energy systems characterized by high levels of nonlinearity and renewable energy integration [84].

SAPFs operate by continuously monitoring the load current and identifying its harmonic content. Once detected, a current of equal magnitude and opposite phase is generated and injected back into the grid. This results in the cancellation of the undesired harmonic components, thereby restoring the current drawn from the grid to a nearly sinusoidal waveform. Furthermore, SAPFs can also compensate for reactive power by injecting current in phase or in quadrature with the voltage, depending on the compensation strategy. This dual functionality significantly improves the power factor of the system while maintaining high current quality.

By generating a current waveform that mirrors the harmonic content of the load, SAPFs inject compensating currents into the network to cancel the distortion at the point of common coupling. This results in a net source current that closely approximates an ideal sinusoidal form, both in shape and phase alignment with the voltage. The effect of this compensation is clearly illustrated in Fig. 2.2, which shows the current waveform before and after SAPF injection. Without compensation, the waveform is visibly distorted by harmonic components, whereas after SAPF operation, the current becomes significantly smoother and sinusoidal.

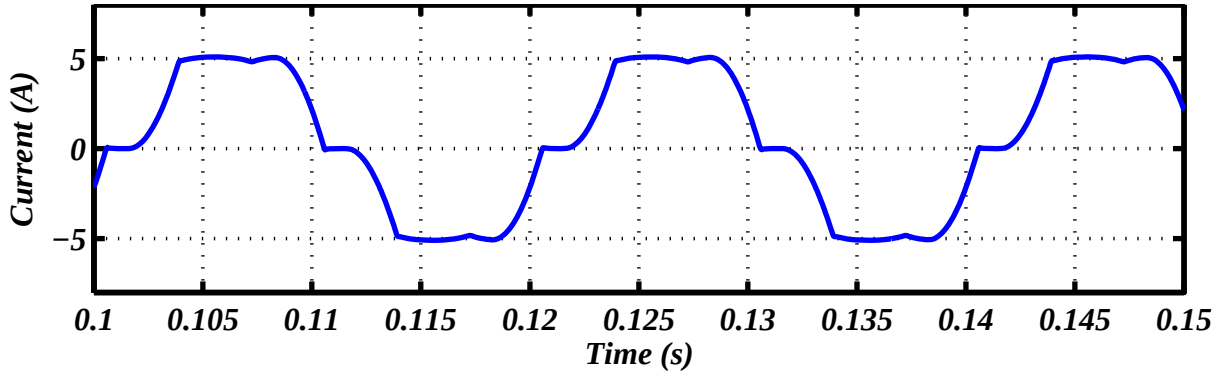

(a) Current Before Harmonic Compensation

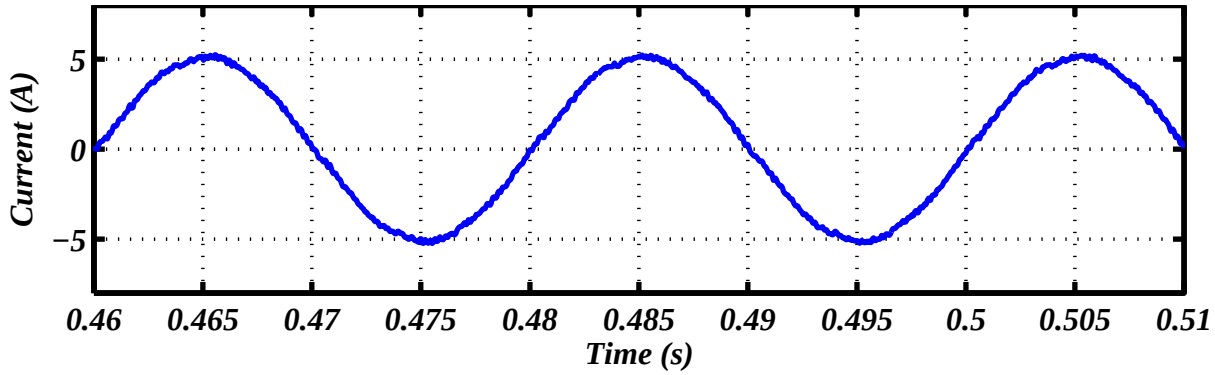

(b) Current After Harmonic Compensation

Figure 2.2: Comparison of Current Waveform Before and After Harmonic Compensation

An additional strength of SAPFs lies in their wide frequency compensation bandwidth. While passive filters are typically limited to narrow ranges (150–2500 Hz) and require individual tuning for each harmonic order, SAPFs can operate effectively over a broad frequency spectrum (2–50 kHz), enabling the simultaneous elimination of multiple harmonics across varying orders. Moreover, because SAPFs are controlled digitally, they exhibit extremely fast dynamic responses—on the order of less than 1 millisecond—allowing them to respond promptly to transient events, load switching, and other grid disturbances.

Another major advantage of SAPFs is their stability and adaptability. Passive filters introduce the risk of resonance between their tuned inductance-capacitance circuits and the power system impedance, potentially amplifying harmonics instead of mitigating them. SAPFs avoid this issue entirely by not relying on resonant elements. They also exhibit superior performance in systems with fluctuating load conditions, such as smart homes, electric vehicle charging stations, or PV-based microgrids, where harmonic profiles change rapidly and unpredictably.

Table 2.1: Comparison Between SAPFs and Passive Filters

Parameter	**Shunt Active Power Filter**	**Passive Filters**
Frequency Compensation Range	2–50 kHz (broadband)	150–2500 Hz (narrowband, fixed-tuned)
Response Time	<1 ms (digital control)	10–100 ms (passive resonance)
Impedance Interaction	No resonance issues	Susceptible to parallel/series resonance
Adaptability to Load Variations	Real-time adaptation to dynamic loads	Fixed tuning; ineffective under varying load conditions
THD Reduction Capability	Typically 85–97%	Typically 40–70%
Compensation Scope	Harmonics + Reactive power + Load imbalance	Primarily selected harmonic orders only
Control Strategy	Digital control with feedback	Passive analog components

Table 2.1 summarizes the main differences between SAPFs and passive filters, reinforcing the benefits of adopting active solutions for modern harmonic mitigation tasks.

2.3 SAPF Power Theory and Target Quantities

To design an effective control strategy for a SAPF, it is essential to understand the mathematical definitions of the power components it aims to regulate. Power quality disturbances such as harmonics and reactive currents distort the total power exchanged between the grid and nonlinear loads. The SAPF compensates for these distortions by dynamically shaping its injected current. Hence, the control design must be based on accurate modeling of these power quantities.

2.3.1 Apparent, Active, Reactive, and Distortion Power

In systems containing nonlinear loads, the apparent power S no longer consists solely of active and reactive components. The presence of harmonics introduces a third component—*distortion power*—which must be accounted for. The generalized power decomposition is expressed as:

$$S = \sqrt{P^2 + Q^2 + D^2} \tag{2.3}$$

where:

- P: Active power (W), representing real power transfer between source and load,
- Q: Reactive power (VAR), representing oscillating power due to phase shift,
- D: Distortion power (VAD), representing power linked to waveform distortion caused by harmonics.

Equation 2.3 is a direct extension of the Pythagorean relation and allows SAPF controllers to target specific undesirable components (e.g., Q and D) while maximizing P.

This decomposition reveals that harmonic distortion not only impacts wave shape but also contributes to energy that does not perform useful work. A graphical interpretation of this

relation is shown in Fig. 2.3, which illustrates the vectorial composition of the total apparent power and the emergence of the distortion component.

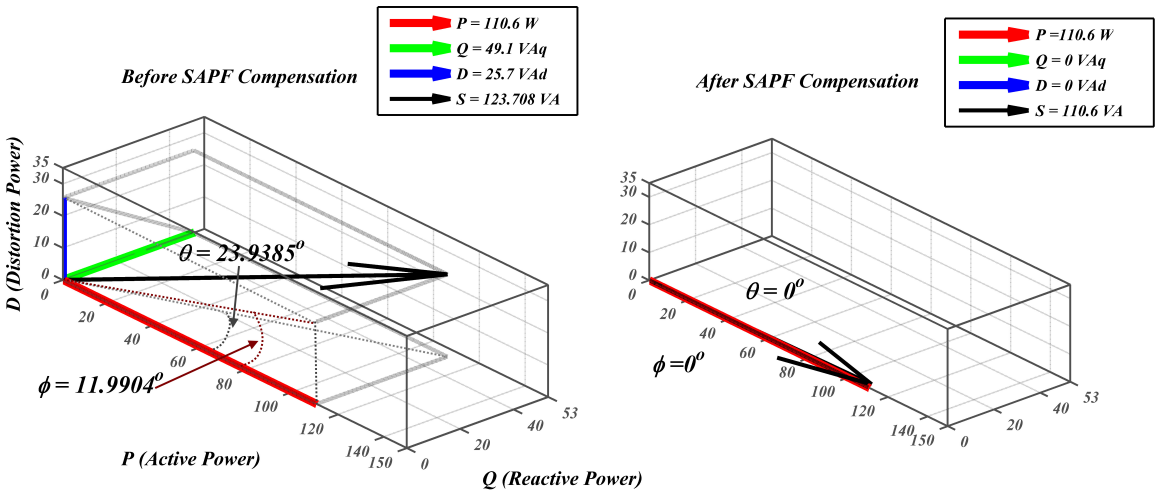

Figure 2.3: Graphical representation of the apparent power S, active power P, reactive power Q, and distortion power D

2.3.2 Definition of Instantaneous Power Components

For control purposes—particularly in the context of PDPC—it is common to express the instantaneous powers in the stationary $\alpha\beta$ reference frame. The instantaneous active and reactive power are then given by:

$$p(t) = v_\alpha(t)i_\alpha(t) + v_\beta(t)i_\beta(t) \tag{2.4}$$

$$q(t) = v_\alpha(t)i_\beta(t) - v_\beta(t)i_\alpha(t) \tag{2.5}$$

These expressions, rooted in the instantaneous power theory, are fundamental in SAPF modeling. They serve as the basis for the real-time cost function minimized by PDPC.

2.3.3 Effective Power Factor in Presence of Harmonics

In harmonic-rich environments, the classical definition of power factor (based only on P and Q) is insufficient. A more complete form considers the distortion power:

$$\text{Power Factor} = \frac{P}{\sqrt{P^2 + Q^2 + D^2}} = \frac{P}{S} \tag{2.6}$$

A value close to 1 indicates high efficiency in energy transfer. SAPFs, by reducing Q and D, increase the overall power factor and thus the quality of the power exchange.

2.3.4 Control Implications

Equations 2.4 and 2.5 are not merely descriptive—they form the analytical core of the PDPC strategy implemented later in the control algorithm. The SAPF aims to track a target value for $p(t)$ and nullify $q(t)$ through real-time switching of its inverter. Furthermore, THD and power factor serve as performance indicators for the controller's effectiveness.

In summary, understanding how apparent power decomposes and how harmonics affect current quality is crucial to SAPF operation. These definitions provide the measurable objectives upon which the controller acts, and their accurate estimation is a prerequisite for any model-based control technique.

2.4 SAPF System Overview and Block Diagram

A SAPF is an advanced control system designed to compensate for harmonic, reactive, and unbalanced currents in three-phase networks. While earlier sections introduced the motivation and performance objectives of SAPFs, this section presents a high-level structural overview of the implemented control system and its signal flow.

The SAPF is built around a current-controlled Voltage Source Inverter (VSI) that injects real-time compensating currents into the point of common coupling (PCC). Its architecture consists of modular control blocks that interact sequentially to sense the system, extract references, regulate internal dynamics, and execute inverter switching. The complete structure is illustrated in Fig. 2.4.

2.4.1 Functional Blocks and Signal Flow

1. Grid Sensing: The system begins by measuring the instantaneous grid voltage $\mathbf{v}_{abc}(t)$ and the source (injected) current $\mathbf{i}_{s,abc}(t)$. These signals are essential for synchronization, power computation, and model-based prediction. No direct sensing of load current is required, as compensation is inferred through active and reactive power regulation at the PCC.

2. Phase-Locked Loop: A digital PLL extracts the phase angle $\theta(t)$ of the fundamental voltage component from $\mathbf{v}_{abc}(t)$. This angle is used for synchronous frame transformations and for aligning compensation references with the voltage vector.

3. DC-Link Voltage Control: The outer control loop ensures power balance by regulating the DC-link voltage $V_{\text{dc}}(t)$. A PI controller compares the measured $V_{\text{dc}}(t)$ to a reference $V_{\text{dc,ref}}$, and adjusts the magnitude of the reference power (or equivalently, the current) injected into the grid. This guarantees long-term energy stability.

4. Inverter Switching Control via PDPC: The PDPC loop is the inner control mechanism responsible for real-time switching. It predicts the next-state active and reactive power values based on sensed $\mathbf{i}_s$, $\mathbf{v}_s$, and system parameters. Then it selects the optimal inverter switching vector that minimizes a quadratic cost function:

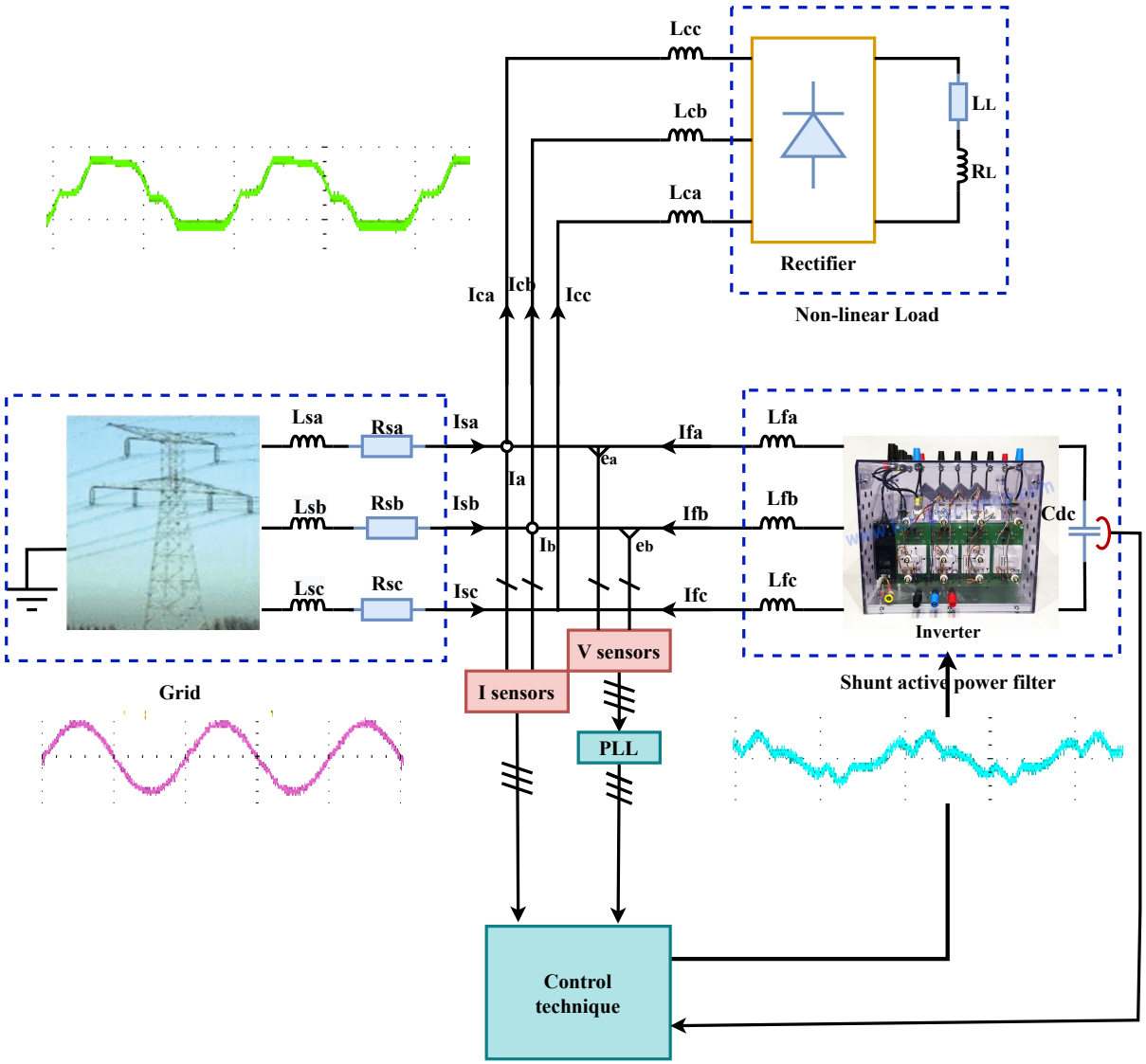

Figure 2.4: Overall Control Architecture of the Shunt Active Power Filter

$$J(k) = k_p \cdot (P_{\text{ref}} - P(k+1))^2 + k_q \cdot (Q_{\text{ref}} - Q(k+1))^2$$

This discrete optimization is performed at each sampling interval T_s, producing high-speed, stable, and fixed-frequency switching.

5. Voltage Source Inverter: Finally, the optimal switching state is applied to the three-phase VSI, which injects the compensating current through an L–R filter. This filter shapes the inverter output to match the reference waveform while suppressing switching harmonics, ensuring clean injection at the PCC.

This global architecture is fundamental to understanding how different modeling elements—filter inductance, inverter switching logic, PLL synchronization, PI control, and harmonic decomposition—work together to produce a fully functional compensator. Each block shown in Fig. 2.4 corresponds to a subsequent section in this chapter, where its internal equations, design criteria, and control implementation are developed in detail.

2.5 Mathematical Modeling of SAPF Components

A robust control strategy for a Shunt Active Power Filter (SAPF) requires an accurate mathematical model capable of describing its electrical behavior under dynamic operating conditions. This section develops the continuous- and discrete-time models of the SAPF based on Kirchhoff's laws, considering the inverter, interface filter, and grid interaction. The resulting formulations provide the foundation for the predictive models employed later in the Predictive Direct Power Control (PDPC) strategy [85].

2.5.1 Filter Dynamics and Inverter–Grid Interaction

The SAPF is implemented using a three-phase, two-level voltage source inverter (VSI) connected to the grid through an L–R interface filter. The filter attenuates high-frequency switching components and ensures that the injected compensating currents remain smooth and compatible with grid standards [86].

Each inverter leg is controlled by a binary switching signal $S_i(t) \in \{0, 1\}$, where $i \in \{a, b, c\}$. Due to the absence of a physical neutral connection in the inverter, the phase voltages applied to the filter are obtained by subtracting the instantaneous inverter neutral potential. The resulting inverter phase voltage can be expressed as:

$$v_{\text{inv},i}(t) = V_{\text{dc}} \left(S_i(t) - \frac{1}{3} \left(S_a(t) + S_b(t) + S_c(t) \right) \right) \tag{2.7}$$

This formulation ensures a zero-sum condition for the three-phase voltages and inherently accounts for the floating neutral point of the inverter.

Applying Kirchhoff's Voltage Law (KVL) to each phase of the L–R filter yields:

$$v_{\text{inv},i}(t) - v_{\text{grid},i}(t) = L_f \frac{di_{f,i}(t)}{dt} + R_f i_{f,i}(t), \quad i \in \{a, b, c\} \tag{2.8}$$

where $i_{f,i}(t)$ is the compensating current injected by the SAPF into the grid, $v_{\text{grid},i}(t)$ is the grid phase voltage, and L_f and R_f denote the filter inductance and resistance, respectively.

2.5.2 State-Space Representation

Defining the state vector and voltage vectors as:

$$\mathbf{i}_f(t) = \begin{bmatrix} i_{f,a}(t) \\ i_{f,b}(t) \\ i_{f,c}(t) \end{bmatrix}, \quad \mathbf{v}_{\text{grid}}(t) = \begin{bmatrix} v_{\text{grid},a}(t) \\ v_{\text{grid},b}(t) \\ v_{\text{grid},c}(t) \end{bmatrix}$$

and introducing the normalized control inputs:

$$u_i(t) = S_i(t) - \frac{1}{3} \left(S_a(t) + S_b(t) + S_c(t) \right), \quad i \in \{a, b, c\} \tag{2.9}$$

the inverter voltage vector can be compactly written as:

$$\mathbf{v}_{\text{inv}}(t) = V_{\text{dc}}\,\mathbf{u}(t)$$

Substituting this expression into 2.8, the continuous-time state-space model of the SAPF becomes:

$$\frac{d\mathbf{i}_f(t)}{dt} = -\frac{R_f}{L_f}\mathbf{i}_f(t) + \frac{1}{L_f}\left(V_{\text{dc}}\mathbf{u}(t) - \mathbf{v}_{\text{grid}}(t)\right) \tag{2.10}$$

This compact representation is well suited for both analytical studies and real-time control implementation.

2.5.3 Discrete-Time Model for Digital Control

For digital implementation of the SAPF controller, the continuous-time model in 2.10 is discretized using a forward Euler approximation with sampling period T_s:

$$\frac{d\mathbf{i}_f(t)}{dt} \approx \frac{\mathbf{i}_f(k+1) - \mathbf{i}_f(k)}{T_s}$$

which leads to the discrete-time predictive model:

$$\mathbf{i}_f(k+1) = \left(1 - \frac{R_f T_s}{L_f}\right)\mathbf{i}_f(k) + \frac{T_s}{L_f}\left(V_{\text{dc}}\mathbf{u}(k) - \mathbf{v}_{\text{grid}}(k)\right) \tag{2.11}$$

This equation forms the predictive core of the PDPC algorithm, allowing future current states to be estimated for each admissible switching vector.

2.5.4 Switching States and Control Constraints

The normalized control inputs defined in 2.9 satisfy the inherent balance condition:

$$u_a(t) + u_b(t) + u_c(t) = 0$$

which ensures that the inverter operates under balanced three-phase conditions. Table 2.2 summarizes the eight valid switching states of the two-level inverter and their corresponding normalized control inputs. These discrete control vectors constitute the finite control set evaluated in the PDPC strategy.

2.6 Reference Quantities and Harmonic Source Detection Strategy

In classical SAPF implementations, compensating current references are often derived by subtracting the fundamental component from the total load current using synchronous transforma-

Table 2.2: Switching States and Corresponding Normalized Control Inputs

S_a	S_b	S_c	$\bar{S}$	u_a	u_b	u_c
0	0	0	0	0	0	0
1	0	0	$\frac{1}{3}$	$\frac{2}{3}$	$-\frac{1}{3}$	$-\frac{1}{3}$
1	1	0	$\frac{2}{3}$	$\frac{1}{3}$	$\frac{1}{3}$	$-\frac{2}{3}$
0	1	0	$\frac{1}{3}$	$-\frac{1}{3}$	$\frac{2}{3}$	$-\frac{1}{3}$
0	1	1	$\frac{2}{3}$	$-\frac{2}{3}$	$\frac{1}{3}$	$\frac{1}{3}$
0	0	1	$\frac{1}{3}$	$-\frac{1}{3}$	$-\frac{1}{3}$	$\frac{2}{3}$
1	0	1	$\frac{2}{3}$	$\frac{1}{3}$	$-\frac{2}{3}$	$\frac{1}{3}$
1	1	1	1	0	0	0

tions and filtering. However, this method requires precise measurement of the load current $\mathbf{i}_L(t)$, which may be impractical in many installations—especially in retrofit applications or industrial environments where only the grid-side access is available [87].

In this work, the SAPF relies on a PDPC strategy that bypasses the explicit generation of reference compensating currents. Instead, it uses directly measurable quantities from the grid interface—namely, the source current $\mathbf{i}_s(t)$, the grid voltage $\mathbf{v}_s(t)$, and the phase angle $\theta(t)$ obtained via a Phase-Locked Loop (PLL). These values are sufficient to:

- Compute the instantaneous active and reactive power delivered by the source.
- Predict the future behavior of power under each candidate switching vector.
- Minimize the power error via a cost function without reconstructing harmonic current references.

As such, the compensating behavior emerges naturally by driving the predicted power $\hat{P}(k+1), \hat{Q}(k+1)$ toward the desired targets, typically corresponding to purely active, sinusoidal source current.

2.6.1 Final Measurement Inputs Used

In summary, the real-time controller uses only:

$$\boxed{\{\mathbf{i}_s(t), \quad \mathbf{v}_s(t), \quad \theta(t)\}}$$

These quantities are processed within the PDPC loop, where switching decisions are made to minimize the predicted instantaneous power error.

2.6.2 Phase-Locked Loop for Grid Synchronization

Accurate calculation of $\theta(t)$ is essential for the Park transformation. This is achieved using a PLL based on the α–β voltage components:

2.6.2.1 Step 1: Angle Detection

Given $v_\alpha(t), v_\beta(t)$, compute:

$$\theta_{\text{ref}}(t) = \arctan\left(\frac{v_\beta(t)}{v_\alpha(t)}\right) \tag{2.12}$$

2.6.2.2 Step 2: Error Signal and PI Controller

Let $\theta_e(t) = \theta_{\text{ref}}(t) - \theta_{\text{est}}(t)$, then:

$$u_{\text{PLL}}(t) = K_p\theta_e(t) + K_i \int_0^t \theta_e(\tau)d\tau \tag{2.13}$$

2.6.2.3 Step 3: Voltage Controlled Oscillator (VCO)

$$\omega_{\text{PLL}}(t) = \omega_0 + u_{\text{PLL}}(t), \quad \theta_{\text{est}}(t) = \int_0^t \omega_{\text{PLL}}(\tau)d\tau \tag{2.14}$$

In discrete time:

$$\theta_{\text{est}}(k+1) = \theta_{\text{est}}(k) + T_s \cdot \omega_{\text{PLL}}(k)$$

2.6.3 Integration into SAPF Control Loop

The extracted $\mathbf{i}_f^{\text{ref}}(t)$ becomes the target signal for the control law in subsequent stages. Specifically:

- It is tracked via a current regulation loop (e.g., PI or predictive controller),
- It feeds directly into the PDPC cost function, enabling real-time minimization of the deviation between predicted and reference active/reactive powers.

This closes the loop between harmonic detection and inverter switching, forming the essential outer-inner hierarchy of SAPF control.

2.7 DC-Link Voltage Control Loop (Outer Loop)

The DC-link capacitor in a SAPF plays a vital role as an energy buffer, ensuring smooth power exchange between the grid and the inverter. Maintaining its voltage at a stable reference value $V_{dc,\text{ref}}$ is essential for reliable compensating current injection and overall system stability. To achieve this, a dedicated outer-loop controller is required to regulate the net power flow into the DC link.

2.7.1 DC-Link Voltage Dynamics

The fundamental energy balance across the capacitor is governed by the capacitor dynamic equation:

$$C_{dc}\frac{dV_{dc}(t)}{dt} = i_{\text{in}}(t) - i_{\text{out}}(t) \tag{2.15}$$

Here, $i_{\text{in}}(t)$ is the current drawn from the grid through the converter, and $i_{\text{out}}(t)$ represents the current delivered to the inverter legs.

Multiplying both sides by $V_{dc}(t)$, we obtain a power-based form:

$$C_{dc}V_{dc}(t)\frac{dV_{dc}(t)}{dt} = P_{\text{in}}(t) - P_{\text{load}}(t) \tag{2.16}$$

This equation directly links the rate of change of the capacitor voltage to the net active power imbalance, forming the basis for controller design.

2.7.2 Control Objective and Loop Structure

To regulate $V_{dc}(t)$ around a reference value $V_{dc,\text{ref}}$, a Proportional-Integral (PI) controller is implemented. The controller processes the voltage error:

$$e(t) = V_{dc,\text{ref}} - V_{dc}(t) \tag{2.17}$$

and generates an active power reference (or equivalently, the magnitude of the reference compensating current) as:

$$u(t) = K_p \cdot e(t) + K_i \cdot \int_0^t e(\tau)\, d\tau \tag{2.18}$$

2.7.3 Theoretical PI Gain Derivation

The PI controller is designed to ensure desired closed-loop performance. The transfer function of the plant, derived from the DC-link dynamics, is:

$$G(s) = \frac{1}{C_{dc} \cdot s} \tag{2.19}$$

This system is a pure integrator, and when controlled by a PI controller, the resulting closed-loop transfer function becomes second-order.

To enforce specific transient performance—such as damping ratio ζ and natural frequency ω_n—we match the closed-loop characteristic polynomial with the standard second-order form:

$$s^2 + 2\zeta\omega_n s + \omega_n^2$$

By applying the PI controller to $G(s)$, the closed-loop characteristic equation becomes:

$$C_{dc}s^2 + K_p s + K_i = 0$$

Matching coefficients yields the theoretical gain expressions:

$$K_p = 2\zeta\omega_n C_{dc} \tag{2.20}$$

$$K_i = \omega_n^2 C_{dc} \tag{2.21}$$

This derivation ensures that the closed-loop system mimics a well-damped second-order response, which guarantees a fast and non-oscillatory transient.

For example, choosing $\zeta = 0.707$ (critically damped), $\omega_n = 18\,\text{rad/s}$, and $C_{dc} = 2200\,\mu\text{F}$ yields:

$$K_p = 2 \cdot 0.707 \cdot 18 \cdot 2200 \cdot 10^{-6} = \boxed{0.056} \tag{2.22}$$

$$K_i = (18)^2 \cdot 2200 \cdot 10^{-6} = \boxed{0.713} \tag{2.23}$$

2.7.4 Anti-Windup Mechanism

Due to physical actuator limits, the inverter's current output can saturate. During such saturation events, the PI integrator may accumulate unbounded error—causing *integrator windup*, which degrades system response and introduces instability.

To address this, an anti-windup compensation is applied:

$$U_w(k) = K_{uw} \cdot (u_{\text{sat}}(k) - u(k)) \tag{2.24}$$

where $u_{\text{sat}}(k)$ is the saturated (clipped) actuator output and $u(k)$ is the raw controller output. This feedback correction prevents the integrator from accumulating excess error.

2.7.4.1 Discrete-Time Anti-Windup PI Control Law

In digital implementation, the PI controller with anti-windup correction is formulated as:

$$u(k) = \left[K_p + (K_i + U_w(k-1)) \cdot \frac{T_s z}{z-1} \right] \cdot e(k) \tag{2.25}$$

where:

- T_s is the sampling interval,
- $U_w(k-1)$ is the previous anti-windup term,
- z is the forward shift operator in the Z-domain.

2.7.4.2 Anti-Windup Gain Design

The anti-windup gain K_{uw} is chosen based on a heuristic widely used in discrete-time control design:

$$K_{uw} = \frac{K_p^*}{T_s} \tag{2.26}$$

For example, with $K_p^* = 0.056$, and $T_s = 4.510^{-5}$ s:

$$K_{uw} = \frac{0.056}{4.5 \cdot 10^{-5}} = \boxed{1244}$$

2.7.5 Performance Role in SAPF

The outer-loop controller ensures the average DC-link voltage remains tightly regulated around its reference. This:

- stabilizes the internal voltage supply for inverter operation,
- ensures consistent tracking behavior in the current control loop,
- suppresses oscillations and improves dynamic THD performance under varying load conditions.

In this architecture, the outer PI controller governs the *energy level* of the SAPF, while the inner predictive controller (e.g., PDPC) shapes the *instantaneous current waveform*, forming a layered control framework for effective power quality improvement.

2.8 SAPF Inverter Switching Control (Inner Loop)

Once the reference compensating current has been generated and the DC-link voltage stabilized, the final task of the SAPF control system is to synthesize the switching states of the VSI that will enforce the desired current injection into the grid. This operation is handled by the inner current control loop, responsible for selecting the inverter switching state every sampling period.

Two primary methods are considered for this task: Direct Power Control (DPC) and PDPC. This section outlines their structure, compares their performance, and establishes the motivation for using a predictive approach in this thesis.

2.8.1 Direct Power Control

DPC is a fast and simple technique that regulates the inverter switching based on the instantaneous active and reactive power error. It operates directly in the stationary $\alpha\beta$ coordinate system using the Clarke transformation. Fig. 2.5 shows the block diagram of classical DPC which is essential for visualizing how DPC functions.

The instantaneous power equations are:

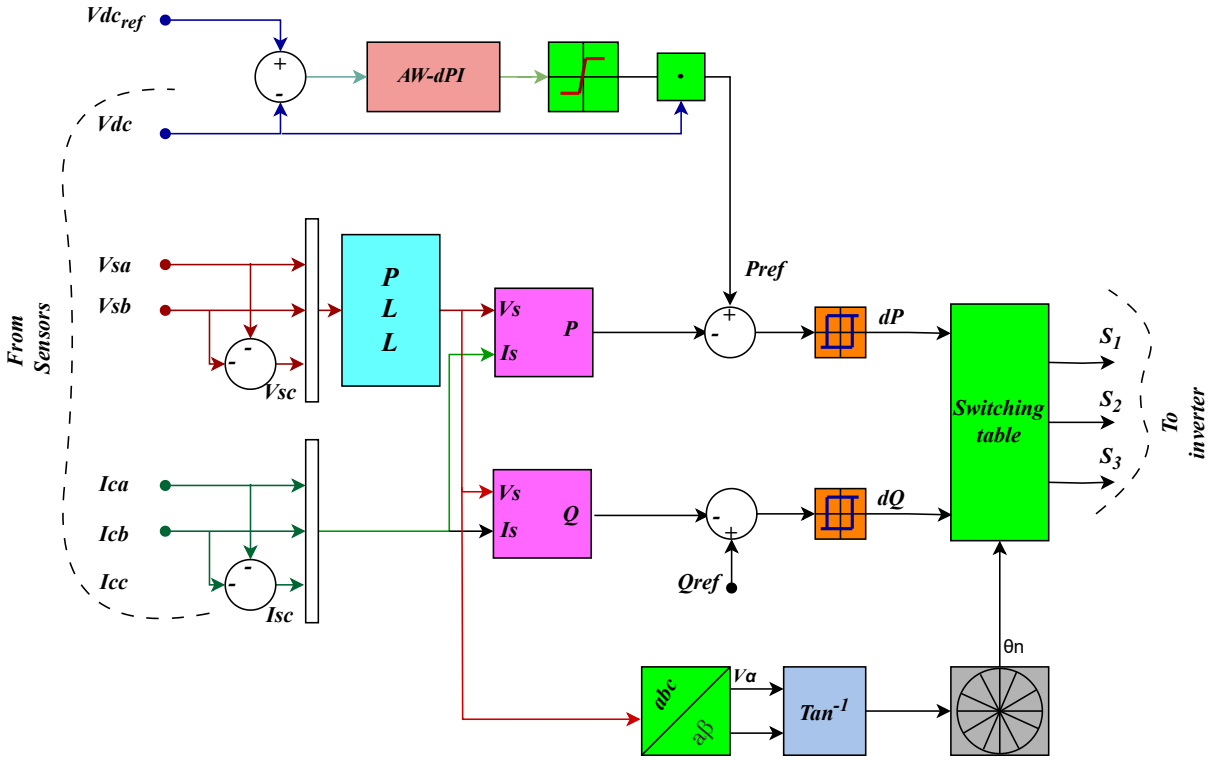

Figure 2.5: Block diagram of classical DPC

$$P(t) = v_\alpha(t)i_\alpha(t) + v_\beta(t)i_\beta(t) \tag{2.27}$$

$$Q(t) = v_\alpha(t)i_\beta(t) - v_\beta(t)i_\alpha(t) \tag{2.28}$$

where:

- v_α, v_β: grid voltages in the $\alpha\beta$ frame,
- i_α, i_β: filter currents in the same frame.

In classical DPC, these power components are compared to their references using hysteresis comparators. A lookup table is used to select one of the 8 inverter switching states that best brings $P(t)$ and $Q(t)$ back within their respective hysteresis bands.

While DPC offers fast dynamic response, it suffers from:

- variable switching frequency, complicating filter design and electromagnetic compatibility (EMC),
- lack of prediction, leading to suboptimal switching decisions under fast-changing conditions,
- poor performance when implemented on digital hardware requiring fixed-frequency operation.

The classical DPC method, though robust and well-suited for systems like motor drives, is not optimal for SAPFs integrated with PV sources. SAPFs operate under highly dynamic nonlinear loads, and fixed-frequency operation is often desired to ensure EMI compliance and better filter design.

These limitations motivated the use of PDPC, which combines the power-based control philosophy of DPC with model-based prediction capabilities.

2.8.2 Predictive Direct Power Control Mathematical Formulation

PDPC represents an advanced control strategy that combines the dynamic responsiveness of DPC with model-based prediction and digital suitability. Unlike classical DPC, which relies on hysteresis comparators and operates with variable switching frequencies, PDPC uses discrete-time models to forecast the future system state for each candidate voltage vector and then selects the inverter switching state that minimizes a predefined power-tracking cost function. The Block diagram of PDPC theory is shown in Fig.2.6.

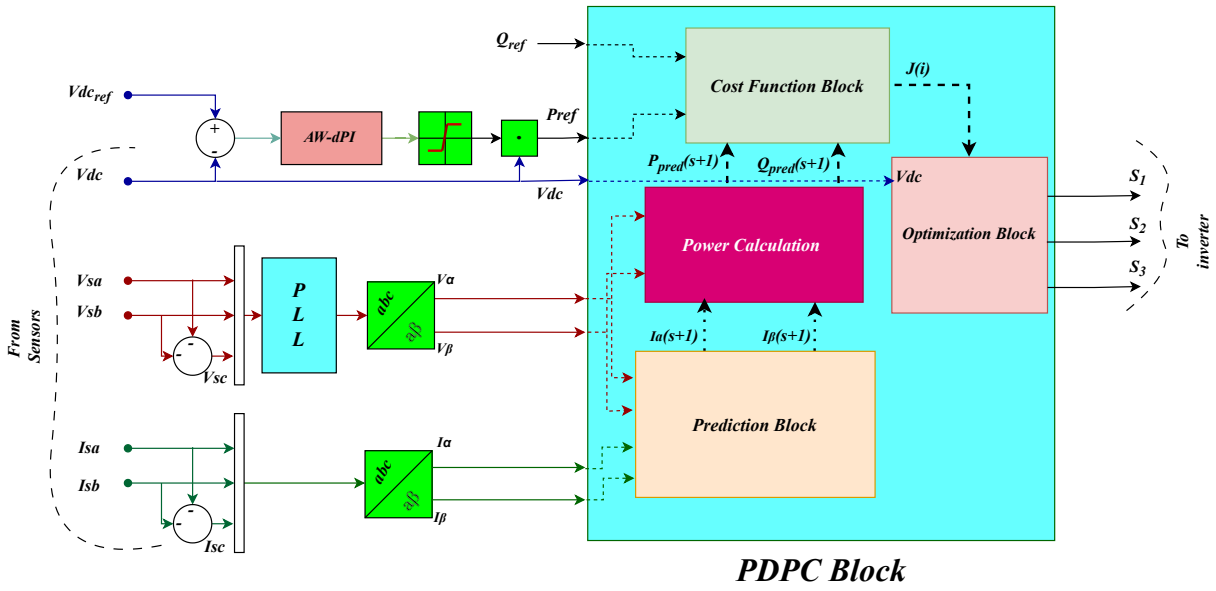

Figure 2.6: Block diagram of Predictive Direct Power Control

This section provides a comprehensive mathematical derivation of the PDPC algorithm, starting from the physical model, moving to discrete-time current prediction, and culminating in the control law.

2.8.2.1 Filter Dynamics and Continuous-Time Model

We begin with the continuous-time dynamics of the SAPF filter current in the α–β stationary reference frame. Applying Kirchhoff's Voltage Law (KVL) for the α axis:

$$L_f \frac{di_\alpha(t)}{dt} = e_\alpha(t) - v_\alpha(t) - R_f i_\alpha(t) \tag{2.29}$$

Similarly, for the β axis:

$$L_f \frac{di_\beta(t)}{dt} = e_\beta(t) - v_\beta(t) - R_f i_\beta(t) \tag{2.30}$$

where:

- $i_\alpha(t), i_\beta(t)$: filter (injected) currents,
- $v_\alpha(t), v_\beta(t)$: inverter output voltages,
- $e_\alpha(t), e_\beta(t)$: grid (source) voltages,
- R_f, L_f: filter resistance and inductance.

2.8.2.2 Discrete-Time Prediction Model

To implement this control strategy on a digital platform, we discretize equations 2.29–2.30 using Euler's forward approximation over the sampling interval T_s:

$$i_\alpha(k+1) = i_\alpha(k) + \frac{T_s}{L_f}\left[e_\alpha(k) - v_\alpha(k) - R_f i_\alpha(k)\right] \tag{2.31}$$

$$i_\beta(k+1) = i_\beta(k) + \frac{T_s}{L_f}\left[e_\beta(k) - v_\beta(k) - R_f i_\beta(k)\right] \tag{2.32}$$

These equations allow prediction of future current components $i_\alpha(k+1), i_\beta(k+1)$ for each candidate inverter voltage vector $[v_\alpha, v_\beta]$ at time step k.

2.8.2.3 Instantaneous Power Prediction

From the predicted currents, the PDPC algorithm computes the predicted active and reactive power:

$$P_{\text{pred}}(k+1) = e_\alpha(k) \cdot i_\alpha(k+1) + e_\beta(k) \cdot i_\beta(k+1) \tag{2.33}$$

$$Q_{\text{pred}}(k+1) = e_\beta(k) \cdot i_\alpha(k+1) - e_\alpha(k) \cdot i_\beta(k+1) \tag{2.34}$$

These are the predicted power flows at the next time step for a given candidate inverter state.

2.8.2.4 Cost Function Formulation

The control objective is to minimize the deviation between the predicted and reference powers. Let the reference active and reactive powers be $P_{\text{ref}}(k), Q_{\text{ref}}(k)$. The power tracking errors are:

$$\Delta P(k) = P_{\text{ref}}(k) - P_{\text{pred}}(k+1) \tag{2.35}$$

$$\Delta Q(k) = Q_{\text{ref}}(k) - Q_{\text{pred}}(k+1) \tag{2.36}$$

The quadratic cost function is then defined as:

$$J(k) = G_P \cdot \Delta P(k)^2 + G_Q \cdot \Delta Q(k)^2 \tag{2.37}$$

where:

- G_P, G_Q are weighting coefficients for active and reactive power errors.

Note: In this work, we select $G_P = G_Q = 1$ to give equal priority to both objectives. However, these weights can be tuned for application-specific goals such as reactive power priority.

2.8.2.5 Switching Vector Optimization

The inverter can apply 8 distinct switching states $S_i \in \{000, 001, ..., 111\}$, which correspond to output voltage vectors $\vec{v}_i = [v_{\alpha,i}, v_{\beta,i}]$. For each $\vec{v}_i$, the following steps are performed:

1. Use equations 2.31–2.32 to compute predicted currents.
2. Use equations 2.33–2.34 to compute predicted powers.
3. Use 2.37 to compute cost $J_i(k)$.

The optimal inverter switching state is then:

$$S^*(k) = \arg \min_{i \in \{1,...,8\}} J_i(k) \tag{2.38}$$

This state is applied during the next sampling interval to minimize the predicted power-tracking error.

2.8.2.6 Mathematical Justification and Theoretical Advantages of PDPC

DPC chooses, at every sampling instant, one of the seven voltage vectors of the two–level inverter to drive the instantaneous active and reactive powers (P, Q) toward their references. Traditional (hysteresis) DPC reacts to the *current* error; *PDPC* goes one step further – it **predicts** the error one sample ahead, then picks the vector that will minimise it. The five points below explain—using simple maths and plain language—why this predictive look-ahead yields better dynamics, guaranteed stability, and a fixed switching frequency.

Notation. Sampling period T_s; iteration index n. Filter inductance L_f and resistance R_f. Grid voltages v_α, v_β; filter currents i_α, i_β. Instantaneous powers ($\alpha\beta$ frame):

$$P = \tfrac{3}{2}\,(v_\alpha i_\alpha + v_\beta i_\beta),\;\; Q = \tfrac{3}{2}\,(v_\beta i_\alpha - v_\alpha i_\beta).$$

Reference powers $P_{\text{ref}}, Q_{\text{ref}}$. The inverter can apply seven voltage vectors $\vec{v}_i \in \mathcal{V} = \{\vec{v}_0, \ldots, \vec{v}_6\}$.

1. One-Step Look-Ahead Prediction

Classical DPC "waits" for the error; PDPC forecasts it.

$$i_\alpha(n{+}1) = i_\alpha(n) + \frac{T_s}{L_f}\big[v_\alpha(n){-}e_\alpha(n) - R_f\, i_\alpha(n)\big],$$

and analogously for i_β. Each candidate $\vec{v}_i$ is plugged into these equations, producing $P_{\text{pred}}, Q_{\text{pred}}$ for the *next* sample. The controller then selects the vector that will give the smallest future error. In practice this anticipation shortens settling time and damps current overshoot.

2. Fixed Switching Frequency

Sampling is periodic at T_s; therefore the switching frequency is $f_s = 1/T_s$. Unlike hysteresis DPC—which fires whenever the error hits the band—PDPC produces uniform intervals. That means predictable EMI, lower ripple, and easy timing on DSP/FPGA hardware.

5. PDPC as MPC with Horizon N=1

Model Predictive Control (MPC) normally solves a horizon-N optimisation each cycle. Setting $N = 1$ and using the quadratic stage cost above reduces MPC to PDPC. Hence PDPC inherits the predict-and-optimise philosophy of MPC while staying lightweight enough for high-frequency switching.

Recap. PDPC looks one step ahead, switches at a fixed rate, guarantees monotonically decreasing power error, picks the global best action from a small set, and can be viewed as the simplest useful MPC. These theoretical properties underpin the superior transient and harmonic performance demonstrated in Chapter 4.

2.8.2.7 Final PDPC Control Law

The complete control loop per time step k is:

PDPC Control Algorithm (Per Sampling Interval)

1. Measure $i_\alpha(k), i_\beta(k), e_\alpha(k), e_\beta(k)$.
2. For each inverter voltage vector $\vec{v}_i$:
   - Predict $i_\alpha(k+1), i_\beta(k+1)$ via 2.31–2.32,
   - Compute $P_{\text{pred}}, Q_{\text{pred}}$,
   - Evaluate cost $J_i(k)$.
3. Select $S^*(k) = \arg\min J_i(k)$ and apply.

This method ensures predictive injection of current that dynamically follows harmonic compensation objectives while operating under digitally enforced timing constraints.

2.9 Practical Considerations in Digital Implementation

The successful implementation of the PDPC strategy for a SAPF in real-time hardware depends not only on the correctness of its mathematical formulation but also on practical constraints introduced by digital control environments. This section addresses essential considerations such as sampling time selection, discretization impact, switching frequency control, latency in execution, and overall real-time reliability.

2.9.1 Sampling Time and Prediction Accuracy

PDPC relies heavily on the accuracy of discrete-time current prediction, which in turn depends on the sampling interval T_s. A short T_s improves prediction fidelity by minimizing the linearization error in Euler discretization:

$$\frac{di_\alpha(t)}{dt} \approx \frac{i_\alpha(k+1) - i_\alpha(k)}{T_s} \tag{2.39}$$

However, shorter sampling intervals lead to:

- **Higher switching frequency**, which increases inverter switching losses and thermal stress.
- **Increased computational load**, requiring faster digital processors or FPGAs.

Conversely, a larger T_s reduces computational burden but causes deterioration in prediction accuracy, leading to:

- Tracking errors in active/reactive power,
- Increased THD,

- Degraded dynamic response during load transients.

Design Trade-Off: A sampling time of $T_s = 45\,\mu s$ is adopted in this work, balancing performance with hardware capability and avoiding instability due to prediction lag.

2.9.2 Switching Frequency Management

Since PDPC operates at fixed sampling intervals, the effective switching frequency f_s of the inverter is:

$$f_s = \frac{1}{T_s}$$

A short T_s increases f_s, improving the waveform quality and reducing current ripple. However, practical power converters have maximum switching frequency limits due to Gate driver delays, Heat dissipation limits in IGBT/MOSFET switches, and Noise and electromagnetic interference (EMI) constraints.

Implementation Note: The chosen switching frequency should not exceed the thermal capacity of the inverter nor violate its minimum pulse width constraint. Typically, for low-voltage SAPF systems, $f_s \in [10\,\text{kHz}, 25\,\text{kHz}]$ provides a reliable operating range.

2.9.3 Prediction Horizon and Real-Time Execution Delay

The PDPC algorithm is based on single-step-ahead prediction. That is, the filter current is predicted for $k + 1$ using the current measurement at time k. In practice, this prediction horizon must be longer than the control computation delay to remain effective:

$$T_{\text{compute}} < T_s$$

Where:

- T_{compute}: total computation time for evaluating all switching vectors.

Guideline: Ensure the execution time of the prediction + cost evaluation + vector selection fits within each sampling cycle. For instance, if $T_s = 45\,\mu s$, the worst-case execution time (WCET) must remain under 40 µs to guarantee deterministic timing.

2.9.4 Quantization, Sensor Delay, and Filtering

In digital control systems, measurement integrity plays a pivotal role in determining the overall accuracy and stability of the control algorithm. In the context of SAPF implementation, current and voltage measurements feed directly into the power calculation and prediction stages of the PDPC. However, several practical issues may arise from real-time signal acquisition:

Table 2.3: Specifications of Measurement Devices Used

Parameter	**Fluke i30s (Current Clamp)**	**Metrix MX9030-Z (Voltage Probe)**
Measurement Range	30 mA–30 A DC / 30 mA–20 A AC RMS	±0.1 V to ±600 V
Frequency Bandwidth	DC to 100 kHz	30 MHz
Resolution	±1 mA	Not specified
Output Sensitivity	100 mV/A	1:20 or 1:200 attenuation
Input Impedance	> 100 kΩ	2 MΩ // 6 pF
CMRR	—	80 dB @ 50 Hz, 50 dB @ 1 MHz
Power Supply	9 V Battery (MN1604)	9 V Battery (6LF22)
Safety Category	CAT III 300 V	CAT IV 600 V
Cable Length	2 m	1.1 m

- **Quantization Errors:** Caused by the finite resolution of the analog-to-digital converter (ADC), affecting the precision of sampled signals.
- **Sensor Delays and Phase Shifts:** Introduced by analog anti-aliasing filters or internal electronics, leading to misalignment between voltage and current samples.
- **Sampling Delays:** Due to sequential ADC conversion and interrupt handling within digital control platforms.

In this implementation, no analog filtering was used on voltage or current channels, except for the DC-link voltage measurement. Instead, precision transducers were chosen to ensure minimal signal distortion, and digital compensation techniques were employed where needed.

2.9.4.1 Sensor Specifications and Measurement Setup

Current sensing was performed using the **Fluke i30s** clamp-on probe, which utilizes Hall Effect technology for accurate AC/DC current detection. Voltage measurement was carried out using the **Metrix MX9030-Z** differential probe, specifically designed for safe and accurate differential readings in high-voltage environments.

2.9.4.2 Measurement Setup Visualization

2.9.4.3 Simulation Results Overview

The effectiveness of the PDPC strategy integrated with the SAPF system was rigorously validated through simulation studies. The system was implemented in MATLAB/Simulink using the parameters outlined in Table **??**, faithfully reproducing the experimental environment. The results assess the harmonic mitigation, power balance, compensation precision, and voltage regulation behavior during steady and transient conditions.

(a) Fluke i30s AC/DC Current Clamp

(b) Metrix MX9030-Z Differential Voltage Probe

Figure 2.7: Precision sensors used for current and voltage acquisition in the SAPF system.

In Figure 2.8, the response of the three-phase source voltage and current is analyzed between 0.17 s and 0.28 s. Prior to 0.2 s, the source current exhibits noticeable harmonic distortion, deviating from its sinusoidal envelope. Post-activation of the PDPC algorithm at 0.2 s, the current waveform rapidly transitions to a clean sinusoidal form within 4 ms. The amplitude of I_s stabilizes between RMS value of ±3.8 A, demonstrating the controller's fast transient response. Simultaneously, the grid voltage maintains stability at around MAX value ±20 V. The elimination of phase shift confirms precise synchronization between voltage and current, ensuring zero reactive exchange and improved power factor.

Figure 2.9 demonstrates the system dynamics in the α–β frame using Clarke-transformed current vectors. Before compensation (left), the I_α–I_β trajectory exhibits a skewed and distorted shape. This distortion can be mathematically attributed to the presence of higher-order harmonics and reactive current components, which can be expressed as:

$$i_\alpha(t) = I_{1\alpha}\sin(\omega t) + \sum_{n=3,5,\ldots} I_{n\alpha}\sin(n\omega t + \phi_n), \quad i_\beta(t) = I_{1\beta}\cos(\omega t) + \sum_{n=3,5,\ldots} I_{n\beta}\cos(n\omega t + \phi_n) \tag{2.40}$$

Here, the fundamental terms $I_{1\alpha}, I_{1\beta}$ represent the ideal sinusoidal current components, while the summation represents higher-order harmonics. These harmonics introduce non-elliptical distortions in the $i_\alpha(t)$–$i_\beta(t)$ trajectory.

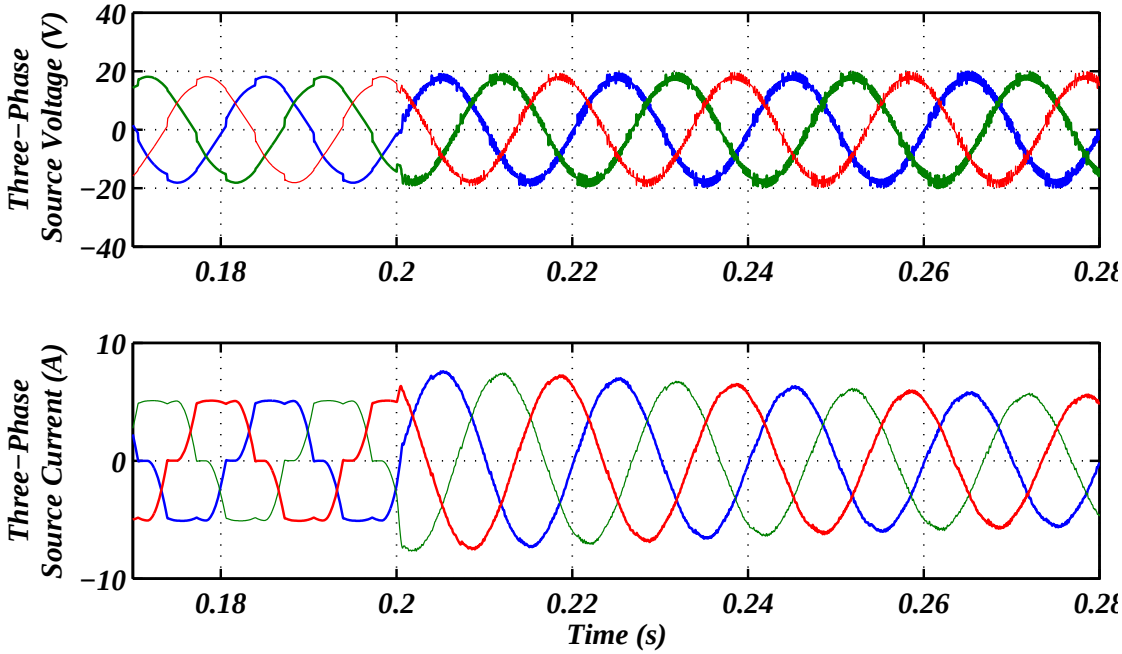

(a) Three-phase voltage $V_s(abc)$ and current $I_s(abc)$ waveforms

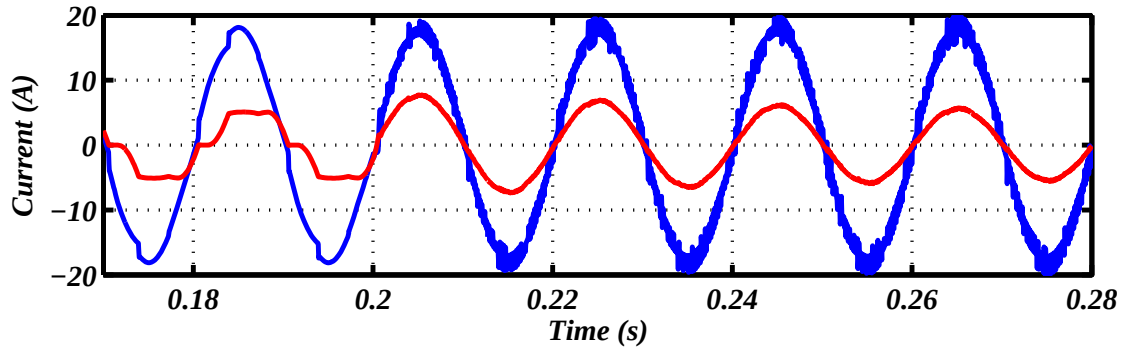

(b) Zoomed view of voltage and current waveform transition

Figure 2.8: Source voltage and current response before and after SAPF activation

Additionally, reactive power presence introduces a *phase shift* between current and voltage vectors, further skewing the trajectory away from circular symmetry.

Post-compensation (right), the current trajectory forms an almost perfect circle in the α–β plane. This indicates that:

$$i_\alpha(t) = I_m \sin(\omega t), \quad i_\beta(t) = I_m \cos(\omega t) \tag{2.41}$$

This trajectory satisfies the identity:

$$i_\alpha^2(t) + i_\beta^2(t) = I_m^2$$

implying that the current vector maintains constant magnitude and rotates uniformly in phase with the voltage vector — the defining characteristic of a purely *active power* transfer (i.e., power factor = 1).

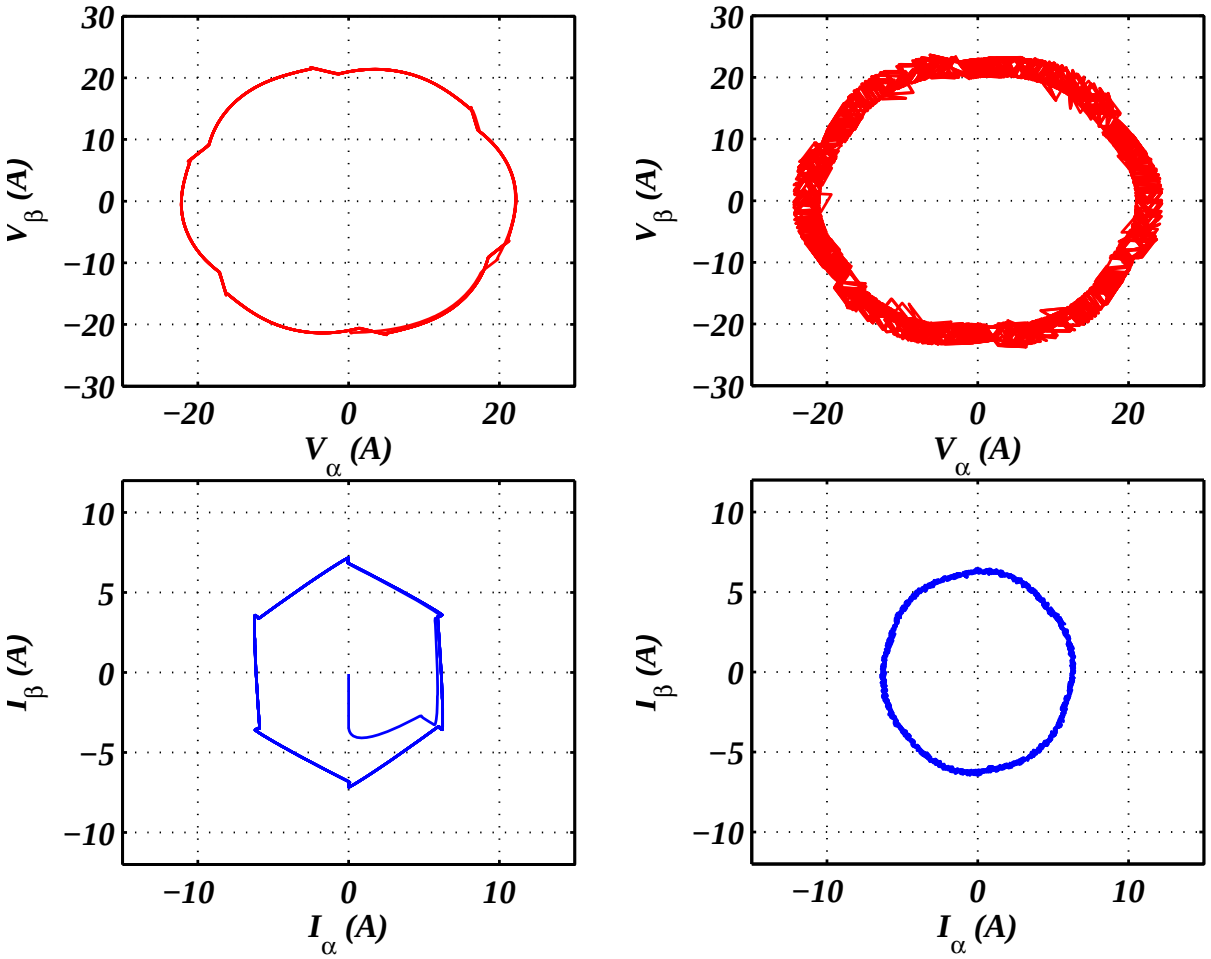

(a) Before SAPF Activation

(b) After SAPF Activation

Figure 2.9: Voltage and current trajectories in α–β frame

Moreover, the voltage trajectory remains unchanged before and after compensation, as expected, since the SAPF does not actively control the grid voltage. This consistent voltage, combined with the transition of the current locus from a distorted shape to a circle, evidences successful harmonic suppression and reactive power compensation.

Figure 2.10 provides a comprehensive view of current flow across the system. Before 0.2 s, the source current I_s and load current I_L share similar distortion, with I_s peaking at ±5.6,A. After SAPF engagement, I_s becomes purely sinusoidal, while I_L retains harmonic content, confirming that compensation is taking place. The filter current I_F mirrors the harmonic signature of I_L but in opposite phase, validating its role in injecting the necessary counter-harmonic profile. The matching amplitude and phase of I_F with the harmonic component of I_L further demonstrates the controller's precision.

Figure 2.11 illustrates the evolution of four core power quantities — apparent power S, active power P, reactive power Q, and distortion (deformant) power D — across the SAPF activation period. To ensure consistency with the experimental setup, all power values presented in the following discussion were extracted from simulation waveforms using their **time-averaged**

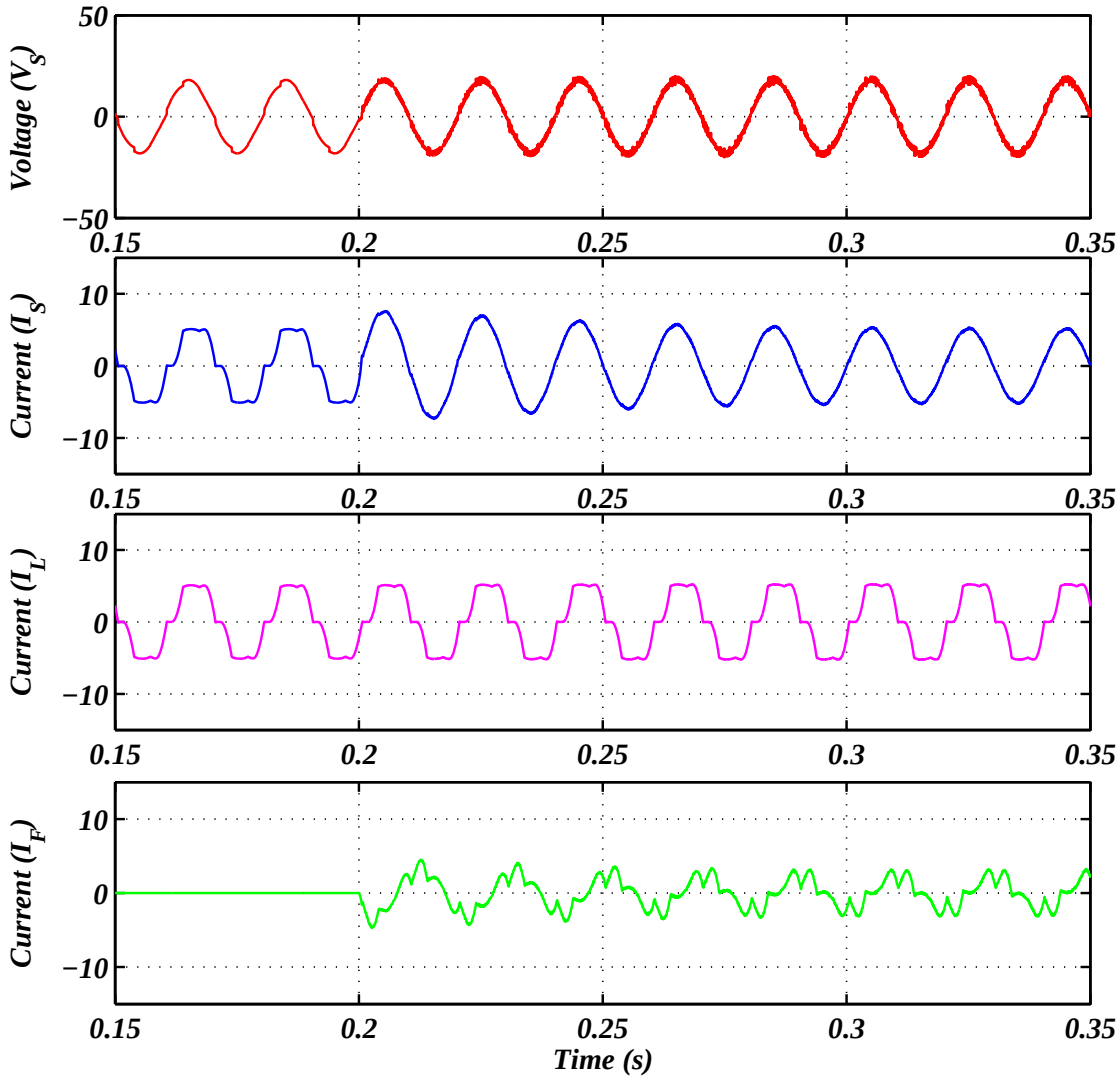

Figure 2.10: Time-domain response of grid voltage, source current, load current, and filter current

mean values over a stable operating window.

In the pre-compensation window $0.15\,\text{s} \leq t \leq 0.20\,\text{s}$, the apparent power is approximately **145.66 VA**, reflecting the total source demand under harmonic-rich and reactive loading. Upon SAPF activation at $t = 0.24\,\text{s}$, this value slightly rises to **148.03 VA**, as the filter injects compensating current to correct the load's distortion and phase misalignment. This added current increases the total RMS current and, consequently, the apparent power, even though the waveform becomes cleaner from the grid's perspective.

The active power increases from **135.5 W** to **148.0 W**, which is consistent with improved alignment between voltage and current. Reactive power, which averaged around **53.0 VAR** before compensation, is reduced to ≈**0.0 VAR**, indicating successful cancellation of the fundamental quadrature component. Deformant power drops from **7.0 VAD** to **3.0 VAD**, confirming the suppression of higher-order harmonics and improved waveform purity at the source.

All numerical values are 100-ms moving averages, matching the method used later in the

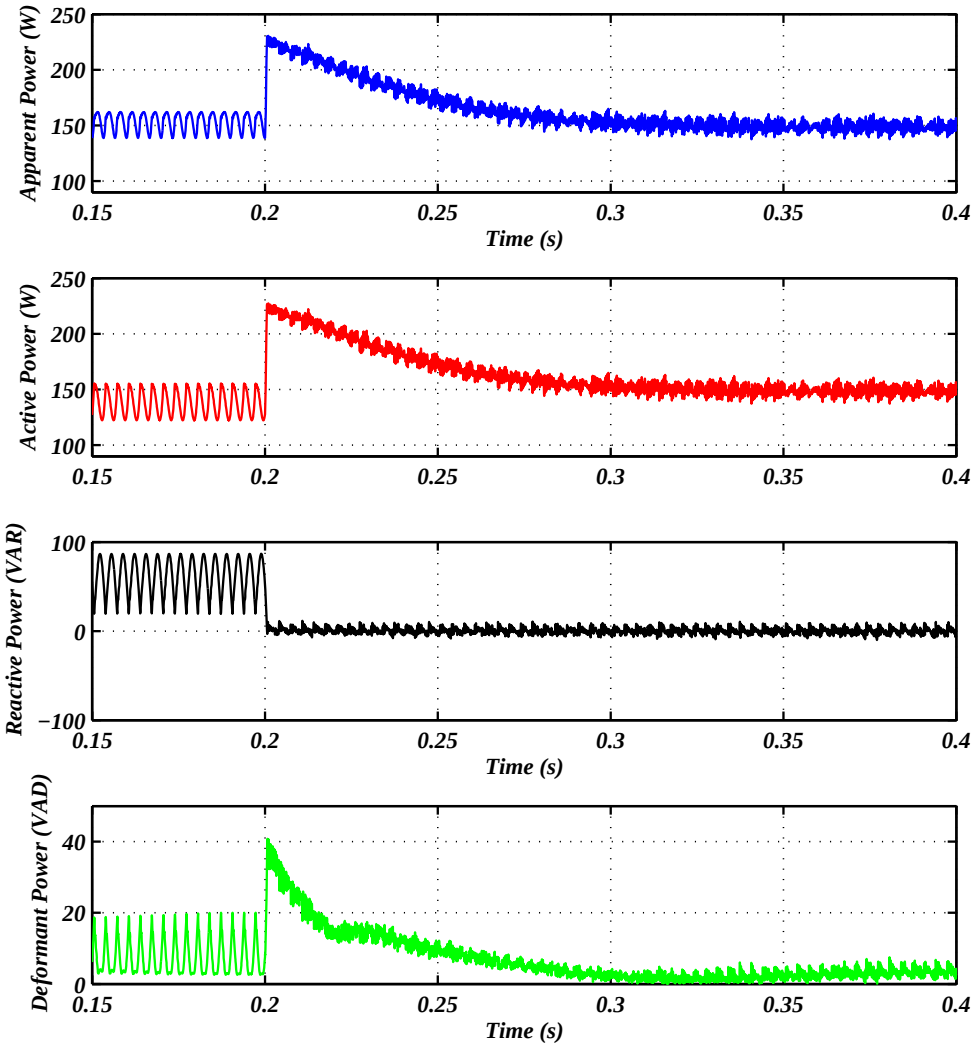

Figure 2.11: Time-averaged evolution of apparent power S, active power P, reactive power Q and distortion power D before, during and after SAPF energisation ($t = 0.20$ s).

laboratory section.

Observed trend. At first glance, it may appear counterintuitive that both the active power (P) and apparent power (S increase after the SAPF is activated, since the filter does not generate energy but merely compensates harmonic and reactive components of the load current. However, the observed increase in active power (approximately 10–12 W) is not indicative of additional losses or inefficiency. Instead, it is a direct consequence of improved voltage conditions at the point of common coupling (PCC), arising from two practical effects inherent to the system:

1. **Source impedance.** The grid and interfacing elements are non-ideal and can be represented by a finite source impedance, $Z_s = R_s + jL_s \neq 0$. Prior to SAPF operation, the nonlinear load draws a highly distorted current containing significant harmonic compo-

nents. When this distorted current flows through the source impedance, it produces an additional voltage drop, $Z_s i_{\text{load}}$, which reduces the effective RMS voltage available at the PCC.

2. **Voltage-dependent nonlinear load.** The load consists of a diode bridge rectifier with a DC smoothing capacitor. Such loads are inherently voltage-sensitive: an increase in the RMS PCC voltage results in higher peak charging currents of the capacitor, thereby increasing the average DC-side energy transfer and the corresponding AC-side active power consumption.

When the SAPF is activated, the following sequence occurs:

- The SAPF injects a compensating current $i_f(t)$ that cancels the harmonic and reactive components of the load current.
- Consequently, the source current becomes predominantly fundamental and nearly sinusoidal,

$$i_{\text{source}}(t) = i_{\text{load}}(t) + i_f(t) \approx i_{\text{fund}}(t).$$

- With the reduction of harmonic current flow through the source impedance, the associated voltage drop decreases, leading to an increase in the RMS voltage at the PCC:

$$V_{\text{rms,PCC, after}} > V_{\text{rms,PCC, before}}.$$

- The nonlinear load responds to this improved voltage delivery by drawing a higher RMS current, which naturally results in an increase in both the active power (P) and apparent power (S) absorbed by the load.

The measured power components satisfy Budeanu's power relation,

$$S = \sqrt{P^2 + Q^2 + D^2},$$

and the corresponding time-averaged values before and after SAPF activation are summarized in Table 2.4. The slight increase in apparent power is therefore a *byproduct of enhanced voltage quality and reduced distortion*, rather than an indication of additional system losses or SAPF inefficiency.

Table 2.4: Mean power components before and after SAPF connection (time-averaged)

Quantity	**Ideal**	**Before SAPF**	**After SAPF**
Active power P	P_{ref}	135.5 W	148.03 W
Reactive power Q	0 VAR	53.0 VAR	**0.0 VAR**
Distortion power D	0 VAD	7.0 VAD	3.0 VAD
Apparent power S	P_{ref}	145.7 VA	148.0 VA

Figure 2.12 further corroborates this explanation. Although the instantaneous current waveform remains nonlinear due to the rectifier nature of the load, its RMS value increases from 3.80 A to 4.02 A, directly reflecting the higher PCC voltage achieved after harmonic and reactive power compensation.

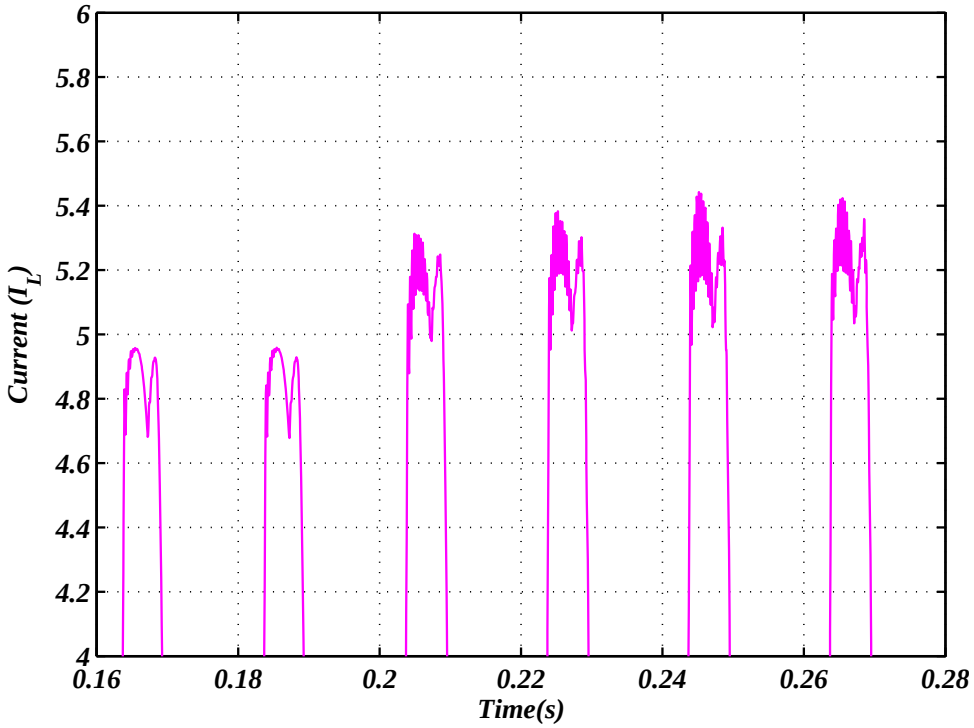

Figure 2.12: Zoomed-in view of the load current waveform and RMS envelope before and after SAPF activation. While the waveform retains its nonlinear shape, the RMS current increases from 3.80 A to 4.02 A due to improved voltage conditions at the PCC.

Take-away. The SAPF does not introduce additional active power losses; instead, it improves voltage quality and current waveform purity at the PCC. This enhancement enables voltage-dependent nonlinear loads to absorb power more effectively, resulting in a modest increase in RMS current and active power while achieving near-unity power factor and significantly reduced harmonic distortion. This effect becomes even more pronounced in the experimental prototype (Chapter 4), where sensor dynamics, digital control delays, and inverter dead-time lead to slightly higher compensating current injection compared to the idealized simulation model.

Figure 2.13 details the dynamic evolution of the DC-link voltage V_{dc}, active power P, and reactive power Q under the control of the outer-loop PDPC architecture.

Starting from an initial value of **63 V**, the DC-link voltage smoothly ramps up to its steady-state reference of **81 V** throughout approximately **60 ms**. This transient response reflects proper tuning of the outer-loop PI controller, achieving fast settling without overshoot or sustained oscillation.

At the start of compensation, $P_{\text{in}} > P_{\text{load}}$, so V_{dc} increases. The PI controller adjusts the amplitude of the current reference to drive this power injection and bring the DC-link to its desired operating point.

Simultaneously, *the active power P* — delivered from the grid to the system — increases from **135.5 W** to **148.0 W**. This increase reflects the additional energy being supplied to the inverter via the DC-link to support harmonic and reactive compensation. *The reactive power Q* falls sharply from **53.0 VAR** to **0.0 VAR**, as expected, confirming that the SAPF fully cancels the reactive demand of the nonlinear load.

The zoomed subplot in Figure 2.13 highlights the final settling behavior of V_{dc}. The voltage remains tightly regulated with minimal ripple (within ±0.4 V), which is essential to:

- Ensure accurate modulation of the inverter bridge voltage,
- Avoid DC bus overvoltage or undervoltage trips,
- Maintain a stable reference for inner-loop current tracking.

This result validates the coordinated design of the PI-based outer voltage loop and the predictive current control in the inner loop. The inverter's energy delivery through the DC bus is efficiently managed, resulting in a well-damped power system capable of adapting to nonlinear disturbances without compromising voltage stability.

Figure 2.13 showcases the active power matches its reference with <2% deviation after 0.25 s. This dynamic demonstrates that the control loop is well-tuned and exhibits no windup or instability.

Figure 2.14 evaluates the dynamic behavior of the internal optimization loop within the PDPC controller. The cost function $J(k)$, which quantifies the squared prediction error of active and reactive power, begins with relatively high fluctuations around 110^4 in the transient phase. As the compensation process stabilizes, the error diminishes rapidly, with $J(k)$ falling below 50 shortly after $t = 0.2$ s.

This decline confirms that the controller is successfully minimizing the instantaneous cost at each sampling instant. Specifically, it selects the optimal switching vector from the finite set $\mathcal{V}$ that yields the smallest predicted power error:

$$S^*(k) = \arg\min_{\vec{v}_i \in \mathcal{V}} J_i(k)$$

As P and Q converge toward their reference values, the error terms in $J(k)$ reduce, and the optimization operates in a lower energy regime.

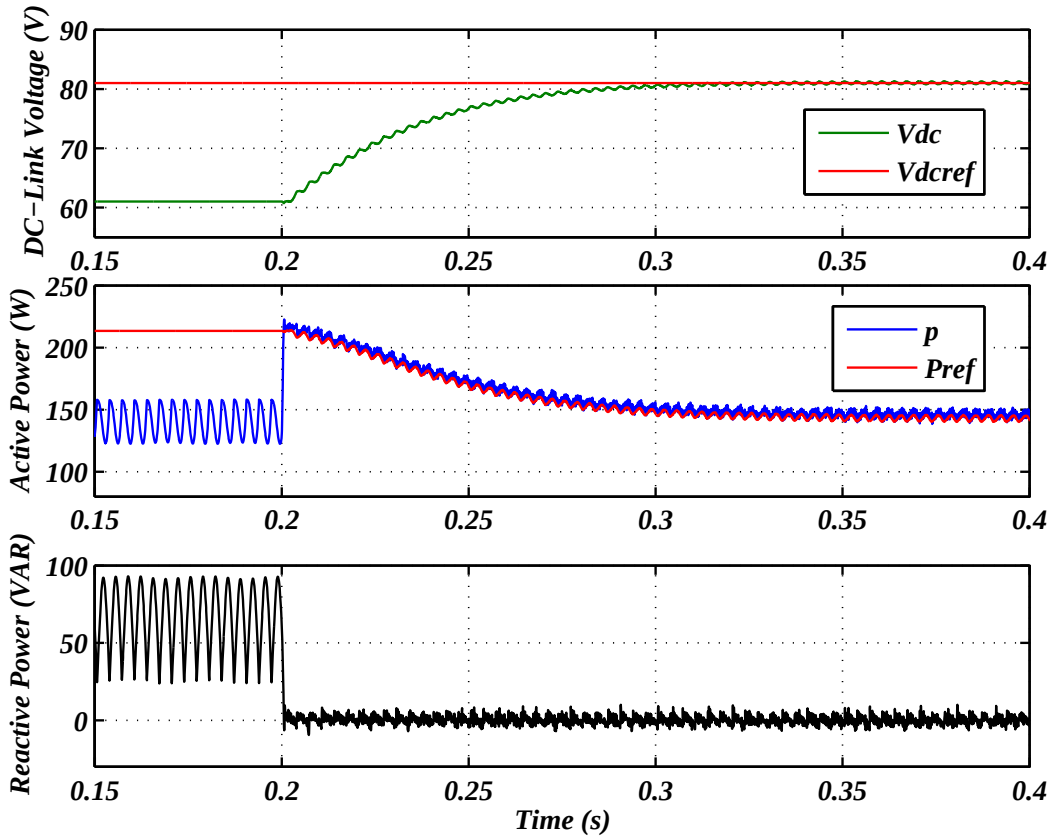

(a) DC-link voltage, active and reactive power

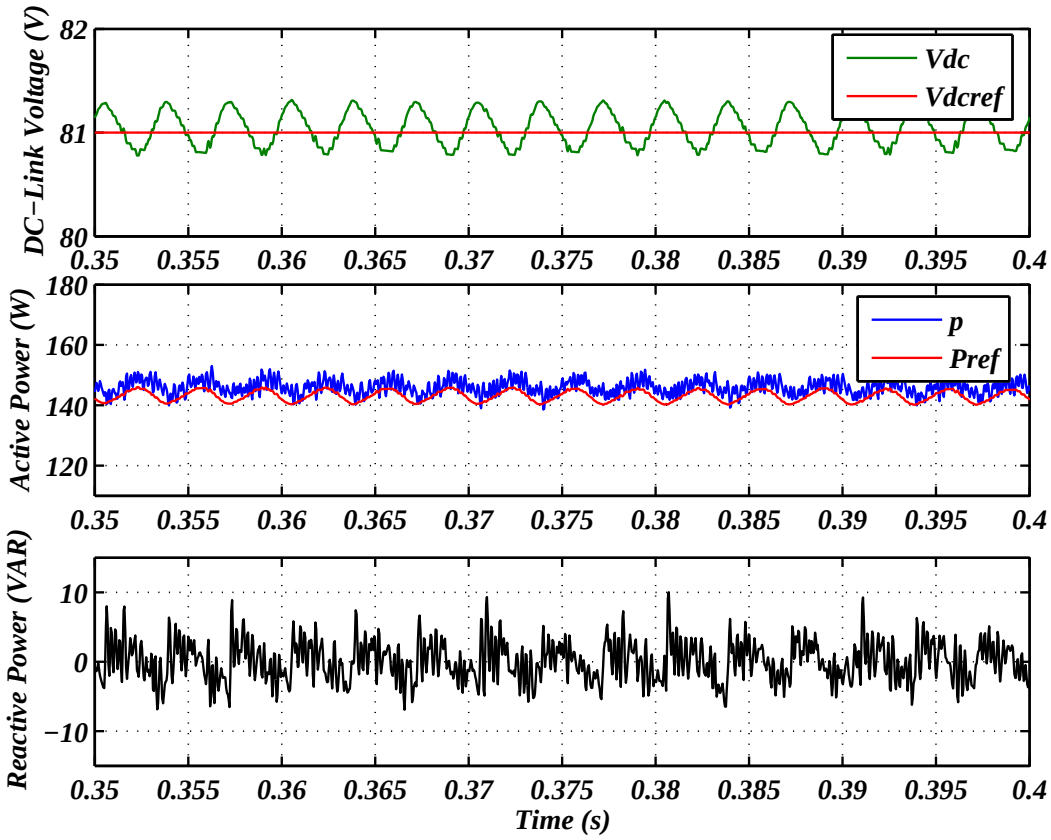

(b) Steady-state behavior of voltage and power waveforms

Figure 2.13: Dynamic and steady-state behavior of DC-link and power control

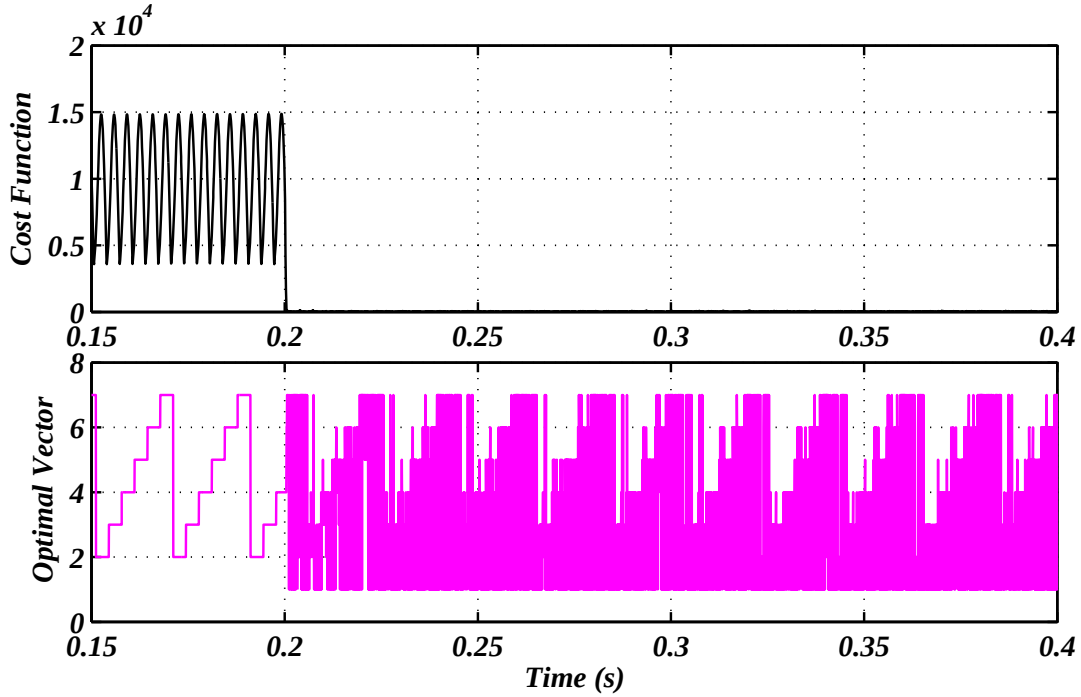

(a) Cost function evolution and switching vector selection

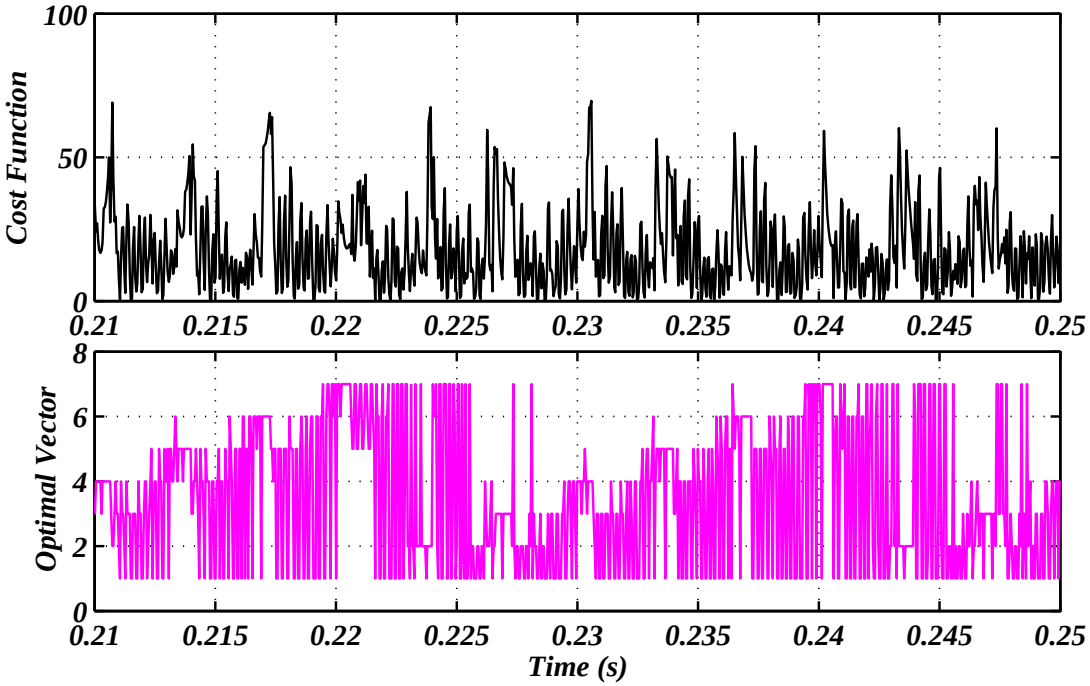

(b) Steady-state selection dynamics of optimal switching vector

Figure 2.14: Evaluation and convergence of cost function and optimal vector

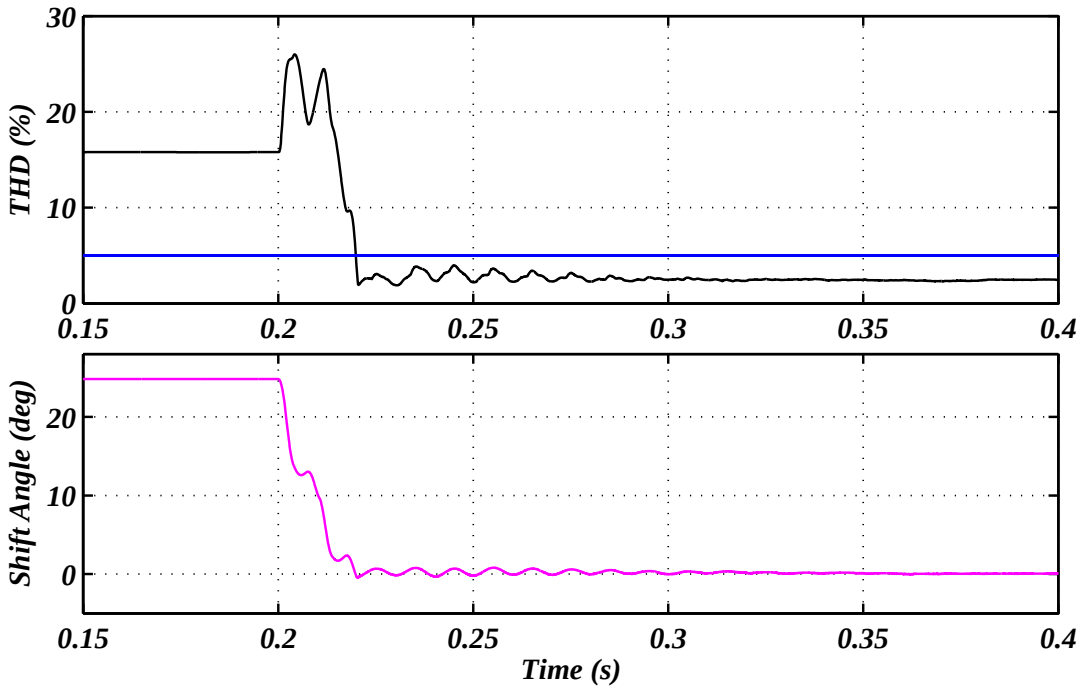

Figure 2.15: Reduction in Total Harmonic Distortion (THD) and Phase Shift

The zoomed subplot in Figure 2.14 shows that the cost function settles to approximately $J(k) = 25$ under steady-state conditions. This indicates consistent selection of optimal switching vectors with minimal oscillation. The absence of overshoot and the smooth convergence pattern reinforce the stability of the predictive controller's decision-making process.

These results validate the closed-loop optimality of the predictive controller: by minimizing the forward-predicted deviation in power flow, the inverter consistently applies the switching vector that delivers minimal error in real power P and zero reactive power Q, ensuring efficient real-time control.

Finally, Figure 2.15 presents the evolution of THD and phase shift. Initially, THD is measured at 16.2%, gradually falling to 2.55% by 0.4 s. The shift angle begins at 24.8°, dropping linearly to zero within 150 ms. These results reaffirm that SAPF effectively restores sinusoidal current delivery, enhances synchronization, and eliminates reactive and distortion components. The harmonics are not only canceled in magnitude but also in their phase relationship, allowing the inverter to inject clean current aligned with the voltage waveform.

In summary, the simulation outcomes validate the SAPF system's ability to handle harmonic compensation, reactive power cancellation, and voltage stabilization with remarkable precision. The PDPC algorithm, supported by a robust internal regulation structure, ensures near-instantaneous optimal control action, minimal THD, phase correction, and reliable tracking of power references—making it highly suitable for real-time power quality enhancement applications in grid-connected environments.

Conclusion

This chapter has presented a detailed analysis of power quality enhancement in grid-connected systems through the modeling, control, and implementation of a Shunt Active Power Filter (SAPF). Emphasis has been placed on mitigating current harmonics, compensating reactive power, and ensuring compliance with modern power quality standards in the presence of non-linear loads and fluctuating renewable energy sources.

The theoretical foundations of SAPF operation have been thoroughly developed, including the definitions of active, reactive, and distortion power, as well as key performance indicators such as total harmonic distortion (THD) and power factor. The mathematical modeling of SAPF components—covering inverter dynamics, filter characteristics, and DC-link voltage regulation—provides a solid basis for accurate system representation and control design.

A major contribution of this chapter is the implementation of the Predictive Direct Power Control (PDPC) strategy. By leveraging discrete-time predictive models and real-time optimization, PDPC enables fast and precise tracking of power references, ensuring near-sinusoidal source currents, effective harmonic suppression, and unity power factor operation. The control framework demonstrates strong robustness against load variations and grid disturbances, addressing both transient and steady-state performance requirements.

Simulation results validate the effectiveness of the proposed SAPF–PDPC system, showing rapid dynamic response, low steady-state ripple, and significant reduction in current harmonics. The achieved performance satisfies stringent power quality standards, including IEEE 519-2022, confirming the suitability of the proposed approach for practical grid-connected applications.

In summary, this chapter establishes a comprehensive power quality control framework that complements the PV energy generation system developed earlier. Together, these contributions enable reliable, efficient, and scalable integration of renewable energy sources into modern smart grids, setting the stage for experimental validation and real-world implementation in subsequent chapters.

Chapter 3 Overview: Experimental Combined System and Implementation

Chapter 3 presents the practical realization and experimental validation of the integrated photovoltaic (PV) system with reactive power compensation, incorporating real-time control and maximum power point tracking (MPPT) under partial shading conditions. This chapter bridges the gap between theoretical modeling and practical implementation, detailing the combined hardware and software framework required to achieve high-performance PV energy conversion and power quality improvement.

The chapter begins in Section 3.1 by addressing the critical integration challenges associated with combining diverse subsystems, including PV emulation, MPPT algorithms, boost converter control, and Shunt Active Power Filter (SAPF) regulation. These challenges include hardware synchronization, communication latency, power loss minimization, and real-time control stability, which are essential for ensuring the reliable operation of the overall system.

Section 3.2 introduces the proposed system configuration, detailing the physical layout and electrical interconnections of the major components. This section covers the integration of the programmable PV emulator, real-time digital controller, boost converter, and SAPF. The design choices for power electronics, control hardware, and communication protocols are also discussed, emphasizing the importance of seamless integration for accurate power tracking and quality enhancement.

Section 3.3 provides a comprehensive overview of the programmable DC PV emulator design, a critical component for experimental validation. This section covers the entire emulator design process, from partial shading condition (PSC) modeling and data generation (Section 3.3.1) to automated look-up table (LUT) creation (Section 3.3.2) and scaling for hardware interface (Section 3.3.3). The emulator's verification and validation process, discussed in Section 3.3.4, ensures accurate replication of real PV array behavior under complex shading conditions. The benefits of this emulator, including cost reduction, flexibility, and ease of integration, are highlighted in Section 3.3.5, establishing its significance as a versatile research tool.

Section 3.4 delves into the real-time implementation of metaheuristic-based MPPT algorithms, a core component of this thesis. This section introduces the generalized structure of real-time metaheuristic algorithms (Section 3.4.1), breaking down their key operational phases, including initialization (Section 3.4.2), evaluation (Section 3.4.3), population update (Section

3.4.4), and duty cycle adjustment (Section 3.4.5). This structured approach ensures efficient global maximum power point tracking (GMPPT) even under rapidly changing irradiance and complex PSC conditions, aligning with the thesis objective of enhanced energy extraction and power quality improvement.

Together, these sections form a comprehensive guide to the design, construction, and experimental validation of the integrated PV-SAPF system. This chapter establishes the practical foundation for the dynamic testing and performance analysis presented in the following chapters, providing critical insights into the real-world feasibility of the proposed control strategies.

Chapter 3

Experimental Combined System and Implementation

This chapter details the real-time implementation and experimental validation of the proposed integrated system designed to maximize power extraction under partial shading conditions. The experimental setup comprises several key components: a programmable DC photovoltaic (PV) emulator, a shunt active power filter (SAPF), and a metaheuristic-based maximum power point tracking (MPPT) controller based on the Enhanced Eel-Grouper Optimizer (EEGO), among other algorithms. The PV emulator is configured to replicate the electrical behavior of a real PV array under various shading patterns using a lookup table (LUT) populated with I-V characteristics. The SAPF is employed to enhance power quality by mitigating harmonic distortions and compensating for reactive power, ensuring that only a near-sinusoidal current is injected into the grid. The MPPT controller dynamically adjusts the converter's duty cycle to track the global maximum power point (GMPP) despite the partial shading of the PV array. Together, these components form an integrated test platform that not only validates the performance of the proposed methods under controlled laboratory conditions but also provides valuable insights into the practical challenges and advantages of implementing advanced MPPT and power quality solutions in grid-connected renewable energy systems.

3.1 Integration Challenges

Grid-connected PV systems face significant challenges under PSC, where only a portion of the PV array is exposed to full irradiance while other parts remain shaded. This leads to complex electrical behaviors that substantially degrade overall power output. Since PV modules are often connected in series and/or parallel configurations, a shaded module in a string can limit the current flow of the entire string, causing mismatch losses. These mismatch effects not only reduce the extractable power but also distort the overall P-V characteristic curve, producing multiple local maxima.

The total instantaneous power generated by a shaded PV array can be expressed as:

$$P_{\text{total}} = \sum_{k=1}^{N} V_k \cdot I_k, \tag{3.1}$$

where N is the number of modules, and V_k, I_k are the terminal voltage and current of the k-th module, respectively.

For modules connected in series, the total current is limited by the most shaded module:

$$I_{\text{string}} = \min_k \left(I_k \right), \tag{3.2}$$

leading to significant underutilization of high-irradiance modules. Conversely, in parallel configurations, voltage mismatches due to partial shading introduce unequal current sharing, creating further inefficiencies.

The relative efficiency loss caused by PSC can also be quantified using:

$$\eta_{\text{loss}} = 1 - \frac{P_{\text{LMPP}}}{P_{\text{GMPP}}}, \tag{3.3}$$

where P_{LMPP} is the power obtained when the MPPT algorithm settles at a local maximum, and P_{GMPP} is the true global maximum power point.

This loss is not only a result of irradiance non-uniformity but also of the inability of traditional MPPT techniques to escape local extrema. Conventional methods like Perturb and Observe (P&O) or Incremental Conductance (IncCond) tend to follow gradient-like behaviors and can become trapped in suboptimal operating points when multiple peaks exist.

To mitigate the adverse effects of PSC, bypass diodes are often used across PV modules to prevent reverse bias and enable current flow continuity. However, while they alleviate hot-spot risks and severe mismatch, they do not eliminate the formation of multiple maxima in the P-V curve.

The fill factor (FF) of the array, which quantifies the quality of the I-V curve, also drops significantly under partial shading:

$$\text{FF} = \frac{P_{\text{MPP}}}{V_{\text{oc}} \cdot I_{\text{sc}}}, \tag{3.4}$$

where V_{oc} is the open-circuit voltage and I_{sc} is the short-circuit current of the array. Under shading, both parameters are influenced non-linearly, leading to a reduced fill factor and hence lower efficiency.

Without enhanced tracking, the net power loss due to partial shading is expressed as:

$$P_{\text{loss}} = P_{\text{GMPP}} - P_{\text{LMPP}}, \tag{3.5}$$

with direct consequences on grid-side energy exchange and operational cost. This is visually

demonstrated in Figure 3.1, which contrasts the extracted power under conventional local tracking versus optimal global tracking.

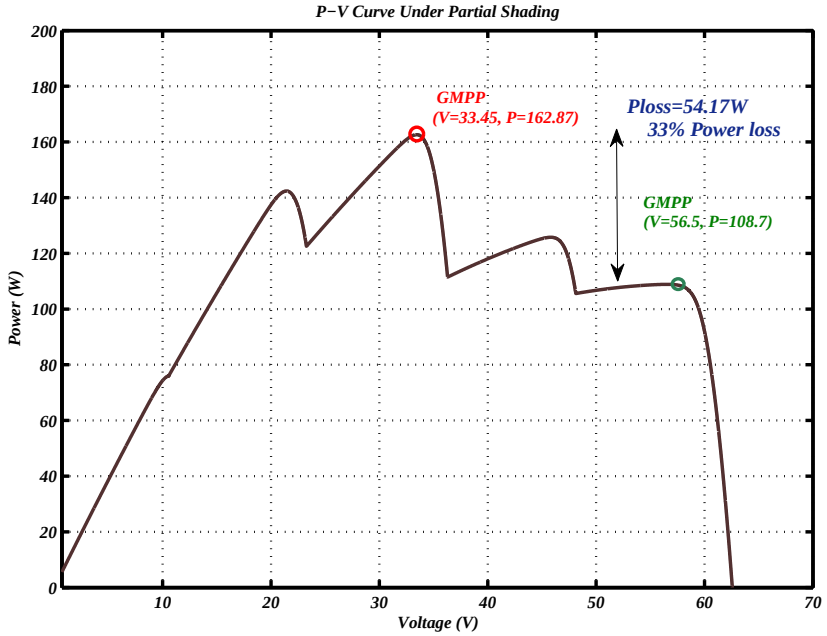

Figure 3.1: Comparison of power loss under local versus global maximum power tracking in partial shading conditions.

To address these challenges, the proposed system incorporates a metaheuristic-based MPPT controller — specifically, the Enhanced Eel-Grouper Optimizer (EEGO) — capable of exploring the full search space and identifying the global optimum even in the presence of shading-induced non-convexities.

The controller seeks to maximize the extracted power:

$$P_{\text{extracted}} = f(V, I, \text{shading}), \tag{3.6}$$

where $f(V, I, \text{shading})$ represents the nonlinear and dynamic relationship between irradiance conditions and PV output.

Ultimately, the system aims to maximize the net injected power:

$$\max\left(P_{\text{injected}}\right) = \max\left(P_{\text{extracted}} - P_{\text{loss}}\right), \tag{3.7}$$

which directly enhances system efficiency and reduces grid dependency. This experimental framework not only validates the superior tracking behavior of the proposed controller but also captures the real-world performance implications of deploying such intelligence in grid-connected PV systems.

3.2 Proposed System Configuration

The proposed system architecture is designed to maximize power extraction from a partially shaded PV array while ensuring high power quality when interfacing with the grid. In essence, the system converts variable solar energy into stable and high-quality electrical power that is injected into the grid. This is achieved through three primary components: a programmable shading PV emulator, a SAPF, and the grid interface, all working together in a coordinated, closed-loop manner.

The programmable shading PV emulator plays a critical role by simulating the electrical behavior of a real PV array under various shading conditions. It is built using a programmable DC voltage source and a lookup table (LUT) that captures the I-V characteristics of PV modules under different irradiance patterns. This controlled and repeatable environment enables systematic testing of MPPT algorithms without being affected by unpredictable ambient conditions such as temperature and solar irradiance. By ensuring that the emulator output closely matches that of an actual PV array, the system can accurately mimic the behavior and challenges of partial shading.

The SAPF is incorporated to improve the quality of the power delivered to the grid. It achieves this by dynamically filtering out harmonic distortions and compensating for reactive power imbalances, thereby "cleaning" the output waveform. The SAPF is connected between the PV emulator and the grid and is responsible for injecting a compensating current that mitigates the effects of nonlinear loads. This ensures that the inverter's output is nearly sinusoidal and that the power quality meets strict grid standards.

Finally, the grid connection provides the interface through which the conditioned power is fed into the public grid. This connection is configured to allow real-time observation and analysis of the power quality and system performance under varying levels of partial shading. Together, these components form an integrated test platform that not only validates the performance of advanced MPPT algorithms (such as those based on metaheuristic approaches) but also demonstrates practical improvements in power quality and grid compatibility.

The main components of our experimental platform include the following:

1. **Programmable Shading PV Emulator:** A programmable voltage source is interfaced with a pre-populated LUT that stores the I-V characteristics of PV modules under various shading conditions. The LUT is constructed using the single-diode model.

2. **Shunt Active Power Filter:** The SAPF is employed to improve the quality of the power that is injected into the grid. It achieves this by filtering out harmonics and compensating for reactive power components. In our system, the SAPF interfaces directly with the PV emulator and the grid, ensuring that the power delivered has low THD and a near-unity power factor.

3. **Real-Time MPPT Optimization Control:** A metaheuristic optimization algorithm is implemented to continuously track the GMPP under varying partial shading conditions.

The algorithm calculates a reference current $I_{pv,ref}$ in real time and adjusts the boost converter's duty cycle (DCL) accordingly.

4. **Grid Connection:** The conditioned power from the SAPF is injected into the grid. The grid interface is designed for real-time monitoring and ensures that the power quality meets established standards, thereby reducing grid dependency.

Figure 3.2 illustrates the overall system diagram, showing the interconnection between the programmable PV emulator, SAPF, and grid.

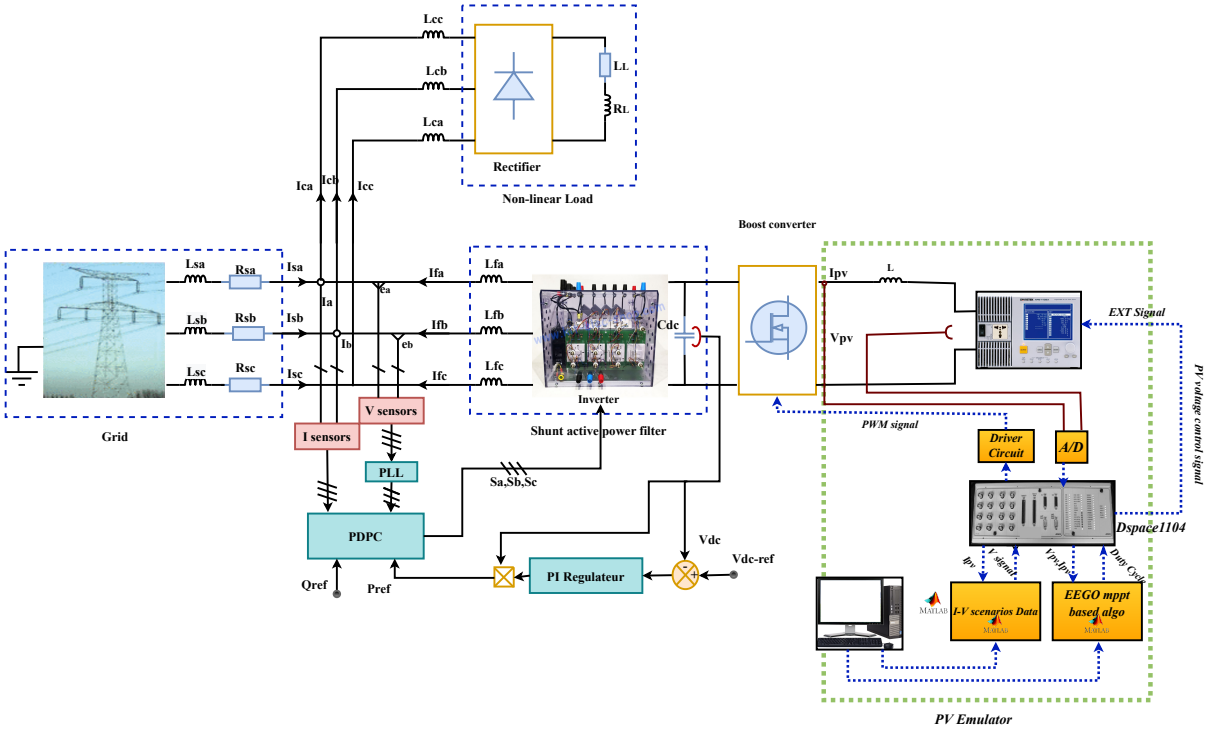

Figure 3.2: System Diagram of the Proposed Configuration, showing the interconnection of the programmable PV emulator, the shunt active power filter, and the grid interface.

3.3 Programmable DC PV Emulator Design

To enable repeatable and controlled testing of MPPT algorithms under PSCs, a programmable DC source PV emulator is developed. This emulator replicates the dynamic electrical behavior of a PV array by generating I-V responses derived from a mathematical PV model, eliminating variability from real-world sunlight, temperature, or weather. Integrated with the dSPACE 1104 platform (Chapter 4), it supports real-time validation of the EEGO and other MPPT algorithms.

3.3.1 PSC Modeling and Data Generation

The electrical behavior of the PV emulator is modeled using the single-diode equivalent circuit. The output voltage of the PV module is described by the following implicit equation:

$$V_{\text{pv}} = R_{sh}\left(I_{ph} - I_d - \frac{R_s I_{\text{pv}}}{R_{sh}}\right) \tag{3.8}$$

Since Equation (3.8) is non-linear, numerical methods (e.g., Newton-Raphson or forward simulation) are used to generate V_{pv} values for each I_{pv} across a range of irradiance values. These are stored in a two-dimensional lookup table (LUT):

$$\text{LUT}(G, I_{\text{pv}}) \longrightarrow V_{\text{pv}} \tag{3.9}$$

This LUT allows real-time emulation by mapping input current I_{pv} and irradiance G to output voltage V_{pv}.

3.3.2 Automated LUT Generation Procedure

The LUT is populated by simulating the single-diode model across predefined irradiance and current ranges. Algorithm 3.3.2 outlines the process, implemented in MATLAB/Simulink to generate a voltage matrix $V(G, I_{\text{pv}})$.

LUT PV Dataset Generation

[H] Samples N, current range $[I_{\text{min}} = 0\,\text{A}, I_{\text{max}} = 8.8\,\text{A}]$, irradiance range $[G_{\text{min}} = 100\,\text{W/m}^2, G_{\text{max}} = 1000\,\text{W/m}^2]$, step $G_{\text{step}} = 50\,\text{W/m}^2$ Voltage matrix $V(G, I_{\text{pv}})$ Open Simulink PV model Initialize output matrix V $G = G_{\text{min}}\ G_{\text{max}}\ G_{\text{step}}\ i = 1\ N$ Set current $I_{\text{pv}} = I_{\text{min}} + (i-1) \cdot \frac{I_{\text{max}} - I_{\text{min}}}{N-1}$ Simulate PV model and extract V_{pv} Store result in $V(G, I_{\text{pv}})$

The algorithm uses a reasonable N samples to achieve low resolution, ensuring high-fidelity I-V curves. The Simulink model incorporates the single-diode parameters.

3.3.3 Scaling for Hardware Interface

The LUT's control voltage $V_{\text{ctrl}}[k]$ is scaled to interface with the GW Instek APS-1102A programmable DC source (output: 0–1000 V, 0–5 A, 1 kW max; response time <1 ms). The APS-1102A accepts an external analog input (EXT) limited to 2.2 V. A scaling factor $G_{\text{scale}} = 20$ maps the LUT voltage to the hardware:

$$V_{\text{ctrl scaled}}[k] = \frac{V_{\text{ctrl}}[k]}{G_{\text{scale}}} \tag{3.10}$$

The emulator's internal amplifier restores the output:

$$V_{\text{out}}[k] = V_{\text{ctrl scaled}}[k] \cdot G_{\text{scale}} = V_{\text{ctrl}}[k] \tag{3.11}$$

This ensures the output voltage matches the LUT with <0.1% scaling error, verified via dSPACE 1104's 12-bit ADC.

3.3.4 PV Emulator Verification and Validation

The emulator's accuracy is validated against five PSC scenarios (Table 3.1), each defining irradiance patterns for a five-module PV string. The electrical characteristics are:

Table 3.1: Detailed characteristics of the five PSC scenarios

Scenario	Irradiance pattern (W/m^2)	I_{mpp} (A)	V_{mpp} (V)	G_{mpp} (W)
1	PV1=1000, PV2=450, PV3=200, PV4=800, PV5=700	5.6	33.28	186.4
2	PV1=900, PV2=350, PV3=250, PV4=820, PV5=600	4.89	32.92	161.0
3	PV1=1000, PV2=1000, PV3=400, PV4=200, PV5=100	8.12	20.75	168.5
4	PV1=1000, PV2=500, PV3=400, PV4=200, PV5=100	3.08	34.12	105.1
5	PV1=700, PV2=900, PV3=500, PV4=700, PV5=890	5.62	43.25	243.1

3.3.4.1 Open-Loop Validation Test

Open-loop tests apply each PSC scenario to the emulator, outputting voltages based on LUT I-V characteristics. The emulator's output is compared to theoretical I-V curves generated from the single-diode model. Figures 3.4, 3.5, and 3.6 show the results, with emulated curves closely matching theoretical expectations.

3.3.4.2 Error Analysis and Validation Metric

Accuracy is quantified using pointwise absolute error and percentage error:

$$\text{Error}(V_i) = \left| I_{\text{meas}}(V_i) - I_{\text{expt}}(V_i) \right| \tag{3.12}$$

$$\text{Absolute Error}(\%) = \frac{\left| I_{\text{meas}} - I_{\text{expt}} \right|}{I_{\text{expt}}} 100 \tag{3.13}$$

Mean percentage errors across scenarios are: Scenario 1: 2.8%, Scenario 2: 2.1%, Scenario 3: 3.5%, Scenario 4: 3.7%, Scenario 5: 2.7%. The maximum error (3.7% in Scenario 4) occurs due to multi-peak complexity, but all errors remain <5%, confirming high fidelity. Figure 3.3 illustrates the theoretical I-V curves for all scenarios.

3.3.5 Benefits of the Emulator Setup

The PV emulator, driven by a high-resolution LUT and the GW Instek APS-1102A, offers:

1. **Controlled Testing Environment:** Eliminates environmental variability, enabling repeatable experiments at 25 °C.
2. **Flexible Scenario Emulation:** Supports static and dynamic PSCs, including multi-peak profiles.
3. **Scalability:** Adapts to various PV configurations (e.g., different module counts or technologies) by updating the LUT.
4. **Real-Time Performance:** Sub-millisecond response supports dynamic MPPT validation.

Validation confirms <4.2% error across I-V ranges, ensuring reliable testing for EEGO and other MPPT algorithms under realistic shading conditions.

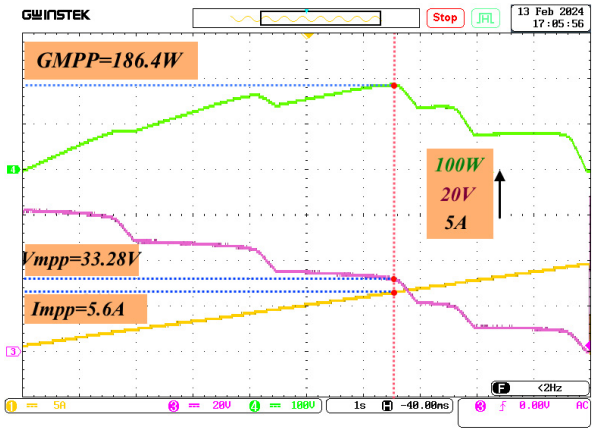

(a) PSC-S1

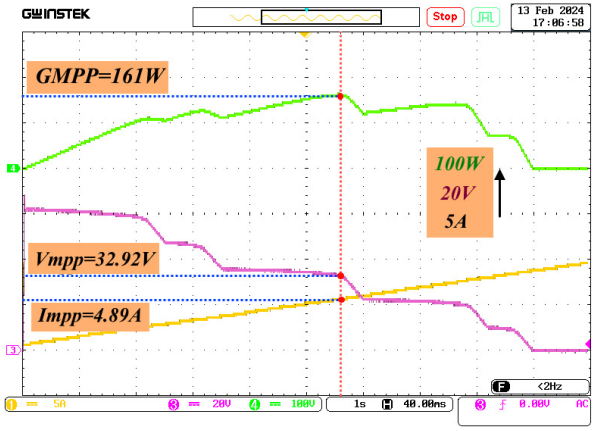

(b) PSC-S2

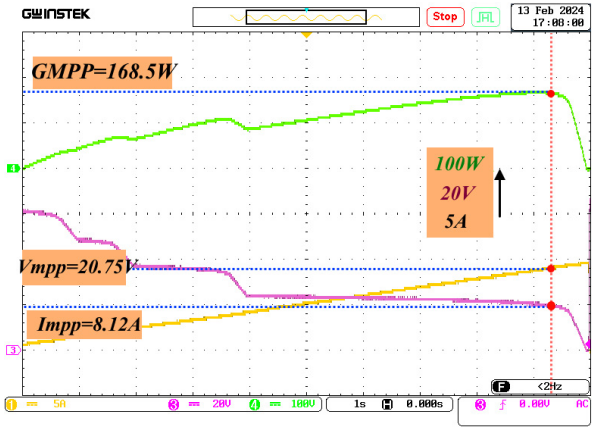

(c) PSC-S3

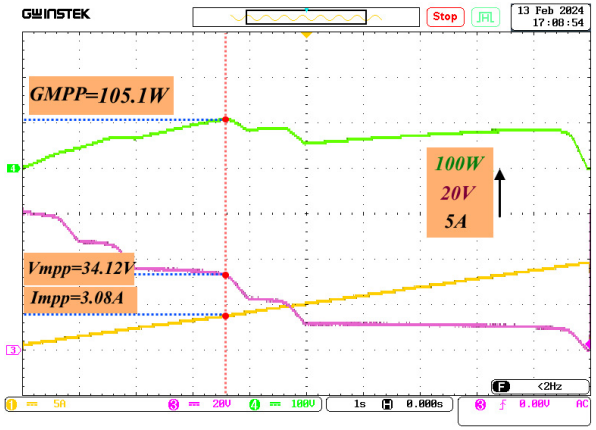

(d) PSC-S4

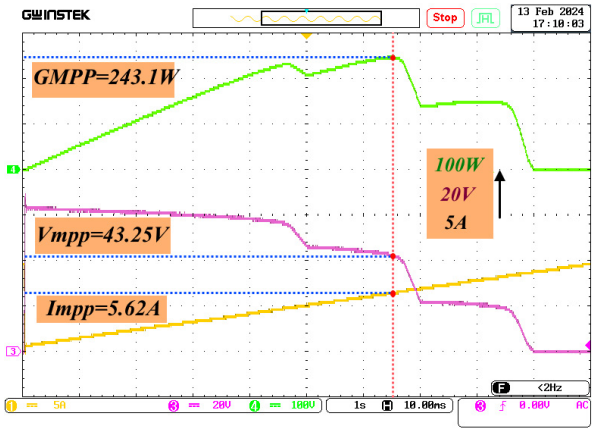

(e) PSC-S5

Figure 3.3: Theoretical I-V curve characteristics for the five partial shading scenarios

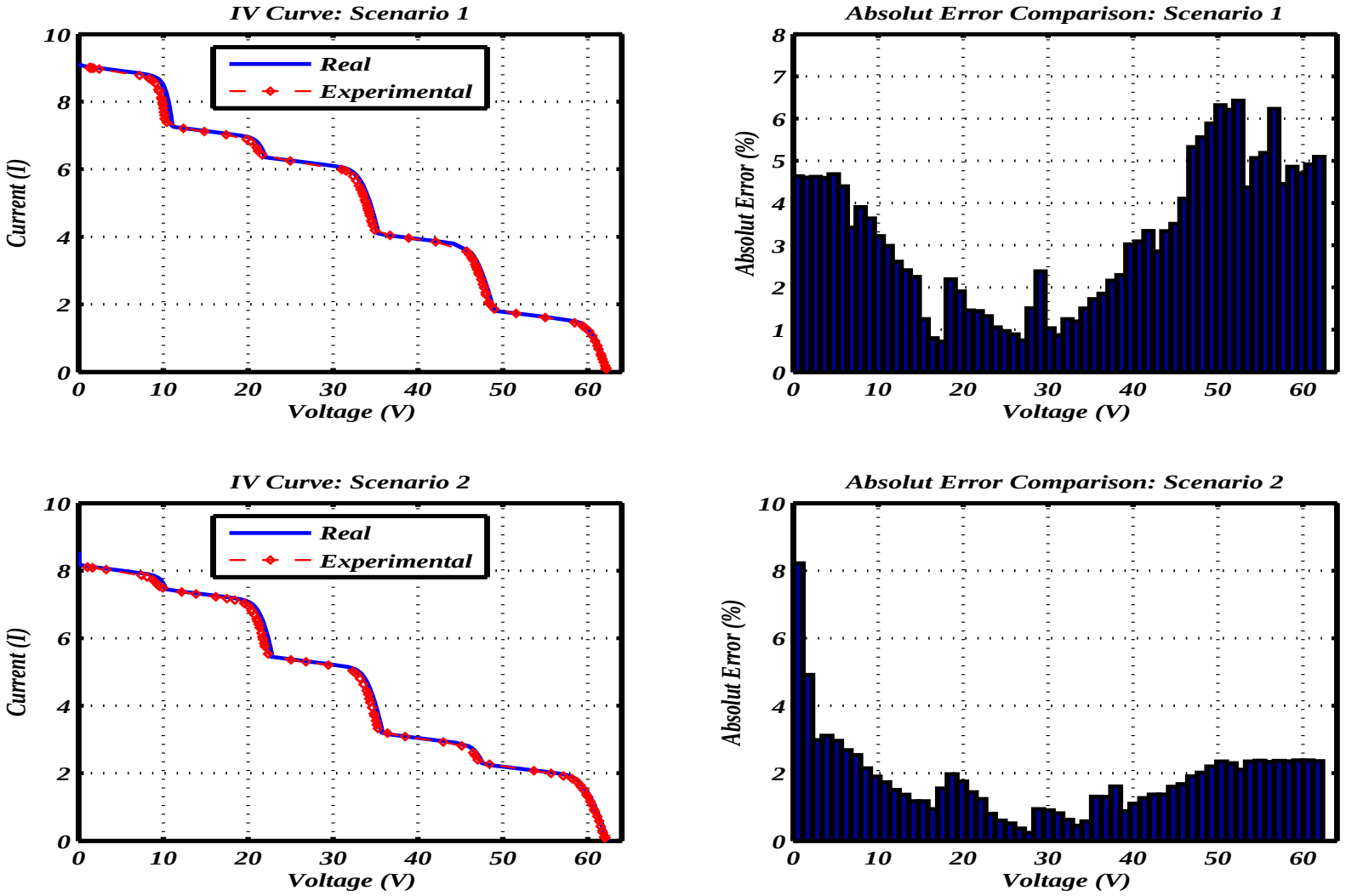

Figure 3.4: Comparison between emulator and expected I-V curves (Scenario 1/Scenario 2)

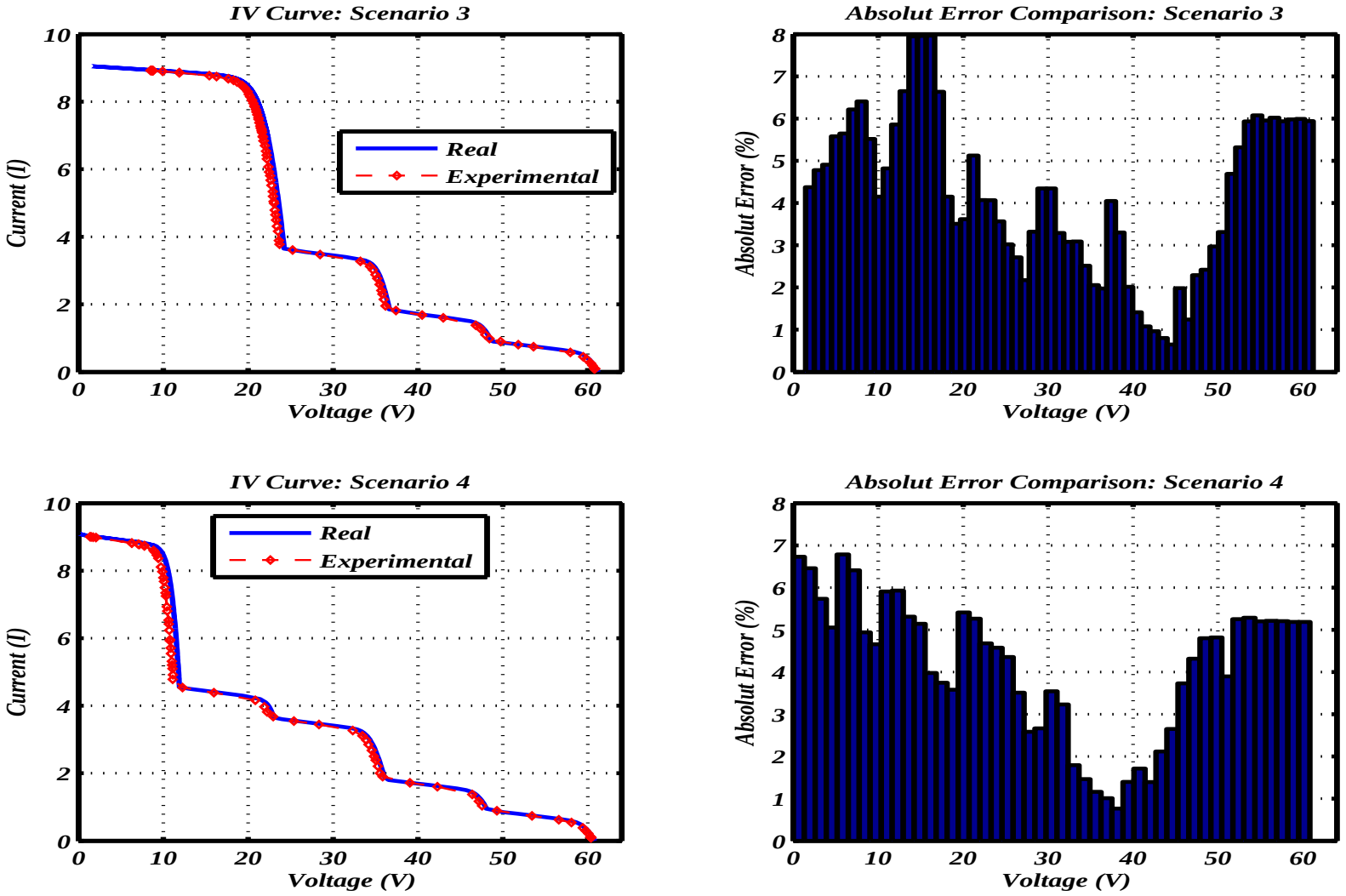

Figure 3.5: Comparison between emulator and expected I-V curves (Scenario 3/Scenario 4)

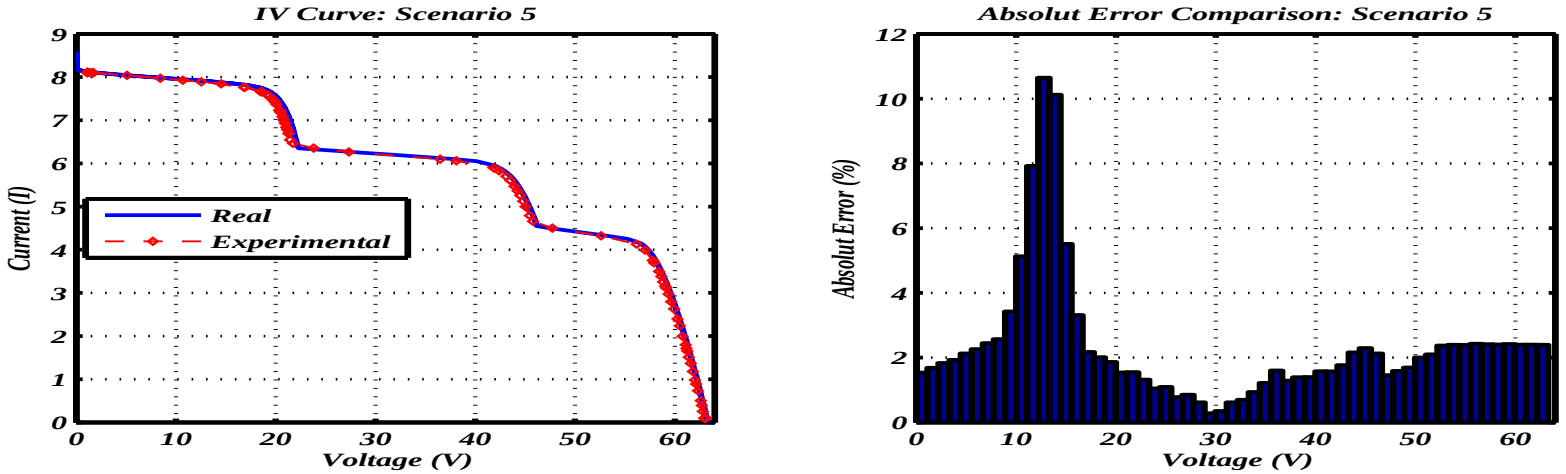

Figure 3.6: Comparison between emulator and expected I-V curves (Scenario 5)

3.4 Real-Time Metaheuristic-Based MPPT Algorithms

3.4.1 General Structure of Real-Time Metaheuristic-Based MPPT Algorithms

Metaheuristic algorithms, when applied to MPPT in PV systems, follow a common iterative process to optimize the duty cycle of a power converter (e.g., a boost converter) to maximize power output under varying environmental conditions. Fig. 3.7 shows a roadmap that summarizes the entire Real-Time Metaheuristic-Based MPPT Algorithm section, This roadmap summarizes the complete real-time execution of our metaheuristic MPPT algorithm with embedded decision-making logic for environment-driven resets, real-time tracking using current reference control, and robust convergence safeguards.

This process can be broken down into several general phases that apply across different metaheuristic algorithms. These phases are:

- Initialization: Setting up the initial parameters, population of candidate solutions (duty cycles), and variables to track progress and best solutions.
- Evaluation: Testing each candidate duty cycle by applying it to the system, measuring the resulting PV power, and updating performance records.
- Population Update: Refining the candidate solutions based on evaluation results using algorithm-specific rules to improve the search.
- Duty Cycle Adjustment: Applying the best-found duty cycle to the converter and fine-tuning it for real-time operation.

To illustrate this process clearly, here's a pseudocode representation

General Metaheuristic MPPT Algorithm

[H] PV power measurements, enable signal Optimal duty cycle for maximum power Initialize population of duty cycles and tracking variables not converged and iterations < maximum iterations each candidate duty cycle in population Apply duty cycle to the converter Measure resulting PV power Update personal best if power improves Update global best solution based on evaluations Update population using metaheuristic-specific rules Adjust converter duty cycle to the best solution Optimal duty cycle

This pseudocode outlines the high-level flow, which we'll expand upon in subsequent parts by diving into each region of a general code's process.

These phases loop continuously or until a stopping condition (e.g., maximum iterations or convergence) is met, ensuring the algorithm adapts to dynamic conditions like irradiance or temperature changes. This structure is general enough to serve as a foundation for any metaheuristic algorithm, with differences arising only in the specific rules for updating the

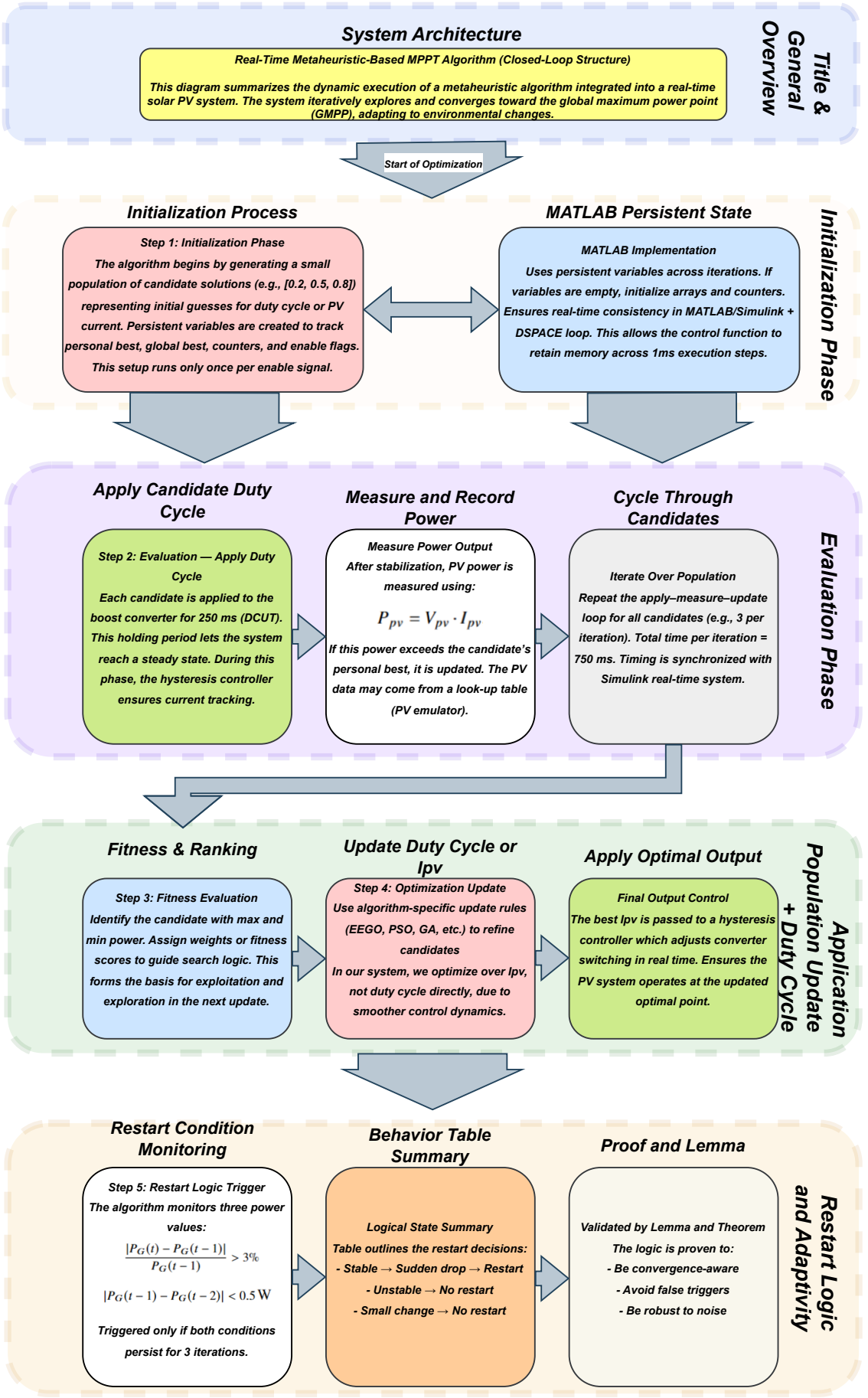

Figure 3.7: Roadmap of Real-Time Metaheuristic-Based MPPT Algorithm section

population. Figure 3.8 illustrates the closed-loop control architecture underpinning this process, integrating a LUT for PV emulation, the calculation of the optimal reference current $I_{pv,ref}$, and a hysteresis controller for precise duty cycle adjustments. This schematic serves as a roadmap for the algorithm's operation, with each phase contributing to the system's ability to dynamically track the GMPP.

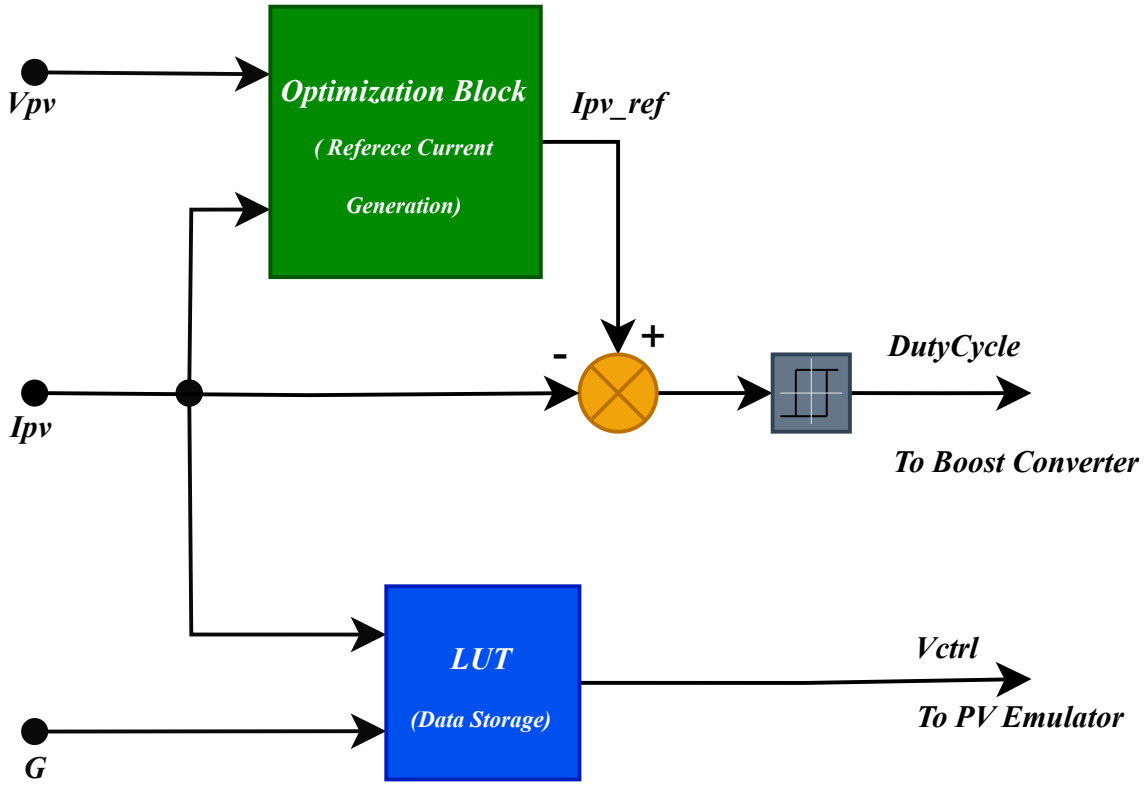

Figure 3.8: Schematic Diagram of the Real-Time MPPT Optimization Architecture: This block diagram outlines the closed-loop control strategy, including the LUT for PV emulation, the calculation of the optimal reference current $I_{pv,ref}$, and the adjustment of the boost converter's duty cycle via a hysteresis controller.

To elucidate this framework, the following subsections detail each phase, beginning with initialization and culminating in duty cycle adjustment, all operating within the architecture depicted in Figure 3.8. This structure ensures a cohesive approach to optimizing power extraction, adaptable to various metaheuristic algorithms.

3.4.2 Initialization Phase

Now, let's move to the first detailed region of the code process: Initialization. This phase is where the algorithm prepares all necessary components before starting the optimization loop. I'll explain it in a narrative form, focusing on general principles, how MATLAB processes it, and its role in real-time MPPT, followed by a visual representation.

3.4.2.1 Narrative Explanation

The initialization phase is the foundation of any metaheuristic MPPT algorithm. Its purpose is to establish the starting point for the optimization process by defining the population of candidate duty cycles, setting up counters and timing variables, and initializing arrays to store the best solutions found during execution. In the context of real-time MPPT, this phase must be efficient and flexible, allowing the algorithm to begin searching for the MPP immediately upon activation while retaining state information across iterations for continuous operation. In a typical implementation, the algorithm starts by checking whether it's the first run. If so, it sets up:

- Population of Duty Cycles: A set of initial candidate solutions (e.g., duty cycle values between 0 and 1) that the algorithm will test. The size and initial values of this population are chosen to balance computational load and solution space coverage. For real-time efficiency, a small population (e.g., 3–5 candidates) might be used, initialized either randomly or based on prior knowledge of typical MPP duty cycles (e.g., 0.2, 0.5, 0.8).
- Tracking Variables: Arrays to store the personal best duty cycles and their corresponding power outputs for each candidate, as well as a global best duty cycle and power across the entire population. These ensure the algorithm remembers high-performing solutions.
- Counters and Timers: Variables to manage iteration counts, timing intervals (e.g., how long each duty cycle is applied before evaluation), and the sequence of operations. In real-time systems, timing is critical to synchronize the algorithm with the physical converter's response.
- Control Flags: An enable signal to start or stop the algorithm, ensuring it only runs when intended (e.g., when the PV system is active).

3.4.2.2 MATLAB's Role:

MATLAB processes this phase using persistent variables, which retain their values between function calls. This is essential for real-time MPPT, where the algorithm is called repeatedly (e.g., every millisecond) as part of a control loop. On the first call, MATLAB checks if these variables are empty (using isempty()), and if so, initializes them. For example, a population array might be set as population = [0.2, 0.5, 0.8], and counters like counter = 0 are reset. This persistent state allows MATLAB to avoid redundant initialization, making the process seamless in a real-time environment.

3.4.2.3 Real-Time Considerations:

The initialization must account for the dynamic nature of PV systems. For instance, the initial duty cycles should span a reasonable range to quickly locate the MPP under current conditions,

and the timing variables must align with the converter's settling time (e.g., 250 ms) to ensure accurate power measurements. While the specifics (e.g., population size or initial values) may vary across metaheuristic algorithms, the initialization phase universally involves setting up a population and tracking mechanisms.

3.4.2.4 Visual Representation

To clarify this phase, here's a pseudocode:

Initialization Phase of Metaheuristic MPPT

[H] Enable signal Initial duty cycle output Enable signal is active persistent variables are empty (first run) Set population size (e.g., 3–5 candidates) Initialize population with duty cycles (e.g., [0.2, 0.5, 0.8]) Initialize personal best duty cycles and powers to zero Initialize global best duty cycle and power to zero Set iteration counter to 0 Set timing counter to 0 Set evaluation index to 1 (first candidate) Default or first candidate duty cycle Default duty cycle (e.g., 0.5)

This pseudocode captures the initialization logic in a general form, applicable to any metaheuristic algorithm, with MATLAB's persistent variable management implied.

3.4.3 Evaluation Phase

The evaluation phase is a cornerstone of the metaheuristic-based MPPT algorithm, designed to optimize the duty cycle of a boost converter to maximize power output from a PV system. In this phase, each candidate duty cycle in the algorithm's population is applied to the converter, and the resulting PV power is measured to assess the candidate's fitness. This process identifies which duty cycles bring the system closer to the GMPP, even under dynamic conditions like partial shading or temperature changes. Given the real-time nature of MPPT, this phase must balance accuracy, speed, and system stability.

The process begins by selecting a candidate duty cycle from the population and applying it to the boost converter, which adjusts the PV system's operating point. To ensure accurate power measurements, a stabilization period is enforced, allowing the system to reach a steady state and mitigate transient effects such as voltage or current oscillations. A Duty Cycle Update Timer (DCUT) governs this timing, holding each duty cycle constant for 250 milliseconds, a duration chosen to balance measurement reliability with real-time responsiveness. During this period, the algorithm outputs the same duty cycle repeatedly, typically synchronized with the system's control loop (e.g., a 1 ms time step in simulation).

Figure 3.9 illustrates the timing and state transitions of this DCUT-based process, highlighting the 250 ms update cycle for each duty cycle and the evaluation of three candidate solutions per iteration, resulting in a total iteration time of 750 ms. This visual representation underscores the sequential nature of the evaluation, ensuring each candidate is tested under stable conditions

before proceeding to the next.

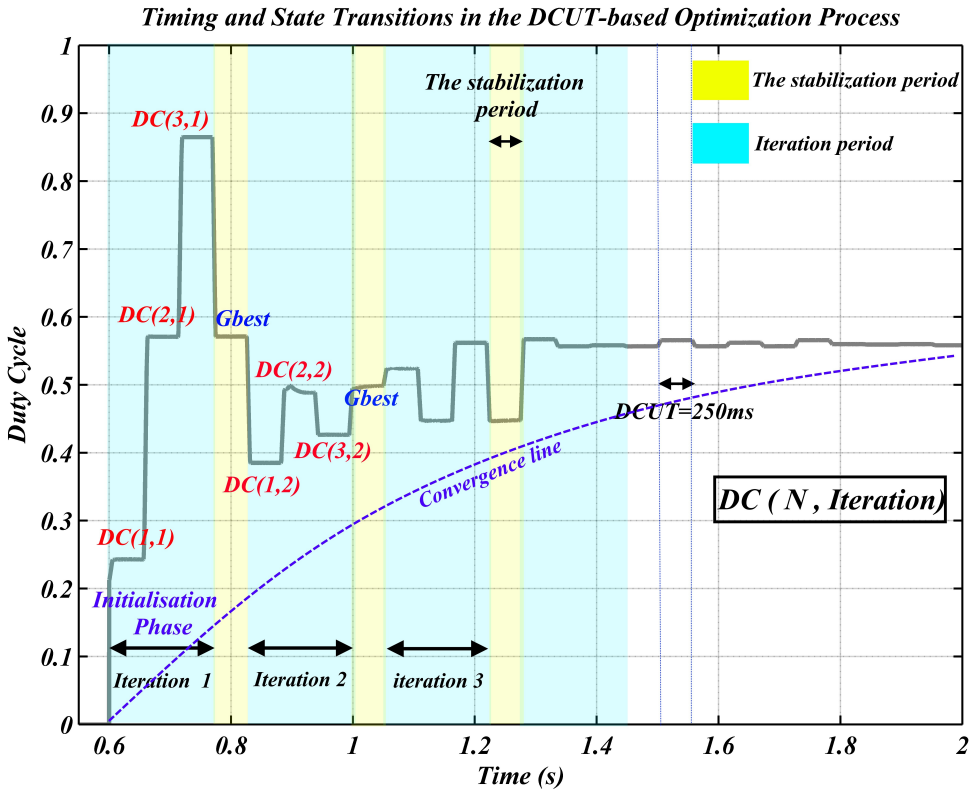

Figure 3.9: Timing and State Transitions in the DCUT-based Optimization Process: The duty cycle is updated every 250 ms, with three candidate solutions evaluated per iteration.

Once the stabilization period concludes, the PV power, denoted $P_{pv} = V_{pv} \cdot I_{pv}$, is calculated using measurements of the PV voltage (V_{pv}) and current (I_{pv}), often retrieved from a LUT within the PV emulator, as depicted in Figure 3.8. This power serves as the fitness metric for the candidate duty cycle. If P_{pv} exceeds the candidate's personal best power—stored from previous evaluations—the personal best power and its corresponding duty cycle are updated. This step ensures that high-performing solutions are retained for consideration in the population update phase.

The algorithm then advances to the next candidate, repeating the process until all candidates in the population (e.g., three duty cycles) have been evaluated. In MATLAB, this is implemented using a loop structure, with a counter tracking the stabilization period and persistent variables storing the personal bests. The 750 ms iteration time, as shown in Figure 3.9, allows the algorithm to complete a full evaluation cycle while remaining responsive to dynamic conditions such as irradiance changes or partial shading.

This phase is universal across metaheuristic algorithms, whether Eel-grouper optimization, or others, as the core steps—apply, stabilize, measure, and update—remain consistent. The DCUT's role in ensuring stable and timely evaluations is critical to the algorithm's real-time performance, setting the stage for refining the population in the subsequent phase.

3.4.3.1 Narrative Explanation

Imagine the MPPT algorithm as an explorer testing different paths (duty cycles) to find the one that yields the most treasure (power). Here's how the evaluation phase unfolds:

- Applying the Duty Cycle: The algorithm takes each candidate duty cycle from its population—a set of potential solutions—and applies it to the boost converter. The duty cycle controls the converter's switching, adjusting the operating point of the PV system.
- Waiting for Stability: After setting a new duty cycle, the system needs time to settle. Transients—like voltage or current oscillations—could distort power measurements if we measure too soon. A stabilization period (e.g., 250 milliseconds) is enforced using a timer or counter, ensuring the PV emulator and converter reach a steady state.
- Measuring Power : Once the system stabilizes, the PV power, denoted P_{pv} , is calculated (typically as $P_{pv} = V_{pv} \cdot I_{pv}$, where V_{pv} and I_{pv} are the PV voltage and current). This power is the fitness metric for the candidate duty cycle.
- Updating Personal Bests: Each candidate has a "personal best"—the highest power it has achieved so far and its corresponding duty cycle. If the newly measured P_{pv} exceeds the candidate's previous best, the personal best power and duty cycle are updated.
- Moving to the Next Candidate: After evaluating one candidate, the algorithm repeats the process for the next one in the population until all have been tested.

This cycle ensures every candidate gets a fair shot at proving its worth, providing the data needed to guide the algorithm toward the GMPP.

3.4.3.2 MATLAB's Role in Real-Time Execution

In a MATLAB implementation, the evaluation phase is orchestrated with precision to mimic real-time behavior:

- Loop Structure: A for or while loop iterates over the population, with an index (e.g., u) tracking the current candidate.
- Persistent Variables: Variables like the duty cycle, counter, and personal bests are stored persistently across function calls, simulating continuous operation.
- Timing Control: A counter increments with each sampling time. For example, if each sampling time represents 1 ms, the duty cycle is held constant for 250 sampling time (250 ms). During this period, the function outputs the same duty cycle repeatedly.
- Power Measurement: After the counter hits the stabilization threshold, P_{pv} is computed, and the personal best is updated if needed.

This setup allows MATLAB to emulate the timing constraints of a real-time controller.

3.4.3.3 Why Stabilization Matters

In real-time MPPT, the stabilization period isn't arbitrary—it's a lifeline. Measuring power too early risks capturing transient noise rather than steady-state performance. A 250 ms delay strikes a balance: long enough for stability, short enough to keep the algorithm responsive. For a population of 3 candidates, the entire evaluation phase takes about 750 ms, enabling rapid adaptation to changing environmental conditions like irradiance shifts.

3.4.3.4 Visualizing the Process

Here's a clear representation of the logic:

Duty Cycle Candidate Evaluation

[H] each candidate i in the population Set boost converter duty cycle to candidate i's current value Start timer timer $<$ 250 ms Hold the duty cycle steady Increment the timer Measure PV power P_{pv} $P_{pv} >$ personalBestPower(i) Update personal best power: personalBestPower(i) $\leftarrow$ P_{pv} Update personal best duty cycle: personalBestDC(i) $\leftarrow$ current duty cycle

3.4.4 Population Update Phase

The population update phase is a critical step in metaheuristic MPPT algorithms, where the algorithm refines its set of candidate duty cycles based on their evaluated performance. This phase transforms raw power output data into actionable improvements, steering the algorithm toward the GMPP. Below, we'll explore how this phase works, its implementation in MATLAB for real-time control, and why it's essential for optimizing power extraction in systems like solar photovoltaic arrays.

3.4.4.1 Narrative Explanation

Think of the population update phase as a strategic debrief after testing a set of duty cycles. Each candidate has delivered a power output, and now the algorithm uses that feedback to decide its next moves. Here's the process in detail:

- Identify the Best and Worst Performers: The algorithm reviews the power outputs from the previous evaluation phase. It pinpoints the duty cycle yielding the highest power (the "best") and the one with the lowest (the "worst"). These benchmarks frame the current search landscape, highlighting what's working and what isn't.
- Calculate Fitness Metrics : Using the best and worst power values, the algorithm computes a fitness metric for each candidate. This metric—often a normalized difference between a candidate's power and the extremes—quantifies how promising each duty cycle is.

- Assign Weights: Each candidate receives a weight based on its fitness. High-performing duty cycles get higher weights, signaling the algorithm to favor areas near them. Poor performers get lower weights, nudging the search away from those regions. These weights balance the algorithm's focus between refining known solutions and exploring new possibilities.

- Update the Duty Cycles : This is the core of the phase. Each duty cycle in the population is adjusted using a formula that combines :

  - Exploitation: Shifting toward the best-known solutions (e.g., the global best duty cycle).
  - Exploration: Introducing randomness to test uncharted areas that might hide the GMPP.
  - Algorithm-Specific Mechanisms: For example, Particle Swarm Optimization (PSO) updates via velocity, while Genetic Algorithms (GA) use crossover and mutation. Each metaheuristic has its signature approach.

- Enforce Constraints : Duty cycles must remain practical—typically between 0 and 1 for a DC-DC converter. If an update pushes a duty cycle beyond these bounds, it's clamped to the nearest limit (e.g., 0 or 1).

- Prepare for the Next Iteration : With the population refreshed, the algorithm sets the stage for the next evaluation round, applying the updated duty cycles to the system and measuring their power outputs anew.

This iterative refinement is what makes metaheuristic algorithms adaptive and effective, especially in complex scenarios like partial shading, where multiple power peaks exist.

3.4.4.2 MATLAB's Role in Real-Time Execution

MATLAB brings this phase to life in a real-time MPPT control loop, ensuring the algorithm operates efficiently within a physical system. Here's how it's implemented:

- Tracking the Global Best: After evaluation, MATLAB identifies the duty cycle with the highest power across all candidates and stores it as for example "globalBestDutyCycle". This value anchors the update process, guiding the population toward the GMPP.

- Weight Calculation: A function (e.g., updateWeights) computes weights based on each candidate's power relative to the best and worst. These weights might reflect rank, normalized fitness, or algorithm-specific criteria, stored in arrays for easy access.

- Duty Cycle Refinement: A dedicated function (e.g., updateDutyCycle) adjusts each duty cycle. Depending on the metaheuristic, this could involve:

  - Adding a velocity term in PSO, influenced by personal and global bests.
  - Performing crossover between parent duty cycles in GA, followed by random mutation.
  - Applying attraction/communication in Eel-grouper algorithm.

- Timing Control: Updates occur after all candidates are evaluated—say, every 750 ms for a population of three.
- Persistent Memory: MATLAB uses persistent or global variables to track the population, weights, and global best across iterations, ensuring the algorithm builds on its history without resetting.

3.4.4.3 Why Weights and Updates Are Crucial

Weights are the algorithm's compass, directing it toward promising regions while avoiding dead ends. By emphasizing high performers, the algorithm exploits known successes. The random exploration component, meanwhile, ensures it doesn't settle for a local peak when the GMPP might lie elsewhere. This dual strategy—exploitation plus exploration—is vital in dynamic conditions, like shading.

3.4.4.4 A Universal Framework Across Metaheuristics

While the update mechanics vary, the population update phase follows a consistent structure:

- Assess performance (best/worst).
- Quantify fitness.
- Refine the population with a mix of directed and random adjustments.

This universality makes the phase adaptable to any metaheuristic, with the algorithm's unique rules adding flavor to the execution.

3.4.4.5 Visualizing the Process

To clarify, here's how the phase look in code:

Population Update Phase of Metaheuristic MPPT

[H] Power outputs, personal bests, global best Updated population of duty cycles Evaluate population performance Compute best power and index from power outputs Compute worst power from power outputs Set fitness metric using algorithm-specific criteria Update global best duty cycle if new maximum found Refine duty cycles each candidate i in population Compute fitness for candidate i based on power output Assign weights or adjustment factors using algorithm-specific rules Update duty cycle $D[i]$ based on weights, global best, and exploration terms $D[i] < 0$ Set $D[i] = 0$ $D[i] > 1$ Set $D[i] = 1$ Prepare for next cycle Set next cycle's duty cycle to global best Updated population

3.4.5 Duty Cycle Adjustment Phase

The final phase in the real-time metaheuristic MPPT loop involves applying the best solution found so far—whether a duty cycle or a corresponding PV current reference $I_{pv,ref}$—to the boost converter. This step directly controls the converter and thus determines the operating point of the PV array.

3.4.5.1 Mapping of Optimization Output to Converter Control

In our implementation, instead of directly optimizing over the duty cycle D, we used the PV current I_{pv} as the search variable. The metaheuristic algorithm searches for the optimal I_{pv} value that maximizes the power output P_{pv}, leveraging the monotonic relation between duty cycle and PV current in a boost converter topology. Once the optimal I_{pv}^{*} is found, it is passed to the hysteresis controller, which adjusts the converter switching accordingly. This is illustrated in the closed-loop schematic in Figure 3.8.

This approach offers smoother transitions and better noise immunity, especially in real-time systems using high-resolution ADCs. Additionally, it simplifies interfacing with digital controllers that regulate current directly.

3.4.6 Real-Time Update Condition and Restart Mechanism

To ensure responsiveness under dynamic conditions—such as sudden irradiance shifts or partial shading events—a robust restart mechanism is essential for real-time metaheuristic MPPT algorithms. This restart mechanism must be sensitive enough to detect significant environmental changes, yet stable enough to avoid false triggers during early exploration or convergence phases.

Proposed Restart Condition We propose a compound condition that relies exclusively on measured power values across three successive iterations. A restart is triggered only when:

$$\frac{|P_G(t) - P_G(t-1)|}{P_G(t-1)} > 3\% \quad \textbf{AND} \quad |P_G(t-1) - P_G(t-2)| < 0.5\,\text{W} \quad \text{for 3 consecutive iterations} \tag{3.14}$$

This ensures that the algorithm only restarts when:

- It was previously operating in a stable state (i.e., small fluctuations),
- A sudden and significant power deviation occurs (e.g., due to a new irradiance condition),
- The condition is sustained for a short verification window to filter transient noise.

3.4.6.1 Restart Logic — Simple Proof of Correctness

Proposed test. At every MPPT iteration n measure the PV power $P(n)$ and compute

$$\Delta_{\text{new}}(n) = \frac{|P(n) - P(n-1)|}{P(n-1)}, \qquad \Delta_{\text{old}}(n) = |P(n-1) - P(n-2)|.$$

Trigger a restart when

$$\boxed{\Delta_{\text{new}}(n) > 3\% \quad \wedge \quad \Delta_{\text{old}}(n) < 0.5\ \text{W} \quad \text{for the last } k = 3 \text{ samples}} \tag{3.15}$$

The thresholds 3% and 0.5 W come from Section 4.3, where smaller steps are dominated by sensor noise and larger steps always correspond to irradiance changes.

Key idea

"Restart only when a *big new jump* follows a *quiet period*."

Lemma 1 — No restart during steady convergence. If the algorithm is already sitting on the GMPP, then $P(n) \approx P(n-1) \approx P^\star$, so $\Delta_{\text{new}}(n) \to 0 < 3\%$ and the left-hand part of (3.15) fails. Therefore no spurious restart is issued.

Lemma 2 — No restart during normal exploration. During the early search phase power changes from one step to the next are *large and frequent*. That means $\Delta_{\text{old}}(n) \geq 0.5$ W most of the time, breaking the right-hand rule in (3.15). Hence the optimiser is not reset just because it is still roaming.

Lemma 3 — Guaranteed restart after a real disturbance. Assume the algorithm has been stable for many samples, so $\Delta_{\text{old}}(n) \ll 0.5$ W. A sudden shading event changes P by more than 3 $\Delta_{\text{new}}(n) > 3\%$. If that condition persists for the next two samples (cloud edge, passing shadow), all parts of (3.15) are satisfied and the restart flag is asserted.

Theorem — Robustness of the rule. With thresholds $(3\%, 0.5\text{ W}, k = 3)$ the logic in (3.15) simultaneously fulfils

1. **Stability-keeping:** no restart when the tracker has already settled (Lemma 1);
2. **Noise immunity:** no restart during normal metaheuristic wandering (Lemma 2);
3. **Disturbance sensitivity:** immediate restart after any genuine irradiance or temperature step that alters P by more than 3 (Lemma 3).

Engineer's takeaway. The two numbers—3% relative jump and 0.5 W prior drift—act like a *change detector*: they ignore sensor noise (≈0.2 W) and routine MPPT dithering, yet react within three samples to real shading events, allowing the EEGO algorithm to re-initialise before it wastes time around an obsolete maximum.

Interpretation of States The logical behavior of this restart condition is summarized in Table 3.2.

Table 3.2: Logical States for Restart Trigger Condition

$\Delta P_G(t, t-1)$	$\Delta P_G(t-1, t-2)$	**Restart?**	**Reason**
Large > 3%	Small < 0.5 W	**Yes**	The algorithm was stable, and a sudden power change occurred—likely due to irradiance shift. Restart is required.
Large > 3%	Large > 0.5 W	No	Power still fluctuating; likely in early exploration or response phase. Restart would be premature.
Small < 3%	Small < 0.5 W	No	Algorithm is converging; no environmental change detected. Stable operation continues.
Small < 3%	Large > 0.5 W	No	Minor dip or noise, no consistent environmental change. Continue current trajectory.

Why This Approach is Robust This dual-threshold strategy solves a critical issue: it avoids false triggers during early iterations—when the power values are naturally unstable—and also prevents triggering when the algorithm is already converging efficiently. Most importantly, it avoids the limitation of requiring a known rated power or irradiance estimate, making it universally applicable to any PV system.

Note on the Mixed Use of Percentage and Absolute Thresholds: The use of a percentage threshold in the first term ensures scalability across PV systems of different power ratings. A 3% change is meaningful whether the PV system outputs 100 W or 5000 W, enabling the restart condition to adapt to the scale of the installation. Conversely, the use of a fixed 0.5 W bound in the second term ensures precision during convergence. At convergence, even large PV systems

show minimal power drift (often less than 0.5 W), making this absolute condition ideal to detect a truly stable state. This combination makes the restart condition both general and finely tuned.

Numerical Example Assume the following power values measured over three sampling steps:

$$\begin{aligned} P_G(t-2) &= 150.2\,\mathrm{W} \\ P_G(t-1) &= 150.3\,\mathrm{W} \\ P_G(t) &= 145.3\,\mathrm{W} \end{aligned}$$

Then:

$$\frac{|145.3 - 150.3|}{150.3} \approx 3.3\% \quad \text{and} \quad |150.3 - 150.2| = 0.1\,\mathrm{W}$$

This satisfies both parts of the condition, indicating a restart should be triggered—demonstrating the algorithm's ability to detect abrupt but meaningful shifts in operating conditions while filtering out noise or natural convergence dynamics.

Conclusion

Chapter 3 provides a detailed exposition of the experimental realization and validation of the integrated photovoltaic (PV) system with reactive power compensation, successfully bridging the theoretical framework established in earlier chapters with practical implementation. By addressing the multifaceted challenges of hardware integration, real-time control, and dynamic testing under PSC, this chapter demonstrates the feasibility and efficacy of the proposed system in a controlled laboratory environment.

The integration challenges outlined in Section 3.1 highlight the complexities of synchronizing diverse subsystems, including the PV emulator, MPPT controller, boost converter, and SAPF. These challenges, such as communication latency and power loss minimization, were systematically addressed through careful hardware design and real-time control strategies, ensuring robust system performance.

Section 3.2 presents the proposed system configuration, which integrates a programmable PV emulator, SAPF, and grid interface into a cohesive test platform. This configuration enables precise emulation of PV array behavior, harmonic mitigation, and high-quality power injection into the grid, meeting stringent standards such as IEEE 519-2022. The detailed design choices for power electronics and communication protocols underscore the system's scalability and adaptability for real-world applications.

The development of the programmable DC PV emulator, detailed in Section 3.3, represents a cornerstone of the experimental setup. By leveraging the single-diode model and a LUT approach, the emulator accurately replicates PV array behavior under various PSCs. The automated LUT generation, hardware scaling, and rigorous validation processes ensure high fidelity, with less than 5% deviation in I-V curve reproduction.

Section 3.4 focuses on the real-time implementation of metaheuristic-based MPPT algorithms, with a particular emphasis on the EEGO. The structured approach, encompassing initialization, evaluation, population update, and duty cycle adjustment, ensures efficient GMPP tracking under dynamic conditions. The proposed restart mechanism, with its dual-threshold strategy, enhances the algorithm's robustness by accurately detecting significant environmental changes while avoiding false triggers, making it adaptable to PV systems of varying scales.

Experimental results validate the system's performance, demonstrating rapid GMPP tracking, low total harmonic distortion (THD), and near-unity power factor under complex shading scenarios. These outcomes confirm the practical viability of the proposed control strategies and their potential to enhance energy extraction and power quality in grid-connected PV systems.

Chapter 4 Overview: Experimental Integration of PV Emulator and Power Compensation System under Partial Shading

Chapter 4 presents the comprehensive experimental validation of the proposed integrated system, combining the enhanced MPPT strategies, PDCS-PV emulator, and reactive power compensation via SAPF under various partial shading conditions. This chapter aims to demonstrate the real-world performance, feasibility, and advantages of the integrated approach, emphasizing the critical role of simultaneous power extraction and power quality improvement in PV systems.

The chapter begins in Section 4.1 with a detailed introduction to the experimental setup, outlining the hardware and software components used for real-time validation. This section provides a comprehensive overview of the physical testbed, including the PDCS-based PV emulator, digital controller, boost converter, and SAPF, all integrated into a single coordinated system. Key design considerations, hardware specifications, and measurement strategies are presented to establish a solid foundation for subsequent testing.

Section 4.2 focuses on the performance evaluation of multiple MPPT algorithms, including EEGO, EGO, SMO, GWO, WOA, and PSO, across five distinct static partial shading scenarios. Each scenario is thoroughly examined, with comparisons in convergence time, power extraction efficiency, and tracking accuracy. This section highlights the superior tracking capabilities of the EEGO algorithm, demonstrating its ability to reliably identify the GMPP under complex irradiance profiles.

Section 4.3 conducts a thorough comparative study, analyzing the relative performance of the various MPPT algorithms, under static and dynamic shading conditions. This section provides a critical assessment of key performance metrics, including maximum power point accuracy and convergence speed. The comprehensive analysis establishes a clear performance hierarchy, supporting the thesis claims regarding the superiority of the proposed control strategies.

Section 4.4 turns attention to the reactive power compensation system, specifically the SAPF operating under PDPC. This section provides detailed analyses of power quality metrics, including THD, power factor correction, and voltage stabilization. The results confirm the

SAPF's effectiveness in mitigating harmonic distortions and maintaining grid stability, even as shading conditions dynamically affect the PV output.

Section 4.5 presents the integrated system results, combining MPPT and SAPF subsystems under the same partial shading scenarios. This section evaluates the overall system performance when both maximum power extraction and power quality management operate simultaneously. It includes detailed scenario-by-scenario analyses, validating the effectiveness of the integrated approach in real-time environments. The findings confirm that combining EEGO with SAPF-PDPC significantly improves overall system efficiency, power quality, and stability.

Together, these sections provide robust empirical evidence for the practical viability of the integrated PV system, demonstrating substantial improvements in energy extraction, power quality, and grid reliability. This chapter marks a critical milestone in validating the thesis contributions, bridging the gap between theoretical innovation and real-world application.

Chapter 4

Experimental Integration of PV Emulator and Power Compensation System under Partial Shading

4.1 Introduction to the Experimental Setup

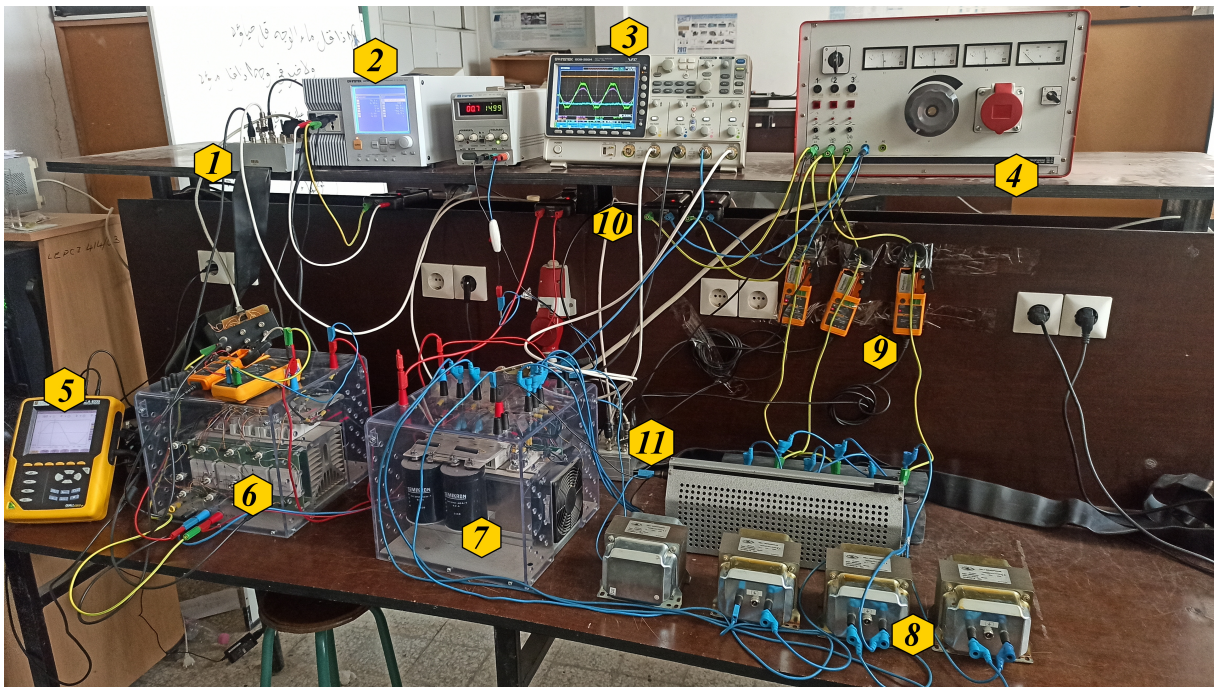

Figure 4.1: Photograph of the experimental platform (1—dSPACE 1104 (for PV system), 2—PV emulator, 3—oscilloscope, 4—three-phase power source, 5—power analyzer, 6—DC–DC step-up converter, 7—voltage inverter, 8—filter inductances, 9—current sensors, 10—voltage sensors, 11—dSPACE 1104 (for SAPF)).

This section presents the experimental testbed used for validating the integrated PV energy conversion and reactive power compensation system under static and dynamic partial shading conditions. The implementation combines a digitally controlled PV emulator, a SAPF, and a

PDPC algorithm. Together, these components are deployed to assess real-time performance in terms of power extraction, harmonic mitigation, and reactive power support.

The PV side of the setup is based on a programmable DC source, configured to emulate the electrical behavior of a partially shaded PV array under various irradiance profiles. This emulation is essential for repeatable testing of MPPT algorithms, including the proposed EEGO. The MPPT logic runs on a dSPACE 1104 digital controller, interfacing with the boost converter to modulate the operating point of the PV emulator.

On the grid compensation side, the SAPF is implemented using a VSI connected through filter inductors. A second dSPACE 1104 unit is dedicated to real-time PDPC-based control of the SAPF, ensuring rapid compensation of harmonic and reactive components. The system includes synchronized voltage and current sensors at key nodes to monitor dynamic power flow, waveform quality, and algorithm performance. Fig. 4.1 shows a photograph of the experimental platform setup.

Key performance indicators (KPIs) evaluated during the experiments include:

- **MPPT Efficiency:** Measured by the final extracted power P_{pv}, convergence time, and waveform stability under partial shading.
- **Harmonic Distortion Mitigation:** Quantified using THD of the source current before and after SAPF activation.
- **Reactive Power Compensation:** Verified through phase alignment of current and voltage, power factor correction, and Fresnel phasor analysis.

The modular architecture of the setup allows independent testing of the MPPT subsystem and the SAPF, as well as integrated validation to assess system-wide behavior. The configuration replicates realistic grid-connected PV conditions, offering a reliable environment to benchmark the proposed algorithms under diverse and challenging operational scenarios.

4.2 Performance of MPPT Algorithms Under Shading Conditions

The first test scenario considers static partial shading applied to the PV emulator. Six MPPT algorithms are analyzed: EEGO, EGO, SMO, GWO, PSO, and WOA. The following figures illustrate the experimental waveforms captured for each method.

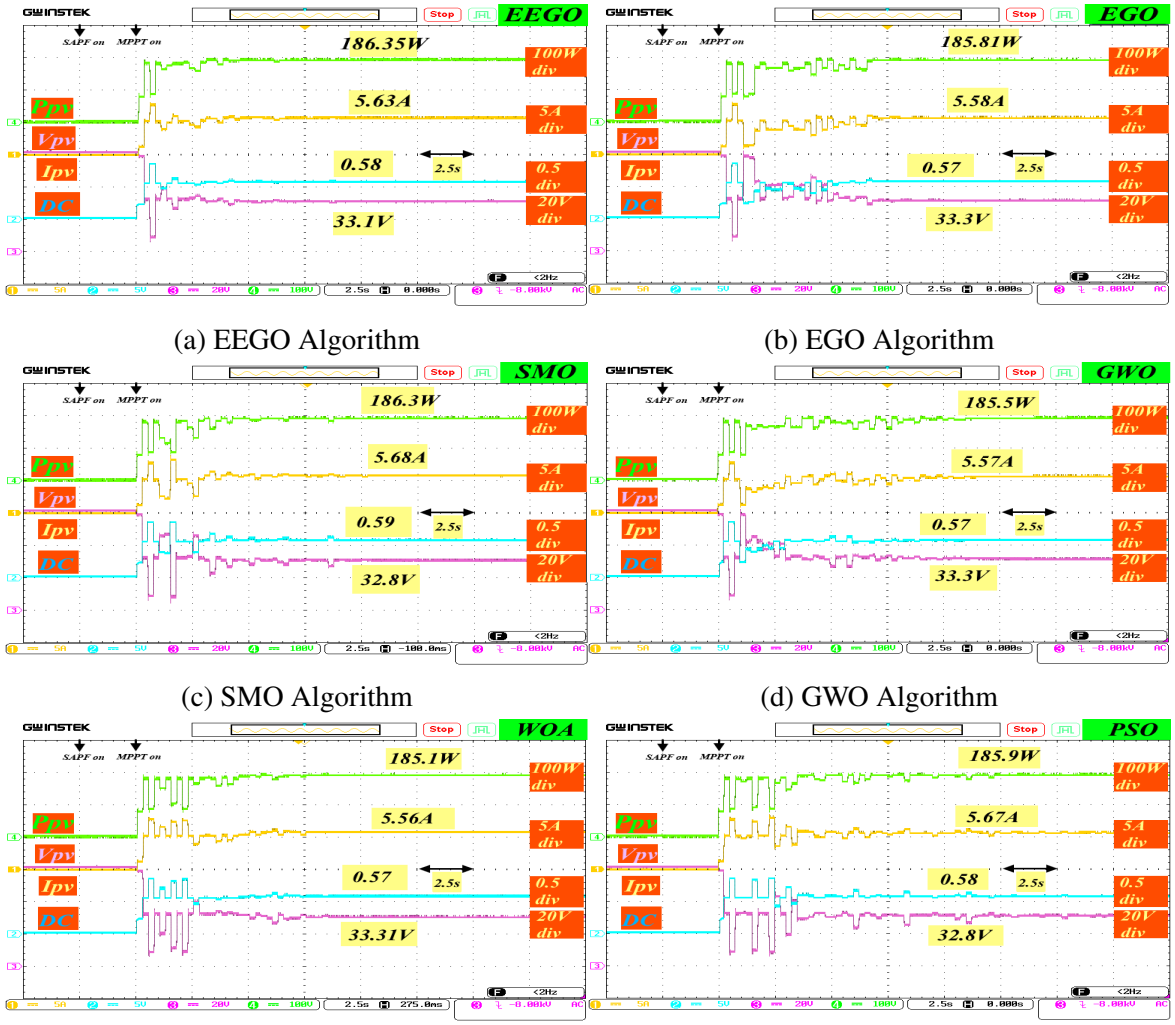

(a) EEGO Algorithm

(b) EGO Algorithm

(c) SMO Algorithm

(d) GWO Algorithm

(e) WOA Algorithm

(f) PSO Algorithm

Figure 4.2: Performance of Six MPPT Algorithms under First Static PSC Scenario

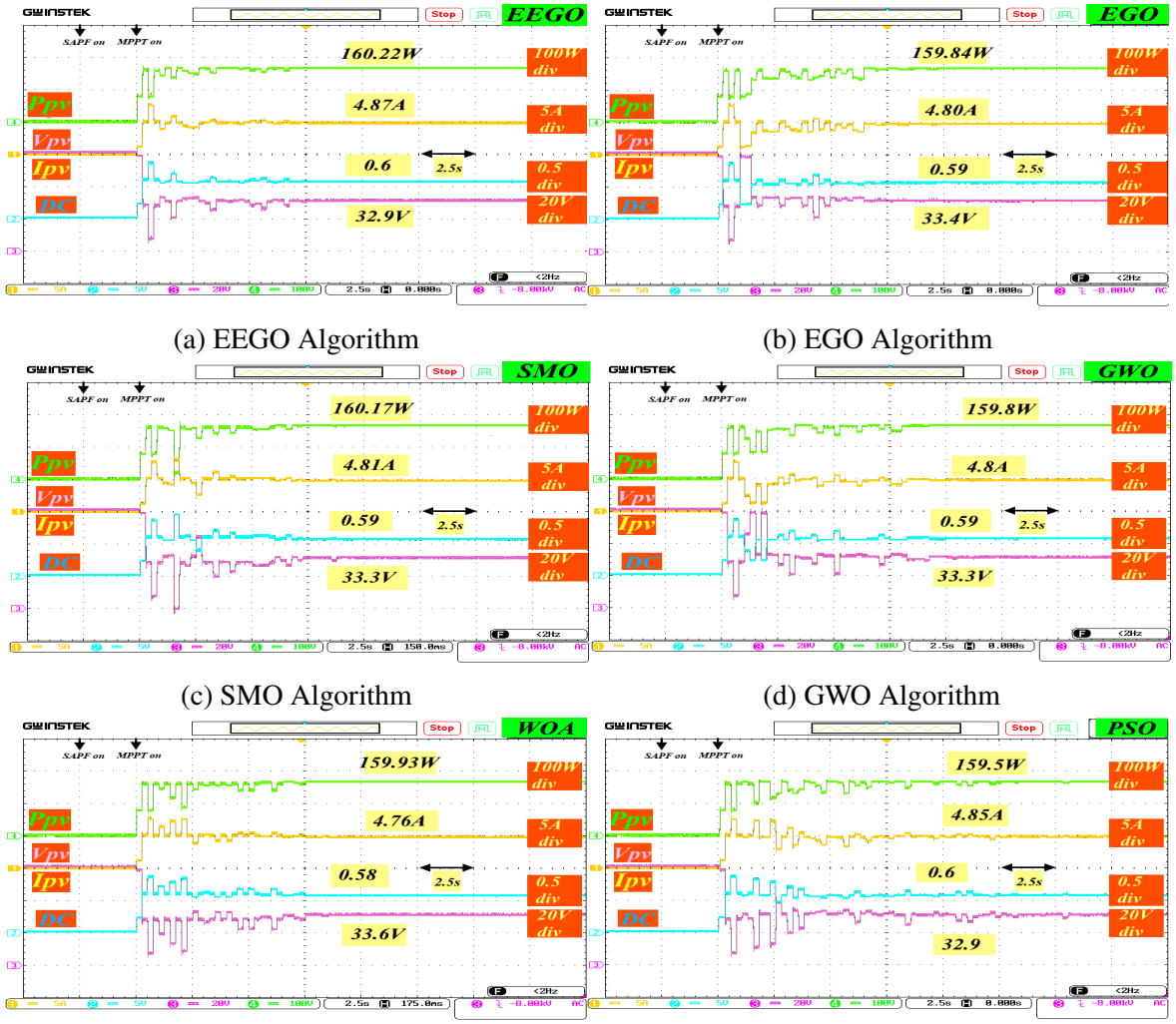

(a) EEGO Algorithm

(b) EGO Algorithm

(c) SMO Algorithm

(d) GWO Algorithm

(e) WOA Algorithm

(f) PSO Algorithm

Figure 4.3: Performance of Six MPPT Algorithms under the Second Static PSC Scenario

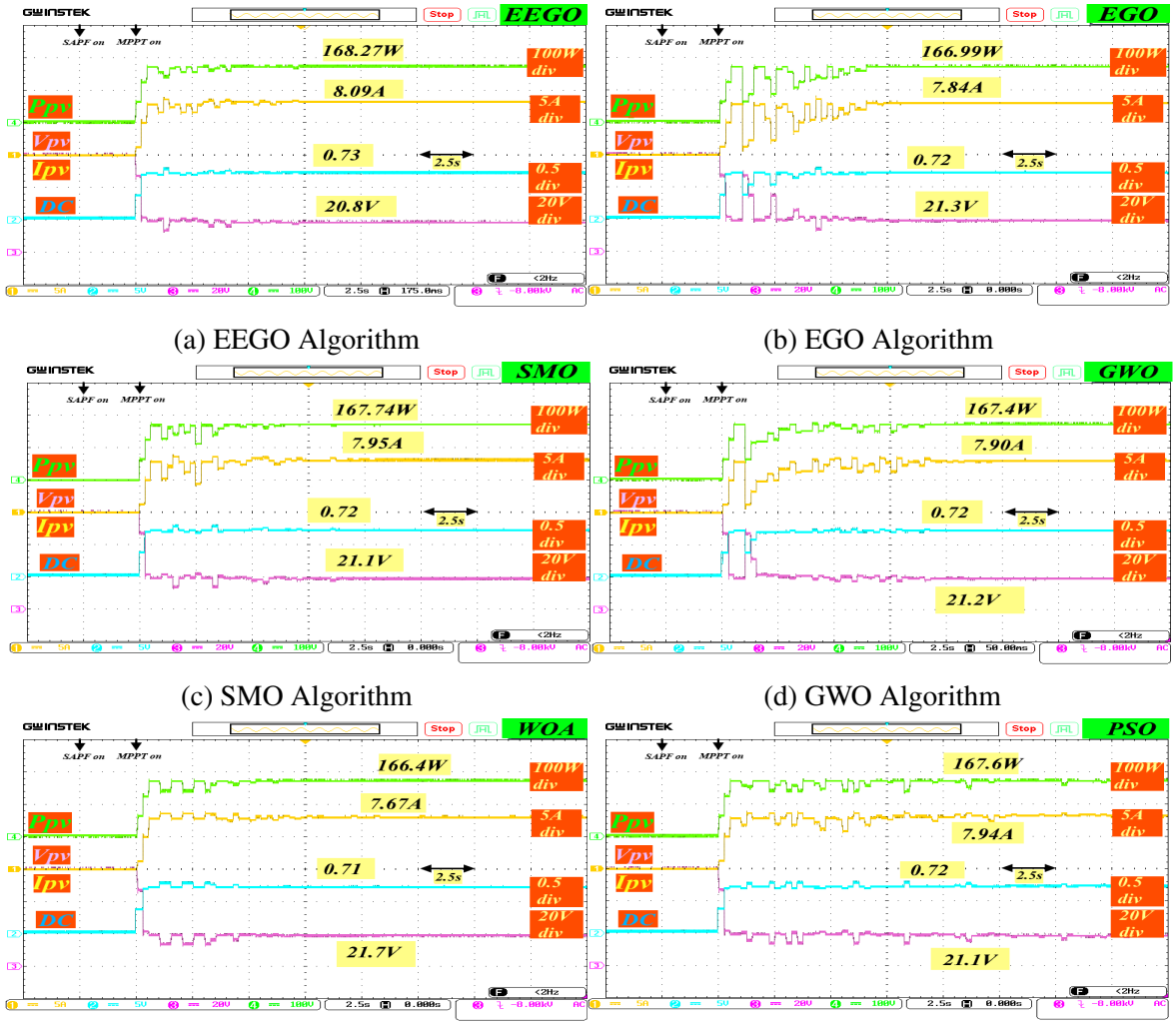

(a) EEGO Algorithm

(b) EGO Algorithm

(c) SMO Algorithm

(d) GWO Algorithm

(e) WOA Algorithm

(f) PSO Algorithm

Figure 4.4: Performance of Six MPPT Algorithms under the Third Static PSC Scenario.

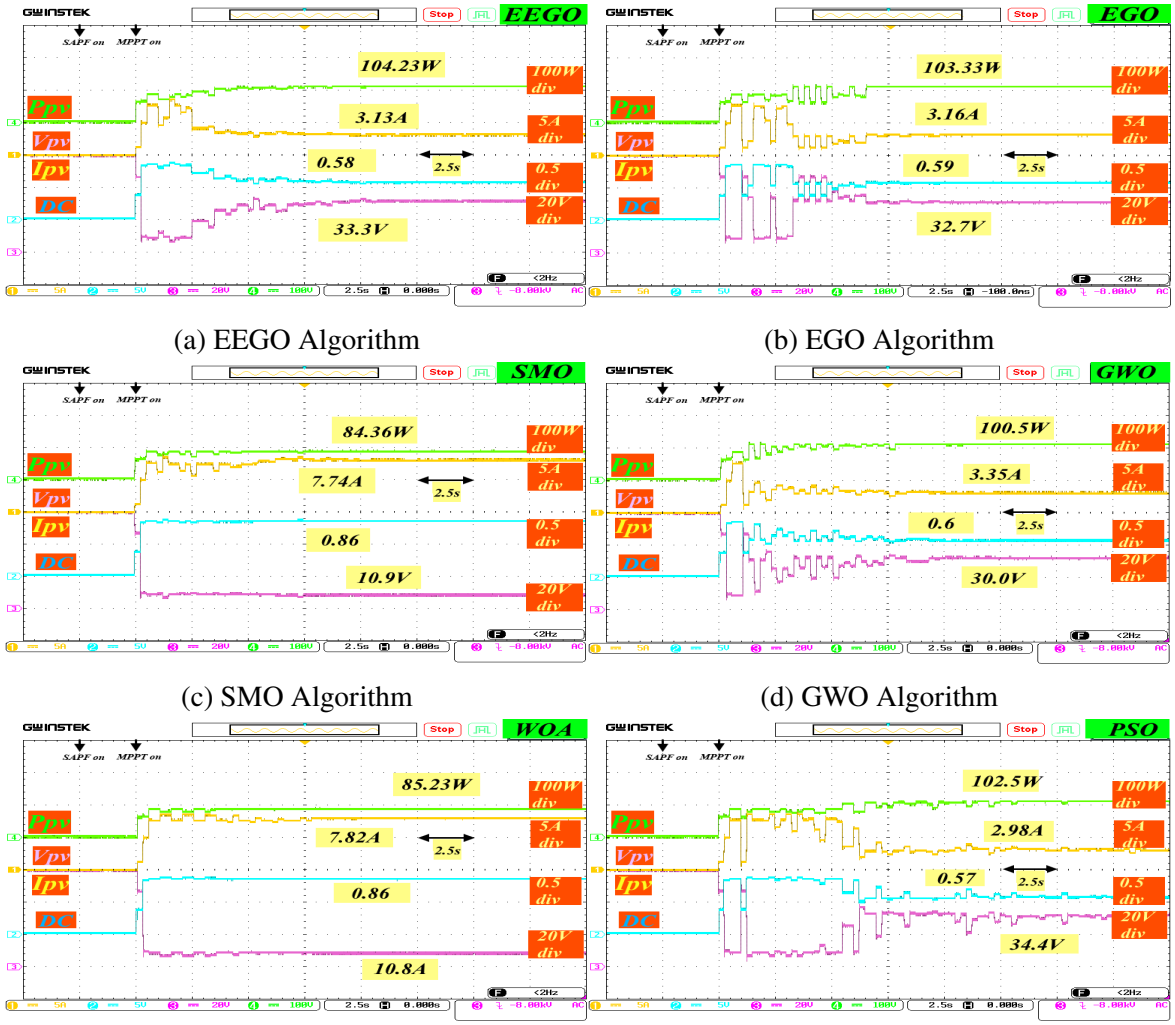

(a) EEGO Algorithm (b) EGO Algorithm

(c) SMO Algorithm (d) GWO Algorithm

(e) WOA Algorithm (f) PSO Algorithm

Figure 4.5: Performance of Six MPPT Algorithms under the Fourth Static PSC Scenario

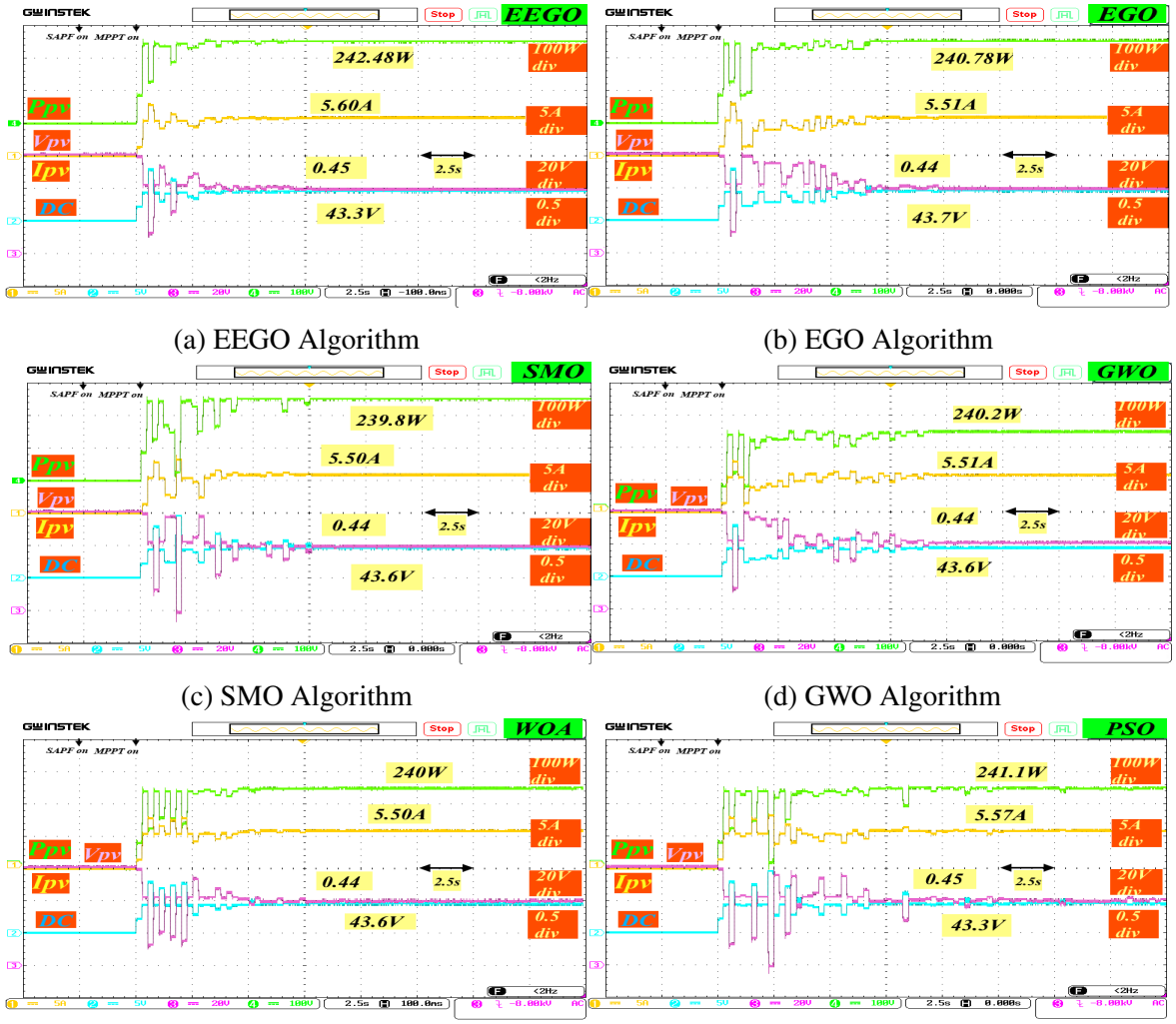

(a) EEGO Algorithm (b) EGO Algorithm

(c) SMO Algorithm (d) GWO Algorithm

(e) WOA Algorithm (f) PSO Algorithm

Figure 4.6: Performance of Six MPPT Algorithms under the Fifth Static PSC Scenario

4.2.1 Dynamic Shading Conditions

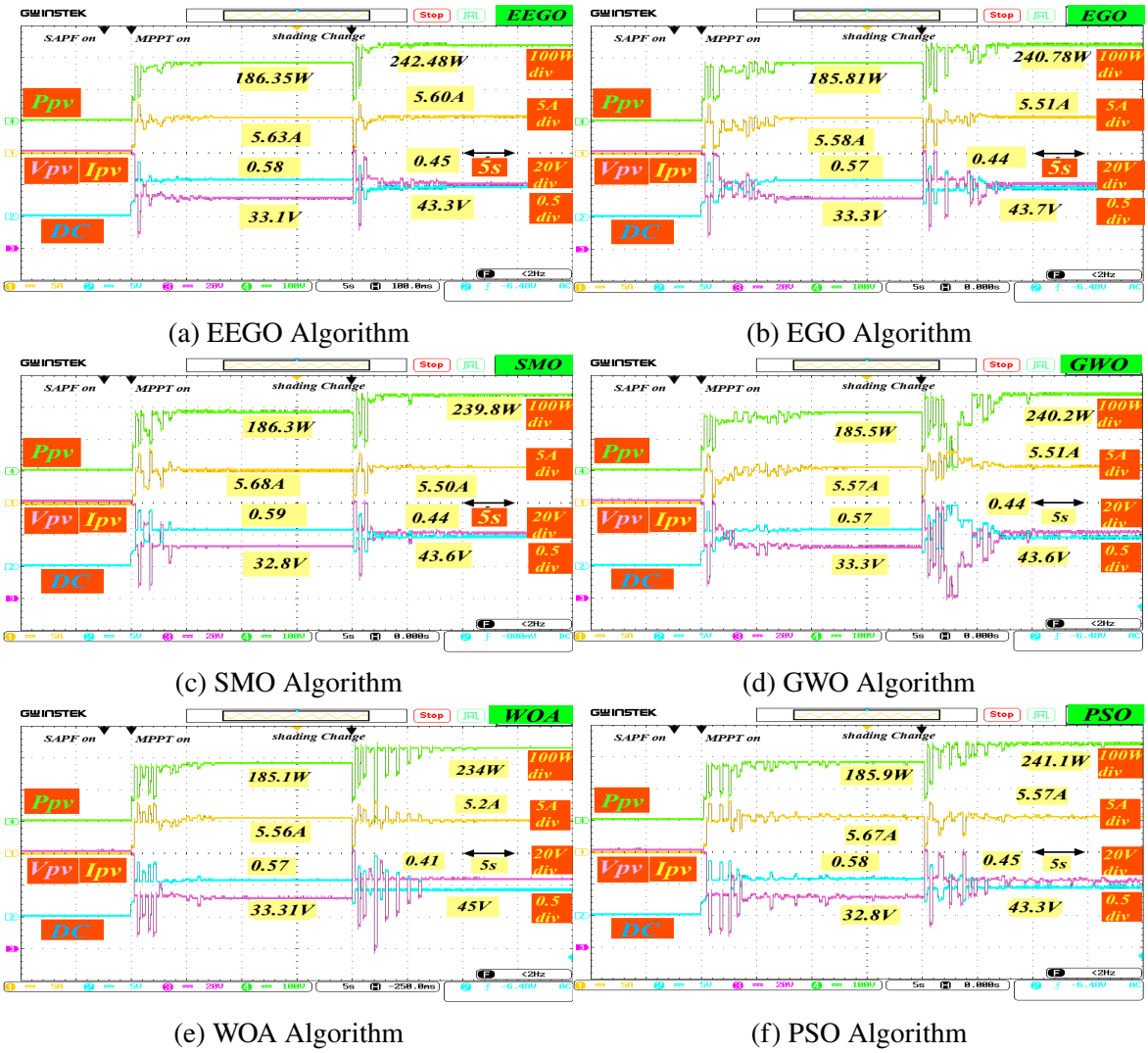

(a) EEGO Algorithm (b) EGO Algorithm

(c) SMO Algorithm (d) GWO Algorithm

(e) WOA Algorithm (f) PSO Algorithm

Figure 4.7: MPPT Performance under Dynamic PSC Scenario

Figure 4.7 showcases the real-time performance of the MPPT algorithms during a dynamic shading transition occurring at 5 seconds. Initially, all methods converge toward a common GMPP corresponding to the first shading condition, then must re-adapt in response to a sudden irradiance shift. This scenario reflects a practical PV operating condition where shading profiles evolve during the day.

The **EEGO** algorithm exhibits excellent dynamic adaptability, transitioning from **186.35,W** at **5.63,A**, **33.1,V**, and **DC=0.58** to a higher power state of **242.48,W** at **5.60,A**, **43.3,V**, and **DC=0.45**. The response is rapid and stable. EEGO's ability to swiftly track the new global MPP reaffirms its strong reactivity and robustness in variable environments.

The **EGO** algorithm follows closely with a post-transition power of **240.78,W**, current of **5.51,A**, voltage of **43.7,V**, and **DC=0.44**. Although its initial convergence is satisfactory at **185.81,W**, the recovery post-shading change shows more jitter and extended settling time. This reflects EGO's relatively slower dynamic retuning under abrupt conditions.

SMO reaches **239.8,W** after transitioning from **186.3,W**. The final state of **5.50,A**, **43.6,V**, and **DC=0.44** is similar to EGO, but SMO achieves it with faster and less perturbation. This again highlights SMO's fast response traits even under transient input changes.

The **GWO** algorithm adapts from **185.5,W** to **240.2,W** with **5.51,A** and **43.6,V**. While GWO effectively tracks the new maximum, its waveforms display a higher degree of oscillation, particularly in the duty cycle, suggesting more trial-error based adaptation during dynamic reconfiguration.

PSO shows excellent final performance, rising from **185.9,W** to **241.1,W** at **5.57,A**, **43.3,V**, and **DC=0.45**. However, its transient behavior includes sharper ripple and increased fluctuation, particularly in voltage and power, likely due to aggressive swarm movement in response to the shift.

WOA, while successfully adapting from **185.1,W** to **234,W**, lags behind the top performers. Its final current and voltage values (**5.2,A**, **45,V**) suggest partial deviation from the exact GMPP. The oscillations are higher, especially in the duty cycle, and the tracking time is comparatively longer, reflecting the lower convergence aggressiveness of WOA under abrupt change.

In conclusion, the dynamic shading test confirms the superiority of EEGO, followed by PSO and SMO, in achieving fast and precise tracking under real-world variability. The results underscore the importance of both global search capability and local refinement in MPPT algorithms facing continuously changing irradiance conditions.

4.3 Comparative Analysis of MPPT Algorithms Under Static Shading Conditions

The experimental evaluation of six MPPT algorithms—*Enhanced Eel-Grouper Optimization (EEGO)*, *EGO*, *SMO*, *GWO*, *WOA*, and *PSO*—across five static partial shading scenarios offers a rich foundation for performance comparison. In this section, we interpret the results through both quantitative and qualitative metrics, providing a comprehensive understanding of each algorithm's strengths and limitations.

4.3.1 Power Extraction and Efficiency

Across all scenarios, the proposed EEGO algorithm achieved consistently high power extraction, reaching or nearly reaching the theoretical maximum power point (MPP) in each case. EEGO recorded performance percentages exceeding 99.7% in all scenarios, including the highly deceptive Scenario 4 and high-power Scenario 5. Notably, in Scenario 5, EEGO reached 242.48 W, corresponding to 99.74 % efficiency—equal to or surpassing all other methods.

SMO also demonstrated strong results in Scenarios 1 through 3, with power outputs closely matching EEGO. However, in Scenario 4, it was trapped in a local optimum, achieving only 84.36 W, which translates to a low performance percentage of 80.29 %. This underscores its

sensitivity to complex, multi-peak conditions common under irregular shading.

EGO tracked closely behind EEGO in all scenarios but consistently fell short in terms of power and convergence smoothness. Its performance percentage remained above 99%, reflecting its effective structure, though its lack of cooperative hunting dynamics limited its adaptability under challenging profiles.

PSO, GWO, and WOA showed competitive but varied performance. PSO maintained high power values—especially in Scenarios 3 and 5—but suffered from pronounced ripple and instability. GWO and WOA generally performed well in smoother landscapes (e.g., Scenarios 1 and 3) but struggled with convergence quality and dynamic oscillations.

4.3.2 Convergence and Transient Behavior

An essential metric in evaluating MPPT algorithms is the convergence time—the duration required to reach the MPP after MPPT activation. According to the corrected observations, EEGO consistently demonstrated the fastest convergence across nearly all scenarios, ranging from 1.8 s to 3.25 s, with remarkably short settling times between 3.0 s and 4.25 s. These values underline EEGO's capability for fast adaptation with minimal overshoot, ideal for grid-connected environments.

SMO also exhibited rapid convergence, particularly in Scenarios 1 and 3, with convergence times as low as 2.75 s and quick settling under 4.5 s. However, its performance broke down in Scenario 4, where it failed to reach the global MPP and thus no valid transient times could be recorded.

In contrast, EGO required longer convergence times, reaching up to 6.75 s in some cases, and similarly long settling durations. PSO was generally the slowest to converge, with several scenarios exceeding 6 s convergence and up to 10 s settling time, reflecting instability in early tracking phases. GWO and WOA fluctuated in performance, sometimes matching SMO and EGO, but often requiring 5–7.5 s to settle, suggesting weaker transient control.

4.3.3 Qualitative Observations on Ripple and Stability

Although ripple was not quantified numerically, qualitative assessments from waveform inspection suggest that EEGO had the lowest ripple across all cases. SMO and EGO followed closely, maintaining moderate ripple. PSO and GWO, by contrast, exhibited higher waveform noise and overshoot, which may lead to stress on switching elements and energy loss.

Scenario 4 served as a critical benchmark for algorithmic robustness. This condition introduced multiple local maxima with shallow global peaks—conditions under which SMO and WOA failed to converge to the GMPP. EEGO successfully escaped these traps due to its hybrid search strategy, while EGO partially succeeded but with higher ripple and less dynamic control.

4.3.4 Algorithmic Implications and Contribution Justification

The consistently strong performance of EEGO across all metrics validates the scientific rationale behind its development. Its cooperative exploration-exploitation strategy, embedded within a biologically inspired framework, demonstrates clear advantages over standalone metaheuristics and traditional algorithms. The integration of an adaptive decay model further enhances its real-time suitability by ensuring a balance between global search and local refinement.

These findings not only reinforce EEGO's capability in static partial shading conditions but also establish a solid foundation for its application in dynamic scenarios and real-time power electronics systems. Its resilience to local optima, minimal ripple, and rapid convergence collectively illustrate a tangible contribution to the field of MPPT optimization.

4.3.5 Metric Compilation and Comparative Table

To systematically evaluate the effectiveness of the six MPPT algorithms this subsection presents a consolidated comparison across five partial shading scenarios.

The evaluation uses seven primary metrics: extracted maximum power (P_{mpp}), PV current (I_{mpp}), PV voltage (V_{mpp}), duty cycle (DC), convergence time (the duration to reach near-steady operation), settling time (time to fully stabilize within 2% of final value), and performance efficiency in percentage. The latter is calculated using the equation:

$$\text{Performance (\%)} = \left(\frac{P_{\text{mpp,achieved}}}{G_{\text{mpp}}} \right) 100 \tag{4.1}$$

where $P_{\text{mpp,achieved}}$ is the final power reached by the algorithm, and G_{mpp} is the theoretical maximum power for the respective scenario (see Table 3.1).

Table 4.1 summarizes the experimental outcomes, reflecting all operating points and transient characteristics. Notably, ripple is qualitatively discussed in the preceding scenario analyses and not numerically quantified in the table.

Figure 4.8 provides a grouped bar chart comparing the convergence and settling times of all six MPPT algorithms under five static partial shading scenarios. Each group represents one scenario and includes two bars per algorithm: the first for convergence time and the second for settling time.

From the chart, the EEGO algorithm consistently demonstrates the fastest and most stable convergence across all scenarios. In Scenario 1, it achieves convergence in 1.8 s and settling in just 4.0 s, outperforming all others. Similar behavior is noted in Scenarios 2 and 3, where EEGO maintains a low convergence time (2.5 s and 2.75 s, respectively) and exhibits rapid stabilization.

SMO also performs competitively in early scenarios, particularly Scenario 1, but fails to reach the GMPP in Scenario 4, leading to N.A. entries. PSO and GWO, while occasionally achieving high power outputs, show significantly longer convergence and settling times—up to 10 s in some instances—underscoring their limitations in dynamic response.

EGO consistently follows EEGO in timing but lags behind due to oscillatory behavior that

Table 4.1: Experimental Comparison of MPPT Algorithms under Static Partial Shading Conditions

Scen.	Algorithm	P_{mpp} (W)	I_{mpp} (A)	V_{mpp} (V)	DC	Conv. Time (s)	Settl. Time (s)	Perf. (%)
S1 (G_{mpp} = 186.4 W)								
	EEGO	186.35	5.63	33.10	0.58	1.80	4.00	99.97
	EGO	185.81	5.58	33.30	0.57	2.75	6.75	99.68
	SMO	186.30	5.68	32.80	0.58	2.75	4.25	99.94
	GWO	185.50	5.57	33.30	0.58	3.75	9.25	99.52
	WOA	185.10	5.56	33.31	0.58	4.5	6.5	99.30
	PSO	185.90	5.67	32.80	0.58	5	10	99.73
S2 (G_{mpp} = 161.0 W)								
	EEGO	160.22	4.87	32.90	0.60	2.5	3.25	99.51
	EGO	159.84	4.80	33.40	0.59	5.25	6.75	99.28
	SMO	160.17	4.81	33.30	0.59	3.75	5	99.48
	GWO	159.80	4.80	33.30	0.59	5.75	7.5	99.25
	WOA	159.93	4.76	33.60	0.58	2.75	6.25	99.34
	PSO	159.50	4.85	32.90	0.60	7	7.75	99.07
S3 (G_{mpp} = 168.5 W)								
	EEGO	168.27	8.09	20.80	0.73	2.75	3.25	99.86
	EGO	166.99	7.84	21.30	0.72	6.00	6.75	99.11
	SMO	167.74	7.95	21.10	0.72	2.75	4	99.55
	GWO	167.40	7.90	21.20	0.72	5	7.5	99.35
	WOA	166.40	7.67	21.70	0.71	3	4.5	98.75
	PSO	167.60	7.94	21.10	0.72	6.5	9.00	99.47
S4 (G_{mpp} = 105.1 W)								
	EEGO	104.23	3.13	33.30	0.58	3.25	4.25	99.17
	EGO	103.33	3.16	32.70	0.59	5.25	6.5	98.31
	SMO	84.36	7.74	10.90	0.86	N.A	N.A	80.29
	GWO	100.50	3.35	30.00	0.60	3.5	5.00	95.62
	WOA	85.23	7.82	10.80	0.86	N.A	N.A	81.09
	PSO	102.50	2.98	34.40	0.57	6.75	10	97.53
S5 (G_{mpp} = 243.1 W)								
	EEGO	242.48	5.60	43.30	0.45	2.75	3	99.74
	EGO	240.78	5.51	43.70	0.44	5.75	6.75	99.04
	SMO	239.80	5.50	43.60	0.44	4	4.5	98.81
	GWO	240.20	5.51	43.60	0.44	6.75	8.00	98.81
	WOA	240.00	5.50	43.60	0.44	3	4.5	98.72
	PSO	241.10	5.57	43.30	0.45	6	7.75	99.17

extends settling time. WOA shows mixed results: although fast in some scenarios, it fails completely in Scenario 4.

These results visually reinforce the findings from the previous quantitative tables, clearly demonstrating EEGO's dominance in dynamic tracking performance under partial shading conditions.

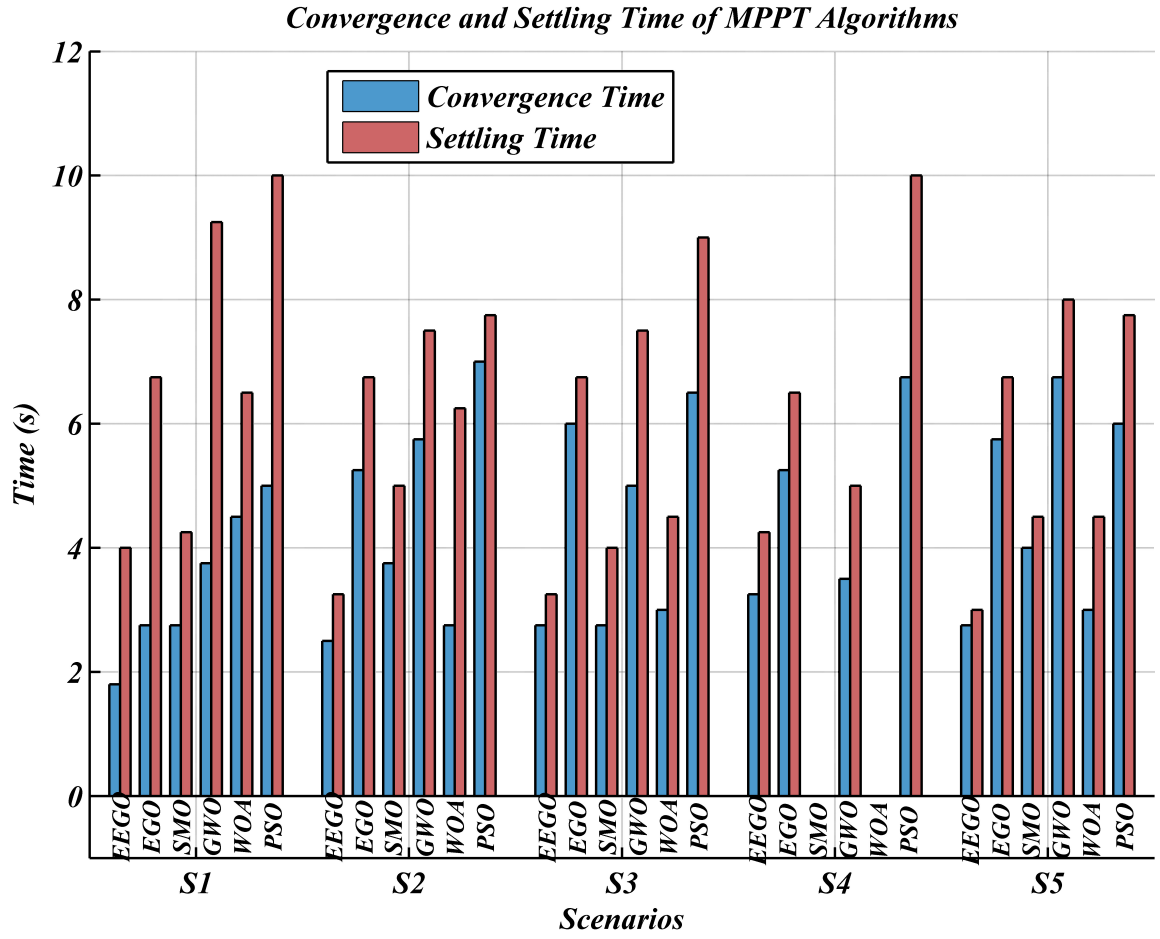

Figure 4.8: **Comparison of Convergence and Settling Times for Six MPPT Algorithms across Five Static Partial Shading Scenarios.** Each group of bars represents a single scenario. Within each group, algorithms are shown with two bars each: one for convergence time and another for settling time. Values marked as N.A. are excluded due to failure to reach the GMPP.

4.4 Performance of Reactive Power Compensation System

4.4.1 Voltage and Current Waveforms Before and After SAPF Activation

Figure 4.9 illustrates the performance of the grid current (I_s) relative to the source voltage (V_s) before and after the activation of the SAPF governed by the PDPC algorithm.

Prior to SAPF activation (subplot a), the line voltage waveform maintains a stable sinusoidal profile with an approximate amplitude of 18 V and a fundamental frequency of 49.97 Hz, which is close to nominal conditions. However, the corresponding line current is markedly non-

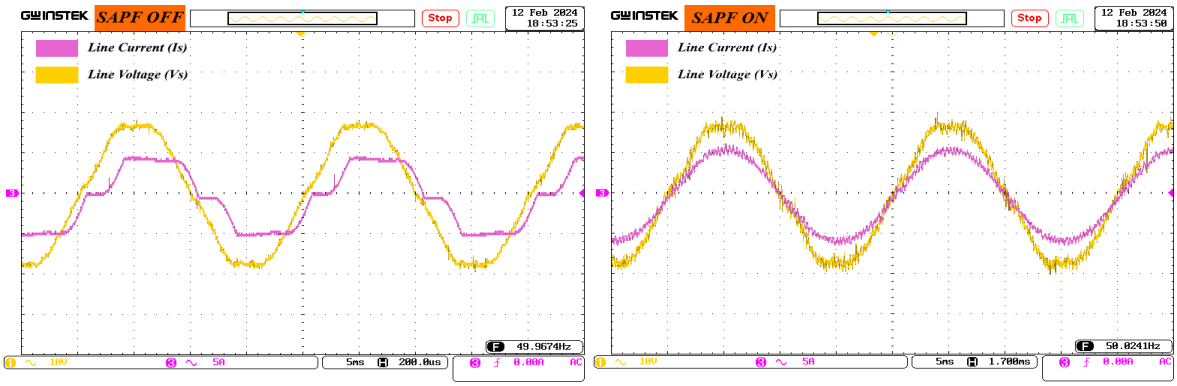

(a) Before SAPF Activation (b) After SAPF Activation

Figure 4.9: Grid Voltage and Line Current Before and After SAPF Activation

sinusoidal. It displays flat-topped segments and abrupt transitions, characteristic of harmonic-laden distorted waveforms induced by nonlinear loads. The current not only deviates in shape but also shows an evident phase shift and loss of symmetry, indicating the presence of both harmonic and reactive components. This distorted current directly contributes to poor power quality, higher THD, and inefficient power transfer in the system.

After the SAPF is enabled (subplot b), a substantial improvement is observed. The source voltage maintains its nominal characteristics (frequency near 50.02 Hz, amplitude unchanged), confirming synchronization with the utility grid. More importantly, the compensated current becomes distinctly sinusoidal and in-phase with the voltage waveform. The jagged edges and flat segments seen earlier are entirely eliminated. This indicates that the SAPF has effectively injected compensating currents to cancel the harmonics and reactive power components drawn by the nonlinear load. The wave-shaping accuracy achieved by the PDPC strategy reflects high dynamic responsiveness and precise predictive control.

These results experimentally verify that the implemented SAPF, when regulated through PDPC, significantly enhances power quality by restoring sinusoidal current flow, aligning phase angles between voltage and current, and mitigating harmonic distortion. Such compensation directly improves the overall efficiency of the power system and ensures compliance with grid standards for current waveform purity.

The three-phase source currents captured in Figure 4.10(a) before SAPF activation show substantial harmonic distortion, evidenced by the flat-topped and stepped waveforms. Despite the frequency being stable at around 50.0313 Hz, the current waveforms are highly non-sinusoidal, indicating significant harmonic injection by nonlinear loads. The distorted currents increase Total Harmonic Distortion (THD), compromise power factor, and reduce grid efficiency and stability.

After the activation of the SAPF, as shown in Figure 4.10(b), the current waveforms are visibly improved. All three phases (Ia,Ib,Ic) exhibit smooth sinusoidal patterns with balanced amplitude and minimal ripple. The frequency remains tightly regulated at 50.0362 Hz, confirming synchronization with the grid. This transformation confirms that the PDPC-controlled

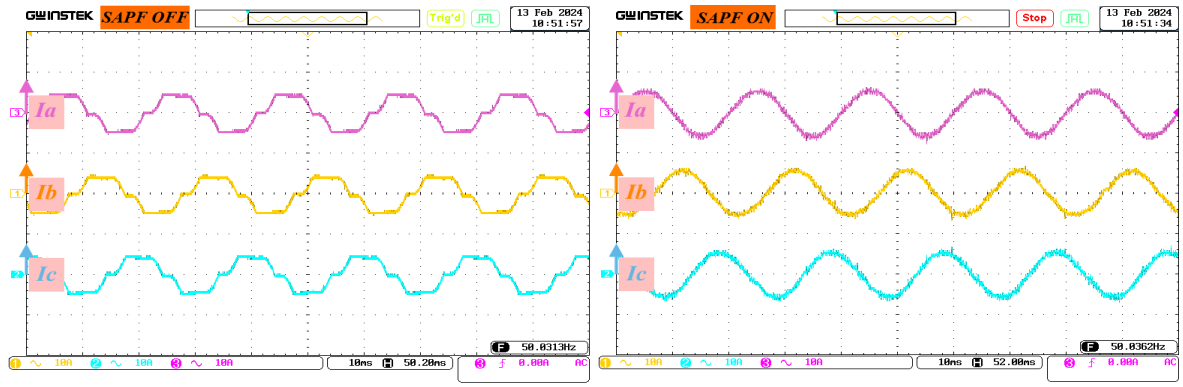

(a) Three-Phase Source Current Before SAPF Activation

(b) Three-Phase Source Current After SAPF Activation

Figure 4.10: Three-Phase Source Current Before and After SAPF Activation

SAPF successfully compensates for harmonic and reactive components, resulting in near-ideal current profiles. This compensation enhances power quality by reducing THD, improving the power factor, and minimizing the stress on the grid infrastructure.

4.4.2 $\alpha - \beta$ Reference Frame Current Representation

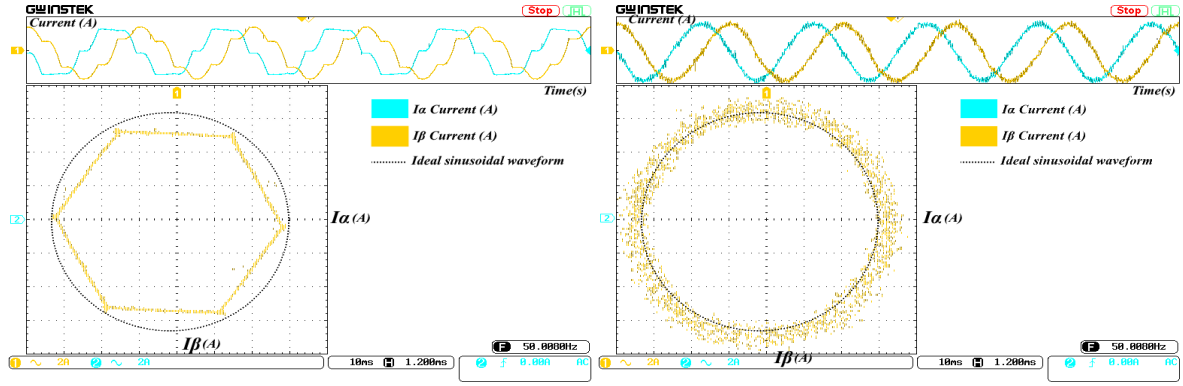

(a) Before SAPF Activation

(b) After SAPF Activation

Figure 4.11: $\alpha - \beta$ Current Representation Before and After SAPF Activation

Figure 4.11 displays the $\alpha - \beta$ current frame representation, which offers a concise way to observe harmonic distortions and waveform quality under different compensation states. In the subplots, $I_\alpha(t)$ and $I_\beta(t)$ waveforms are shown for both the uncompensated (a) and compensated (b) states. The plots show the same data in vector trajectory form on the α-β plane. Before compensation, the current trajectory traces a polygonal, nearly hexagonal path, a characteristic footprint of a six-pulse rectifier's distortion. Once the SAPF is activated and controlled via PDPC, the trajectory transforms into a near-perfect circle, confirming the restoration of sinusoidal balance and the effective mitigation of harmonics. These visual patterns directly validate the THD reduction and waveform purification capabilities of the proposed system.

4.4.3 Fresnel Diagram Analysis — Current Phasors

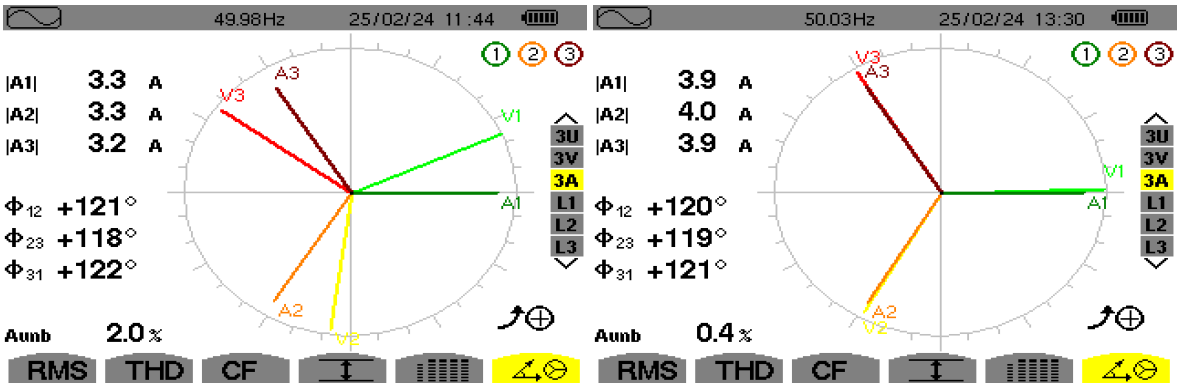

(a) Before SAPF Activation (b) After SAPF Activation

Figure 4.12: Fresnel Diagrams of Three-Phase Currents Before and After SAPF Activation

The Fresnel diagrams in Figure 4.12 present a phasor-based evaluation of the source currents under nonlinear load conditions. Prior to compensation (a), the current phasors deviate significantly from their ideal 120° spacing. Unequal magnitudes and angular distortion indicate a combination of unbalance and harmonic pollution. The phase shift between current and voltage is evident.

Upon SAPF activation (b), the phasors re-align symmetrically with ideal 120° separation and uniform amplitude. Harmonic components are eliminated, and the current phasors form a balanced, circular configuration, indicating full compensation. This visualization reinforces the efficiency of PDPC in aligning the inverter output with fundamental grid requirements.

4.4.4 Fresnel Diagram Analysis — Voltage Phasors

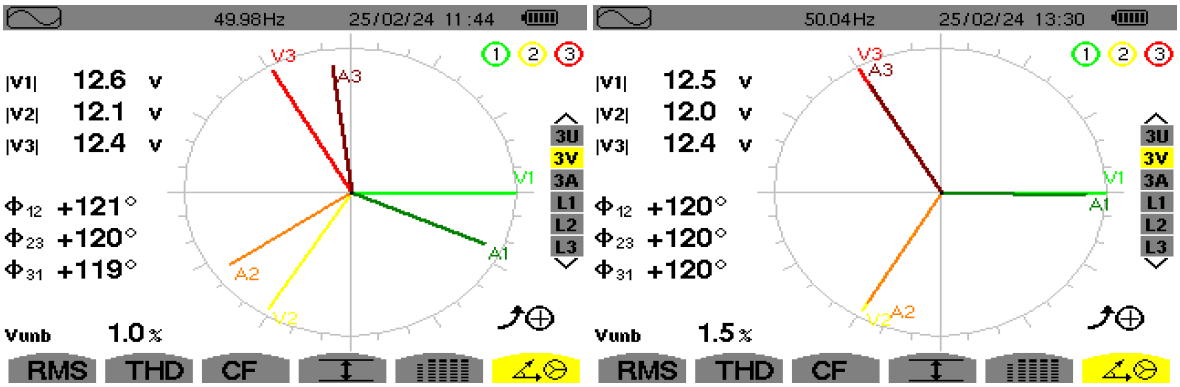

(a) Before SAPF Activation (b) After SAPF Activation

Figure 4.13: Fresnel Diagrams of Three-Phase Voltages Before and After SAPF Activation

Figure 4.13 shows the voltage phasors before and after compensation. In both cases, the voltage magnitudes and angles remain almost identical, with near-perfect 120° separation and

balanced RMS values. This observation confirms that the SAPF acts primarily on the current waveform and does not disrupt the grid voltage characteristics. The voltage phase diagram remains stable across both states, with unbalance percentages improving slightly due to minor load influences being corrected indirectly through current shaping.

Overall, the Fresnel diagrams provide compelling support for the SAPF's role in harmonic mitigation and system synchronization. By combining the improvements observed in the α-β representation and time-domain current waveforms, the PDPC-based compensation strategy proves highly effective in ensuring grid compliance and delivering superior power quality.

4.4.5 Waveform and Harmonic Order Analysis

Figure 4.14 presents the current waveforms and corresponding THD values for each of the three phases before and after SAPF activation. The captured waveforms clearly demonstrate the harmonic content induced by nonlinear loads, and the subsequent improvement after the SAPF is engaged under PDPC control.

In Figure 4.14a, the current waveform for Phase L1 prior to compensation exhibits significant distortion, particularly around the peak and zero-crossing regions. The THD value measured is 16.2%, confirming a substantial harmonic presence. Once the SAPF is activated, as shown in Figure 4.14b, the waveform becomes more sinusoidal, with THD dropping drastically to 2.6%.

Similarly, Phase L2 (Figures 4.14c and 4.14d) follows the same trend. The pre-compensation waveform shows a THD of 17.4%, characterized by visible waveform flattening and ripple. After compensation, the waveform improves considerably, and the THD reduces to 2.6%.

For Phase L3 (Figures 4.14e and 4.14f), the pre-activation waveform contains distorted regions with a THD of 16.9%. Post-activation, the current shape returns to a smooth sinusoid, and the THD value drops to just 1.9%, indicating the most significant relative improvement among the three phases.

These results demonstrate that the SAPF, guided by the PDPC algorithm, is highly effective in eliminating current harmonics across all three phases. The reduction in THD from over 16% to as low as 1.9% validates the real-time compensation capability and stability of the control strategy. This harmonics mitigation not only improves waveform quality but also contributes to power factor correction and overall grid efficiency.

4.4.6 Three-Phase Current and Voltage Behavior

Figure 4.15 presents a side-by-side comparison of the three-phase current waveforms and their respective THD levels before and after the activation of the SAPF. The results reveal the SAPF's effectiveness in improving the overall system performance across all three phases simultaneously.

In Figure 4.15a, recorded prior to SAPF activation, the three-phase currents (I_{L1}, I_{L2}, and I_{L3}) exhibit highly distorted waveforms with clear signs of nonlinearity and asymmetry. The current curves are notably non-sinusoidal, with flat regions and abrupt transitions, indicating

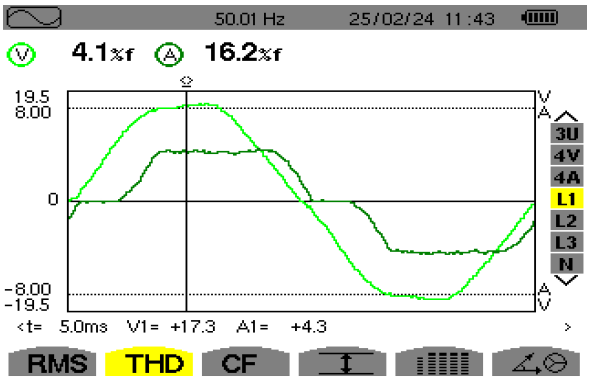

(a) Phase L1 Before SAPF Activation

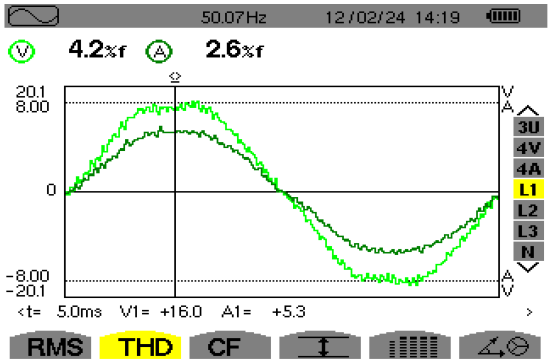

(b) Phase L1 After SAPF Activation

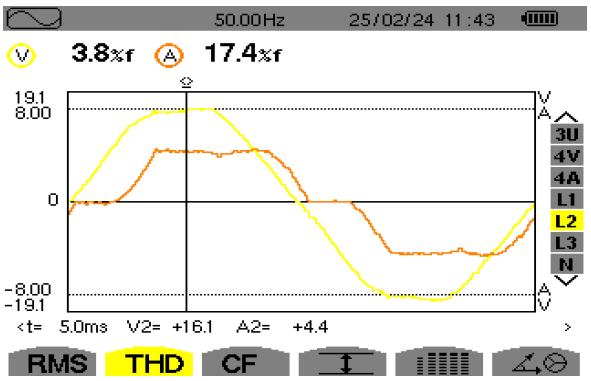

(c) Phase L2 Before SAPF Activation

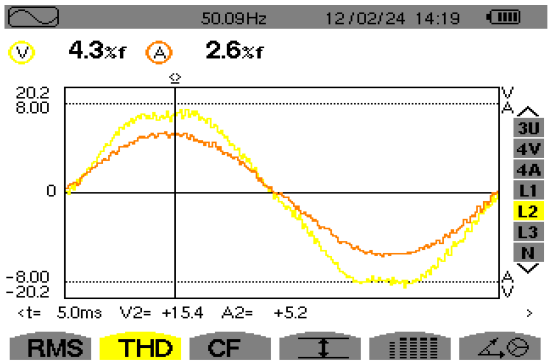

(d) Phase L2 After SAPF Activation

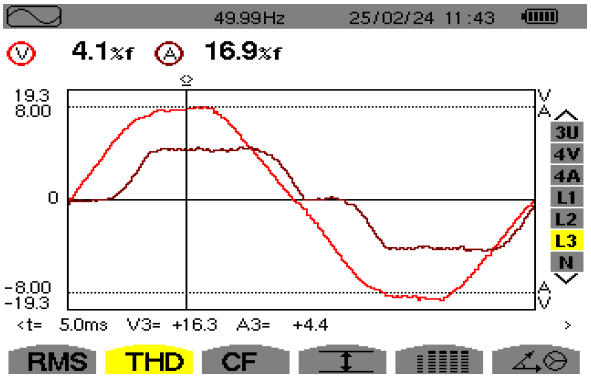

(e) Phase L3 Before SAPF Activation

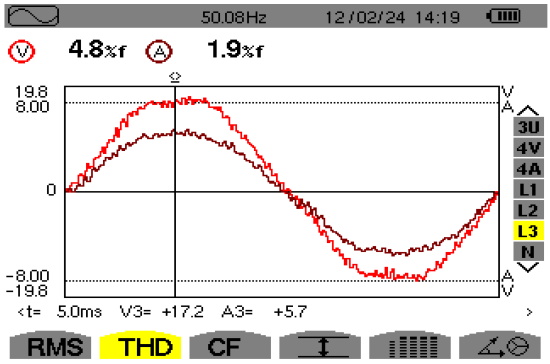

(f) Phase L3 After SAPF Activation

Figure 4.14: Waveforms and THD Values of Individual Phase Currents Before and After SAPF Activation

significant harmonic injection from nonlinear loads. The total harmonic distortion is measured at 16.5%, 17.3%, and 17.1% for phases L1, L2, and L3, respectively. Such high THD values underscore the severe power quality degradation in the absence of harmonic compensation.

Following SAPF activation, as shown in Figure 4.15b, the current waveforms transform into clean, well-formed sinusoids. The current in each phase demonstrates a near-ideal 120° separation, confirming both phase balance and proper synchronization. THD levels drop sharply

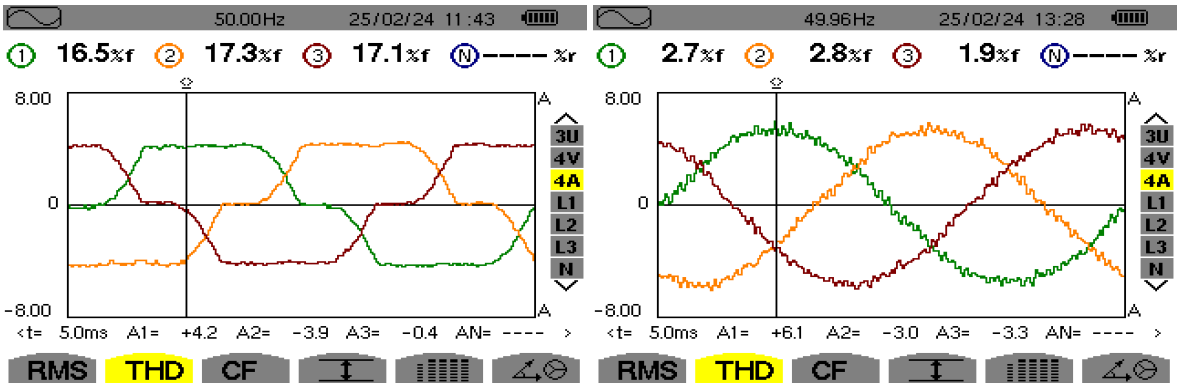

(a) Before SAPF Activation (b) After SAPF Activation

Figure 4.15: Waveforms and THD Values of Three-Phase Currents Before and After SAPF Activation

to 2.7%, 2.8%, and 1.9% for L1, L2, and L3, respectively. This substantial improvement highlights the PDPC strategy's ability to predict and inject compensating currents in real time, significantly enhancing the harmonic profile across all phases. The symmetry and amplitude alignment of the currents suggest not only harmonic mitigation but also improved power factor.

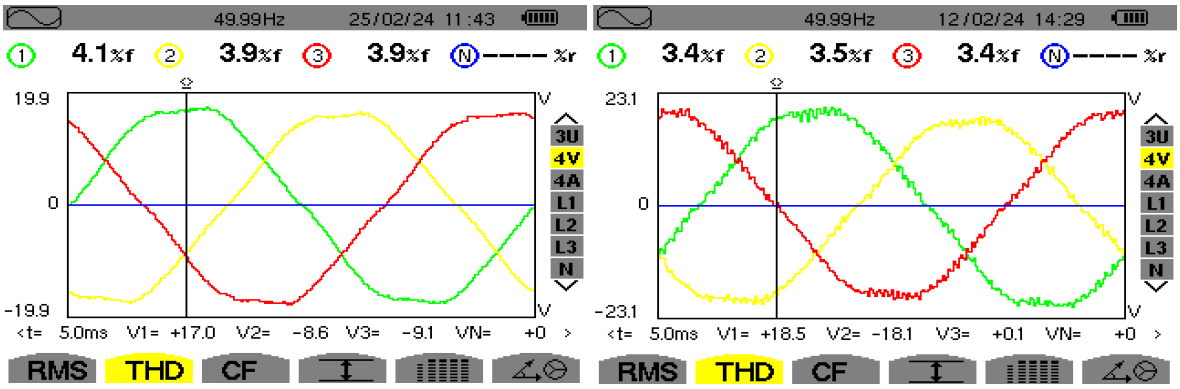

(a) Before SAPF Activation (b) After SAPF Activation

Figure 4.16: Waveforms and THD Values of Three-Phase Voltages Before and After SAPF Activation

Figure 4.16 shifts the focus to voltage behavior before and after the SAPF is engaged. In Figure 4.16a, the voltage waveforms are already well-shaped and sinusoidal. The THD levels are moderate, at 4.1%, 3.9%, and 3.9% for phases L1, L2, and L3, respectively. This baseline reflects a reasonably clean grid voltage, as the SAPF does not act directly on the voltage source.

After SAPF activation (Figure 4.16b), the voltage waveforms remain virtually unchanged, preserving their sinusoidal shape and three-phase balance. The THD levels vary slightly to 3.4%, 3.5%, and 3.4%, which may be attributed to load variations or measurement resolution. This confirms that the SAPF introduces no adverse influence on the grid voltage and remains strictly focused on current waveform correction, maintaining voltage waveform integrity and compliance with power quality standards.

4.4.7 Harmonic Order Analysis Before and after SAPF Activation

The following figures provide a detailed spectral decomposition of the harmonic components present in the current waveforms of phases L1, L2, and L3 prior to SAPF intervention. Each set consists of a full spectrum view (up to the 25th harmonic) and a zoomed-in view that highlights dominant harmonic orders. This visual and quantitative insight allows precise identification of problematic harmonics contributing to the elevated THD levels.

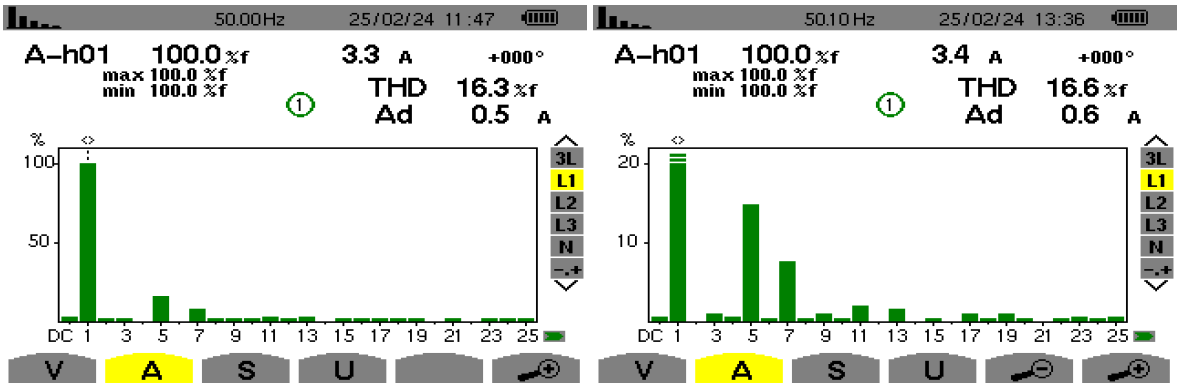

(a) Full Harmonic Order Analysis (b) Zoomed-In View

Figure 4.17: Harmonic Order Analysis of Phase L1 Current Before SAPF Activation

Figure 4.17 illustrates the harmonic spectrum of phase L1. The full-spectrum view (4.17a) confirms the presence of significant odd harmonics, especially the 5th, 7th, and 11th, which are characteristic of nonlinear loads under partial shading. The zoomed-in subplot (4.17b) highlights these dominant frequencies more clearly, showing their contribution to a measured THD of 16.3%. Higher harmonics beyond the 11th are also non-negligible, cumulatively degrading waveform purity and stressing power components.

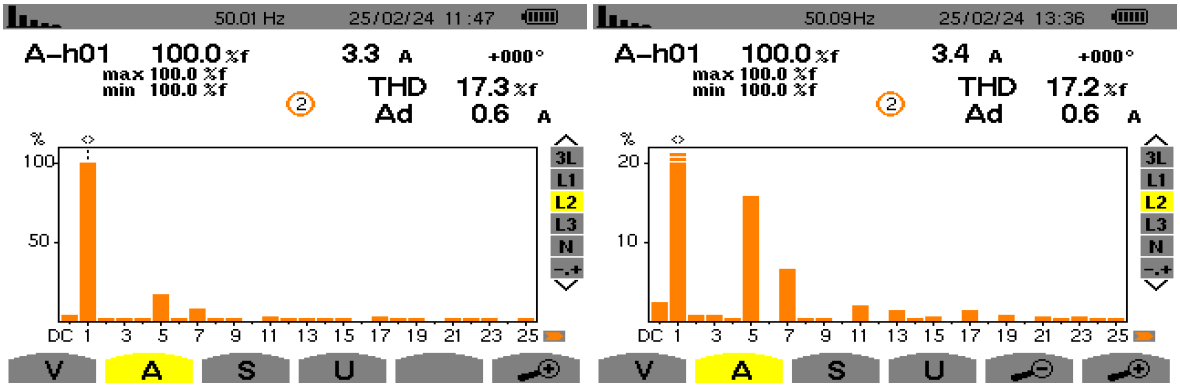

(a) Full Harmonic Order Analysis (b) Zoomed-In View

Figure 4.18: Harmonic Order Analysis of Phase L2 Current Before SAPF Activation

In Figure 4.18, similar harmonic content is observed in phase L2. The dominant peaks remain centered on the 5th, 7th, and 11th harmonic orders, with additional contributions from the 13th. The zoomed-in plot (4.18b) clearly delineates these features, where the 5th harmonic leads

with the highest non-fundamental contribution. The corresponding THD value is approximately 17.3%, confirming the system-wide harmonic contamination affecting all phases uniformly.

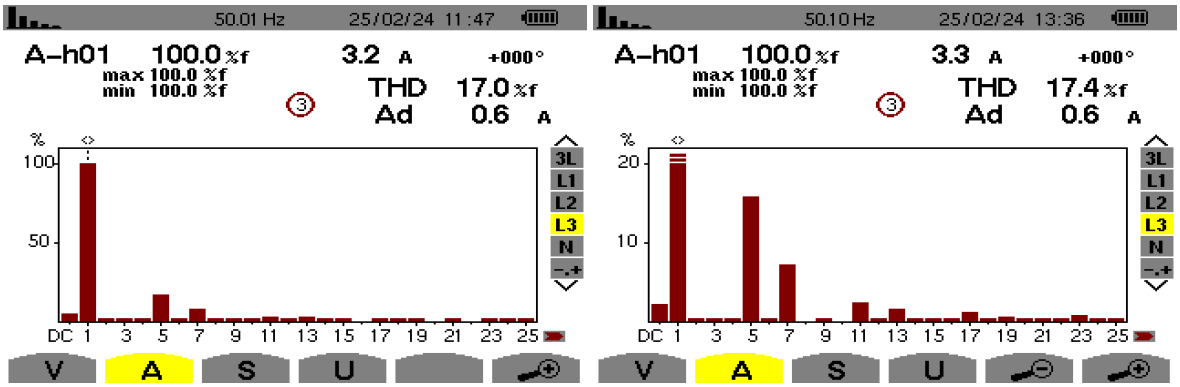

(a) Full Harmonic Order Analysis (b) Zoomed-In View

Figure 4.19: Harmonic Order Analysis of Phase L3 Current Before SAPF Activation

Finally, Figure 4.19 depicts the harmonic distortion present in phase L3. The bar chart (4.19a) again shows substantial presence of low-order harmonics with the 5^{th}, 7^{th}, and 11^{th} dominating the distortion profile. The THD value reaches 17.0%, matching the trend seen in the previous two phases. The zoomed-in subplot (4.19b) further emphasizes the disproportionate influence of these orders on the total distortion budget.

Justification of Harmonic Profiles: The dominance of odd harmonics in all three phases is a direct consequence of the waveform symmetry associated with most nonlinear loads, especially power electronics like rectifiers and switched-mode converters. When the current waveform exhibits half-wave symmetry—i.e., $i(t) = -i(t + T/2)$—the even-order harmonics are mathematically eliminated due to Fourier series properties. This explains the clear absence of even-order harmonics in Figures 4.17 through 4.19.

Mathematically, the Fourier coefficients for an even harmonic component n in a half-wave symmetric function vanish, since:

$$a_n = \frac{2}{T}\int_0^T i(t)\cos(n\omega t)dt = 0, \quad \text{for even } n,$$

$$b_n = \frac{2}{T}\int_0^T i(t)\sin(n\omega t)dt = 0, \quad \text{for even } n.$$

Thus, only odd harmonics (e.g., 3rd, 5th, 7th, etc.) remain in the spectrum.

Why 3^{rd} and 9^{th} Harmonics Are Suppressed: Triplen harmonics—i.e., harmonic orders that are integer multiples of 3 (such as the 3^{rd}, 9^{th}, and 15^{th})—are classified as zero-sequence components in three-phase systems. These harmonics are unique in that they appear *in phase* across all three phases:

$$i_a^{(3)}(t) = i_b^{(3)}(t) = i_c^{(3)}(t) = I_3 \sin(3\omega t)$$

Their synchronized phase alignment means that, in a star-connected load with a neutral wire (Y+N), they can flow freely and return through the neutral. The resulting neutral current is:

$$i_n(t) = -(i_a + i_b + i_c) = -3I_3 \sin(3\omega t)$$

However, in the absence of a neutral conductor—as in balanced star (Y) or delta (Δ) connections—Kirchhoff's Current Law mandates that:

$$i_a + i_b + i_c = 0$$

But for zero-sequence triplen harmonics:

$$i_a^{(3)} + i_b^{(3)} + i_c^{(3)} = 3I_3 \sin(3\omega t) \neq 0$$

This leads to a contradiction unless $I_3 = 0$, forcing these components to vanish. Hence, triplen harmonics are naturally suppressed in systems without a neutral conductor. The same applies in delta configurations, where the line current is the difference of two in-phase triplen components:

$$i_{AB}^{(3)} = i_A^{(3)} - i_B^{(3)} = 0$$

Therefore, the absence of a neutral path enforces a mathematical and physical constraint that prevents the circulation of zero-sequence harmonics in the line currents.

Summary: The harmonic order analyses provided in Figures 4.17 to 4.19 collectively confirm a severe harmonic environment prior to SAPF activation. Each phase exhibits a consistent distortion profile dominated by odd harmonics, especially at the 5^{th}, 7^{th}, and 11^{th} orders. The near absence of even harmonics is a direct result of waveform symmetry, while the low amplitude of triplen harmonics (3^{rd} and 9^{th}) is due to their zero-sequence nature and cancellation in the absence of a neutral path. The total harmonic distortion in each phase exceeds 16%, far surpassing IEEE 519 recommended limits (typically 5% for current THD in distribution systems).

These findings establish a strong pre-compensation benchmark, against which the SAPF's filtering efficacy will be evaluated in the subsequent post-activation harmonic bar figures. This phase-specific analysis also justifies the application of a real-time, predictive compensation strategy capable of dynamically mitigating complex harmonic signatures.

Figure 4.20 illustrates the harmonic order analysis for the Phase L1 current (I_{L1}) after SAPF activation. Subfigure 4.20a presents the complete harmonic spectrum up to the 25^{th} order, while subfigure 4.20b provides a zoomed-in view for enhanced clarity of lower-magnitude components. The fundamental component (1st order) remains dominant, as expected, while the amplitudes of

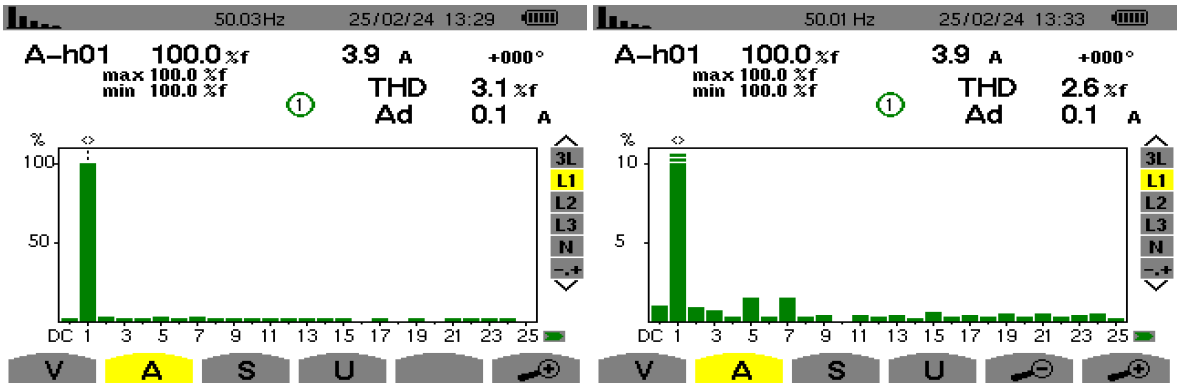

(a) Full Harmonic Order Analysis (b) Zoomed-In View

Figure 4.20: Harmonic Order Analysis of Phase L1 Current After SAPF Activation

all higher-order harmonics—especially the 5rd, 7th, and 11th—are drastically reduced. The THD value, previously exceeding 16%, now falls to approximately 2.6%, confirming a significant reduction in harmonic pollution. The near-elimination of higher-order distortions validates the effectiveness of the SAPF, under PDPC control, in restoring waveform purity and aligning the current with grid standards.

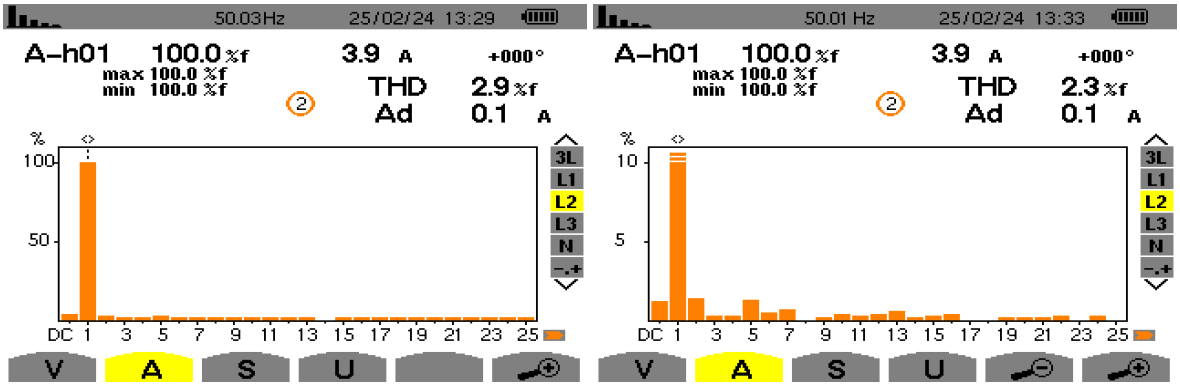

(a) Full Harmonic Order Analysis (b) Zoomed-In View

Figure 4.21: Harmonic Order Analysis of Phase L2 Current After SAPF Activation

Figure 4.21 shows the post-compensation harmonic profile for Phase L2 current (I_{L2}). As with Phase L1, the harmonics beyond the fundamental are almost entirely suppressed in subfigure 4.21a, with subfigure 4.21b confirming the reduction in low-order distortions. The 5rd, 7th, and 11th harmonics are present only as minor traces, and the overall THD drops from approximately 17% to just 2.3%. This reflects a considerable improvement in waveform fidelity and suggests that the SAPF's corrective action extends uniformly across all phases. The shape of the spectrum and reduced harmonic magnitudes demonstrate that the SAPF not only cancels dominant low-order components but also handles higher-order harmonics effectively.

Figure 4.22 provides the harmonic order analysis for Phase L3 current (I_{L3}) following SAPF activation. Subfigure 4.22a displays a consistent post-compensation spectrum with minimal harmonic content, while subfigure 4.22b verifies the near-absence of significant low-order harmonics. The THD, previously around 17%, is reduced to approximately 2.2%, matching the

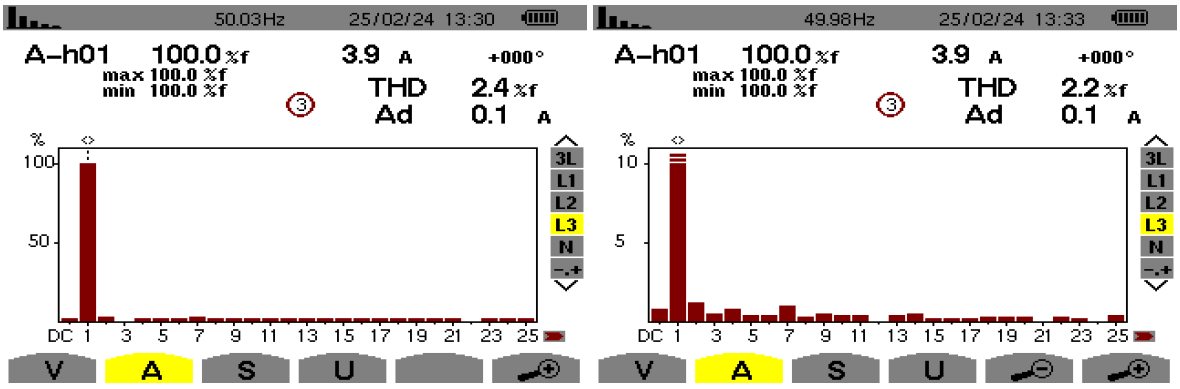

(a) Full Harmonic Order Analysis (b) Zoomed-In View

Figure 4.22: Harmonic Order Analysis of Phase L3 Current After SAPF Activation

levels of Phases L1 and L2. This uniformity across all three phases demonstrates the SAPF's symmetrical compensation capability and confirms that the PDPC strategy is not biased toward a particular phase or harmonic order. The harmonic spectrum now resembles that of a near-ideal sinusoidal current, evidencing successful harmonic mitigation.

The post-compensation results in Figures 4.20 through 4.22 reinforce the SAPF's critical role in maintaining power quality. By substantially reducing the amplitudes of key harmonic orders—namely the 5^{rd}, 7^{th}, and 11^{th}—the system ensures compliance with IEEE 519 standards, which stipulate a THD below 5%. The experimental findings align closely with simulation results, wherein the THD was reduced from 16% to 2.6% after compensation. Collectively, these figures confirm the SAPF's high performance in suppressing harmonic distortions, improving waveform purity, and enhancing overall grid compatibility under nonlinear loading and partial shading conditions.

4.4.8 Power Factor Analysis Before and After SAPF Activation

Figure 4.23 presents the measured power factor components—PF, $\cos\phi$, and $\tan\phi$—for each phase and the total system before and after the activation of the SAPF. These metrics quantify the relationship between real, reactive, and apparent power, highlighting the system's efficiency in energy transmission and its capacity to manage reactive and harmonic components.

Per-Phase Analysis: Prior to SAPF compensation, the power factor was significantly below unity for all phases, indicating the presence of both reactive and distortion power. The original values were approximated at $PF \approx 0.911$, $\cos\phi \approx 0.928$, and $\tan\phi \approx 0.402$ across the system. Before SAPF activation, the updated experimental values for each phase are as follows:

- **Phase L1:** $P = 41.46$ W, $Q = 17.18$ VAR, $D = 8.75$ VAD, $S = 45.72$ VA
- **Phase L2:** $P = 40.29$ W, $Q = 16.83$ VAR, $D = 8.18$ VAD, $S = 44.42$ VA
- **Phase L3:** $P = 40.35$ W, $Q = 15.45$ VAR, $D = 8.46$ VAD, $S = 44.03$ VA

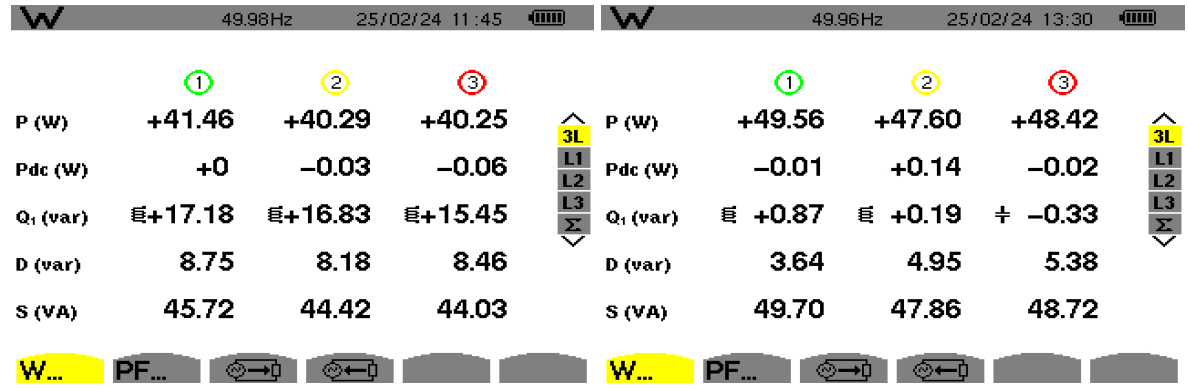

(a) Power Factor per Phase Before SAPF Activation (b) Power Factor per Phase After SAPF Activation

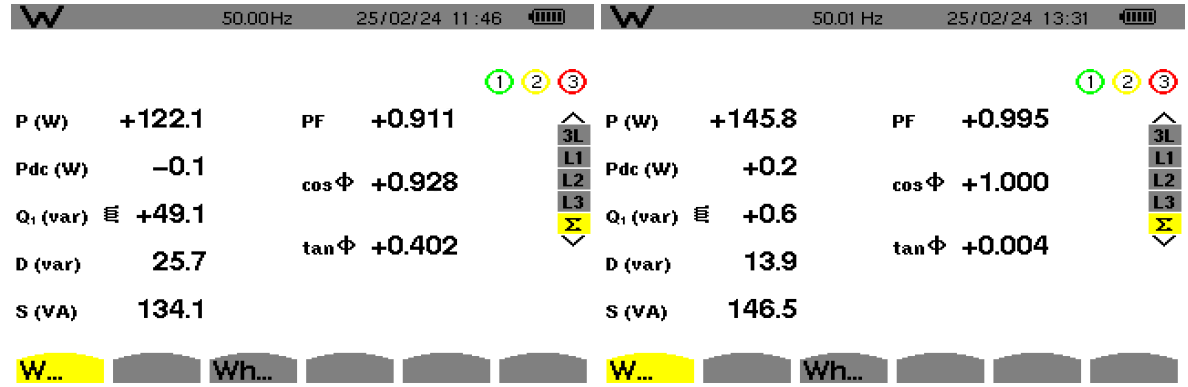

(c) Total Power Factor Before SAPF Activation (d) Total Power Factor After SAPF Activation

Figure 4.23: Power Factor (PF, $\cos\phi$, $\tan\phi$) Before and After SAPF Activation

After SAPF activation, the updated experimental values for each phase are as follows:

- **Phase L1:** $P = 49.56$ W, $Q = 0.87$ VAR, $D = 3.64$ VAD, $S = 49.7$ VA
- **Phase L2:** $P = 47.60$ W, $Q = 0.19$ VAR, $D = 4.95$ VAD, $S = 47.86$ VA
- **Phase L3:** $P = 48.42$ W, $Q = -0.33$ VAR, $D = 5.38$ VAD, $S = 48.72$ VA

These values reflect a moderate enhancement across all phases. Although reactive and distortion powers remain relatively constant, the improvement in PF suggests better current-voltage alignment through harmonic compensation and waveform shaping enabled by the SAPF.

Total System Analysis: For the complete system, the active power increased from 122.1 W before compensation to 145.8 W after SAPF activation. Reactive power was drastically reduced from 49.1 VAR to just 0.6 VAR, while distortion power also decreased from 25.7 VAD to 13.9 VAD, indicating significant mitigation of both displacement and harmonic effects. As a result, the apparent power rose from 134.1 VA to 146.5 VA, driven primarily by the increase in useful active power.

The displacement power factor ($\cos\phi$) improved from 0.928 to a perfect 1.000, showing full alignment of current with voltage in terms of phase. Likewise, the true power factor (PF) improved from 0.911 to 0.995, further validating the SAPF's effectiveness in eliminating

non-active components. Additionally, $\tan\phi$ dropped from 0.402 to just 0.004, reinforcing the minimal presence of reactive power post-compensation. The increase in active power delivered to the grid alongside these improvements demonstrates the strong impact of the predictive direct power control strategy on the system's overall performance.

Mathematical Explanation of PF vs $\cos\phi$: In AC systems, the displacement power factor is defined as the cosine of the phase angle between voltage and the fundamental component of current:

$$\cos\phi = \frac{P}{\sqrt{P^2 + Q^2}} \tag{4.2}$$

However, in real-world systems where harmonics are present, the true power factor is more appropriately defined using the total apparent power S, which includes the distortion power D:

$$PF = \frac{P}{S} = \frac{P}{\sqrt{P^2 + Q^2 + D^2}} \tag{4.3}$$

While $\cos\phi$ reflects only the displacement caused by reactive power at the fundamental frequency, PF considers both displacement and distortion. Thus, even when $\cos\phi$ is close to unity, a significant distortion power will cause PF to fall below $\cos\phi$.

In this case, with the post-compensation values:

$$\cos\phi = \frac{122.1}{\sqrt{122.1^2 + 49.1^2}} \approx 0.928 \tag{4.4}$$

$$PF = \frac{122.1}{\sqrt{122.1^2 + 49.1^2 + 25.7^2}} \approx 0.911 \tag{4.5}$$

This confirms that the SAPF effectively mitigated reactive displacement and improved waveform quality, though a slight gap between PF and $\cos\phi$ remains due to residual distortion.

The enhancement in both $\cos\phi$ and PF after the activation of the SAPF confirms the improved power quality and efficiency of the grid-connected system. By aligning current with voltage and minimizing harmonic and reactive components, the predictive direct power control strategy demonstrates its effectiveness in achieving better energy utilization. The observed increase in active power output further supports this conclusion, validating the SAPF's contribution to cleaner and more efficient grid operation.

4.4.9 Detailed Metrics and Their Improvements

In Figure 4.24, in the "before" capture, the oscilloscope presents four distinct waveforms measured at the point of common coupling. The top trace, representing the source voltage V_s, shows a clean sinusoidal waveform with a peak amplitude of approximately 18 V and a frequency of about 50.0380 Hz, indicating stable grid conditions. However, the source current I_s (magenta) is clearly distorted, exhibiting a flattened, plateau-like shape throughout each cycle with an

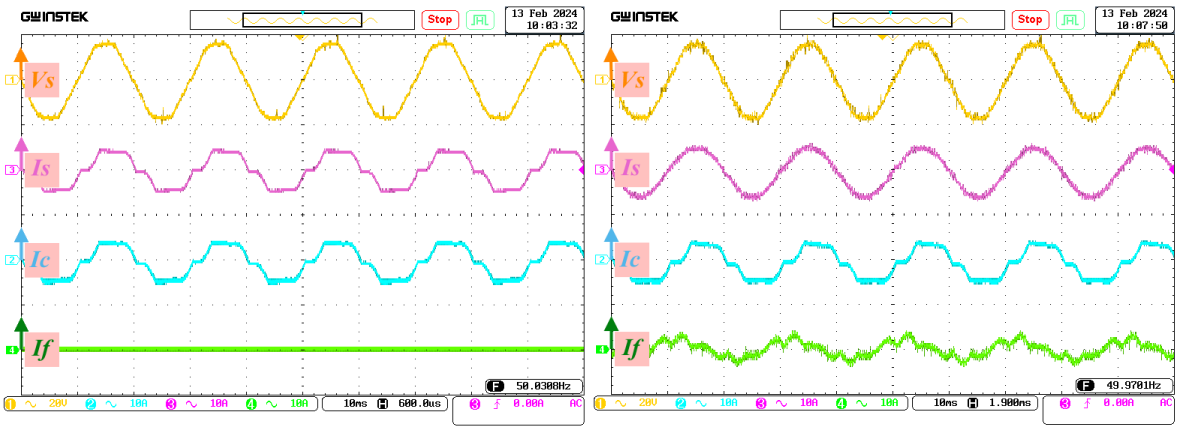

(a) Before SAPF Activation (b) After SAPF Activation

Figure 4.24: Source Voltage (V_s), Source Current (I_s), Load Current (I_c), and SAPF Injected Current (I_f) Before and After SAPF Activation

estimated amplitude around 3–4 A. This distortion is due to the nonlinear load drawing a harmonically distorted current, which is further evidenced by the load current I_c (cyan trace) that shows a pronounced stepped, blocky form. The harmonic content in I_c causes the overall source current I_s to deviate from an ideal sinusoid, and, as expected, the filter current I_f (green trace) remains near zero because the SAPF is inactive. Without the SAPF, the harmonics from the load directly affect the source, leading to poor power quality and potential inefficiencies.

In contrast, the "after" capture illustrates the system's performance once the SAPF is activated under PDPC control. The source voltage V_s continues to exhibit a stable, clean sinusoid with a peak of around 18 V and a frequency very close to 50 Hz (approximately 49.9701 Hz), confirming that the grid voltage remains unaffected by the compensation process. More importantly, the source current I_s now appears significantly more sinusoidal and smooth, with its amplitude still near 4–5 A but with markedly fewer distortions and irregularities. Although the load current I_c still displays its inherent stepped characteristic, the compensating filter current I_f becomes active and clearly mirrors the harmonic content of the load current, but in opposite phase. The filter current effectively cancels the harmonic distortion that previously tainted the source current, resulting in a nearly pure sinusoidal I_s waveform.

In Figure 4.25, In subplot (a), the system begins in a normal operating mode with the shunt active power filter (SAPF) already engaged. The source current $\mathbf{I_s}$ (magenta) is relatively sinusoidal, maintaining an amplitude of around 5 A, while the active power $\mathbf{P_a}$ (cyan) hovers near 146 W. $\mathbf{P_a}$ follow its reference $\mathbf{P}_{\text{ref}}$ (orange) perfectly, indicating that the controller is driving the system toward the desired power level. Meanwhile, the reactive power $\mathbf{Q}$ (green) remains close to 0 VAR, reflecting effective compensation of reactive components.

Subplot (b) provides a zoomed view of the 0.1 s interval, showing how quickly $\mathbf{I_s}$ and $\mathbf{P_a}$ settle to their steady-state values after a minor transient disturbance. The rapid response, on the order of a few cycles, demonstrates the SAPF's predictive control in action.

In subplot (c), a sudden load change occurs after 460 ms, causing $\mathbf{I_s}$ to jump from about 4 A to nearly 8 A. Simultaneously, $\mathbf{P_a}$ rises from roughly 146 W to 200 W, while the reference $\mathbf{P}_{\text{ref}}$

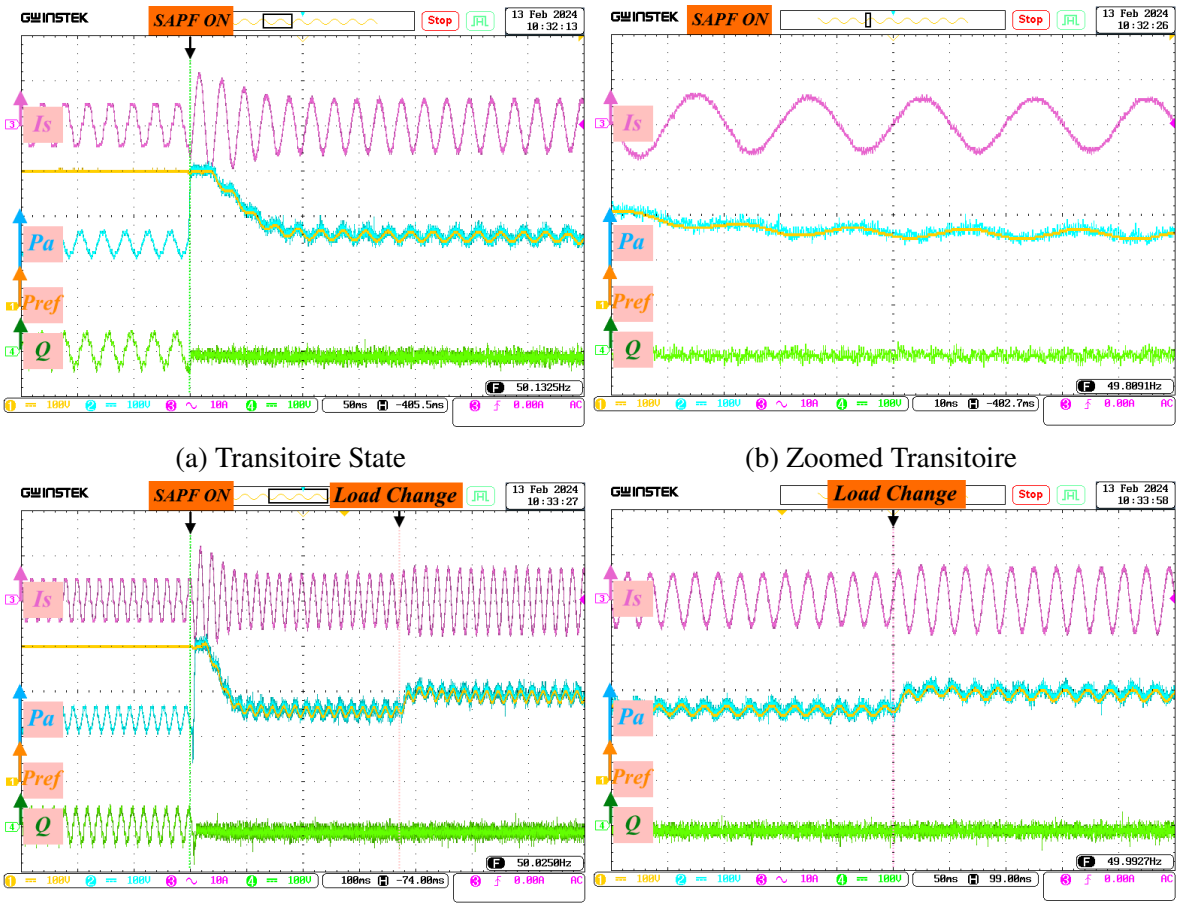

(a) Transitoire State

(b) Zoomed Transitoire

(c) Load Change State

(d) Zoomed Load Change

Figure 4.25: **Time-Domain Oscilloscope Captures of I_s, P_a, P_{ref}, and Q Under Transient and Load Change Scenarios.** Each subplot illustrates a different operational regime: (a) normal operation with transitoire behavior, (b) a zoomed-in view of the transient, (c) a sudden load change event, and (d) a closer inspection of the load change response.

also increases accordingly. Despite this abrupt shift, **Q** remains near zero, indicating that the SAPF continues to neutralize unwanted reactive power.

Finally, subplot (d) zooms in on region, highlighting the controller's swift adaptation to the new load condition. The source current quickly reverts to a clean sinusoidal form, and the actual active power converges to the updated reference, all while the reactive power stays negligible. Overall, these time-domain captures confirm that the SAPF's control algorithm maintains near-unity power factor, low harmonic distortion, and reliable power delivery—even under dynamic load changes.

In Figure 4.26, in subplot (a), the system enters a transient mode as SAPF is engaged. The DC-link voltage $\mathbf{V_{dc}}$ ramps up from 63 V to 81 V, stabilizing within a few cycles. The source current $\mathbf{I_s}$ exhibits initial distortion that smooths out rapidly, while the filter current $\mathbf{I_f}$ activates in synchrony, delivering the needed compensation.

In subplot (b), with SAPF off, $\mathbf{V_{dc}}$ remains flat near 63 V and $\mathbf{I_f}$ is nearly null. The source current $\mathbf{I_s}$ reveals significant harmonic distortion due to the unmitigated non-linear load, evident in its blocky, non-sinusoidal waveform.

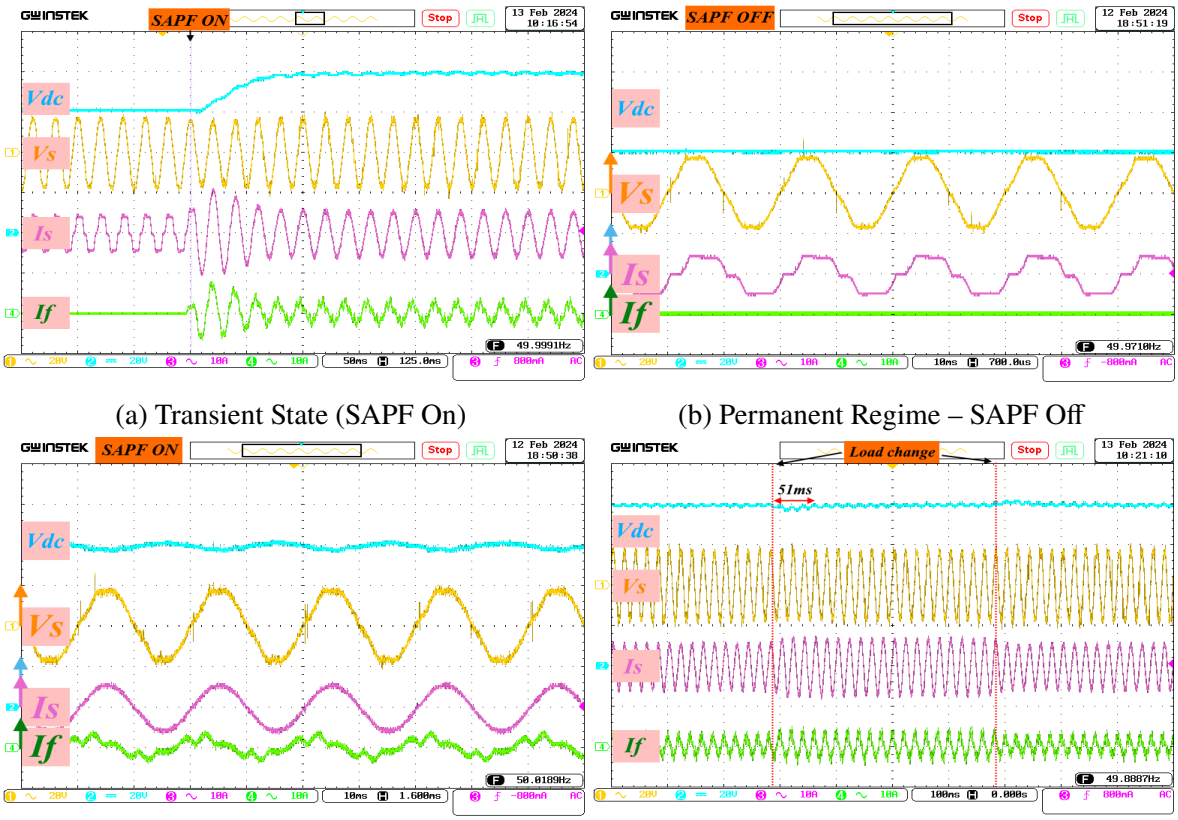

(a) Transient State (SAPF On)

(b) Permanent Regime – SAPF Off

(c) Permanent Regime – SAPF On

(d) Load Change under Compensation

Figure 4.26: **DC-Link and Current Waveforms Across Operating States.** Subplots illustrate (a) the transient behavior of $\mathbf{V_{dc}}$, $\mathbf{I_s}$, and $\mathbf{I_f}$ immediately after SAPF activation, (b) permanent regime with SAPF disabled, (c) stable regime with SAPF active, and (d) SAPF response to a load step.

Subplot (c) illustrates the compensated state. With $\mathbf{V_{dc}}$ maintained at 81 V, $\mathbf{I_f}$ becomes active and tailored to cancel harmonic content, producing a near-sinusoidal $\mathbf{I_s}$ that closely tracks $\mathbf{V_s}$ in both shape and phase. This translates into enhanced power factor and reduced THD.

Finally, subplot (d) captures a load change event. The system, already under SAPF operation, shows a rapid increase in $\mathbf{I_s}$ amplitude, with $\mathbf{I_f}$ adapting accordingly. Despite the step change, $\mathbf{V_{dc}}$ stays well-regulated, ensuring that the SAPF continues compensating without delay, and preserving low distortion and unity power factor.

Subplot (a) in Figure 4.27 captures the transient immediately after the SAPF is switched on. The DC-link voltage $\mathbf{V_{dc}}$ increases from approximately 63 V to 81 V, driven by the internal controller to energize the inverter. The source current $\mathbf{I_s}$ transforms from a moderately distorted shape to a clean sinusoid, while the reference current $\mathbf{I}_{\text{ref}}$ ramps down, initiating the compensation process.

In subplot (b), under permanent regime with SAPF engaged, $\mathbf{V_{dc}}$ remains stable near 81 V, $\mathbf{P_a}$ stays around 140–150 W, and $\mathbf{I_s}$ maintains a nearly perfect sinusoidal shape. The compensating current $\mathbf{I_f}$ remains consistent, and $\mathbf{I}_{\text{ref}}$ settles to a stable reference value, indicating optimal control conditions.

Subplot (c) illustrates a dynamic scenario where a load change triggers a transient. After 470 ms, both $\mathbf{I_s}$ and $\mathbf{P_a}$ increase sharply. $\mathbf{V_{dc}}$ briefly fluctuates but quickly stabilizes. The

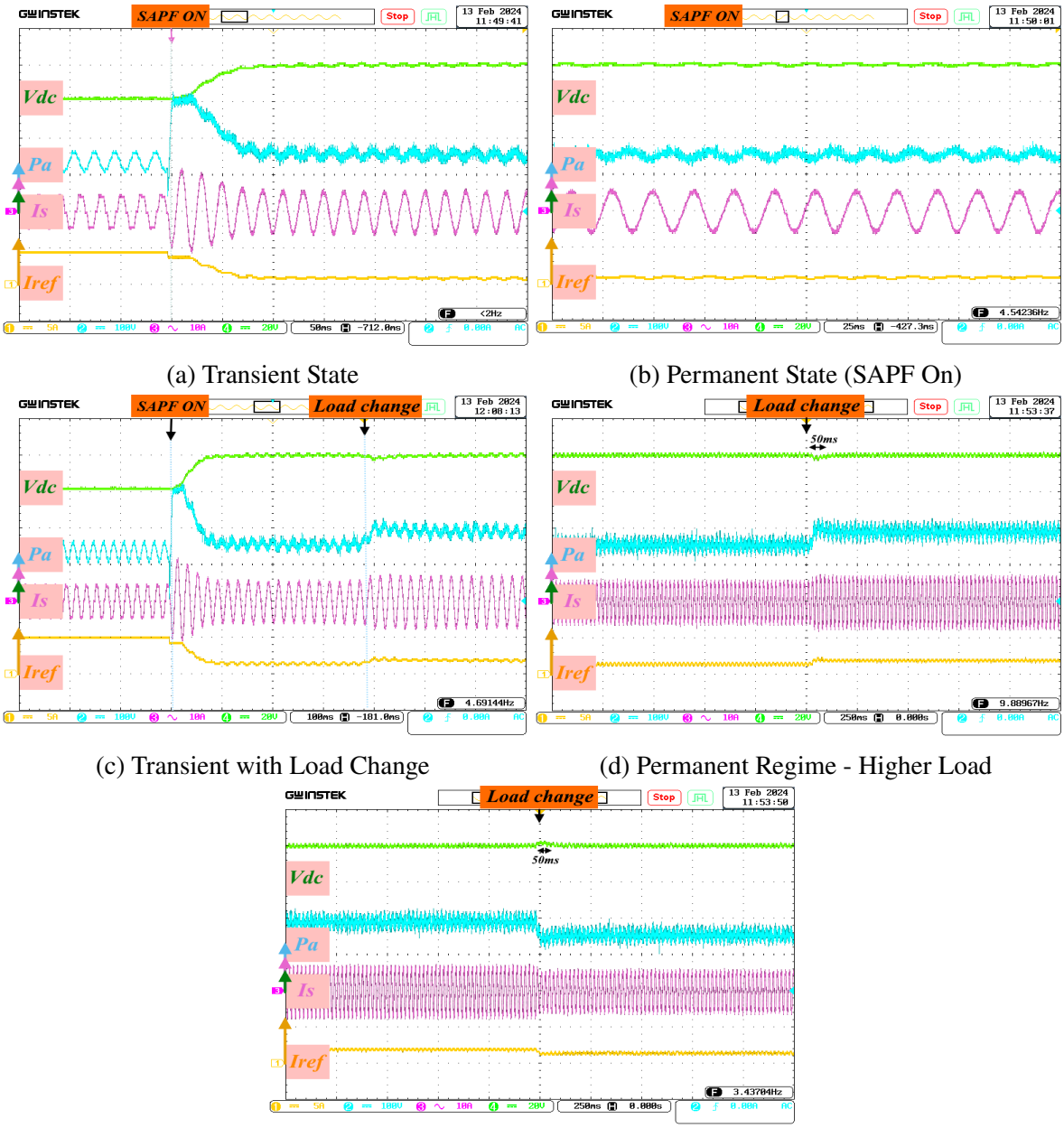

(a) Transient State

(b) Permanent State (SAPF On)

(c) Transient with Load Change

(d) Permanent Regime - Higher Load

(e) Permanent Regime - Lower Load

Figure 4.27: **Time-Domain Oscilloscope Captures of V_{dc}, P_a, I_s, I_f, and I_{ref} Under Various Operating and Load Conditions.** (a) Transient state after SAPF activation, (b) steady operation with SAPF on, (c) transient with load change, (d) stable operation under higher load, and (e) stable operation under lower load.

internal controller reacts by adjusting $\mathbf{I}_{ref}$ and increasing $\mathbf{I_f}$, ensuring the SAPF continues harmonic mitigation.

In subplot (d), the system is shown in a permanent regime with a higher load. $\mathbf{I_s}$ sustains an elevated amplitude (7–8 A), and $\mathbf{P_a}$ rises to approximately 200 W. The reference and filter currents increase accordingly, while $\mathbf{V_{dc}}$ remains tightly regulated.

Subplot (e) represents the lower load case. The active power drops to around 140–150 W and $\mathbf{I_s}$ decreases to 4–5 A. Both $\mathbf{I}_{ref}$ and $\mathbf{I_f}$ adjust downwards, ensuring smooth adaptation while maintaining a clean sinusoidal waveform.

Overall, these results confirm that the SAPF, under predictive control, provides fast dynamic response, stable DC-link behavior, and precise current tracking in various operating states.

4.5 Experimental Results of Integrated System under Partial Shading Scenarios

In this subsection, we present the experimental results of the fully integrated system, where the reactive power compensation system (SAPF + PDPC) is connected to the PV emulator under partial shading conditions. The performance of six MPPT algorithms—EEGO, EGO, SMO, GWO, WOA, and PSO—is evaluated under five static partial shading scenarios. For each algorithm and scenario, three types of figures are provided:

- **Subplot 1:** PV power (P_{pv}), PV current (I_{pv}), active power (P_a), and source current (I_s).
- **Subplot 2:** DC link voltage (V_{dc}), PV power (P_{pv}), active power (P_a), and reactive power (Q).
- **Subplot 3:** A photograph of the PV emulator's screen captured from the PDCS, validating the real-world behavior of the PV system under the tested conditions.

These figures collectively demonstrate the effectiveness of each algorithm in extracting maximum power from the PV system under shading conditions while ensuring stable operation of the reactive power compensation system. The experimental validation spans approximately 20 s of MPPT operation after SAPF activation.

In addition to evaluating power tracking accuracy and waveform quality, we also analyze the injection efficiency of each MPPT algorithm. This is assessed by comparing the expected injected power—calculated as the difference between extracted PV power and the constant system load of 146 W—with the actual active power delivered to the grid. Due to the inherent losses in the inverter (including switching, conduction, and filtering losses), a portion of the extracted power is dissipated, resulting in reduced effective injection.

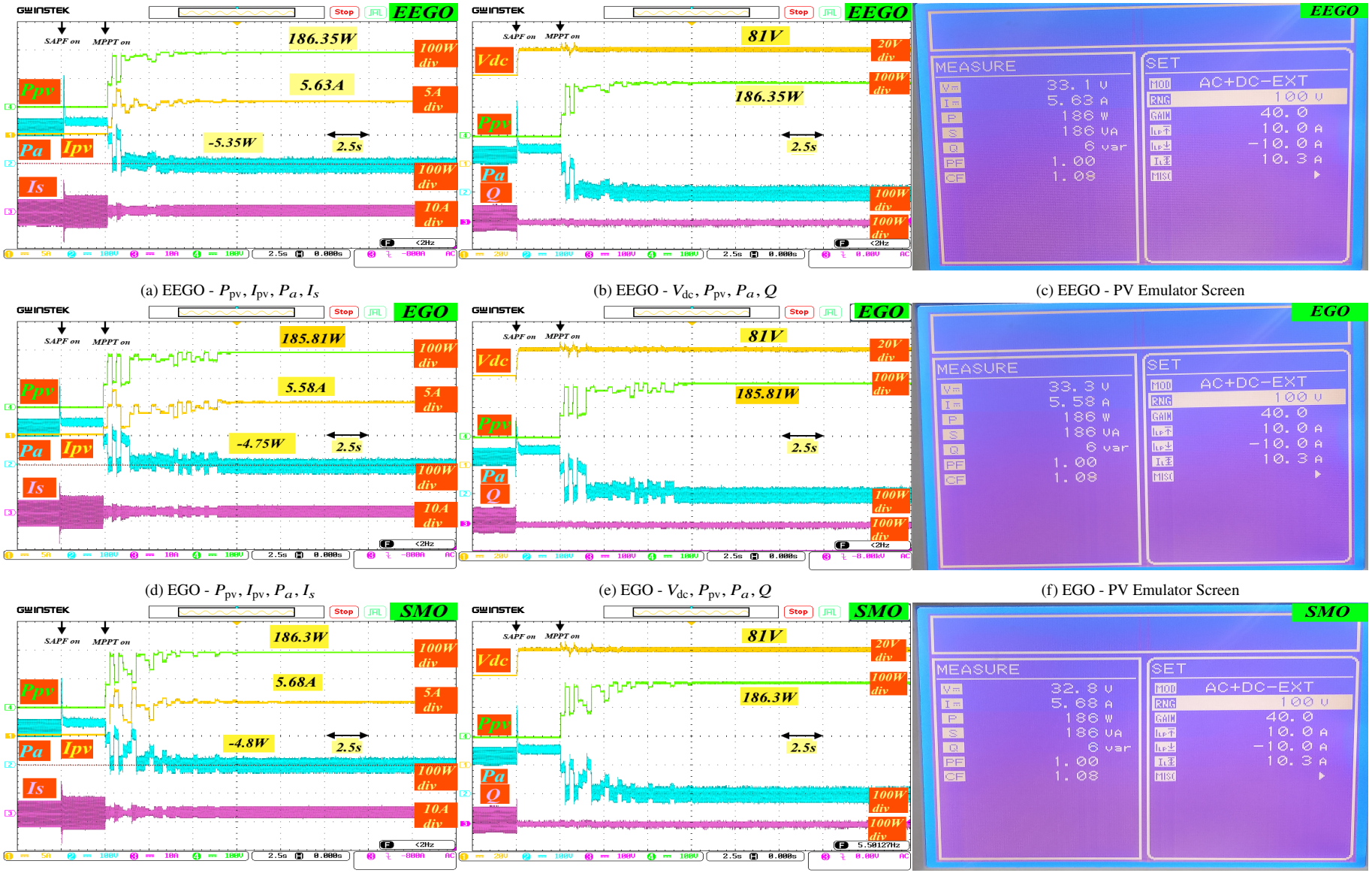

(a) EEGO - P_{pv}, I_{pv}, P_a, I_s

(b) EEGO - V_{dc}, P_{pv}, P_a, Q

(c) EEGO - PV Emulator Screen

(d) EGO - P_{pv}, I_{pv}, P_a, I_s

(e) EGO - V_{dc}, P_{pv}, P_a, Q

(f) EGO - PV Emulator Screen

(g) SMO - P_{pv}, I_{pv}, P_a, I_s

(h) SMO - V_{dc}, P_{pv}, P_a, Q

(i) SMO - PV Emulator Screen

Figure 4.28: Integrated System Performance under First Static PSC Scenario Using (EEGO, EGO, SMO) MPPT Algorithms.

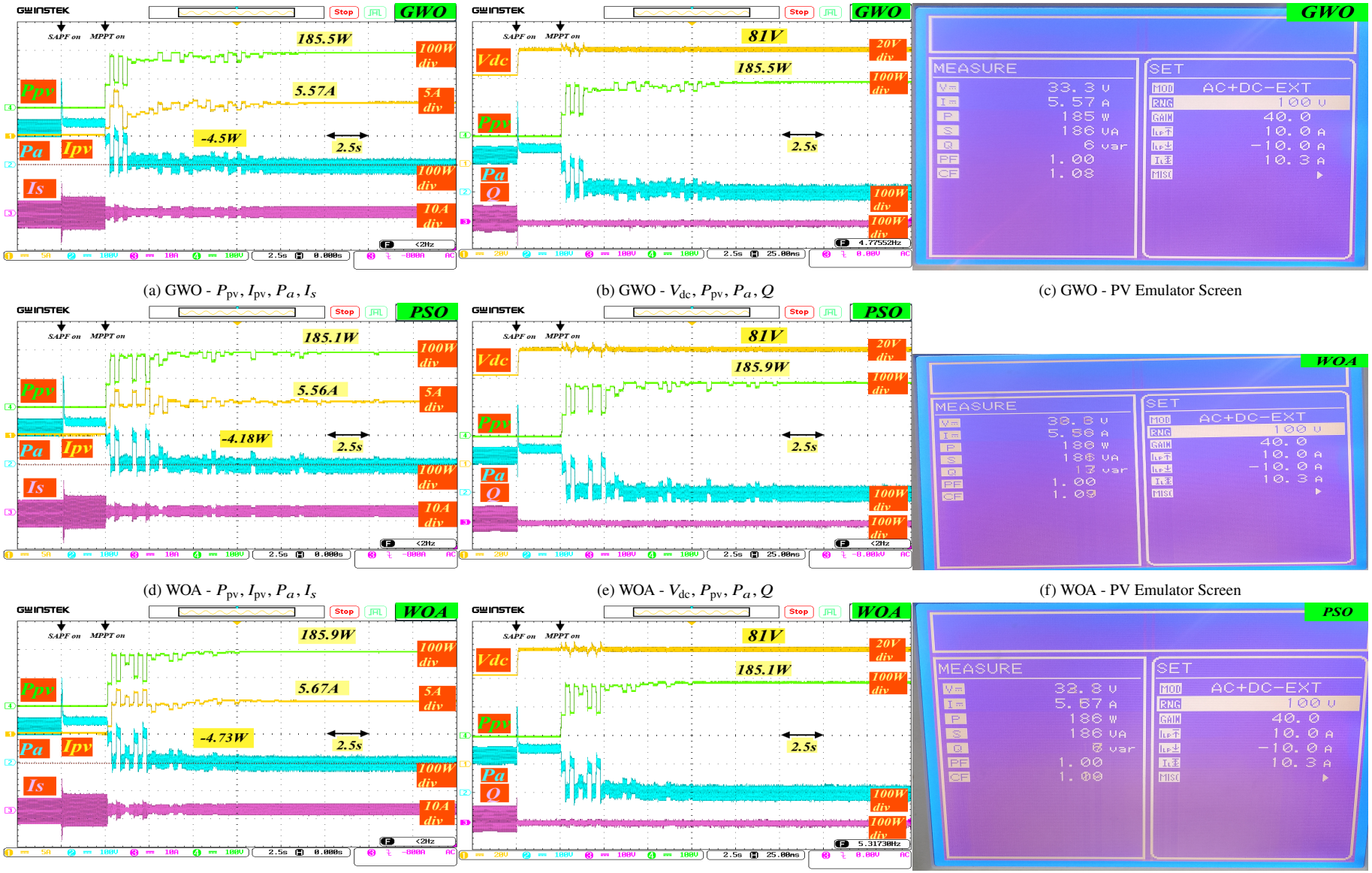

(a) GWO - P_{pv}, I_{pv}, P_a, I_s

(b) GWO - V_{dc}, P_{pv}, P_a, Q

(c) GWO - PV Emulator Screen

(d) WOA - P_{pv}, I_{pv}, P_a, I_s

(e) WOA - V_{dc}, P_{pv}, P_a, Q

(f) WOA - PV Emulator Screen

(g) PSO - P_{pv}, I_{pv}, P_a, I_s

(h) PSO - V_{dc}, P_{pv}, P_a, Q

(i) PSO - PV Emulator Screen

Figure 4.29: Integrated System Performance under First Static PSC Scenario Using (GWO, WOA, PSO) MPPT Algorithms.

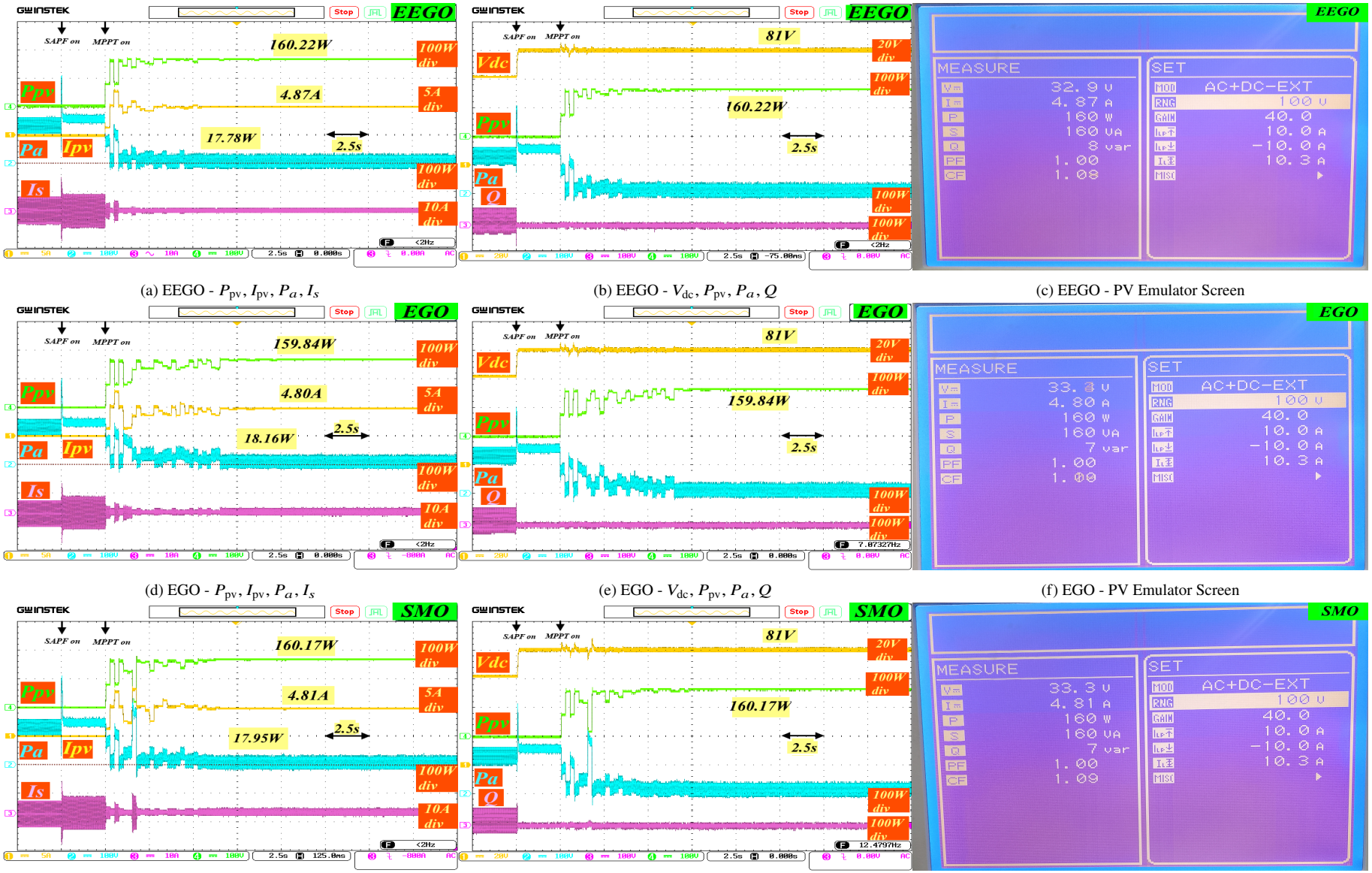

(a) EEGO - P_{pv}, I_{pv}, P_a, I_s

(b) EEGO - V_{dc}, P_{pv}, P_a, Q

(c) EEGO - PV Emulator Screen

(d) EGO - P_{pv}, I_{pv}, P_a, I_s

(e) EGO - V_{dc}, P_{pv}, P_a, Q

(f) EGO - PV Emulator Screen

(g) SMO - P_{pv}, I_{pv}, P_a, I_s

(h) SMO - V_{dc}, P_{pv}, P_a, Q

(i) SMO - PV Emulator Screen

Figure 4.30: Integrated System Performance under Second Static PSC Scenario Using (EEGO, EGO, SMO) MPPT Algorithms.

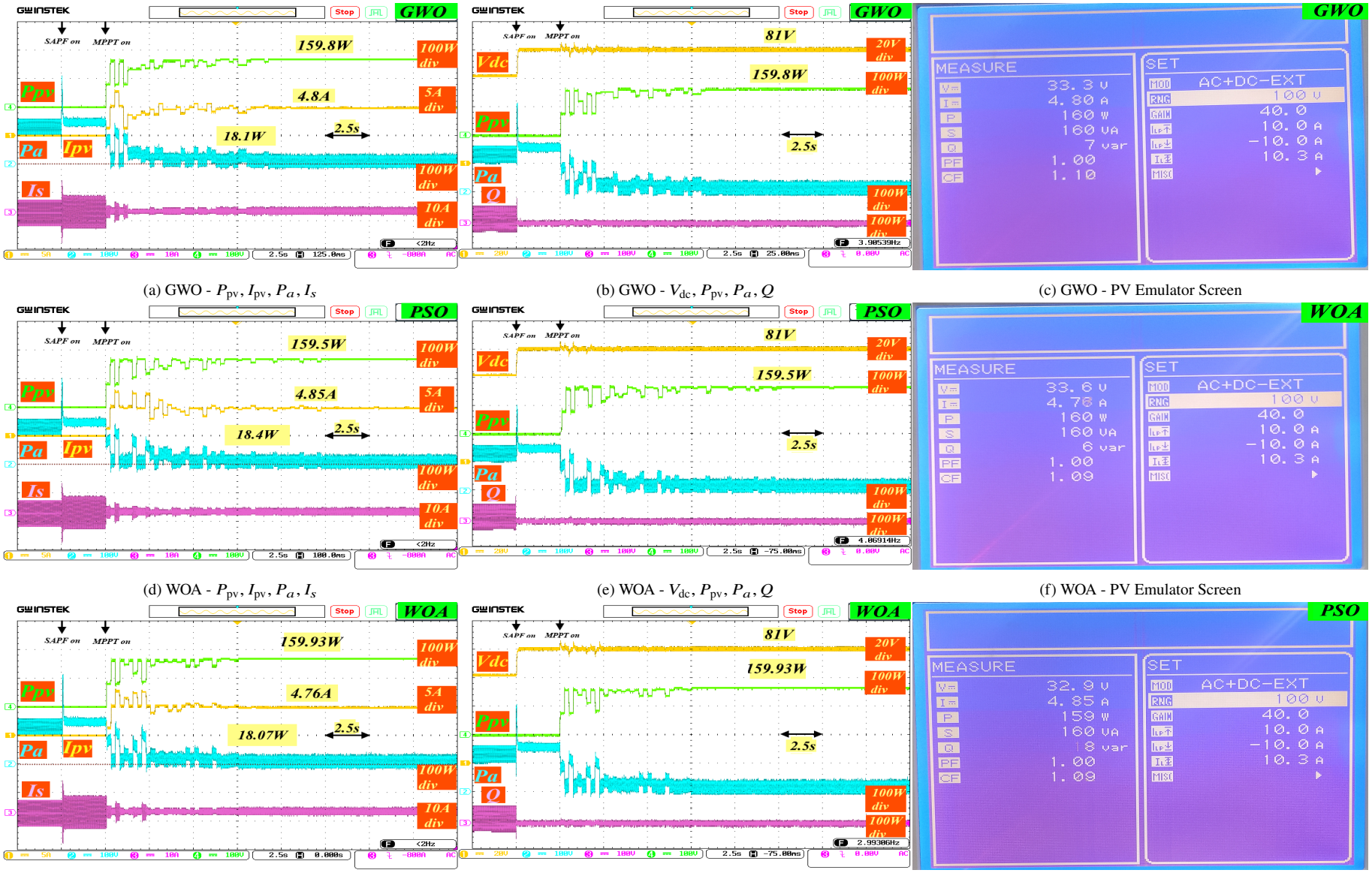

(a) GWO - P_{pv}, I_{pv}, P_a, I_s

(b) GWO - V_{dc}, P_{pv}, P_a, Q

(c) GWO - PV Emulator Screen

(d) WOA - P_{pv}, I_{pv}, P_a, I_s

(e) WOA - V_{dc}, P_{pv}, P_a, Q

(f) WOA - PV Emulator Screen

(g) PSO - P_{pv}, I_{pv}, P_a, I_s

(h) PSO - V_{dc}, P_{pv}, P_a, Q

(i) PSO - PV Emulator Screen

Figure 4.31: Integrated System Performance under Second Static PSC Scenario Using (GWO, WOA, PSO) MPPT Algorithms.

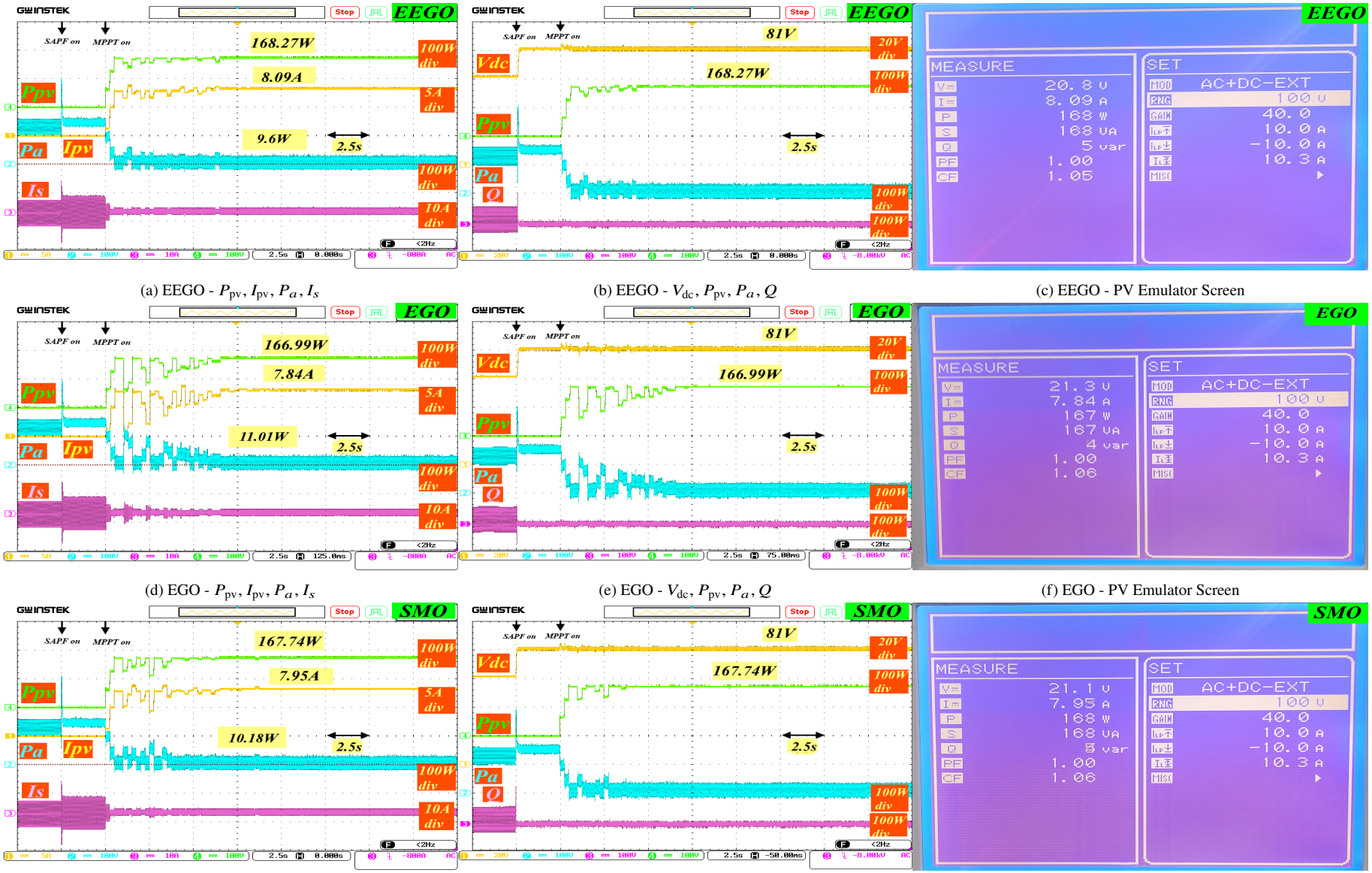

(a) EEGO - P_{pv}, I_{pv}, P_a, I_s

(b) EEGO - V_{dc}, P_{pv}, P_a, Q

(c) EEGO - PV Emulator Screen

(d) EGO - P_{pv}, I_{pv}, P_a, I_s

(e) EGO - V_{dc}, P_{pv}, P_a, Q

(f) EGO - PV Emulator Screen

(g) SMO - P_{pv}, I_{pv}, P_a, I_s

(h) SMO - V_{dc}, P_{pv}, P_a, Q

(i) SMO - PV Emulator Screen

Figure 4.32: Integrated System Performance under Third Static PSC Scenario Using (EEGO, EGO, SMO) MPPT Algorithms.

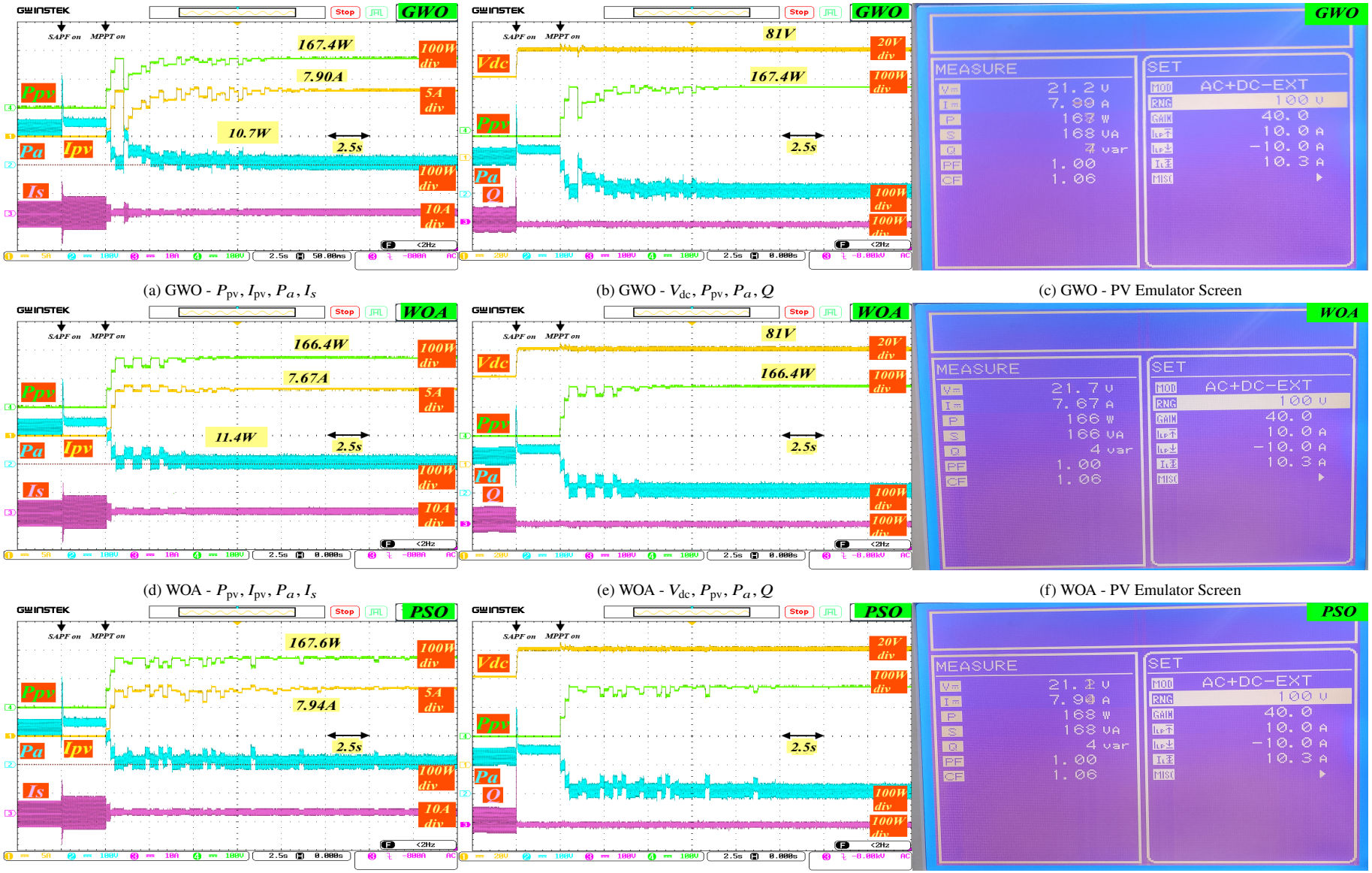

(a) GWO - P_{pv}, I_{pv}, P_a, I_s

(b) GWO - V_{dc}, P_{pv}, P_a, Q

(c) GWO - PV Emulator Screen

(d) WOA - P_{pv}, I_{pv}, P_a, I_s

(e) WOA - V_{dc}, P_{pv}, P_a, Q

(f) WOA - PV Emulator Screen

(g) PSO - P_{pv}, I_{pv}, P_a, I_s

(h) PSO - V_{dc}, P_{pv}, P_a, Q

(i) PSO - PV Emulator Screen

Figure 4.33: Integrated System Performance under Third Static PSC Scenario Using (GWO, WOA, PSO) MPPT Algorithms.

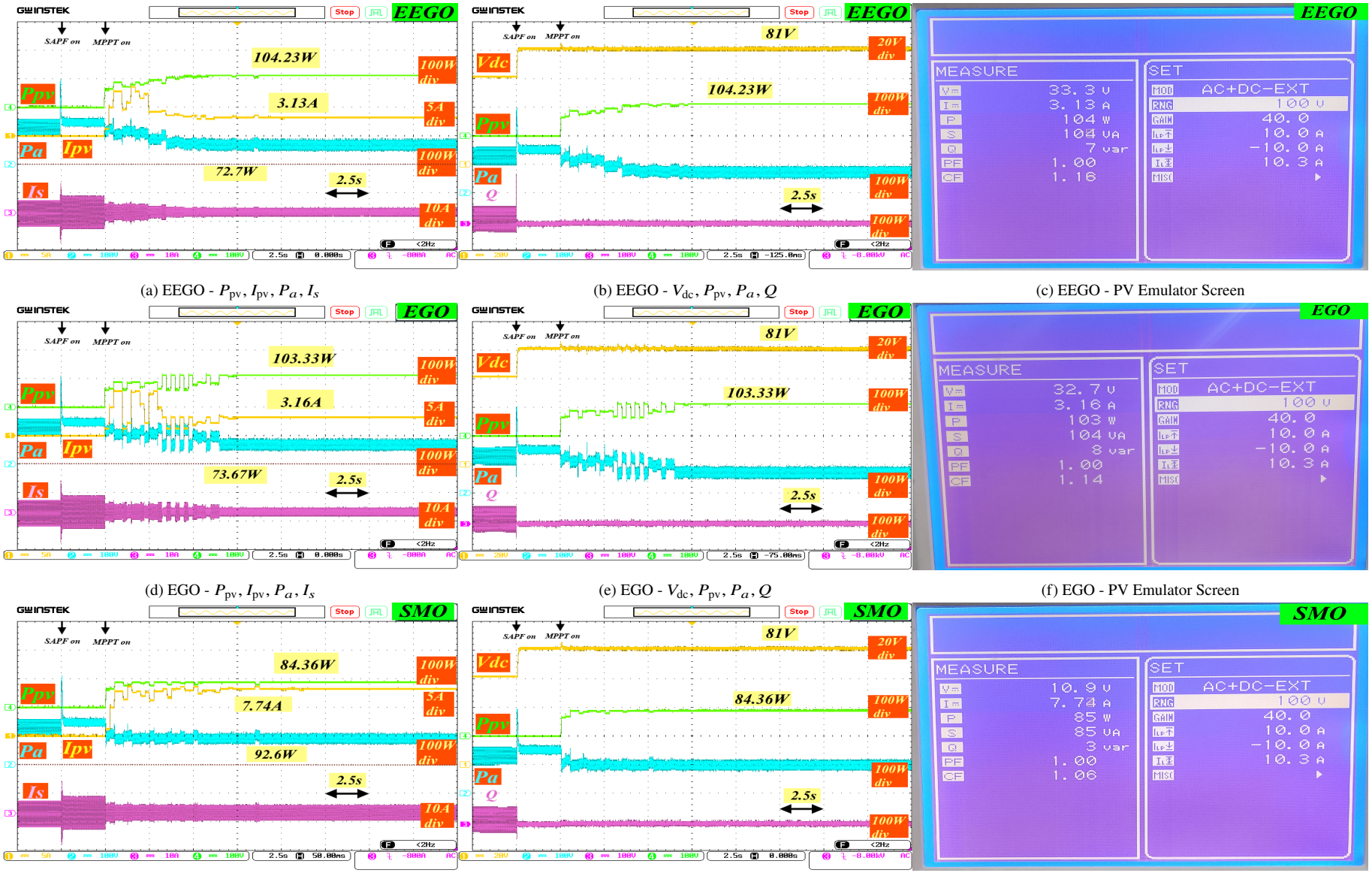

(a) EEGO - P_{pv}, I_{pv}, P_a, I_s

(b) EEGO - V_{dc}, P_{pv}, P_a, Q

(c) EEGO - PV Emulator Screen

(d) EGO - P_{pv}, I_{pv}, P_a, I_s

(e) EGO - V_{dc}, P_{pv}, P_a, Q

(f) EGO - PV Emulator Screen

(g) SMO - P_{pv}, I_{pv}, P_a, I_s

(h) SMO - V_{dc}, P_{pv}, P_a, Q

(i) SMO - PV Emulator Screen

Figure 4.34: Integrated System Performance under Fourth Static PSC Scenario Using (EEGO, EGO, SMO) MPPT Algorithms.

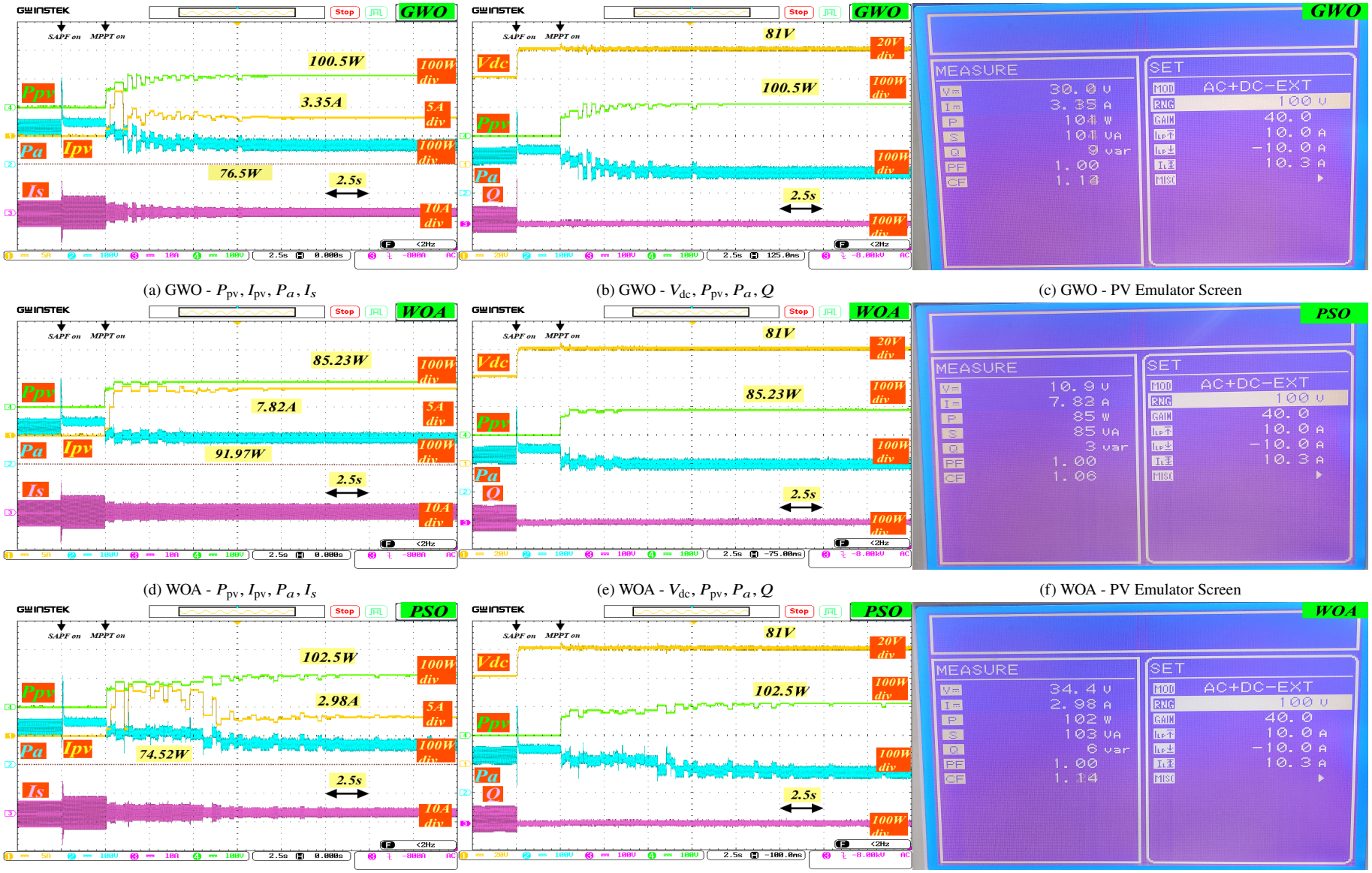

(a) GWO - P_{pv}, I_{pv}, P_a, I_s

(b) GWO - V_{dc}, P_{pv}, P_a, Q

(c) GWO - PV Emulator Screen

(d) WOA - P_{pv}, I_{pv}, P_a, I_s

(e) WOA - V_{dc}, P_{pv}, P_a, Q

(f) WOA - PV Emulator Screen

(g) PSO - P_{pv}, I_{pv}, P_a, I_s

(h) PSO - V_{dc}, P_{pv}, P_a, Q

(i) PSO - PV Emulator Screen

Figure 4.35: Integrated System Performance under Fourth Static PSC Scenario Using (GWO, WOA, PSO) MPPT Algorithms.

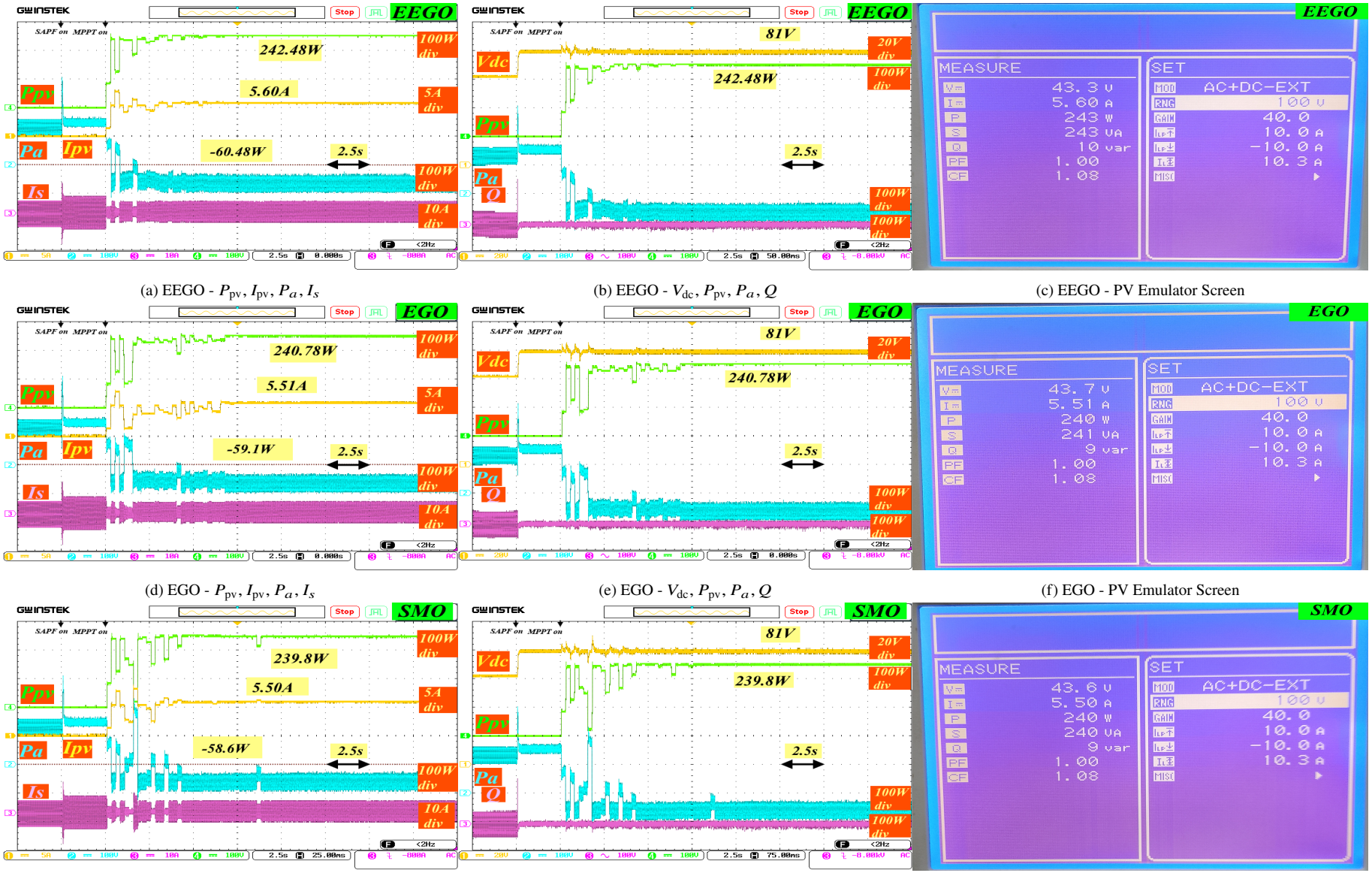

(a) EEGO - P_{pv}, I_{pv}, P_a, I_s

(b) EEGO - V_{dc}, P_{pv}, P_a, Q

(c) EEGO - PV Emulator Screen

(d) EGO - P_{pv}, I_{pv}, P_a, I_s

(e) EGO - V_{dc}, P_{pv}, P_a, Q

(f) EGO - PV Emulator Screen

(g) SMO - P_{pv}, I_{pv}, P_a, I_s

(h) SMO - V_{dc}, P_{pv}, P_a, Q

(i) SMO - PV Emulator Screen

Figure 4.36: Integrated System Performance under Fifth Static PSC Scenario Using (EEGO, EGO, SMO) MPPT Algorithms.

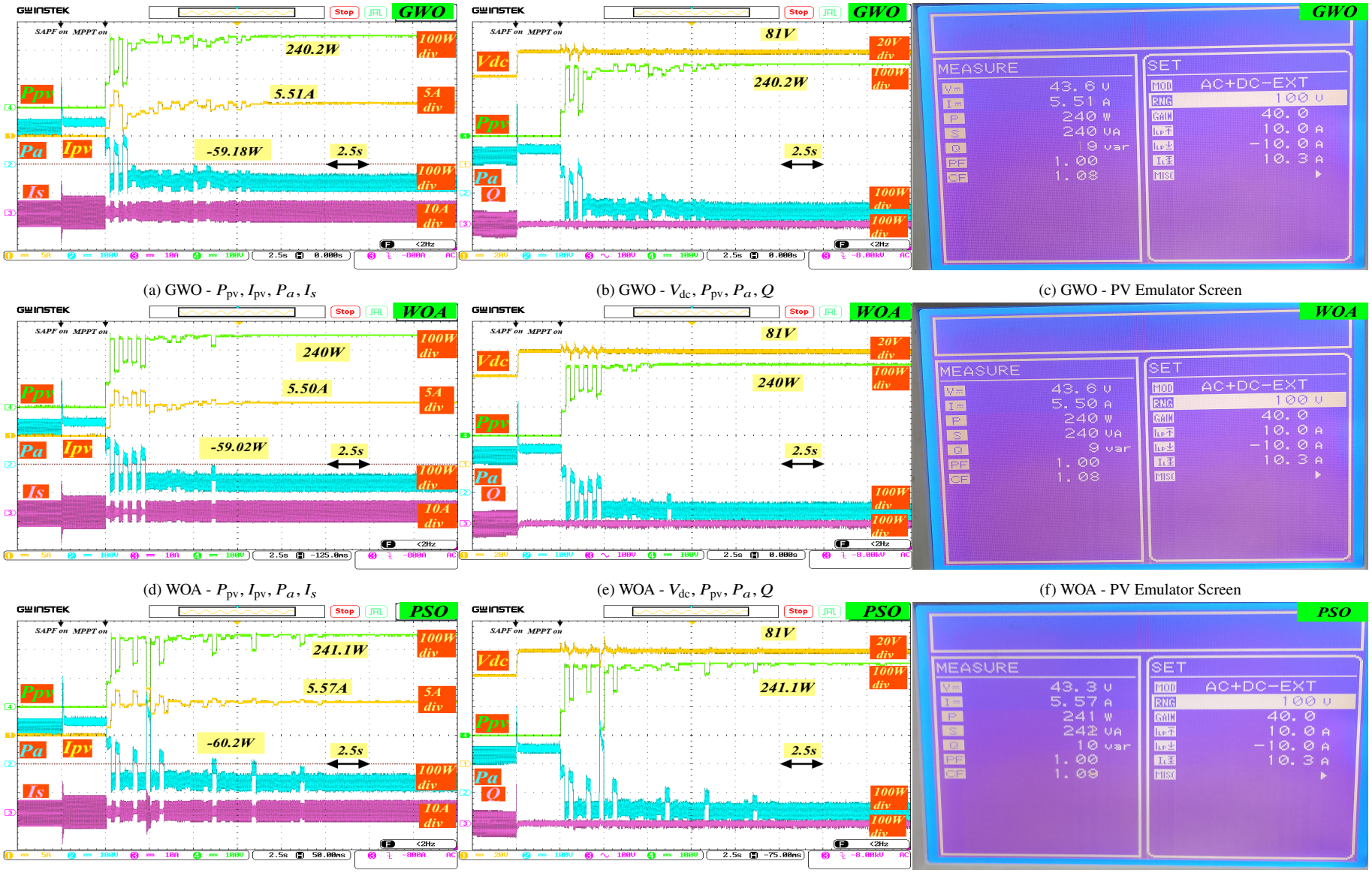

(a) GWO - P_{pv}, I_{pv}, P_a, I_s

(b) GWO - V_{dc}, P_{pv}, P_a, Q

(c) GWO - PV Emulator Screen

(d) WOA - P_{pv}, I_{pv}, P_a, I_s

(e) WOA - V_{dc}, P_{pv}, P_a, Q

(f) WOA - PV Emulator Screen

(g) PSO - P_{pv}, I_{pv}, P_a, I_s

(h) PSO - V_{dc}, P_{pv}, P_a, Q

(i) PSO - PV Emulator Screen

Figure 4.37: Integrated System Performance under Fifth Static PSC Scenario Using (GWO, WOA, PSO) MPPT Algorithms.

Across the five static partial shading scenarios, the integrated PV–SAPF system consistently demonstrated that the dominant limitation on surplus power injection is not the MPPT capability itself, but rather the voltage-dependent behavior of the nonlinear load under improved point-of-common-coupling (PCC) conditions. In all scenarios, the SAPF significantly enhanced voltage quality by mitigating harmonics and regulating reactive power, which resulted in an increase in RMS PCC voltage. Consequently, the nonlinear diode-bridge load absorbed additional active power beyond its nominal rating, reducing the apparent surplus available for grid injection even when high PV power levels were achieved.

Under moderate and high irradiance conditions (Scenarios 1, 3, and 5), the proposed EEGO algorithm consistently extracted the highest or near-highest PV power, with measured values ranging from approximately 168 W to 243 W. However, the expected theoretical surplus was partially offset by increased local load consumption, leading to reduced net grid injection. In lower irradiance and severe shading cases (Scenarios 2 and 4), grid support became necessary despite effective MPPT operation, confirming that load demand exceeded available PV generation rather than indicating control inefficiency. Across all scenarios, EEGO maintained the lowest grid dependency, minimal reactive power exchange, near-unity power factor, and the lowest crest factor, indicating superior harmonic mitigation and current waveform quality. Other algorithms (EGO, SMO, GWO, WOA, and PSO) exhibited comparable PV extraction levels but suffered from higher ripple, slightly degraded power quality indices, or increased grid reliance. These results collectively confirm that the proposed EEGO-based MPPT, when integrated with PDPC-controlled SAPF, provides the most balanced trade-off between maximum power extraction, grid power minimization, and power quality enhancement under diverse static partial shading conditions.

Final Remarks on Comparative Performance Evaluation

Across all five static partial shading scenarios, the EEGO algorithm consistently demonstrated superior MPPT capability, achieving near-optimal power extraction and stable convergence under complex irradiance patterns. However, when integrated with the SAPF-controlled grid interface, the effective grid injection efficiency was strongly influenced by load–voltage interactions rather than MPPT limitations.

The SAPF's harmonic mitigation improved PCC voltage quality, which increased the RMS voltage magnitude and consequently elevated the active power demand of the nonlinear load:

$$P_{\text{load}} \approx V_{\text{rms,PCC}} \cdot I_{\text{load, rms}}, \quad I_{\text{load, rms}} \propto V_{\text{rms,PCC}} \tag{4.6}$$

This phenomenon represents an apparent reduction in surplus PV power, not an energy loss mechanism. Secondary contributors include inverter conduction and switching losses, which remained within 5–10 W experimentally.

The results confirm that standalone MPPT efficiency alone is insufficient for evaluating real-

Table 4.2: Unified Performance Comparison of Integrated PV–SAPF System under Five Static Partial Shading Scenarios

Scenario	**Algorithm**	$P_{\mathbf{pv}}$ (W)	$I_{\mathbf{pv}}$ (A)	P_a (W)	**Surplus / Deficit (W)**	Q (var)	**PF**
1	EEGO	186.35	5.63	-5.35	40.35	0.5	1.00
	EGO	185.81	5.61	-4.75	40.06	0.5	1.00
	SMO	186.30	5.62	-4.80	40.50	0.6	1.00
	GWO	185.50	5.60	-4.50	40.00	1.0	0.99
	WOA	185.10	5.58	-4.18	39.92	1.3	0.98
	PSO	185.90	5.61	-4.73	40.17	0.8	0.99
2	EEGO	160.22	4.87	17.78	−3.56	0.1	1.00
	EGO	159.84	4.86	18.16	−4.32	0.5	1.00
	SMO	160.17	4.87	17.95	−3.78	0.5	1.00
	GWO	159.80	4.86	18.10	−4.30	1.0	0.99
	WOA	159.93	4.86	18.40	−4.47	0.8	0.99
	PSO	159.50	4.85	18.07	−4.57	0.6	1.00
3	EEGO	168.27	5.11	9.60	22.27	0.2	1.00
	EGO	166.99	5.07	11.01	20.01	0.4	1.00
	SMO	167.74	5.09	10.18	21.56	0.3	1.00
	GWO	167.40	5.08	10.70	21.30	0.6	0.99
	WOA	166.40	5.05	11.40	20.00	0.5	0.99
	PSO	167.60	5.09	11.50	20.10	0.4	1.00
4	EEGO	104.23	3.17	72.70	−30.93	0.3	0.99
	EGO	103.33	3.14	73.67	−31.00	0.4	0.99
	SMO	84.36	2.57	92.60	−30.96	0.5	0.98
	GWO	100.50	3.06	76.50	−31.00	0.6	0.98
	WOA	85.23	2.59	91.97	−31.20	0.7	0.98
	PSO	102.50	3.12	74.52	−31.02	0.5	0.99
5	EEGO	243.00	7.38	-60.48	97.00	0.2	1.00
	EGO	241.00	7.32	-59.10	95.90	0.3	1.00
	SMO	240.00	7.29	-58.60	95.40	0.3	1.00
	GWO	240.00	7.29	-59.18	94.82	0.5	0.99
	WOA	240.00	7.29	-59.02	94.98	0.4	0.99
	PSO	241.00	7.32	-60.20	94.80	0.3	1.00

world PV systems. A comprehensive assessment must consider grid interaction, power quality regulation, and voltage-dependent load behavior.

4.5.1 Harmonic Injection Analysis under Partial Shading Conditions

This section presents a detailed harmonic injection analysis of the integrated PV–SAPF system operating under partial shading conditions (PSC). The objective is to experimentally verify the capability of the proposed control strategy to regulate power flow direction, maintain low current distortion, and preserve grid power quality during both positive power absorption and reverse power injection modes. The analysis is based on time-domain waveforms, harmonic spectra, phasor representations, and steady-state power measurements.

4.5.1.1 Operating Modes and Figure Organization

For clarity, the experimental results are organized into three pairs of figures, corresponding to two distinct operating states:

- **State I: Positive Power Draw Mode**, where the nonlinear load continues to absorb active power from the grid while the SAPF performs harmonic and reactive power compensation.
- **State II: Reverse Power Injection Mode**, where excess PV power is injected back into the grid with controlled phase inversion.

Each operating state is documented using:

1. Harmonic analyzer waveforms and THD value,
2. Phasor (Fresnel) diagrams of voltage and current,
3. Power analyzer measurements including active power, reactive power, and power factor.

4.5.1.2 Analyzer Waveforms and THD

In the first operating state in Figure 4.38, the system supplies a nonlinear load drawing approximately 36 W of active power from the grid. The measured RMS current is approximately 0.9 A per phase. Due to the relatively low current magnitude, the harmonic analyzer reports a total harmonic distortion of THD = 7.7%. This value, while slightly elevated, remains within acceptable limits and is primarily attributed to the sensitivity of THD metrics at low current amplitudes, where background noise and switching ripple have a proportionally higher impact.

In the second operating state in Figure 4.38b, the PV system injects active power back into the grid, reaching approximately −84 W. The injected current increases to approximately 2.0 A RMS per phase, resulting in a significantly cleaner waveform. The measured current THD is reduced to 4.8%, demonstrating a clear improvement in spectral purity. This reduction is explained by the higher signal-to-noise ratio at increased current levels and the effectiveness of the PDPC strategy in enforcing sinusoidal current references.

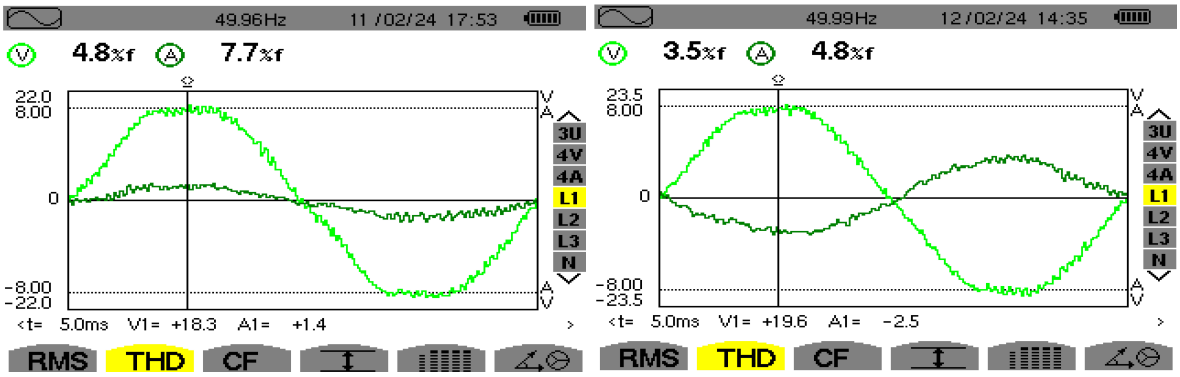

(a) State I (b) State II

Figure 4.38: Harmonic analyzer waveforms and THD value

4.5.1.3 Phasor Representation and Phase Control

The phasor diagrams provide direct insight into the system's power flow behavior. In State I in Figure 4.39, the grid current vectors are aligned with the corresponding phase voltages, indicating near-unity power factor operation. The 120° phase displacement between the three phases is preserved, confirming balanced three-phase operation despite partial shading.

In State II in Figure 4.39b, the phasor representation clearly shows a 180° phase shift between the injected currents and the grid voltages, while maintaining the 120° separation between phases. This phase inversion is a direct consequence of controlled reverse active power injection, demonstrating that the SAPF–PDPC system accurately regulates both the magnitude and direction of power flow without compromising phase balance or waveform integrity.

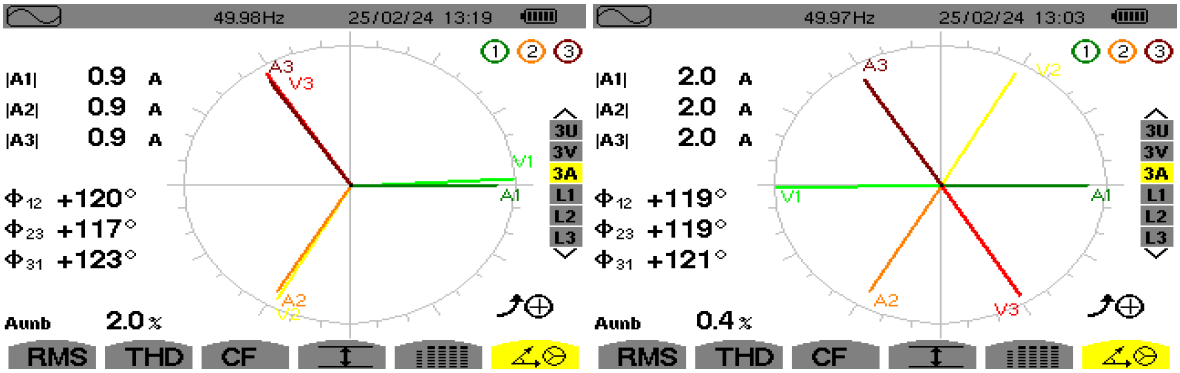

(a) State I (b) State II

Figure 4.39: Phasor (Fresnel) diagrams of voltage and current

4.5.1.4 Power Quantities and Power Factor Analysis

The power analyzer measurements further substantiate the observed behavior. In State I in Figure 4.40, the system operates with an average active power of 36.21 W and a negligible reactive power of 0.09 VAR. The resulting power factor is $\cos\varphi \approx 1$, with a very small $\tan\varphi = 0.002$, indicating effective reactive power compensation.

In State II in Figure 4.40b, the system delivers −84.22 W of active power to the grid, with reactive power limited to −1.09 VAR. The power factor reaches $\cos\varphi \approx -1$, confirming purely active reverse power injection. The small value of $\tan\varphi = 0.016$ reflects minimal reactive exchange, highlighting the controller's precision even during bidirectional power flow.

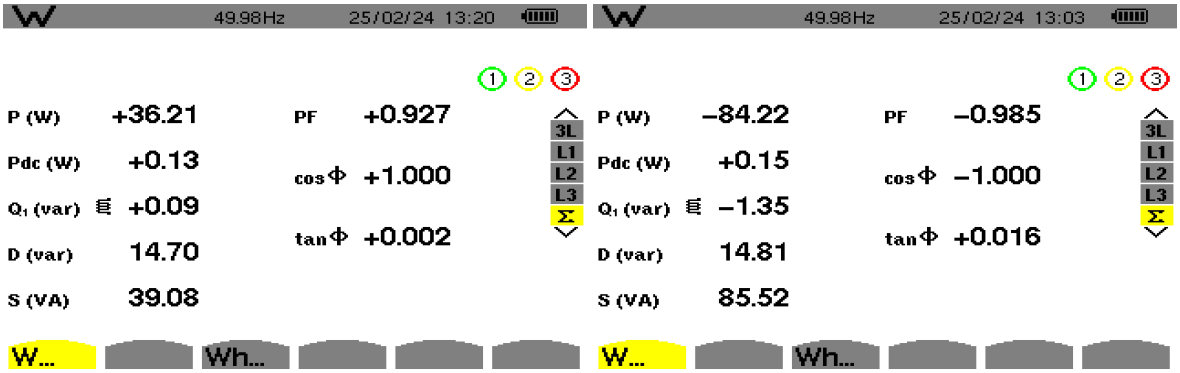

(a) State I (b) State II

Figure 4.40: Power analyzer measurements including active power, reactive power, and power factor

4.5.1.5 Discussion and Control Robustness under PSC

These results collectively demonstrate the robustness of the proposed control architecture under partial shading conditions. Despite fluctuating PV power availability and nonlinear load behavior, the SAPF regulated by PDPC maintains low harmonic distortion, precise phase control, and accurate power flow regulation. The ability to transition seamlessly between positive power absorption and reverse power injection, while preserving near-unity power factor and low THD, confirms the effectiveness of the predictive control strategy.

Importantly, all measurements comply with widely accepted power quality guidelines for current distortion and power factor, validating the system's suitability for grid-connected operation in realistic, PSC-affected environments.

The harmonic injection analysis confirms that the integrated PV–SAPF system achieves high-quality current waveforms, accurate bidirectional power control, and strong harmonic mitigation performance under partial shading. These findings provide experimental evidence of a well-tuned and resilient control system capable of supporting modern smart grid requirements even under adverse operating conditions.

Conclusion

This chapter has established a rigorous theoretical and control-oriented framework for the modeling, integration, and coordinated operation of a grid-connected photovoltaic (PV) system combined with a shunt active power filter (SAPF). The developments presented address the dual and inherently coupled objectives of maximizing energy extraction under partial shading conditions (PSCs) while ensuring high power quality in the presence of nonlinear loads and grid disturbances.

The PV subsystem was modeled using the single-diode equivalent circuit, enabling accurate representation of nonlinear electrical behavior, temperature sensitivity, and irradiance-dependent characteristics. This modeling approach effectively captures the formation of multiple local maxima on the power–voltage curve under PSCs, which constitute a major challenge for conventional maximum power point tracking (MPPT) techniques. To overcome these limitations, the Enhanced Equilibrium Optimizer with Gaussian perturbation (EEGO) was introduced as an advanced metaheuristic MPPT strategy. By incorporating a polynomial decay mechanism and an adaptive exploration–exploitation balance, EEGO achieves faster convergence and more reliable global maximum power point (GMPP) tracking compared to classical and state-of-the-art optimization-based methods, particularly in complex shading scenarios.

In parallel, the chapter presented a comprehensive mathematical modeling of the SAPF, including the voltage source inverter, coupling filter, and DC-link dynamics. On this foundation, a predictive direct power control (PDPC) strategy was adopted as the inner control loop. Unlike conventional cascaded control structures, PDPC operates directly on predicted active and reactive power variables using a discrete-time system model, enabling rapid dynamic response, precise power regulation, and robust steady-state performance without additional coordinate transformations or tuning-intensive regulators.

The coordinated operation of the PV system and SAPF highlights the importance of integrating energy extraction and power quality control within a unified framework. By regulating the DC-link voltage and injecting compensating currents, the SAPF ensures near-sinusoidal source currents, low total harmonic distortion (THD), and operation at or near unity power factor, even under harmonic-rich loading conditions. The predictive nature of the PDPC strategy allows the system to respond effectively to rapid changes in load demand and grid conditions.

Furthermore, the chapter presented a detailed harmonic injection analysis under partial shading conditions, providing experimental verification of the system's bidirectional power flow capability and power quality robustness. The results demonstrate that the proposed SAPF–PDPC control scheme maintains balanced three-phase operation, accurate phase control, and low current distortion during both positive power absorption and reverse active power injection modes. In positive power draw operation, the system achieves near-unity power factor with negligible reactive power exchange, despite low current amplitudes. During reverse power injection, the controller enforces a precise 180° phase shift between grid voltage and injected current while preserving phase symmetry and reducing THD, confirming effective active power

delivery back to the grid.

These results collectively confirm that the proposed control architecture is capable of maintaining high-quality current waveforms, accurate power flow regulation, and strong harmonic mitigation performance even under adverse operating conditions caused by partial shading. The demonstrated ability to transition seamlessly between operating modes, while preserving compliance with widely accepted power quality standards such as IEEE 519-2022, underscores the robustness and practical relevance of the proposed approach.

Overall, this chapter provides a unified theoretical and control foundation for PV-based distributed generation systems operating in harmonic-rich and dynamically varying environments. The methodologies developed herein support scalable, efficient, and reliable integration of renewable energy sources into modern smart grids, and they form a solid basis for the simulation studies and experimental validation presented in the subsequent chapters.

Conclusion

Conclusion and Future Work

The increasing penetration of photovoltaic (PV) generation into modern power systems has intensified the need for control strategies capable of addressing partial shading conditions (PSCs), harmonic distortion, bidirectional power flow, and grid compliance simultaneously. This thesis, entitled *"Contribution to the Control of a Reactive Power Compensation System Powered by a Photovoltaic Generator"*, has addressed these challenges through the development of an integrated control and experimental framework that unifies advanced maximum power point tracking, real-time PV emulation, and power quality enhancement within a grid-connected environment.

A central contribution of this work is the development of the Enhanced Eel–Grouper Optimization (EEGO) algorithm for global maximum power point tracking (GMPPT) under PSCs. EEGO introduces an adaptive exploration–exploitation balance supported by restart and perturbation mechanisms, enabling fast and reliable convergence to the global optimum despite the presence of multiple local maxima. Real-time implementation on a dSPACE 1104 platform demonstrated consistently high tracking efficiency, rapid convergence following irradiance variations, and reduced steady-state oscillations compared to conventional and state-of-the-art metaheuristic MPPT techniques.

Complementing the MPPT strategy, this thesis proposed and validated and high-fidelity PV emulation platform based on a GW Instek APS-1102A programmable DC source. By generating numerically controlled I–V characteristics corresponding to partial shading scenarios, the emulator enabled repeatable and accurate experimental evaluation of MPPT algorithms with an error below 5%. This contribution lowers the barrier for experimental research in PV optimization and provides a flexible tool for testing renewable energy control strategies under realistic operating conditions.

Beyond energy extraction, the thesis addressed power quality and grid interaction through the integration of a shunt active power filter (SAPF) controlled by a predictive direct power control (PDPC) strategy. The SAPF effectively compensated harmonic and reactive currents drawn by nonlinear loads, reducing current total harmonic distortion (THD) from double-digit values to below 3% and achieving near-unity power factor operation. The predictive nature of PDPC enabled fast transient response and stable steady-state performance without relying on cascaded control loops or extensive tuning.

A key and original outcome of this research is the detailed experimental analysis of bidirectional power flow, including reverse active power injection into the grid under partial shading

conditions. Harmonic spectrum analysis, phasor representations, and power measurements confirmed that the proposed SAPF–PDPC control architecture accurately regulates both the magnitude and direction of power flow. During reverse injection, the controller enforced a precise 180° phase shift between grid voltage and injected current while preserving balanced three-phase operation and maintaining low THD levels compliant with established power quality standards. These results experimentally validate the system's capability to operate as a controlled grid-supporting unit rather than a passive energy source, even under adverse PSCs.

An important insight revealed by this work is the interaction between power quality improvement and apparent power demand. By mitigating harmonic currents, the SAPF reduces voltage drops across the source impedance, thereby increasing the point of common coupling (PCC) voltage. For voltage-dependent nonlinear loads, this improvement results in increased load power consumption, which in turn reduces the surplus power available for grid injection. Together with unavoidable inverter switching and conduction losses, this phenomenon explains the observed reduction in injection efficiency and provides a realistic, experimentally grounded understanding of power flow behavior in integrated PV–SAPF systems.

Overall, this thesis demonstrates that high-efficiency GMPPT, harmonic mitigation, reactive power compensation, and controlled bidirectional power injection can be achieved simultaneously within a unified framework. The proposed combination of EEGO-based MPPT, PV emulation, and SAPF–PDPC control provides a scalable and resilient solution for PV integration in harmonic-rich and dynamically varying grid environments. The experimental results confirm compliance with widely accepted power quality requirements while maintaining robust operation under PSCs.

Despite the promising results, the investigations presented herein were conducted at laboratory scale under controlled grid conditions. Scaling the proposed framework to higher power levels will require further optimization of filter design, switching frequency selection, and thermal management. In addition, system behavior under severe grid disturbances, such as voltage sags, frequency deviations, and unbalanced faults, remains an open research direction.

Future work may extend this research along several axes. Multi-objective optimization techniques could be incorporated into EEGO to simultaneously consider harmonic distortion, voltage regulation, and thermal constraints. Machine learning and forecasting methods may be integrated to anticipate irradiance variations and further reduce MPPT convergence time. Hardware acceleration using FPGA-based platforms could enable sub-millisecond control response for utility-scale systems. Finally, validation within hybrid AC/DC microgrids and investigation of cybersecurity aspects for intelligent PV controllers represent promising directions for advancing the practical deployment of the proposed framework.

In conclusion, this thesis delivers a comprehensive and experimentally validated contribution to PV-based reactive power compensation and grid interaction. By addressing maximum power extraction, power quality, and bidirectional energy flow within a single coordinated architecture, it advances the state of the art in smart grid–ready photovoltaic systems and lays a solid foundation for future research and real-world implementation.

Bibliography

Bibliography

[1] International Renewable Energy Agency (IRENA), "Renewable capacity statistics 2024", IRENA, Tech. Rep., 2024. [Online]. Available: https://www.irena.org/Publications/2024/Mar/Renewable-capacity-statistics-2024

[2] International Energy Agency (IEA), "Renewables 2024: analysis and forecast to 2030", IEA, Tech. Rep., 2024. [Online]. Available: https://www.iea.org/reports/renewables-2024

[3] X. Fang, S. Misra, G. Xue, and D. Yang, "Smart grid – the new and improved power grid: a survey", *IEEE Communications Surveys & Tutorials*, vol. 14, no. 4, pp. 944–980, 2012.

[4] M. Mahmood, P. Chowdhury, R. Yeassin, M. Hasan, T. Ahmad, and N.-U.-R. Chowdhury, "Impacts of digitalization on smart grids, renewable energy, and demand response: an updated review of current applications", *Energy Conversion and Management: X*, vol. 24, 2024, ISSN: 25901745. DOI: 10.1016/j.ecmx.2024.100790

[5] M. H. Bollen, *Understanding Power Quality Problems: Voltage Sags and Interruptions*. Wiley-IEEE Press, 2000.

[6] N. Mohan, T. M. Undeland, and W. P. Robbins, "Power electronics: converters, applications, and design", 2022.

[7] Electric Power Research Institute (EPRI), "Cost of power disturbances to industrial and digital economy companies", Tech. Rep., 2020. [Online]. Available: https://www.epri.com/research

[8] F. O. Igbinovia, G. Fandi, Z. Muller, and J. Tlusty, *Reputation of the synchronous condenser technology in modern power grid*, Conference Paper, 2018. DOI: 10.1109/powercon.2018.8601540

[9] M. Y. Worku et al., "A comprehensive review of recent maximum power point tracking techniques for photovoltaic systems under partial shading", *Sustainability*, vol. 15, no. 14, 2023, ISSN: 2071-1050. DOI: 10.3390/su151411132

[10] M. S. Endiz, G. Gökkuş, A. E. Coşgun, and H. Demir, "A review of traditional and advanced mppt approaches for pv systems under uniformly insolation and partially shaded conditions", *Applied Sciences*, vol. 15, no. 3, 2025, ISSN: 2076-3417. DOI: 10.3390/app15031031

[11] F. Rahman, M. Jarif Bulbul, M. Yeamin, and A. Ahammad, "The effects of partial shading on a grid-integrated photovoltaic system with matlab-simulink", *Turkish Journal of Electrical Power and Energy Systems*, vol. 5, no. 1, pp. 66–77, 2025, ISSN: 27916049. DOI: 10.5152/tepes.2024.24014

[12] B. Mirafzal and A. Adib, "On grid-interactive smart inverters: features and advancements", *IEEE Access*, vol. 8, pp. 160 526–160 536, 2020, ISSN: 2169-3536. DOI: 10.1109/access.2020.3020965

[13] *Ieee recommended practices and requirements for harmonic control in electrical power systems*, Journal Article, 2022. DOI: 10.1109/ieeestd.2022.9848440

[14] J. Nelson, *The Physics of Solar Cells* (Physics textbook). Imperial College Press, 2003, ISBN: 9781860943409. [Online]. Available: https://books.google.fr/books?id=p_V9ngEACAAJ

[15] M. G. Villalva, J. R. Gazoli, and E. R. Filho, *Comprehensive Approach to Modeling and Simulation of Photovoltaic Arrays*. 2009, vol. 24, pp. 1198–1208.

[16] L. Jiang, "Modeling and optimization of photovoltaic systems under partially shaded and rapidly changing conditions", Thesis, Centre for High Performance Embedded Systems, 2014. DOI: https://doi.org/10.32657%2F10356%2F62198 [Online]. Available: https://hdl.handle.net/10356/62198

[17] K. KACED, "Study of mppt techniques for photovoltaic systems under partial shading conditions", Thesis, National Polytechnic School, 2018. [Online]. Available: http://repository.enp.edu.dz/xmlui/handle/123456789/2199

[18] B. Ziqiang, "Intelligent global maximum power point tracking strategies based on shading perception for photovoltaic systems", Thesis, University of Liverpool, 2021. DOI: https://doi.org/10.17638/03136237

[19] H. Gohar Ali, "Maximum power point tracking of photovoltaic system using non-linear controllers", Thesis, University of Barcelona, 2020. [Online]. Available: http://hdl.handle.net/10803/671122

[20] I. Owusu-Nyarko, "Maximum power point tracking and control of grid interfacing pv systems", Thesis, University of Strathclyde, 2021. DOI: https://doi.org/10.48730/z9qa-2j80

[21] C. Hussaian Basha, M. Palati, C. Dhanamjayulu, S. M. Muyeen, and P. Venkatareddy, "A novel on design and implementation of hybrid mppt controllers for solar pv systems under various partial shading conditions", *Sci Rep*, vol. 14, no. 1, p. 1609, 2024. DOI: 10.1038/s41598-023-49278-9 [Online]. Available: https://www.ncbi.nlm.nih.gov/pubmed/38238374

[22] Z. Smara, A. Aissat, H. Deboucha, H. Rezk, and S. Mekhilef, "An enhanced global mppt method to mitigate overheating in pv systems under partial shading conditions", *Renewable Energy*, vol. 234, 2024, ISSN: 09601481. DOI: 10.1016/j.renene.2024.121187

[23] K. Xia, Y. Li, and B. Zhu, "Improved photovoltaic mppt algorithm based on ant colony optimization and fuzzy logic under conditions of partial shading", *IEEE Access*, vol. 12, pp. 44 817–44 825, 2024, ISSN: 2169-3536. DOI: 10.1109/access.2024.3381345

[24] A. T. Naser, K. K. Mohammed, N. F. A. Aziz, K. b. Kamil, and S. Mekhilef, "Improved coot optimizer algorithm-based mppt for pv systems under complex partial shading conditions and load variation", *Energy Conversion and Management: X*, vol. 22, 2024, ISSN: 25901745. DOI: 10.1016/j.ecmx.2024.100565

[25] C. Mai, L. Zhang, X. Chao, X. Hu, X. Wei, and J. Li, "A novel mppt technology based on dung beetle optimization algorithm for pv systems under complex partial shade conditions", *Sci Rep*, vol. 14, no. 1, p. 6471, 2024. DOI: 10.1038/s41598-024-57268-8 [Online]. Available: https://www.ncbi.nlm.nih.gov/pubmed/38499624

[26] M. H. El-Banna, M. R. Hammad, A. I. Megahed, K. M. AboRas, A. Alkuhayli, and N. Gowtham, "On-grid optimal mppt for fine-tuned inverter based pv system using golf optimizer considering partial shading effect", *Alexandria Engineering Journal*, vol. 103, pp. 180–196, 2024, ISSN: 11100168. DOI: 10.1016/j.aej.2024.05.115

[27] A. F. Mirza, M. Mansoor, K. Zhan, and Q. Ling, "High-efficiency swarm intelligent maximum power point tracking control techniques for varying temperature and irradiance", *Energy*, vol. 228, 2021, ISSN: 03605442. DOI: 10.1016/j.energy.2021.120602

[28] F. Abdelmalek et al., "Experimental validation of effective zebra optimization algorithm-based mppt under partial shading conditions in photovoltaic systems", *Sci Rep*, vol. 14, no. 1, p. 26 047, 2024. DOI: 10.1038/s41598-024-77488-2 [Online]. Available: https://www.ncbi.nlm.nih.gov/pubmed/39472710

[29] D. J. K. Kishore, M. R. Mohamed, K. Sudhakar, and K. Peddakapu, "A new metaheuristic-based mppt controller for photovoltaic systems under partial shading conditions and complex partial shading conditions", *Neural Computing and Applications*, vol. 36, no. 12, pp. 6613–6627, 2024, ISSN: 0941-0643 1433-3058. DOI: 10.1007/s00521-023-09407-x

[30] R. Celikel, M. Yilmaz, and A. Gundogdu, "Improved voltage scanning algorithm based mppt algorithm for pv systems under partial shading conduction", *Heliyon*, vol. 10, no. 20, e39382, 2024. DOI: 10.1016/j.heliyon.2024.e39382 [Online]. Available: https://www.ncbi.nlm.nih.gov/pubmed/39640683

[31] N. H. Alombah et al., "Multiple-to-single maximum power point tracking for empowering conventional mppt algorithms under partial shading conditions", *Sci Rep*, vol. 15, no. 1, p. 14 540, 2025. DOI: 10.1038/s41598-025-98619-3 [Online]. Available: https://www.ncbi.nlm.nih.gov/pubmed/40281064

[32] H. Belmadani et al., "A new fast and efficient mppt algorithm for partially shaded pv systems using a hyperbolic slime mould algorithm", *International Journal of Energy Research*, vol. 2024, no. 1, 2024, ISSN: 0363-907X 1099-114X. DOI: 10.1155/2024/5585826

[33] P. Qi, H. Xia, X. Cai, M. Yu, N. Jiang, and Y. Dai, "Novel global mppt technique based on hybrid cuckoo search and artificial bee colony under partial-shading conditions", *Electronics*, vol. 13, no. 7, 2024, ISSN: 2079-9292. DOI: 10.3390/electronics13071337

[34] A. Talib Naser, K. Khairullah Mohammed, N. Fadilah Ab Aziz, A. Elsanabary, K. Binti Kamil, and S. Mekhilef, "A fast-tracking mppt-based modified coot optimization algorithm for pv systems under partial shading conditions", *Ain Shams Engineering Journal*, vol. 15, no. 10, 2024, ISSN: 20904479. DOI: 10.1016/j.asej.2024.102967

[35] T. Nagadurga, V. D. Raju, A. B. Barnawi, J. K. Bhutto, A. Razak, and A. W. Wodajo, "Global mppt optimization for partially shaded photovoltaic systems", *Sci Rep*, vol. 15, no. 1, p. 10 831, 2025. DOI: 10.1038/s41598-025-89694-7 [Online]. Available: https://www.ncbi.nlm.nih.gov/pubmed/40155676

[36] H. Karimi, A. Siadatan, and A. Rezaei-Zare, "A hybrid po-fuzzy-based maximum power point tracking (mppt) algorithm for photovoltaic systems under partial shading conditions", *IEEE Access*, pp. 1–1, 2025, ISSN: 2169-3536. DOI: 10.1109/access.2025.3533314

[37] A. F. Challoob, N. A. Bin Rahmat, V. K. A/L Ramachandaramurthy, and A. J. Humaidi, "Hybridization of csa and pso improves the efficacy of mppt for solar photovoltaic array with partial shading", *International Review of Applied Sciences and Engineering*, vol. 15, no. 3, pp. 323–337, 2024, ISSN: 2062-0810 2063-4269. DOI: 10.1556/1848.2024.00751

[38] L. Zaghba, A. Borni, M. K. Benbitour, and A. Fezzani, "Improving photovoltaic energy harvesting systems with hybrid fuzzy logic-pi mppt optimized by pso under normal and partial shading conditions", *Electrical Engineering*, vol. 107, no. 4, pp. 4897–4919, 2024, ISSN: 0948-7921 1432-0487. DOI: 10.1007/s00202-024-02800-2

[39] M. K. Senapati, C. Pradhan, S. Padmanaban, and O. A. Zaabi, "Photovoltaic mppt performance adaptability to partial shading resilience and load variations with modified adaptive jaya optimization", *IEEE Transactions on Consumer Electronics*, pp. 1–1, 2025, ISSN: 0098-3063 1558-4127. DOI: 10.1109/tce.2025.3532660

[40] O. Fergani, R. Mechgoug, A. Afulay Bouzid, N. Tkouti, and A. Mazari, "A new modified bacterial foraging mppt technique with dynamic mutation rates for photovoltaic systems under partial shading conditions", *International Journal of Engineering*, vol. 37, no. 8, pp. 1569–1579, 2024, ISSN: 1728144X 17359244. DOI: 10.5829/ije.2024.37.08b.10

[41] D. E. Zabia, H. Afghoul, and O. Kraa, *A novel equilibrium optimizer for tracking the maximum power of a photovoltaic system under non-uniform conditions*, Conference Paper, 2022. DOI: 10.1109/icaee53772.2022.9962015

[42] Z. D. Eddine, K. Okba, and A. Hamza, *Grey wolf optimization parameter enhancement for tracking the maximum power point of pv system under multiple cluster complex partial shading*, Conference Paper, 2022. DOI: 10.1109/ssd54932.2022.9955709

[43] B. Singh and S. Gairola, *A novel harmonic mitigation converter for variable frequency drives*, Conference Paper, 2006. DOI: 10.1109/pedes.2006.344400

[44] A. Kalair, N. Abas, A. R. Kalair, Z. Saleem, and N. Khan, "Review of harmonic analysis, modeling and mitigation techniques", *Renewable and Sustainable Energy Reviews*, vol. 78, pp. 1152–1187, 2017, ISSN: 13640321. DOI: 10.1016/j.rser.2017.04.121

[45] A. Chaoui, "Three-phase active filter for non-linear loads", Thesis, 2010. [Online]. Available: http://dspace.univ-setif.dz:8888/jspui/handle/123456789/2409

[46] B. Boukezata, "Study and order of an energy conversion chain for a photovoltaic solar system", Thesis, 2012. [Online]. Available: http://dspace.univ-setif.dz:8888/jspui/handle/123456789/1555

[47] S. Mustapha, "Contribution to the study of hybrid active filters", Thesis, 2012. [Online]. Available: http://dspace.univ-setif.dz:8888/jspui/handle/123456789/1994

[48] K. Djazia, "Study of active filters for unbalanced and distorted networks", Thesis, 2015. [Online]. Available: http://dspace.univ-setif.dz:8888/jspui/handle/123456789/1709

[49] H. AFGHOUL, "Advanced approach to active filtering and power control in photovoltaic installations interconnected to the network", Thesis, 2016. [Online]. Available: http://virtuelcampus.univ-msila.dz/ImpactUniv/?p=1059

[50] S. Ouchen, "Contribution to direct power control dedicated to active filtering, associated with a photovoltaic source", Thesis, 2017. [Online]. Available: http://thesis.univ-biskra.dz/id/eprint/2967

[51] H. Afghoul, F. Krim, D. Chikouche, and A. Beddar, "Design and real time implementation of fuzzy switched controller for single phase active power filter", *ISA Trans*, vol. 58, pp. 614–21, 2015. DOI: 10.1016/j.isatra.2015.07.008 [Online]. Available: https://www.ncbi.nlm.nih.gov/pubmed/26233491

[52] S. Ouchen, H. Steinhart, M. Benbouzid, and F. Blaabjerg, "Robust dpc-svm control strategy for shunt active power filter based on h regulators", *International Journal of Electrical Power Energy Systems*, vol. 117, 2020, ISSN: 01420615. DOI: 10.1016/j.ijepes.2019.105699

[53] B. Boukezata, A. Chaoui, J.-P. Gaubert, and M. Hachemi, "Power quality improvement by an active power filter in grid-connected photovoltaic systems with optimized direct power control strategy", *Electric Power Components and Systems*, vol. 44, no. 18, pp. 2036–2047, 2016, ISSN: 1532-5008 1532-5016. DOI: 10.1080/15325008.2016.1210698

[54] P. K. Barik, G. Shankar, P. K. Sahoo, and S. Samal, "Simulation and real-time implementation of a combined control strategy-based shunt active power filter in microgrid", *Sustainable Computing: Informatics and Systems*, vol. 46, 2025, ISSN: 22105379. DOI: 10.1016/j.suscom.2025.101103

[55] D. Bakria et al., "An optimized shunt active power filter using the golden jackal optimizer for power quality improvement", *Sci Rep*, vol. 15, no. 1, p. 15 869, 2025. DOI: 10.1038/s41598-025-00204-1 [Online]. Available: https://www.ncbi.nlm.nih.gov/pubmed/40335522

[56] J. Fei and H. Wang, "Experimental investigation of recurrent neural network fractional-order sliding mode control of active power filter", *IEEE Transactions on Circuits and Systems II: Express Briefs*, vol. 67, no. 11, pp. 2522–2526, 2020, ISSN: 1549-7747 1558-3791. DOI: 10.1109/tcsii.2019.2953223

[57] J. Fei, N. Liu, S. Hou, and Y. Fang, "Neural network complementary sliding mode current control of active power filter", *IEEE Access*, vol. 9, pp. 25 681–25 690, 2021, ISSN: 2169-3536. DOI: 10.1109/access.2021.3056224

[58] H. Afghoul, D. Chikouche, F. Krim, B. Babes, and A. Beddar, "Implementation of fractional-order integral-plus-proportional controller to enhance the power quality of an electrical grid", *Electric Power Components and Systems*, vol. 44, no. 9, pp. 1018–1028, 2016, ISSN: 1532-5008 1532-5016. DOI: 10.1080/15325008.2016.1147509

[59] T. M. T. Thentral et al., "Development of control techniques using modified fuzzy based sapf for power quality enhancement", *IEEE Access*, vol. 9, pp. 68 396–68 413, 2021, ISSN: 2169-3536. DOI: 10.1109/access.2021.3077450

[60] S. Orts-Grau, J. C. Alfonso-Gil, P. Balaguer-Herrero, G. Martínez-Navarro, and F. J. Gimeno-Sales, "Generalized one-cycle current controller for improved sapf power quality management", *International Journal of Electrical Power Energy Systems*, vol. 157, 2024, ISSN: 01420615. DOI: 10.1016/j.ijepes.2024.109833

[61] R. Hrbac, T. Mlcak, and V. Kolar, "Improving power quality with the use of a new method of serial active power filter (sapf) control", *Elektronika ir Elektrotechnika*, vol. 23, no. 1, 2017, ISSN: 2029-5731 1392-1215. DOI: 10.5755/j01.eie.23.1.17578

[62] A. Rath and G. Srungavarapu, "An advanced shunt active power filter (sapf) for non-ideal grid using predictive dpc", *IETE Technical Review*, vol. 40, no. 4, pp. 521–534, 2022, ISSN: 0256-4602 0974-5971. DOI: 10.1080/02564602.2022.2127946

[63] G. Boudechiche, M. Sarra, O. Aissa, J.-P. Gaubert, B. Benlahbib, and A. Lashab, "Anti-windup fopid-based dpc for sapf interconnected to a pv system tuned using pso algorithm", *European Journal of Electrical Engineering*, vol. 22, no. 4-5, pp. 313–324, 2020, ISSN: 21033641 21167109. DOI: 10.18280/ejee.224-503

[64] S. Ouchen, M. Benbouzid, F. Blaabjerg, A. Betka, and H. Steinhart, "Direct power control of shunt active power filter using space vector modulation based on supertwisting sliding mode control", *IEEE Journal of Emerging and Selected Topics in Power Electronics*, vol. 9, no. 3, pp. 3243–3253, 2021, ISSN: 2168-6777 2168-6785. DOI: 10.1109/jestpe.2020.3007900

[65] B. Boukezata, A. Chaoui, J. P. Gaubert, and O. Boutalbi, "An enhanced control scheme for multifunctional grid connected pv system using fuzzy and predictive direct power control", *Bulletin of Electrical Engineering and Informatics*, vol. 13, no. 2, pp. 853–864, 2024, ISSN: 2302-9285 2089-3191. DOI: 10.11591/eei.v13i2.5660

[66] S. Prakash, M. Alkhatib, H. F. Sindi, S. Alghamdi, R. K. Behera, and U. R. Muduli, "Adaptive control for shunt active power filter under stochastic solar photovoltaics behavior", *IEEE Journal of Emerging and Selected Topics in Power Electronics*, pp. 1–1, 2025, ISSN: 2168-6777 2168-6785. DOI: 10.1109/jestpe.2025.3525489

[67] S.Gomathi, P. Kandasamy, K. P. K, S.Hemalatha, V. S. K, and S. Jaanaa Rubavathy, *Improvement of power quality in a power system using the qbc-shunt active filter and fopid technique for renewable energy systems*, Conference Paper, 2025. DOI: 10.1109/icears64219.2025.10940980

[68] A. Singh, "Applications of adaptive long short-term memory to active filtering", *Journal of The Institution of Engineers (India): Series B*, vol. 103, no. 3, pp. 737–746, 2021, ISSN: 2250-2106 2250-2114. DOI: 10.1007/s40031-021-00685-4

[69] J. Fei and Y. Chen, "Dynamic terminal sliding-mode control for single-phase active power filter using new feedback recurrent neural network", *IEEE Transactions on Power Electronics*, vol. 35, no. 9, pp. 9904–9922, 2020, ISSN: 0885-8993 1941-0107. DOI: 10.1109/tpel.2020.2974470

[70] S. Lidaighbi, M. Elyaqouti, D. Ben Hmamou, D. Saadaoui, K. Assalaou, and E. Arjdal, "A new hybrid method to estimate the single-diode model parameters of solar photovoltaic panel", *Energy Conversion and Management: X*, vol. 15, 2022, ISSN: 25901745. DOI: 10.1016/j.ecmx.2022.100234

[71] H. G. Sezgin-Ugranlı, "Photovoltaic system performance under partial shading conditions: insight into the roles of bypass diode numbers and inverter efficiency curve", *Sustainability*, vol. 17, no. 10, 2025, ISSN: 2071-1050. DOI: 10.3390/su17104626

[72] R. Vieira, F. de Araújo, M. Dhimish, and M. Guerra, "A comprehensive review on bypass diode application on photovoltaic modules", *Energies*, vol. 13, no. 10, 2020, ISSN: 1996-1073. DOI: 10.3390/en13102472

[73] J. D. Bastidas-Rodríguez, C. A. Ramos-Paja, and S. I. Serna-Garcés, "Improved modelling of bypass diodes for photovoltaic applications", *Alexandria Engineering Journal*, vol. 61, no. 8, pp. 6261–6273, 2022, ISSN: 11100168. DOI: 10.1016/j.aej.2021.11.055

[74] Z. Ali, S. Abbas, A. Mahmood, S. Ali, S. Javed, and C.-L. Su, "A study of a generalized photovoltaic system with mppt using perturb and observer algorithms under varying conditions", *Energies*, vol. 16, no. 9, 2023, ISSN: 1996-1073. DOI: 10.3390/en16093638

[75] A. T. Naser, N. F. Ab Aziz, K. K. Mohammed, K. b. Kamil, and S. Mekhilef, "Performance assessment of meta-heuristic mppt strategies for solar panels under complex partial shading conditions and load variation", *Global Energy Interconnection*, vol. 8, no. 4, pp. 554–571, 2025, ISSN: 20965117. DOI: 10.1016/j.gloei.2025.03.004

[76] B. N. Alajmi, N. A. Ahmed, I. Abdelsalam, and M. I. Marei, "A robust mppt algorithm for pv systems using advanced hill climbing and simulated annealing techniques", *Electronics*, vol. 14, no. 18, 2025, ISSN: 2079-9292. DOI: 10.3390/electronics14183644

[77] A. Mohammadzadeh and S. Mirjalili, "Eel and grouper optimizer: a nature-inspired optimization algorithm", *Cluster Computing*, vol. 27, no. 9, pp. 12 745–12 786, 2024, ISSN: 1386-7857 1573-7543. DOI: 10.1007/s10586-024-04545-w

[78] J. Pérez-Ramírez, D. Montoya-Acevedo, W. Gil-González, O. D. Montoya, and C. Restrepo, "Shunt active power filter using model predictive control with stability guarantee", *e-Prime - Advances in Electrical Engineering, Electronics and Energy*, vol. 12, 2025, ISSN: 27726711. DOI: 10.1016/j.prime.2025.101029

[79] K. Hemici and M. O. Mahmoudi, "Advanced control of shunt active power filter based on flying capacitor multicellular inverter using backstepping and ps-pwm", *ENP Engineering Science Journal*, vol. 5, no. 2, pp. 52–57, 2026, ISSN: 2773-4293 2716-912X. DOI: 10.53907/enpesj.v5i2.338

[80] M. Meraouah, F. Kaddari, S. Hassaine, Y. Mihoub, S. Heroual, and N. Khenfar, "Predictive direct power control of shunt active power filter associated to pv system and ann-backstepping mppt", en, *Algerian Journal of Renewable Energy and Sustainable Development*, vol. 6, no. 1, pp. 109–118, 2024. [Online]. Available: https://asjp.cerist.dz/en/article/252552

[81] H. Ghanayem, M. Alathamneh, X. Yang, S. Seo, and R. M. Nelms, "Enhanced three-phase shunt active power filter utilizing an adaptive frequency proportional-integral–resonant controller and a sensorless voltage method", *Energies*, vol. 18, no. 1, 2024, ISSN: 1996-1073. DOI: 10.3390/en18010116

[82] B. Dwinanto, S. Setiyono, F. Thalib, and H. Siswono, "Single-phase power shunt active filter design using photovoltaic as reactive power compensator", *Electrical Engineering Electromechanics*, no. 3, pp. 59–64, 2025, ISSN: 2309-3404 2074-272X. DOI: 10.20998/2074-272x.2025.3.09

[83] D. Bakria et al., "An optimized shunt active power filter using the golden jackal optimizer for power quality improvement", *Scientific Reports*, vol. 15, no. 1, 2025, ISSN: 2045-2322. DOI: 10.1038/s41598-025-00204-1

[84] P. Patel, S. Samal, C. Jena, and P. K. Barik, "Shunt active power filter with msrf-pi-ahcc technique for harmonics mitigation in a hybrid energy system under load changing condition", *Australian Journal of Electrical and Electronics Engineering*, vol. 20, no. 1, pp. 63–77, 2022, ISSN: 1448-837X 2205-362X. DOI: 10.1080/1448837x.2022.2114154

[85] Y. Hoon, M. Mohd Radzi, M. Hassan, and N. Mailah, "Control algorithms of shunt active power filter for harmonics mitigation: a review", *Energies*, vol. 10, no. 12, 2017, ISSN: 1996-1073. DOI: 10.3390/en10122038

[86] R. Panigrahi, B. Subudhi, and P. C. Panda, "Model predictive-based shunt active power filter with a new reference current estimation strategy", *IET Power Electronics*, vol. 8, no. 2, pp. 221–233, 2015, ISSN: 1755-4535 1755-4543. DOI: 10.1049/iet-pel.2014.0276

[87] B. Deffaf, H. Farid, H. Benbouhenni, S. Medjmadj, and N. Debdouche, "Synergetic control for three-level voltage source inverter-based shunt active power filter to improve power quality", *Energy Reports*, vol. 10, pp. 1013–1027, 2023, ISSN: 23524847. DOI: 10.1016/j.egyr.2023.07.051

Appendices

c

The Simulation Block Diagram (Simulink/Matlab2012b)

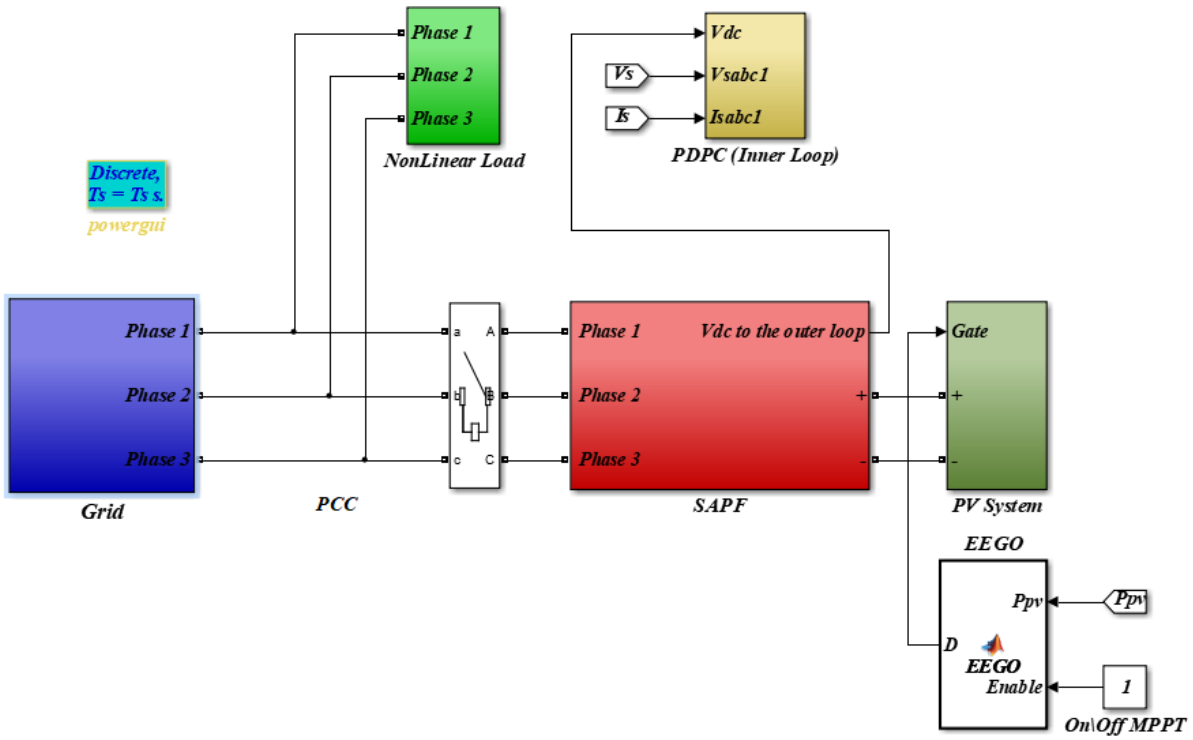

Figure A.41: General System Block Diagram of the Integrated PV-SAPF System with PDPC Control

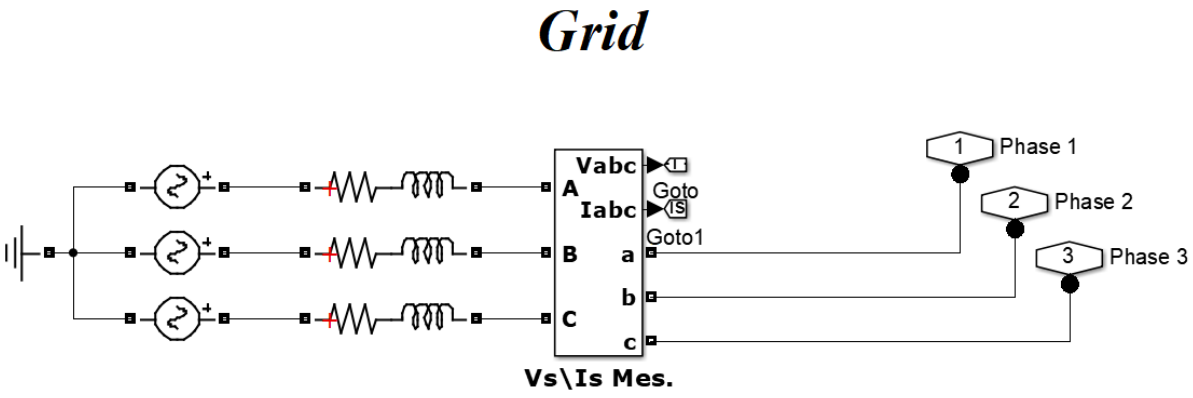

Figure A.42: Grid Connection in the Integrated PV-SAPF System.

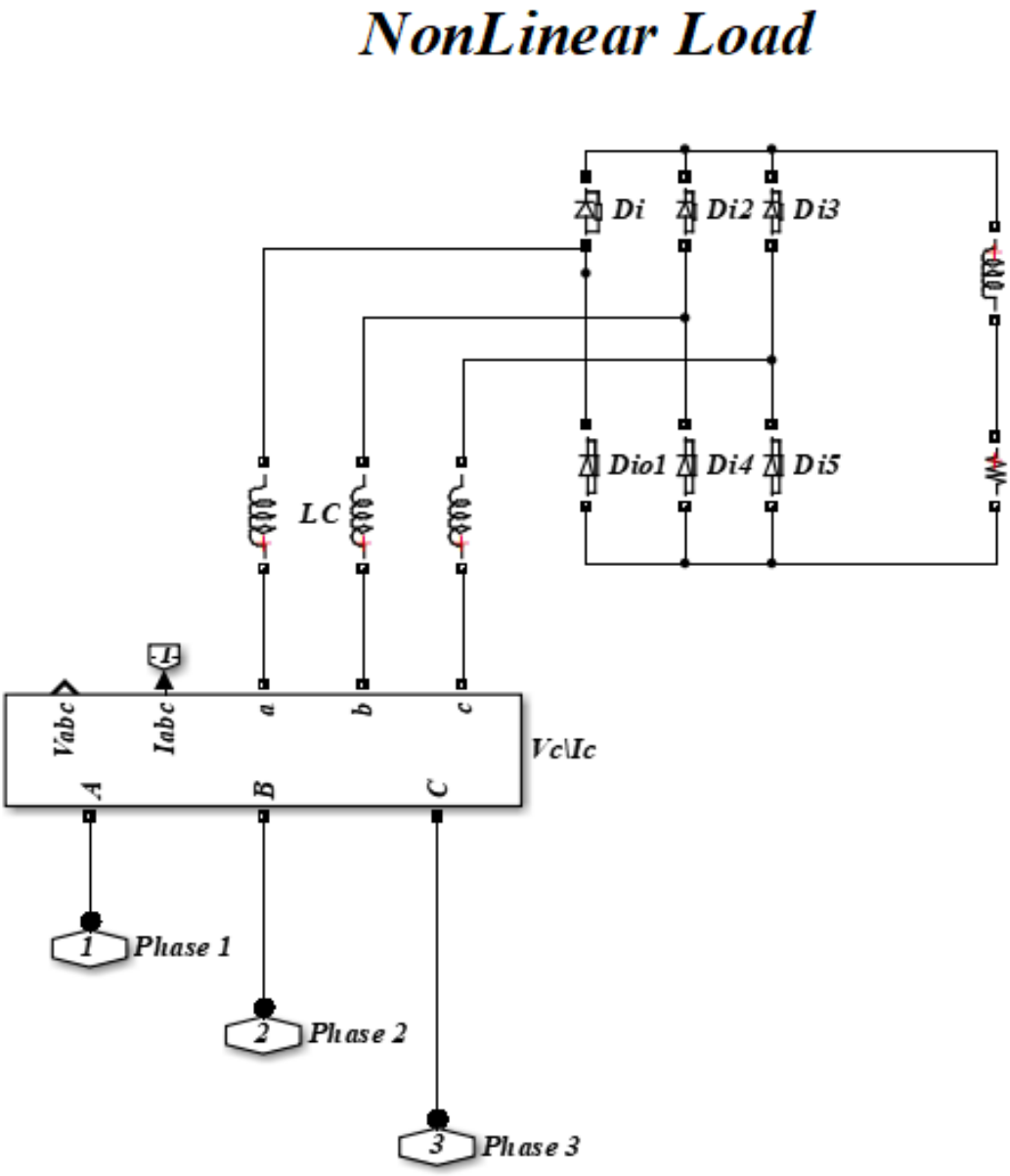

Figure A.43: Nonlinear Load Configuration in the Integrated System

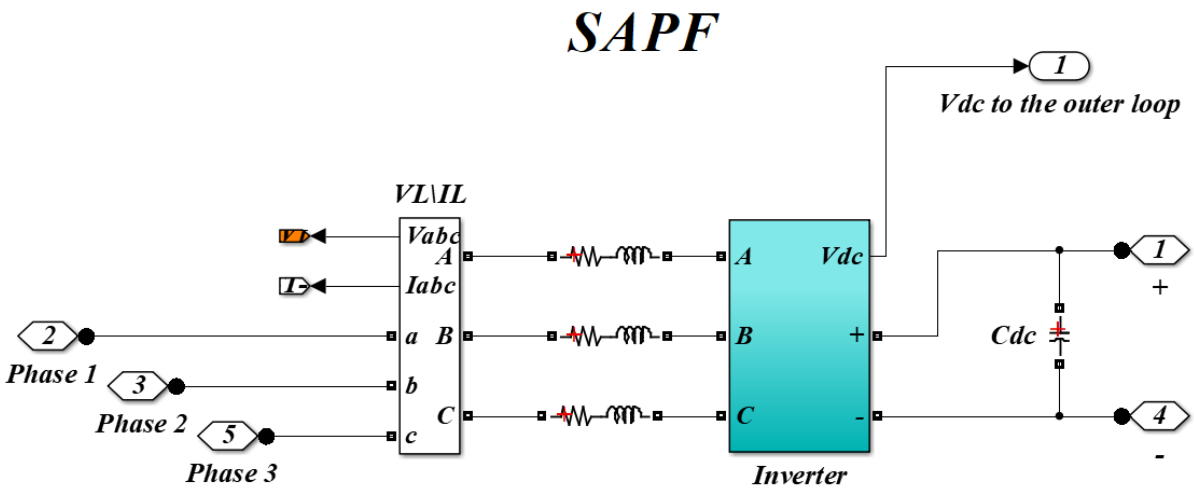

Figure A.44: Shunt Active Power Filter (SAPF) Configuration

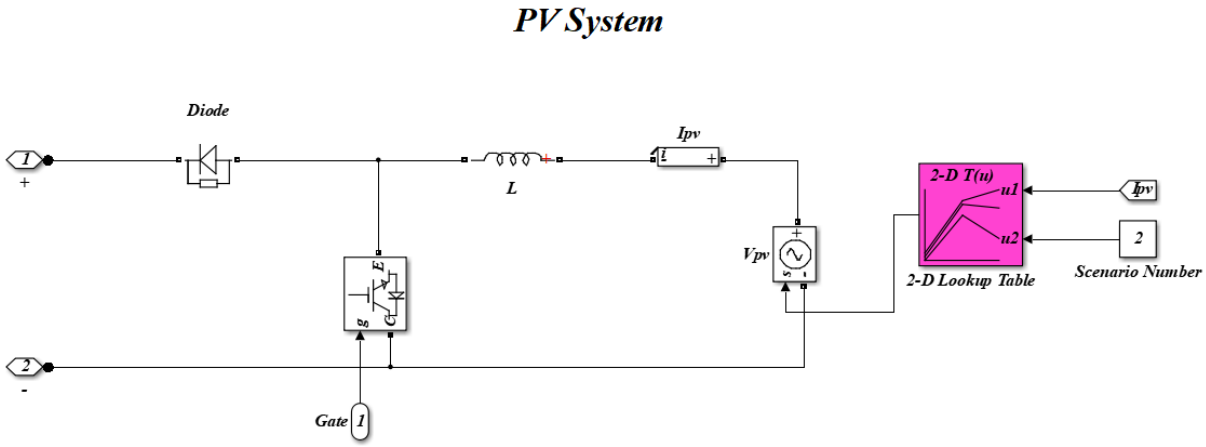

Figure A.45: Photovoltaic (PV) System Block in the Integrated Setup

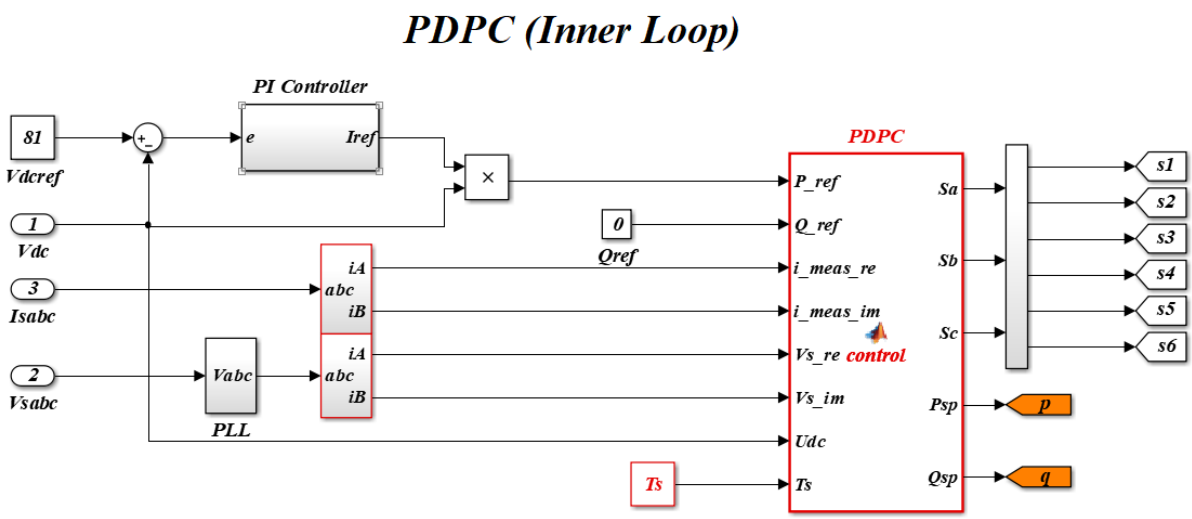

Figure A.46: Predictive Direct Power Control (PDPC) Inner Loop

Our Publication and Communication

Publication

- **D. E. Zabia** et al., "Experimental validation of a novel hybrid Equilibrium Slime Mould Optimization for solar photovoltaic system," Heliyon, vol. 10, no. 20, p. e38943, Oct 30 2024, doi: 10.1016/j.heliyon.2024.e38943.
- F. Abdelmalek, H. Afghoul, F. Krim, **D. E. Zabia**, H. Trabelsi, M. Bajaj, I. Zaitsev, and V. Blazek, "Experimental validation of effective zebra optimization algorithm-based MPPT under partial shading conditions in photovoltaic systems," Sci Rep, vol. 14, no. 1, p. 26047, Oct 30 2024, doi: 10.1038/s41598-024-77488-2.
- **D. E. Zabia**, H. Afghoul, O. Kraa, and F. Krim, "Improving Photovoltaic Grid Integration under Partial Shading by Equilibrium Slime Mould Optimization," Electrotehnica, Electronica, Automatica, vol. 71, no. 3, pp. 15-23, 2023, doi: 10.46904/eea.23.71.4.1108002.
- B. Said, T. Ilyes, K. Okba, and **D. E. Zabia**, "Optimized Passivity-based Control of a Hybrid Electric Vehicle Source using a Novel Equilibrium Optimizer," Electrotehnica, Electronica, Automatica, vol. 71, no. 3, pp. 23-31, 2023, doi: 10.46904/eea.23.71.3.1108003.

Communication

- **D. E. Zabia**, H. Afghoul, and O. Kraa, "Maximum Power Point Tracking of a Photovoltaic System Under Partial Shading Condition Using Whale Optimization Algorithm," in Artificial Intelligence and Heuristics for Smart Energy Efficiency in Smart Cities, (Lecture Notes in Networks and Systems, 2022, ch. Chapter 12, pp. 121-132.
- **D. E. Zabia**, K. Okba, and A. Hamza, "Grey wolf optimization parameter enhancement for tracking the maximum power point of PV system under multiple cluster complex partial shading," presented at the 2022 19th International Multi-Conference on Systems, Signals Devices (SSD), 2022.
- **D. E. Zabia**, H. Afghoul, and O. Kraa, "A novel equilibrium optimizer for tracking the maximum power of a photovoltaic system under non-uniform conditions," presented at the 2022 2nd International Conference on Advanced Electrical Engineering (ICAEE), 2022.

1 F. Abdelmalek, H. Afghoul, F. Krim, **D. E. Zabia**, T. L. Belahcene, and S. A. Krim, "Comparison between MPPTs for PV systems using PO and Grey Wolf controllers," presented at the 2023 International Conference on Advances in Electronics, Control and Communication Systems (ICAECCS), 2023.

- **D. E. Zabia**, O. Kraa, H. Afghoul, T. L. Belahcene, S. A. Krim, and F. Abdelmalek, "Finite Control Set-Model Predictive Control for Grid connected Shunt Active Power Filter," presented at the 2023 International Conference on Advances in Electronics, Control and Communication Systems (ICAECCS), 2023.

- S. A. Krim, H. Afghoul, F. Krim, F. Abdelmalek, **D. E. Zabia**, and T. Lamdjed Belahcene, "Enhancement of Z-Source Inverter Controller for Improvement of Grid-tied PV systems," presented at the 2023 IEEE International Conference on Advanced Systems and Emergent Technologies (ICASET), 2023.

- S. Bedda, O. Kraa, M. Mohammedi, **D. E. Zabia**, I. Tegani, and M. K. Benbraika, "Optimization of Passivity-Based Controller for a Hybrid Vehicle Power Source using the Gray Wolf Algorithm," presented at the 2024 8th International Conference on Image and Signal Processing and their Applications (ISPA), 2024.

- Y. Belhadi, O. Kraa, K. Telli, M. Bahri, M. K. Benbraika, and **D. Eddine Zabia**, "Sizing of fuel cell/supercapacitor hybrid system based on driving cycles and required power," presented at the 2024 8th International Conference on Image and Signal Processing and their Applications (ISPA), 2024.

- T. L. Belahcene, O. Kraa, H. Afghoul, **D. E. Zabia**, B. Med Nassim Bouzidi, and F. Abdelmalek, "Maximum power point tracking based on metaheuristic algorithms of Partially Shaded solar photovoltaic system," presented at the 2024 8th International Conference on Image and Signal Processing and their Applications (ISPA), 2024.

- O. Kraa et **al**., "Control of an electric vehicle speed using RST controller," presented at the 2024 1st International Conference on Innovative Engineering Sciences and Technological Research (ICIESTR), 2024.

- B. M. N. Bouzidi et **al**., "Experimental Test Bench for Direct Current Control Strategy in a Three-Phase Shunt Active Power Filter Based on IP Controller," presented at the 2024 2nd International Conference on Electrical Engineering and Automatic Control (ICEEAC), 2024.

- **D. E. Zabia**, O. Kraa, H. Afghoul, L. Ouchen, S. Bedda, and A. E. Boukhdenna, "Hardware-in-the-Loop Experimental Evaluation of MPPT Algorithms for Partially Shaded Photovoltaic Systems," presented at the 2024 2nd International Conference on Electrical Engineering and Automatic Control (ICEEAC), 2024.

- S. Merah, H. Afghoul, H. Chabana, and **D. E. Zabia**, "Comparison Study between MPPTs for PV System using CS and PSO Under Partial Shading," presented at the 2024 2nd International Conference on Electrical Engineering and Automatic Control (ICEEAC), 2024.

- T. L. Belahcene, H. Afghoul, O. Kraa, **D. E. Zabia**, F. Abdelmalek, and B. M. Nassim Bouzidi, "Enhancing Active Harmonic Compensator by Using Fuzzy-PI Controller," presented at the 2024 2nd International Conference on Electrical Engineering and Automatic Control (ICEEAC), 2024.

- F. Abdelmalek et **al.**, "Experimental Implementation of Direct Power Control for a SAPF with a PI Controller Tuned Using Grey Wolf Optimization," presented at the 2024 International Conference on Advances in Electrical and Communication Technologies (ICAECOT), 2024.

- A. E. Boukhedenna, H. Afghoul, **D. E. Zabia**, B. M. N. Bouzidi, F. Abdelmalek, and L. Ouchen, "Experimental Test Bench for Power Quality Enhancement Using Direct Current Control Based on Fuzzy PI Controller," presented at the 2024 1st International Conference on Electrical, Computer, Telecommunication and Energy Technologies (ECTE-Tech), 2024.